THE ACOUSTIC PROPERTIES OF GASSY SOIL

A thesis submitted to

The University of Oxford

by

Trevor Noel Gardner BSc.

St. Catherine's College

for

The Degree of Doctor of Philosophy

Hilary 1988

ABSTRACT

TITLE: The Acoustic Properties of Gassy Soil

AUTHOR: Trevor Noel Gardner

COLLEGE: St. Catherine's College

DEGREE: D Phil

TERM SUBMITTED: HILARY, 1988

Compression wave sound speed and attenuation measurements are made in the laboratory over frequencies in the range from 10 kHz to 1 MHz on samples of estuarine silty clay that have been provided with varying amounts of uniformly distributed gas bubbles. The soil can be idealised as a two phase material of spherical gas pockets within a matrix of saturated soil, where the pocket sizes are in the range from 100 to 2000 μm diameter. It is shown that the acoustic response of this soil is dominated by the gas fraction and bubble size of the gas phase, and by the elastic moduli of the matrix phase, within the frequency range that causes bubbles to pulsate radially (resonate). Below this range, it is shown that the sound speed response is not significantly affected by bubble size, except close to the saturated soil condition.

The gas fraction and bubble size distribution of each sample is measured and used, with values of the appropriate elastic moduli from the literature, to provide curves from current theory. The theory is evaluated in comparison to the experiment results, and proposals are made, which may provide the basis for the prediction of the gas fraction and bubble sizes of sea-bed sediments that are suspected of containing gas. Such a process would involve the use of an acoustic probe to obtain in situ sound speed and attenuation measurements using the signal analysis techniques developed in this study.

ACKNOWLEDGEMENTS

I would like to thank my supervisor Dr. Gilliane Sills, who provided help and encouragement throughout the research, and Dr. N.G. Pace (University of Bath) and Dr. G.A.D. Briggs (University of Oxford) for technical advice whenever it was needed.

I am grateful to the support staff of the soil mechanics group who constructed all the mechanical and some of the acoustical equipment. The financial support of S.E.R.C. and of Marconi Underwater Systems is gratefully acknowledged, as is the assistance of Miss Sukie Clark in typing the thesis.

Finally, I would like to thank my wife Maryam, and my children, Adelina, Selina and Daniel, for the understanding that they have shown through a long period during which I have not been able to spend time with them. Special thanks are reserved for my wife who has worked to support us and provide for us. This work is therefore dedicated to her.

CONTENTS

Abstract		i
Acknowledgements		ii
Notation		iv
List of Figures		vii
List of Tables		xi
Chapter 1	INTRODUCTION	1
Chapter 2	DESIGN AND OPERATION OF THE MECHANICAL SYSTEM	22
Chapter 3	DESIGN AND OPERATION OF THE ACOUSTICAL SYSTEM	52
Chapter 4	THE BUBBLE SIZE DISTRIBUTION (BSD) MEASURING SYSTEM	103
Chapter 5	THE RESEARCH TESTS	125
Chapter 6	ACOUSTIC RESULTS - SOUND SPEED (At resonance)	129
Chapter 7	ACOUSTIC RESULTS - ATTENUATION	152
Chapter 8	ACOUSTIC RESULTS - SOUND SPEED (Below resonance)	162
Chapter 9	CONCLUSIONS AND RECOMMENDATIONS	172
Figures		175
Tables		230
Appendices		240
References		244

NOTATION

A/W interface = standard air/water interface pressure chamber

B.S.D = bubble size distribution

BUS = constant potential supply rail

CW = continuous wave

SW = square wave

TTC = transit time correction ((S) before this abbreviation means 'spike')

MTT = measured transit time ((S) before this abbreviation means 'spike)

TTT = true transit time ((S) before this abbreviation means 'spike')

S.E.M = scanning electron microscope

ω = rotational frequency ($=2\pi f$)

ω_o = resonant rotational frequency ($=2\pi f_o$)

ρ = bulk density

ρ_g = gas density

ρ_m = mineral density

ρ_w = water density

γ = ratio of specific heats

ρ_s = sediment density

σ_1 = total stress (vertical stress applied by piston)

λ = wavelength ($=c/f$)

ϕ_f = correct phase angle displacement at the coincident point frequency

a = zero datum to leading edge delay difference (μs)

a_i, a_r, a_t = voltage amplitude of incident, reflected and transmitted waves, respectively

c = sound speed

c_g = conductivity of gas

c_o = sound speed in saturated sediment

c_s = shear wave speed

d = damping constant

d_r = radiation damping constant

d_f = friction/viscous damping constant

f_o = resonance frequency

f = frequency

k = wave number ($=2\pi/\lambda$)

l = 1,M (range of size categories of bubbles)

l_{al} = length of aluminium (transmitting transducer)

l_s = length of steel (transmitting transducer)

l_a = thickness of araldite (transmitting transducer)

n_g = gas porosity (= $\frac{\text{volume of gas}}{\text{total volume}}$) or gas fraction

n = total void porosity (= $\frac{\text{volume of voids}}{\text{total volume}}$) or total void fraction

n'_g = fraction of sediment pore volume occupied by gas

r_o = equilibrium bubble radius

r = bubble radius

r_{sb} = radius of curvature of menisci

tc and degc = time delay and phase shift of calibration signal

ts and degs = time delay and phase shift of soil signal

u_g = pore gas pressure

u_w = pore water pressure

Cu_{sat} = the undrained shear strength of a saturated soil

D = diameter (transmitting transducer)

D_b = largest established sphere diameter

D'_b = observed sphere diameter

G = shear modulus

G^* = complex shear modulus

G' = imaginary part of complex shear modulus

K = bulk modulus

K_g = gas bulk modulus

K_m = mineral particle bulk modulus

K_w = water bulk modulus

K'_w = water bulk modulus, modified by gas

L = transducer face separation (path length of a medium)

L_R = loss due to reflection

N_i = number of images

P_o = ambient hydrostatic pressure (back pressure)

Q = reciprocal specific dissipation function

R = Rayleigh reflection coefficient

S_p = specific heat at constant pressure

S = sampling speed

S_s = average space between sections (in pixels)

S_d = degree of saturation

T = signal period (μs)

T = surface tension at menisci

LIST OF FIGURES

1.1 (a) The large bubble model (b) The small bubble (compressible fluid) model (c) Bubble curvature

1.2 (a) In situ gassy soil (muddy sand) core sample, North Sea (Fannin, 1979) (b) In situ gassy soil, Bristol Docks

1.3 Acoustic blanking (Fig 15, Fannin, 1974)

1.4 (a) Sound speed versus frequency (Anderson 1974)

(b) Attenuation versus frequency (Anderson 1974)

(c) Sound speed versus gas fraction (Anderson 1974)

1.5 Laboratory gassy soil (Gas fraction = 0.12, sample depth = 3 cm)

2.1 (a) Outlines diagram of Cell 2

(b) The consolidation cell (Schematic diagram)

2.3 Piston face (Cell 2 only)

2.4 Top plate and transmitting transducer

2.5 (a) Elevation to the reaction plate assembly

(b) The acoustic cell and sling device

2.6 (a) Acoustic transducers (i) transmitting (ii) receiving

(b) Layout of the mechanical system

2.7 (a) The flow restrictor

(b) Pressure variation during loading

2.8 (a) Volume change of Cell 1 and burettes (500 kPa)

(b) Volume change of Cell 1 (100 kPa) with, and without, perspex creep and absorption

(c) Volume change of Cell 2 (25 kPa) (use for cell 1 also)

2.9 Cyclic loading tests (a) Void ratio versus load

(b) Gas fraction versus load

2.10 Pore fluid pressure versus time

3.1 Layout of acoustic system

3.2 The pressure wave propagation pattern

3.3 (a) Transducer (20-40) kHz

(b) Transducer (40-95) kHz

(c) Transducer (95-200) kHz

3.4 (a) Waveform of S.W pulse (input to the transmitting transducer)

(b) Frequencies spectrum of S.W pulse (input to receiver)

(c) Received signal waveform of S.W pulse (input to receiver)

3.5 (a) Waveform of spike (unloaded output of power drive module)

(b) Frequency spectrum of spike (input to receiver) Cell 1

(c) Received signal waveform of spike (input to receiver) Cell 1

3.6 Waveform of CW plus spike (unloaded output of power drive module)

3.7 Transducer travel time delays

3.8 (a,b,c,d) The transit time correction system

(e) Example of the model CW curve fitting

3.9 Multiple reflection within the transmitting transducer

(a) Received waveform showing multiple arrivals

(b) Internal path lengths and transit times

(c) Example of beat waveform

3.10 Phase displacement reference in the FT Method

3.11 Rotation diagrams for cumulative phase displacement

3.12 (a and b) Beat frequency components for a gassy soil (diagrammatical)

3.13 Beat frequency components for a gassy soil (actual)

(a) Fourier transform received through hexane

(b) Fourier transform received through gassy soil

(c) Attenuation versus frequency

(d) Received beat waveform through gassy soil

3.14 (a to e) Actual received waveforms during staged decoupling

3.15 (a to g) Contributions to the combined received signal waveform

3.16 Relative penetrations of CW and SW pulse signals

3.17 Received waveform records of the CW plus spike marker system

3.17 (a) No bandpass filter

(b) Bandpass filter at 15/25 kHz passband

4.1 Resin-impregnation apparatus

(a) feeder arm

(b) assembled apparatus

4.2 SEM sample (mounted and carbon coated)

4.3 SEM video image of gassy soil

4.4 (a) Frequency versus luminance intensity of gassy soil

(b) Boundary treatment for SEM images

4.5 Measurement accuracy of the largest sphere diameter

4.6 (a) SEM image of a single gas void (6μm ϕ)

(b) SEM image of a saturated soil matrix surrounding a gas pocket (250 μm ϕ)

4.7 Sphere size distribution plots for different soils

4.8 (a to h) BSD curves

5.1 (a to h) BSD histogram - cumulative, grouped bin sizes

5.2 (a to h) BSD histogram - single bin sizes

6.1 (a to g) (i) Soil Fourier transform

(ii) Calibration Fourier transform

6.2 (a to d) Experiment results - sound speed (at resonance) versus frequency

6.3 (a to h) Theoretical results - sound speed (at resonance) versus frequency

6.4 Varying ambient hydrostatic pressure (at resonance) (sample E50-1)

6.5 Varying reciprocal specific dissipation function (at resonance) (sample E50-1)

6.6 (a) Varying bulk modulus (at resonance) (sample E50-1)

(b) Varying shear modulus (at resonance) (sample E50-1)

6.7 Experiment/literature results comparison for sound speed (at resonance)

7.1 (a to d) Experiment results - attenuation (at resonance) versus frequency
(e to g) Extended range of attenuation results (minimum values only)

7.2 (a to h) Theoretical results - attenuation (at resonance) versus frequency

7.3 Varying ambient hydrostatic pressure - at resonance (sample E50-1)

7.4 Varying reciprocal specific dissipation function - at resonance (sample E50-1)

7.5 (a) Varying bulk moduli - at resonance (sample E50-1)
(b) Varying shear modulus - at resonance (sample E50-1)

7.6 Experimental/Literature results comparison for attenuation - at resonance

8.1 Experiment and theory results - sound speed (below resonance versus gas fraction)

8.2 Varying ambient hydrostatic pressure - Anderson's compressible fluid model (below resonance)

8.3 Bulk shear wave speed versus gas fraction

8.4 Theoretical reflection coefficients versus grazing angles (below resonance)

8.5 Theoretical losses at a mudline interface versus grazing angle (below resonance)

LIST OF TABLES

3.1 Transmitting transducer internal dimensions

3.2 Sound speed measurement accuracy - Leading Edge and TTC Methods

3.3 Waveform phase position delay due to beat effect

3.4 TTC values for distilled water (varying frequency and path length) - SW pulse waveform

3.5 TTC calibration results

(a) Cell 1

(b) Cell 2

3.6 TTC values for distilled water (varying frequency and path length) - CW waveform

4.1 Comparison between raw input and reconstructed data

4.2 Gas contents of the specimens in Figure 4.7

4.3 Soil confining pressures for the specimens in Figure 4.8(d)

4.4 Soil confining pressures for the specimens in Figure 4.8(e)

5.1 Properties of the soil used in the research programme tests

6.1 Resonance frequencies of bubble sizes (calculated using Anderson's (1974) equation A8)

6.2 ($f_o r$) products from experiment sound speed results

7.1 ($f_o r$) products from experiment attenuation results

8.1 Theoretical values of elastic moduli (below resonance)

8.2 Theoretical values of (K) for varying (P_o) - Anderson's compressible fluid model (below resonance)

CHAPTER 1 - INTRODUCTION

1.1 WHY THE INTEREST IN SEDIMENT ACOUSTICS?

1.2 WHAT IS IN SITU GASSY SOIL?

- 1.2.1 The model analogy
- 1.2.2 The origins of gassy soil
- 1.2.3 The size and shape of bubbles
- 1.2.4 Where gassy soil may be found

1.3 THE ACOUSTIC RESPONSE OF GASSY SEDIMENTS FROM THE LITERATURE

- 1.3.1 The work of Anderson (1974)
  - 1.3.1.1 Sound speed below the resonance frequency range
  - 1.3.1.2 Sound speed within the resonance frequency range
  - 1.3.1.3 Attenuation within the resonance frequency range
    - 1.3.1.3.1 Sound speed and attenuation curves from theory
  - 1.3.1.4 Reflectivity and scatter within the resonance frequency range
- 1.3.2 The work of others

1.4 THE TEST MATERIAL (Laboratory gassy soil)

1.5 THE AIMS OF THIS RESEARCH

1. INTRODUCTION

1.1 WHY THE INTEREST IN SEDIMENT ACOUSTICS?

Over the past few years the demands of industry have generated interest in the structure and engineering properties of marine sediments. Motivation has come from the oil industry in connection with the foundation design of offshore structures and for drilling in exploration and appropriation of oil and gas. Site investigation techniques have been developed which contend with the problem of accessibility provided by the water environment. Methods consist of remotely operated tools such as cone penetrometers, piezometers and acoustic probes, and of indirect methods such as acoustic reflection techniques.

Acoustic instruments are useful since the values of sound speed and attenuation can be used to indicate the type and structural condition of sediments. Hamilton (1972, 1982) has assembled sound speed and attenuation tables of measurements correlated to the classification properties of saturated sediments such as mean grain size, porosity and density. Further work on identification has been carried out by the analysis of the level of coherence of received sonar signals, reflected off the mudline, related to the r.m.s. grain sizes of saturated sediments. Contributions here have been made by Clay and Leong (1974) using scattering theory, Le Blance et al (1980) and Milligan et al (1978), generating porosity, density and soil classifications. Dunsiger et al (1981) adopt the scatter coherence function, Denbigh and Tucker (1983) use the autocorrelation function and Stanton (1983) uses the correlation area for extra discrimination between topography and relief.

The requirements of other areas of industry have brought about further developments in acoustic instruments such as sub-bottom profilers, high resolution sonar for locating buried pipelines, explosive mines and mineral

deposits, or long distance signal communication via the sea floor. All of these uses depend on a comprehensive knowledge of the levels of acoustic response of sediments due to signal transmission and reflection.

This interest has led to the development of mathematical models to describe sound speed and absorption (loss) such as the linear viscoelastic solid theory of Bucker and Morris (1964), the 'squeeze film' frequency dependent viscous dissipation of energy of Stoll (1980, 1988) and allowance for pore size in the theory of Biot (1956, 1962), presented by McCann and McCann (1985). Models for loss due to specular reflection or transmission at the interfaces of beds have been suggested by Strutt, Rayleigh (1877) assuming a liquid/liquid interface. MacKensie (1960) adopts Rayleigh theory and an allowance for absorption losses at the interface, and Stoll and Kan (1981) use a liquid/porous viscoelastic interface theory extended from that of Biot. Multiple interfaces can be dealt with by Brekhovskikh (1960) and further general theory and models have been developed more recently by Hastrup (1980), Thomson (1983), Fryer (1978) and Chapman (1983). In addition to specular reflection at interfaces, models have been devised to assess the scatter loss due to interface roughness. Eckart (1953) introduces the Gaussian probability function to describe the power spectrum of the signal reflected from a rough bottom. Clay, Medwin and Wright (1973) further demonstrate the application of this function, while Clay and Medwin (1977) developed theory based on the use of Helmholtz-Kirchoff integrals and Tappert (1977) considers range dependence in a parabolic equation model. Complete single interaction scattering models are given by Novarini and Medwin (1978) and Kinney and Clay (1982). Further models are provided by Tolstoy (1979, 1982), Medwin (1983), Rutherford and Hawker (1978), Rutherford et al (1979) and Thorn and Pace (1983), to mention only a few of the vast number that have become available during the last 10 years.

In order to assess the validity of the above models for reflection and scatter, laboratory and field measurements are available for comparison. Unfortunately, the authors of models have not always used independent experimental data for corroborating their own work, although this may be due to the difficulty in selecting exactly comparable data. Breslau (1965, 1967) and Hastrup (1970) investigated signals normally incident at the mudline interface while MacKensie (1960) provides data for varying angles of incidence. Further results are given by Chapman (1983), Frisk et al (1981) and Muir et al (1979) and backscatter, or reverberation, loss is measured by Boehme et al (1985), Chotiros et al (1985) and McKinney and Anderson (1964).

During the development of the theory and practice of acoustic work on saturated sediments some speculation has arisen over the acoustic response of soils containing gas. Field tests have indicated large variations in sound speed, huge values of attenuation and large proportions of reflection and scatter in sediments which have been found to contain free gas as discrete bubbles. Further speculation has arisen over records from sub-bottom profiling and high resolution sonar scatter surveys of acoustically impenetrable localised areas within regions such as river deltas, harbours and lakes where soft silty clay sediments are likely to contain gas. Concern has been expressed over the consequences of siting offshore structures on these sediments and also over the hazards of drilling through them for the offshore oil and gas industry. The development of an expertise in predicting the acoustic response of such materials could therefore be of value to industry. Further development of the principles of acoustic theory for gassy soil will also have a worthwhile offshoot value in the interpretation of sub-bottom profiling records and the design of high resolution sonar equipment to cope with the additional problems of energy loss in a region where gassy sediments exist.

1.2 WHAT IS IN SITU GASSY SOIL?

1.2.1 The model analogy

Sediments which consist of the three phases of gas, liquid and solid may be modelled as two phases - a saturated soil matrix containing free gas-filled pockets greater in diameter than the soil particles (Figure 1.1(a) the large bubble model) or a solid skeletal framework with free gas bubbles wholly contained within a pore fluid, (Figure 1.1(b) the compressible fluid, or small bubble model). It is feasible that both types of sediments exist separately or as a combination and it is shown by Wheeler (1986) that the engineering response of the separate sediment types is significantly different. By using elastic moduli from Wheeler (large bubble model) and Anderson's (1974) (compressible fluid model) it will be shown that the acoustic response of the separate sediment types is also significantly different. Thus, the subject of this report will remain exclusively that of the large bubble model, since it will be shown that this is appropriate to the material to be tested. It must also be stated that since a silty clay sediment would be unlikely to have interstitial pore sizes greater than 10 microns, the compressible fluid model of gas wholly surrounded by water may not be practical, because of a restriction to the minimum possible size of a gas bubble in water as will be seen in section 1.2.2.

Gas which wholly exists as dissolved gas within the pore fluid is not discussed and has no influence on engineering or acoustic properties providing it remains in solution during any changes in consolidation and ambient hydrostatic pressure.

1.2.2 The origins of gassy soil

The gas can be produced by biogenic, thermogenic and vulcanogenic processes. The latter two are less common and entail the thermal cracking of complex

organic and inorganic compounds at great depth (thermogenic) and submarine volcanic and geothermal behaviour (vulcanogenic). In oxygen-depleted soil biogenic gas is produced from the anaerobic decomposition of organic matter by nitrate, sulphate and carbonate reducing bacteria which produce nitrogen with ammonia, hydrogen sulphide and methane respectively (Stainer et al, 1963). Since aerobic decomposition of organic matter in the top metre of sediment quickly depletes the store of available oxygen, anaerobic activity producing the above gases can prevail up to within 1 cm of the mudline (Kanwisher, 1962a). Although all three bacteria may exist in a sediment usually only one will predominate. Methane forming bacteria tend to dominate in freshwater due to the lesser nitrate and sulphate contents, whereas hydrogen sulphide formers are most common in marine conditions because of concentrated sulphate ions. Gas increases in concentration within the pore fluid, causing slow diffusion into the overlying water. It may however combine with metal cations to form authigenic minerals or, more commonly, produce gassy soil when free gas bubbles form as supersaturation is reached for one of the gases (Mortimer, 1941; Kanwisher, 1962a and b; Anderson,1974). Other dissolved gases may then diffuse across the bubble boundary until diffusion equilibrium is reached. A more detailed analysis of these processes is presented in Claypool and Kaplan (1974), Martens and Berner (1974) and Mechalas (1974).

1.2.3 The size and shape of bubbles

The size of bubbles commonly observed, as reported by Anderson (1974), is in the range 0.5 to 5 mm diameter. Blanchard and Woodcock (1957) state that 0.010 mm diameter is a theoretical minimum for bubbles in water at any degree of supersaturation. However, for bubbles formed in sediments, where menisci are in contact with solid particles, the curvature of the bubble wall, and therefore the gas pressure, may not correspond to that of

spherical bubbles of equal volume. Figure 1.1(c) illustrates the nature of the menisci where curvature is linked to gas pressure by the equation:

$$u_g = \frac{2T_m}{r_{sb}} + u_w \qquad 1.0$$

where u_g = pore gas pressure

u_w = pore water pressure

T_m = surface tension at menisci

r_{sb} = radius of curvature of menisci

Hence smaller volumes than the 0.010 mm diameter spheres may exist without dissolving into the pore fluid.

The bubble size distribution (B.S.D) measurements for laboratory soil at different confining pressures, which will be shown later, indicate that larger bubbles are created at lower pressures. Hence maximum size seems to be controlled by consolidation and is possibly effected by the soil characteristics, in terms of particle size and shape, since this influences menisci curvature and soil permeability. Both factors will control the ability of the bubble to deform the saturated soil matrix locally, as it increases in volume from the diffusion process at the gas/water interface during formation of the pocket. It is perhaps reasonable therefore to expect large bubbles to develop in surficial deposits that are loosely compacted and less resistant to local plastic deformation. This progressive deformation may ultimately lead to fractures opening between bubbles, and gas escaping upwards through interconnected pockets due to buoyancy.

The shape of discrete bubbles would be expected to be spherical in a homogeneous, isotropic matrix because of the pressure of the growing volume

of gas causing the matrix deformation. In practice the structure of the matrix, due to the settlement process is anisotropic, resulting in a stress/strain behaviour which may cause bubbles to be elongated in the weaker direction of the bedding plane (horizontal, for recently deposited sediments). This elongation may be increased by the rise in consolidation stress as further sediments are deposited over those which are producing gas.

1.2.4 Where gassy soil may be found

It is noted from the literature that gassy soil is more commonly found in loosely compacted silty clay sediments which contain organic matter, such as lake beds, river deltas and harbours where tributary streams have always brought a supply of organic matter with the silt and clay particles to be settled out together in comparatively slow moving, deeper waters. Whelan et al (1976, 1977) discuss gas charged sediments in the Mississippi Delta. Esrig and Kirby (1977) and Whelan and Lester (1980) also report finding gas in the Gulf of Mexico, although Chiou Wen-Au (1981) reports the taking of pressurized cores in the Delta without clear evidence of gas pockets in the sediment structure (despite plentiful gas in the pore water). Hochstein (1970) investigates free gas in sediments in Suva Harbour, Fiji, Egerton (1965) gas bubbles in surface layers in Boston Harbour, and Schubel (1974) interstitial gas bubbles in Chesapeake Bay. Gassy soil is found by Anderson et al (1971) in a study of the three freshwater lakes of Central Texas, Travis, Austin and Bastrop, with complementary work being provided by Muir (1972) and Jones et al (1964) for Lake Travis and Anderson et al (1968) for the Brazos River (Texas). Grindley (1955) discussed gas in the mud of the River Thames, England. McCartney and Bary (1965) looked at gas bubbles rising from the sediment of Saanich Inlet, British Columbia and found simularities with echo-sounding records from Ohle (1959, 1960) at the Great Plon Lake. Discoveries at sea have been reported by Fannin (1979), showing

gas bubbles in a core sample from the Irish sea, as illustrated in Figure 1.2(a) and in the sub-bottom profiling records of Figure 1.3. Also Jones et al (1985) investigated gas concentrations in pore water in the Western Irish Sea and Holyhead Harbour, Anglesey.

Mid-ocean sites are also the source of much discussion in the literature regarding gas induced erosion features recorded by sub-bottom profiling. The features include 'mud volcanoes' in the Caspian Sea (Yakubov et al, 1971), 'gryphons and salses' in various regions (Newton et al, 1980), 'pockmarks' in the Scotian Shelf, Aegean Sea, Orinoco Delta and South China Sea (King and Maclean (1970), Newton et al (1980), Butenko and Barbot (1979) and Platt (1977) respectively) and coast parallel depressions, elongated depressions or terraces (Hovland, 1984). Also on sub-bottom profiling records, features such as 'acoustic blanketing' and 'phase reversal' are discussed in connection with shallow gas in the North Sea (McQuillin et al 1979a). Gas in sediment due to geothermal activity is recorded by Duncan and Pantin (1969) and from the study of sewage and waste water treatment by McKinney (1962), microbiology by Zobell (1946) and Wood (1946) and geochemical element cycling by Hutchinson (1957), Erikson (1960) and Jensen (1960).

In addition to the above literature, the author has found free gas bubbles to be present in gravity cores taken in the region of Bristol Docks. Figure 1.2(b) shows a sample from a 0.5 m depth of sediment in around 3 meters of water. Gas pockets are 0.5 to 1.0 mm in diameter and the measured degree of saturation is 99.5%.

Other field tests on the River Cherwell, (Oxford) and Holyhead Harbour (Anglesey) did not indicate any gas pocket structure despite the liberation of bubbles when mud was disturbed. Two examples of gassy sand have also been found at Marazion (Cornwall) and Porthcawl (Wales), known in the

literature as 'cavernous sands'. They have a bubble size distribution (B.S.D) range of approximately 1 to 10 mm diameter and occur in beach areas where air is entrapped within pockets in the sand by a rising tide. Continual draining and flooding then causes the bubbles to enlarge. Hoyt and Henry Jr. (1964), Trefethen (1941) and Emery (1945) provide a detailed analysis.

1.3 THE ACOUSTIC RESPONSE OF GASSY SEDIMENTS FROM THE LITERATURE

1.3.1 The work of Anderson (1974)

The most notable contribution to date has been made by Anderson (1974) who developed equations for compression wave sound speed and attenuation and carried out laboratory experiments using plastic air-filled bubbles in order to verify the effects of bubble resonance. The equations are not derived for gassy soil but are modified from those derived and tested for use with other materials. It is believed that there are shortcomings in the modifications and these will be discussed in this section. However, it will be useful to present theoretical results, using Anderson's theory alongside the experimental work of the thesis, to illustrate the disparity between the two and therefore provide the means of modifying further the equations outside the scope of this research project.

Bubbles in all media resonate, or pulsate, radially at a frequency related to their size. Anderson shows that bubble resonance dominates the sound speed, attenuation and reflectivity of loosely compacted gassy soils which can be found in harbours, lakes and river deltas and contributes to a lesser extent, for example, in the response of those gassy ocean sediments which are overconsolidated. The material is therefore dispersive. This means that its sound speed response is frequency dependent in the range affected by bubble resonance. The frequency range extends from the point at which resonance effects begin to be apparent (where bubble radii are two orders of

magnitude less than wavelengths) to the point at which they cease (where radii approximately equal wavelengths). Below this range of frequency, sound speed remains constant at a value commensurate with the bulk properties of the material, and above this range, it remains constant at a value commensurate with the properties of the saturated soil matrix only (where the sound speed of a saturated soil is around 1500 m/s). The acoustic properties of gassy soil are therefore modelled in two sections: 'below resonance' and 'at resonance' while the region 'above resonance' simply provides a saturated soil response.

1.3.1.1 Sound speed below the resonance frequency range

Anderson uses the wave equation which is the exact solution of the equation of motion for an elastic solid of homogeneous and isotropic behaviour:

$$c = \sqrt{\left[\frac{K + 4/3\ G}{\rho} \right]} \qquad (1.1)$$

where: c = sound speed

K = bulk modulus

G = shear modulus

ρ = bulk density.

Spitzer (1943) shows that, below resonance, only the bulk properties of the material contribute to the acoustic response. It is therefore reasonable for Anderson to adopt the equations for an elastic solid, provided the bulk properties (K) and (G) can be defined for a gassy soil. However, the theory that Anderson uses to provide the values of these properties is open to question. Rather than derive suitable equations to define (K) and (G) for a gassy sediment, he chooses to bracket any possible range of values by upper and lower bounds. These upper and lower bounds are provided by theory relevant to a saturated soil with a compressible fluid, to model the

behaviour of relatively well consolidated gassy soil, and by the theory of a soil suspension to indicate the behaviour of a loosely compacted gassy soil, respectively.

The lower bound values of (K) and (G) are derived from the suspension theory of Wood (1930), in which G = 0 and where (K) and (ρ) are defined in equations A1 and A2 of Appendix A which suggests that each phase contributes to the composite property in proportion to its volume. The use of G = 0 and equations A1 and A2 however is unlikely to represent even the softest of sediments at the lower bound end, since suspension theory cannot hope to generate the response of a soil with some shear rigidity.

The upper bound values of (K) and (G) make use of Gassman (1951) where (K) is defined using equations A3 and A4 of Appendix A. The value of dynamic (G) is taken from measurements by Smith (1973) and Hamilton (1971) which are for saturated, not gassy, sediments, and Gassman's dynamic (K) is relevant to a two phase material appropriate to saturated soil. It is amended to allow for the presence of gas by redefining the bulk modulus of water (K_w), as shown in equation A5 of Appendix A, using the theory of proportional contribution by phase volumes. This adjustment causes the gassy sediment response to be that of the compressible fluid, while (ρ) remains as in equation A2. Section 1.2.1 discusses the unsuitability of the compressible fluid model for the laboratory gassy soil and its doubtful relevance to the majority of in situ gassy soils. Furthermore, the results of the test programme reported later will show that both upper and lower bounds are largely inappropriate.

1.3.1.2 Sound speed within the resonance frequency range

For the case of 'at resonance', the wave equation of a single phase elastic solid is not appropriate. It is necessary to develop an equation directly for gassy soil which reflects the domination of the acoustic response by gas bubble dynamics. However, Anderson has chosen only to amend the sound speed equation for gas bubbles in water in the same manner that the equation derived for the resonance frequency in water differs from that derived for fish tissue. This he does as follows.

Minneart (1933) developed an equation for the resonance frequency of single-sized bubbles in liquid for adiabatic conditions from energy considerations. Anderson follows Devin's (1959) suggested adjustment in allowing for the effects of varying to an isothermal condition for small bubbles and low frequencies by the introduction of the polytropic coefficient (A), to give equation A6 (Appendix A). The coefficient is derived by considering the changes of state during the gas bubble resonance action which is considered as a thermodynamic system. Anderson then uses the equation of Andreeva (1964), developed for bubbles in fish tissue, given as equation A7 (Appendix A). He then adds (A) to Andreeva's equation in the same manner as the adjustment to Minneart's, as shown in equation A8 (Appendix 8).

The addition of the term $(\frac{4G}{3})$ to (γP_o) appears to provide all that he requires to allow for the shear rigidity of an elastic solid (equation A7) from the G=0 condition of a water medium (equation A6). Anderson appears to use this observation to convert Silberman's (1957) equation (corroborated by measurement) for the sound speed of water containing single-sized bubbles to that of a gassy sediment:

$$\left(\frac{c_o}{c}\right)^2 = \frac{1}{2}\left(1 + W X_1\right)\left\{1 \pm \left[1 + \left[\frac{W Y_1}{1 + W X_1}\right]^2\right]^{1/2}\right\} \quad (1.2)$$

$$\text{where} \quad W = \frac{K}{\gamma P_o + \frac{4G}{3}}$$

The equations to derive X_1 and Y_1 are given in equations A9 and A10 (Appendix A), in addition to the other parameters already described. Dynamic (K) is calculated using Gassman's A3 and A4 where (K_w), the dynamic bulk modulus of water, is used instead of (K'_w). It is correct to use Gassman's (K) for equation 1.2 since it is the dynamic bulk modulus of a two phase (solid/liquid) porous material such as a saturated soil, rather than a gassy soil. Silberman's equation was derived for bubbles in water where (K) is the modulus of the host material, which is water; it is therefore appropriate that, for bubbles in a saturated soil matrix, (K) should be the modulus of the saturated host material. The same argument applies to the sediment dynamic shear rigidity (G^*), in equation A10, the bulk density (ρ_s) in equation A8, and the total void porosity (n), in equation A4, where the values to be used are also appropriate to a saturated soil.

In order to include absorption effects, the moduli were considered to be complex. Also Spitzer (1943), on which Silberman's (1957) equation for sound speed is based, recommends that the theory is applied only where the average distance between bubbles is 5r, or greater. This recommendation avoids considering the effects of the kinetic energy of oscillation, and the external pressure producing the oscillation between bubbles, when signal frequencies are higher than resonance. A 5r average separation corresponds to a gas fraction of 0.03, where gas fraction is the gas-to-total volume ratio. (This also corresponds to a degree of saturation of 94% for the

soils produced as described in section 5.1. Where the soil samples used for measurement in this research exceed this value of gas fraction, this will be stated in conjunction with the use of equation 1.2. (No indication of the level of error due to over-ranging is offered by Spitzer).

1.3.1.3 Attenuation within the resonance frequency range

Attenuation for gassy sediments is a result of the loss of energy from absorption and the redirection of energy out of the propagating wave front by scattering. Since resonance effects dominate the attenuation of gassy soil then the greatest energy loss must occur through thermal radiation and the viscous/friction damping of the pulsating bubble wall. In addition to this the effect of scattering at the bubble surface is enhanced by resonance which increases the scattering cross section significantly (by greater than 100 times for air bubbles in water). A second order effect is that of normal wave front propagation loss due to beam spread and viscous/friction damping that is also present in saturated soils. Thermal damping results from heat energy conducted from the gas during compression, whereas radiation damping is the omnidirectional scatter of energy. Viscous damping is the loss of energy due to particle drag moving through the pore fluid and, together with intergranular friction, causes a mechanical to heat energy conversion. The friction term is by far the largest contributor to damping in a sediment.

Anderson once again adjusts Silberman's (1957) equation for signals through a water and gas bubble medium to give an expression for the attenuation of gas bubbles in sediment by adding the $(\frac{4G}{3})$ term to (γP_o):

$$\alpha = \frac{\pi f}{c_o} \cdot \frac{c}{c_o} \cdot \frac{K\ Y_1}{\gamma P_0 + \frac{4G}{3}} \qquad (1.3)$$

where (c_o) is the sound speed for the saturated sediment, and other parameters are as previously defined by reference to Appendix A. Once again Spitzer's (1943) recommendation of a gas fraction maximum of 0.03 applies.

1.3.1.3.1 Sound speed and attenuation curves from theory

Equations 1.2 and 1.3 have been used to generate curves of sound speed and attenuation versus frequency as shown in Figures 1.4(a) and (b) respectively and using the parameter values shown. Figure 1.4(c) similarly presents the sound speed versus gas fraction curve computed from equation 1.1 and Anderson's lower bound (K) and (G). (c) and (c_o) represent the sound speed of the gassy soil and the fully saturated soil, whereas (f) and (f_o) represent the signal frequency and the resonance frequency of the single-sized bubbles, respectively. Both sound speed and attenuation curves in Figure 1.4(a) and (b) indicate a large response at the resonance frequency of the single-sized bubble where, for a soft harbour mud of shear modulus 1 MPa, attenuation increases to around 20 times that of a saturated sediment. Also from Figure 1.4(c) it can be seen that sound speed falls by around 67% due to the presence of only 0.1% of gas as a proportion of the void space. The variation of sound speed for the stiffer ocean-bottom silt of shear modulus 2.5 GPa, is not as great.

1.3.1.4 Reflectivity and scatter within the resonance frequency range

Silberman (1957), from Spitzer (1943), also produced expressions for reflection and transmission coefficients and scattering cross sections for bubbles in water, but which Anderson was unable to convert for use with gassy sediments. However the scattering cross section at resonance of up to 200 times the physical cross section (indicated by the theory of Spitzer for a gas bubble in water), suggests that the level of scatter in gassy

sediments at resonance, despite additional damping, could still be very much greater than for frequencies out of the range of resonance. This, together with the high absorption losses at resonance, would explain the inpenetrability of gassy sediments to sub-bottom acoustic profiling. However, a solution is not provided by lowering transmission frequency in an effort to get below the effects of resonance, since this would cause problems with resolution due to the larger wavelengths.

Another feature which suggests the presence of gassy sediment is the phase reversal of received sub-bottom profiling signals. This can be explained by the occurrence of a negative reflection coefficient (R) in the Rayleigh equation (Strutt, Lord Rayleigh 1877):

$$R = \frac{\rho_2 c_2 - \rho_1 c_1}{\rho_2 c_2 + \rho_1 c_1} \qquad (1.4)$$

This equation concerns the near normal trajectory of the incident and reflected wave at the mudline due to a signal propagating vertically downwards through the water. The sediment/water interface is formed from two materials of unequal bulk acoustic impedance (ρc). For saturated sediments, both density (ρ_2) and sound speed (c_2) exceed that of the overlying water (ρ_1, c_1), resulting in a positive coefficient. However, for a gassy sediment it is likely that $\rho_2 c_2 < \rho_1 c_1$, since, although its density may exceed that of water, its sound speed can be much less. Since (R) is the ratio between pressure amplitudes of the reflected to incident signal, a sign change indicates a 180° phase reversal to the received signal, in a profiling operation which passes from a saturated to a gassy sediment mudline.

1.3.2 The work of others

A model for gassy sediment has been developed by Bedford and Stern (1983) using the principle of conservation of energy as a basis for deriving equations of motion. They allow for resonance within an expression for the kinetic energy associated with the pulsating radial motion of bubbles. However, no relative motion is allowed for between liquid and gas, which means that the model assumes the 2 phase (solid and compressible fluid) response of the compressible fluid model discussed earlier. Their testing of the model to replicate the response of genuinely two phase materials, such as bubbles in water and glass beads in water, does not validate its use for gassy sediment. The equations of Adler et al (1986) also deal with the two phase model of gas pores in aluminium castings. They develop expressions for attenuation in terms of frequency and pore size gas fractions in order to determine the bubble size distribution from attenuation measurements below, at, and above resonance. However, the theory uses 'total scattering cross sections' computed from Ying and Truell (1956) which are more applicable to a metal host material than to a saturated soil matrix.

Practical work has been carried out by only a few. Kepkay (1977) provided both laboratory measurements and in situ testing results for velocity below resonance. In the laboratory, methane gas was dissolved, under pressure, into water which was used to saturate a silty clay soil. Free gas then nucleated to provide bubbles as the pressure was released. Although gas fraction was eventually high (up to 0.2 corresponding to a degree of saturation of <70%) the measured sound speeds were only up to 11% reduced from a saturated sediment velocity. Anderson's predictions for gassy sediments and, less importantly, Rawson's (1976) emulsion theory adapted for unconsolidated sediments, predict greater than 66% reduction. Kepkay suggests that his 'first arrival' signals may be transferred through less

gassy "patches" in the test medium. Since gas fraction observed close to the measuring point during the tests seems always to have agreed with the gas fraction measured from the total sample water displaced by gas, Kepkay's explanation would not seem likely.

Domenico's (1976) tests on uniformly and non-uniformly distributed bubbles in a sand medium of the small bubble model offers some proof of high velocities due to non-uniform distribution. However, Kepkay's high velocities in silty sands which are structured in the manner of Figure 1.1(a) may be a bubble size effect, not distribution, since these bubbles are very small and correspond in size to coarse silt particles (20-60 microns diameter, M.I.T.). In theory, below resonance sound speed depends on the bulk elastic moduli (as equation 1.1). These may correspond to Wheeler's (1986) theory for bubbles an order of magnitude greater than the soil particles, but may not when bubbles are approximately equal. Some velocity probe measurements with approximately similar results to those from the laboratory were taken in the harbour and bay areas of Nova Scotia by Kepkay without gas fraction and bubble size data.

Attenuation measurements were made in loose laboratory soil and sand by Nyborg et al (1950) from 2 to 25 dB/cm at 10 Hz and 74 dB/cm at 35 Hz depending on the amount of air entrained (unmeasured) during sample preparation. In situ attenuation measurements and sound speeds are reported by Edrington and Calloway (1984) using a gun-launched implanted probe in the Mississippi Delta to generate explosive charges to be picked up by a hydrophone array at the mudline. Results in sediment at a gas fraction of 0.00065 were around 800 m/s using a signal frequency of bandwidth 50 Hz to 20 kHz. Unfortunately the gas fraction figure is calculated using the 'proportional volume' bulk modulus introduced by Wood (1930) and relevant only to a soil suspension.

Interface reflection techniques also indicate low sound speeds such as 540 to 1100 m/s in Suva Harbour (Fiji), Hochstein (1970), 46 to 1768 m/s in Lake Travis, Jones et al (1964) and further reduced values from Brandt (1960), Levin (1962) and Lewis (1966). Also highly reflective pressure release boundaries are reported in gassy sediments by Schubel (1974), Bobber (1959), Levin (1962), Leslie (1960), Grubnik (1961) and Ruff (1967), which are a direct result of very low sediment velocities in equation 1.4 and high absorption losses, leading to acoustically inpenetratable barriers or widespread acoustic turbidity. Levin (1962) illustrates the pressure release effect by placing a charge in gassy soil, just below the mudline, which caused a vertical conical beam of 12.8° to spread out over 180° when refracting at the interface into the water above. The pressure of the beam reduced dramatically when measured at increasing angles from the vertical through the charge position. Figure 1.3 from Fannin (1979) illustrates a typically high reflectivity, here attributed to gassified silty clay sediments in the North Sea. Also shown are the pockmarks referred to in section 1.2.4.

1.4 THE TEST MATERIAL (Laboratory gassy soil)

Figure 1.5 is a picture of a 3 cm sample depth of dried laboratory gassy soil with a gas fraction of around 0.12, consolidated to a stress of 35 kPa and having bubble diameters from 0.2 - 1.0 mm. From visual examination it is reasonable to suggest that the laboratory gassy soil shown in Figure 1.5, when varied in gas content, may replicate fairly closely the macroscopic structures of the two in situ samples of greater and lesser gas contents shown in Figures 1.2(a) and (b), respectively. Gassy soil is made in the laboratory by the following process. Zeolite powder (calcium alumina silicate) is oven-dried and left under vacuum for 8 hours to remove all moisture. The chamber inlet port is then switched over to receive methane gas from a cylinder at a pressure of 200 kPa for 17 hours, in order to allow

the methane molecules to occupy the pore spaces within the zeolite. This methane-saturated powder is then added to a soil slurry of estuarine silty clay from the River Parrett, Combwich at a moisture content of 184% and a bulk density of 1280 kg/m^3. Since the zeolite has an affinity for water molecules, gas is liberated in exchange for water from the slurry after the soil is loaded into the test cell and put under a consolidation stress of 25kPa. Free gas forms uniformly distributed bubbles within a saturated soil matrix over a period of 36 hours, during which the rate of liberation is initially high and then exponentially decays. The zeolite content is 17% by weight of the total soil plus zeolite solids and any alteration to the soil structure is reduced since the calcium alumina silicate has fine silt-size particles with a specific gravity close to that of the soil solids. The resulting gas fraction of the soil can be controlled by reducing the pressure or period in which the zeolite is kept under methane pressure, or by reducing the methane-impregnated zeolite content in the soil below 17% and adding a water-saturated zeolite quantity to make up the shortfall. This latter method was used for the tests to be described. A more detailed description of this process may be found in Nageswaran (1983).

1.5 THE AIM OF THIS RESEARCH

Laboratory measurements of sound speed and attenuation will be presented for the frequency range 20 kHz to 1 MHz, using soil samples of gas fraction in the range 0.00357 to 0.198.

Bubble size distributions (B.S.Ds) and their effect on the acoustic response of the soil will be measured and investigated to see if an empirical relationship exists that could be used to define the bubble size range from the in situ sound speed and attenuation data taken by an acoustic probe.

The 'below resonance' elastic wave equation 1.1 will be adopted to calculate sound speeds, using different theoretical derivations of the elastic moduli (K) and (G). These sound speeds will be compared to the author's measured 'below resonance' sound speeds, in order to identify the more successful model for the moduli. This analysis will therefore provide a corroborated method of predicting gas fraction in sediments from in situ sound speed measurements using an acoustic probe, and will then allow the prediction of possible values for the elastic moduli for given bulk densities.

Finally a study of Anderson's equations for sound speed and attenuation at, and below, resonance will be made in comparison with the results presented here, and in conjunction with varying values of the ambient hydrostatic pressure, the specific dissipation function and the elastic moduli. Hence the effect on the acoustic response of a sediment due to the above parameters, may be evaluated to an accuracy within the bounds of the previously assessed performance of Anderson's equations against measured data.

CHAPTER 2 - DESIGN AND OPERATION OF THE MECHANICAL SYSTEM

2.1 AN OUTLINE DESCRIPTION OF THE OPERATION

2.2 THE ACOUSTIC CONSOLIDATION CELLS

- 2.2.1 The cell chamber assembly (Cylinder walls and end plates)
- 2.2.2 The piston (Transducers, soil filters cell 2 bottom-face drainage)
- 2.2.3 The piston push rod and swell-back stop
- 2.2.4 Top sections (Block and cone sections and transmitting transducer)
- 2.2.5 Reaction plate system (Plate, ram and ram-pressure cylinder)
- 2.2.6 Precise soil depth measurement (LVDT and deflection gauge)
  - 2.2.6.1 Special calibration for the LVDTs
  - 2.2.6.2 LVDT assembly
  - 2.2.6.3 Setting the LVDTs for soil measurement
  - 2.2.6.4 Gauge displacement measurement of the reaction plate assembly
  - 2.2.6.5 Additional measures
- 2.2.7 Construction of the acoustic transducers

2.3 OTHER EQUIPMENT IN THE MECHANICAL SYSTEM

- 2.3.1 Hydraulic pressure (A/W interface, filter and regulator)
- 2.3.2 Loading and unloading (Flow restrictor)
- 2.3.3 Phase volume measurement (Burettes)
- 2.3.4 Data recording (Chart recorder and voltmeter)

2.4 MECHANICAL CONSIDERATIONS

- 2.4.1 The choice of confinement pressures
  - 2.4.1.1 The bubble shape constraint on total stress
  - 2.4.1.2 The back pressure constraint
  - 2.4.1.3 The acoustic transducer face-displacement constraint on total stress
  - 2.4.1.4 The volume change measurement correction, and constraint on total stress
- 2.4.2 Slow consolidation and non-homogeneity of the soil sample
- 2.4.3 Cyclic loading to investigate transmitter replacement during testing
- 2.4.4 Elevated residual pore water pressure measurement

2. DESIGN AND OPERATION OF THE MECHANICAL SYSTEM

2.1 AN OUTLINE DESCRIPTION OF THE OPERATION

Two acoustic consolidation cells have been designed and built so that a single gassy soil slurry can be divided to provide two very similar samples for testing concurrently. Cell 2 is shown in the outline diagram of Figure 2.1 (a). Soil can be consolidated within the cells to reproduce varying sea bed confining pressures by controlling total stress (σ_1) and ambient hydrostatic pressure to provide the required consolidation stress ($\sigma_1 - u_w$). Acoustic compression wave signals can be transmitted through the soil and analysed to provide sound speed and attenuation versus frequency data for soil samples of varying gas fraction.

Gassy soil slurry is poured into the cell above the piston. The top sections of the cell are bolted down and the top cone reservoir filled with water, while the connecting pipe to the burettes is primed to eliminate gas. Pressure in the below-piston hydraulic reservoir is increased to provide the required total stress during consolidation, as measured by a pressure transducer in the piston face, while back pressure may be applied at the burette outlet. Drainage water and some gas, initially dissolved in the pore water, is discharged from the soil through the drainage passages in the top section, where free gas collects in the top cone. Water is forced back through the burette tubes to replace the volume of gas vented through the outlet point, at the apex of the cone, before using the burettes to measure the volume of water discharged from the soil. A bottom face drainage facility is supplied to Cell 2 in addition to the top face drainage on both cells. The bottom face drainage outlet point is connected to the top cone outlet. Since Cell 1 is designed for a consolidated soil depth of approximately 20 mm, and Cell 2 for 65 mm, the periods of primary

consolidation for both cells are made closer by draining Cell 2 from both faces.

Bubbles are generated in the soil over the 36 hours following load application with primary consolidation also being completed during this stage. A period of time is allowed to enable excess water and gas pressure to dissipate before the soil sample is raised in the cell to bring the cell top section in contact with a reaction plate assembly for acoustic testing. This extrusion process is carried out while holding the total stress on the soil constant. Finally, the soil is removed from the cell and sub-sampled for bubble size and phase volume measurement.

2.2 THE TWO ACOUSTIC CONSOLIDATION CELLS

Figure 2.1(b) is a detailed schematic of the consolidation cell. The following description of the cell will refer to this figure and, where necessary for greater detail, to additional figures.

2.2.1 The cell chamber assembly (Cylinder walls and end plates)

The cylinder wall of 10 mm thickness is formed from stainless steel hollow rod for strength and rigidity and the internal face has been bored, and honed using stress releasing intervals to avoid distortion. Great care was taken to provide a smooth surface to reduce soil-to-wall and piston-to-wall friction. Excessive soil-to-wall friction would, in theory, cause reduction in the total stress at the outside upper face of the soil, and lead to radial variation in the soil of void ratio and gas fraction. Significant piston-to-wall friction would cause difficulties in unloading fully the soil slowly back to atmospheric pressure before removing it from the cell for structural analysis. Despite reducing fully the external load to the piston, between 10 and 50 kPa of total stress would remain on the soil for

this diameter of cell depending on the smoothness of the cell wall and the type of piston seals used. Incorporating honed walls and low friction seals reduces the problem to a minimum level which can be dealt with using the flow restrictor device under vacuum, to be discussed later in this chapter.

The cylinder diameter was set at an arbitrary 170 mm to minimise signal wall reflection problems and to provide space for the large diameter transmitting transducers. A cylinder length of 550 mm was selected by considering the combined length of acoustic transducers and soil slurry depths to provide up to 170 mm of consolidated sample depth.

The stainless steel cylinder base plate is provided with a common 'o' ring seal (Dowty Seals Ltd) set in a channel and compressed by the end face of the cylinder. A single passage is bored through it to connect the below-piston water reservoir with the source of hydraulic pressure. The piston push rod is allowed to move freely through the plate due to the provision of a low friction quadring seal (Technical Sealing Design Ltd) set in the channel as shown in Figure 2.1 (b). The four-lobe section of this type of seal can withstand pressures up to 250 bars while providing minimum friction resistance to static, dynamic and even rotary action. Four large diameter bolts fix the cell base securely to a substantial steel framework table with legs set into a rigid concrete foundation.

The duralumin retaining plate fits over the cylinder top end face and is held down by the eight bolts which clamp together the cell chamber assembly, without the remaining sections in place. Since duralumin suffers from corrosion when it is in contact with this acidic type of soil, a silver plate anodising process was used to build-up a protection layer of 0.02mm on all sections. It was successful in preventing corrosion except at the section surfaces that remained in contact with the soil within the cell for durations of around 2 weeks. The piston face, in particular, became badly

etched at the edges of all the transducer recesses, until a zinc-based paint (Galvafroid) was applied before each test. As a precaution, recommended by the quadring manufacturers, the top inside edge of the retaining plate is bevelled to enable both piston and top section to be pushed into the cylinder without damage to the seals.

2.2.2 The piston (Transducers, soil filters and Cell 2 bottom face drainage)

The soil slurry in the cell above the piston is bounded above and below by Millipore membrane filter (Millipore Corporation) of pore sizes below 2 microns. During consolidation they prevent clay-sized particles being washed out of the soil in the drainage fluid. A 4 mm thickness of vyon 'depth filter' is installed below the top membrane in both cells. For Cell 2 bottom face drainage, a further vyon filter is placed below the bottom membrane and within the piston recesses shown in Figure 2.2, to finish flush with the piston face. Millipore filters are made from hydrophobic membranes and are designed to act as a cleansing screen to filter out small particles which are suspended in blood. Vyon is made from semi-rigid microporous polyethylene and is designed specifically as a drainage surface, for 20 micron particle retention, that gives bridging support to the membrane filter over outlet orifices. It allows unrestricted lateral flow to the outlet ports and it is submerged in water under a vacuum for 24 hours to de-air it fully before placing in contact with the soil slurry.

The piston is formed from three bolted duralamin sections, referred to as the piston top section and upper and lower piston bases. All the cell pressure transducers, and also the acoustic receiving transducer, are contained within the piston top section at the lower face of the soil. There are three pressure transducers. Lower face total stress, for the range of tests discussed in section 1.5, is measured by a type PDCR 22

transducer (Druck Ltd) with a 0-35 kPa pressure range, 12 volt supply and a + 0.06, 0.02 and 0.02% rating for hysteresis, zero drift and span drift respectively. Initial work, prior to the test programme, was carried out using a 1.5 MPa transducer. It is pushed into the back face of the top section with an 'o' ring seal on the pressure face side of the shoulder on the transducer body. A stainless steel externally threaded sleeve is then fitted around the transducer and screwed into the piston section, squeezing the 'o' ring and bringing the pressure face flush with the piston face.

Pore water pressure measurement and an attempt at measuring an indication of pore gas pressure after Nageswaran (1983) are carried out using type 3EA/a transducers (Gaeltec Ltd) with a 0-1000 kPa pressure range, 5 volt supply and 0.1% rating for hysterisis. These transducers were chosen because of their extremely small external dimensions in view of a length limitation for installation in the piston. The transducer body was designed to screw into the underneath of the piston top section below the porous stone and 'neck' area. Design of this stone and neck area follows the specification and dimensions of Nageswaran's (1983) recommendations for measuring pore water pressure without gas bubble bridging effects and for measuring gas pressure with bridging. However, it is reported later in section 2.4.4 that both Gaeltec transducers recorded the same pressure. The transducer to piston seal is made by coating the screw threads with Red Hermetite sealant (Hermetite Ltd). Each pressure transducer was calibrated within the cell during a regulated pressure test. The receiving transducer is inserted with its araldite surface fitting flush with the piston face and is sealed by 'o' rings grooved into the internal wall of the receiver housing in the piston.

There are recesses for the vyon filters around the transducers of Cell 2 piston only. These facilitate bottom face drainage as described earlier. Figure 2.3 illustrates the layout of the filter annulus and six adjoining disks. The annulus is connected by two diametrally opposed drainage ducts

drilled through the piston top section at an angle with the vertical. These ducts join with 4 mm diameter plastic tube spirals that are connected through the cell base plate to a junction in the pipe, from the cell top cone to the volume change measuring device. Stainless steel fittings (designed by Enot Ltd) were manufactured in the workshop to connect the spiral pipe ends to the piston top section and cylinder base plate. This avoids the corrosion caused by using the standard brass fittings that , in the presence of duralumin and acidic water, become 'poles' across which potential difference sets up an electric current. A low friction quadring seal, as used in the cell base plate, is installed in a channel in the external wall of the piston, and the edge of the piston face is chamferred so the seal can be fitted without damage. A 4 mm diameter bleed duct is drilled vertically through the piston section with a small clearance from the base of this channel. This duct allows the venting of any air trapped in the below-piston hydraulic reservoir that would cause sponginess in the piston-consolidating action. It is sealed at the top end by a short set screw and 'o' ring countersunk into the piston surface.

The duralumin piston base sections and top section are connected together with stainless steel studs. An open dry area is formed between the piston top and upper base sections to allow cable transfer from the three outlying pressure transducers to the centrally-placed cable collection point at the end of the piston push rod. The upper base section is undercut slightly in diameter to avoid overlapping the top section and obstructing piston movement by touching the cell wall. Also, clearance holes are drilled in this section for the stainless steel fittings and spiral drainage pipes of Cell 2, and a bleed duct continuation hole is drilled for both cells. The composite piston is waterproofed by 'o' ring seals placed in channels between the piston top and upper base (set within the radial distance of the bleed duct) and between the upper and lower bases. Finally a quadring seal is inserted between the lower base and the piston push rod. All the seal

channels are illustrated in Figure 2.1(b) and those which are for quadrings are labelled.

2.2.3 The piston push rod and swell back stop

The 36 mm diameter push rod is built from stainless steel tube for compressive strength and rigidity. Its purpose is threefold. It transfers the transducer cables from inside the piston to outside the cell and enables piston downward movement to be blocked using the swell back stop device to allow piston position control prior to soil testing. Finally it allows measurement of the soil depth by marking the piston position. The thin 3 mm wall allows maximum internal cabling space and a minimum external circumference, to reduce friction at the cell base quadring seal. The tube is slotted at the bottom end for the cable outlet point. As this slot could cause quadring damage during assembly, the external diameter of the push rod is reduced over the length of the slot and increased to full diameter above by a gently sloping shoulder. A fine pitched thread is formed in the external surface at the top end of the push rod that allows the rod to be secured into the piston base, bearing directly against the top section.

The stroke of the piston in its downward direction may be blocked at any time against the 'swell-back stop' device. This consists of a circular plate at the top end of a worm screw that is threaded through a cross member at mid-height in the table below the cell. A hemispherical depression is ground into the circular plate and bears directly on the rounded surface of the push rod base. This device is used to support the piston when soil is loaded into the cell prior to consolidation and during tests with calibration liquids (to be discussed later).

2.2.4 Top sections (Block and cone sections and transmitting transducers)

The photograph in Figure 2.4 illustrates the composite block section and the transmitting transducer inserted centrally with its face uppermost. This composite duralamin block section is made up from a pressure plate, designed to withstand a cell pressure of 1.6 MPa, and the block which penetrates the cylinder and provides the upper rigid boundary of the soil. They are fixed together by countersunk set screws through the plate that fully compress the nitrile rubber gasket between the sections. Eight 4 mm diameter holes transfer the top face drainage water through the composite block section into the top cone water reservoir.

The acoustic transmitting transducer is pushed up into the block section to bear directly against the underneath of the pressure plate. It is fixed by stainless steel set screws through the plate into the end of the transducer wall and its araldite face extension fits through a circular cut out in the vyon to finish flush with the filter/soil interface. A conduit in the pressure plate allows the transducer cable to be transferred from the block section to the outside of the cell. The enlarged conduit orifice in the plate avoids turning the cable too sharply through 90 degrees. A seal is achieved by the provision of an 'o' ring, recessed into the block wall close to the front end of the transducer. Sealing of the composite block section is completed by a similar arrangement where the channel is provided in the external face of the block, close to its bottom face.

The composite cone section is made up from a duralumin cone completed by a perspex top which allows visual assessment of the build-up of gas during consolidation. Since perspex is much weaker than duralumin and suffers from absorption of water and a greater level of creep, only a minimum internal surface area is provided as a window. The internal surface of the duralumin and the perspex is cleaned, and polished before each test, to avoid gas

bubbles adhering to the cone wall and escaping the venting action at the apex point during gas discharge measurement. This gas outlet point consists of a 4 mm diameter pipe and an Enot fitting screwed into the perspex. The short length of transparent pipe is marked just above the pipe fitting to the level at which water rises on initially filling the cone reservoir and on venting gas from the apex point. A pipe tap, positioned immediately above the mark, is closed following the above stage and pore pressures are allowed to equilibriate to atmospheric level at the burette outlet. The 4 mm diameter water pipe connection to the burette tubes is drilled horizontally through the bottom flange plate of the duralumin section. Drainage water discharges through this passage to the volume measuring device during consolidation and flows back through during the venting process. The two sections are bolted together with stainless steel hexagon-headed studs and clamped to the chamber with holding-down bolts to secure the rigid upper soil boundary. Sealing of the perspex to duralumin interface is provide by an 'o' ring recessed into the bottom face of the perspex and the composite cone section is similarly sealed to the composite block.

2.2.5 Reaction plate system (Plate, ram and ram pressure cell)

Figure 2.5(a) presents a diagram of the reaction plate assembly, ram and consolidation cell with the soil in the raised position. This equipment is used to raise the soil in the cylinder, while maintaining the total stress, until the top of the soil is above the retaining plate of the cell chamber. In this position, the composite block section and vyon filter will be entirely separated from the cell chamber, avoiding the transfer of signals around the soil via the cell wall.

The assembly is made from mild steel plate which is coated by Hammerite anticorrosive paint (Hammerite Speciality Paint Ltd). The top plate is bolted to the bottom flange of a 203 x 102 steel joist section dedicated for

this use. The joist has built-in ends and is given added resistance to upward thrust by a holding-down wall bracket at the end close to the position of both cells. Since the plate is 18.75 mm thick it provides a substantial base reaction against which the thrust from the bottom plate structure can be applied without causing significant deformation. Four very finely-threaded M16 studs are used to connect this top plate to the bottom plate, with lock nuts either side of both plates. These studs enable the plane of the lower plate to be fixed precisely for level and height. The bottom plate is extended downwards with two legs formed from 12.5 mm thick rectangular plate and splayed side stiffeners all fixed together by fillet welds. A smooth planar surface is provided on the end faces of the legs by a milling operation. The adjusting screws are used to bring the horizontal plane of the araldite face of the transmitting transducer 1 mm above the top face of the retaining plate, when the upper face of the pressure plate is in contact with the legs.

The hydraulic process of raising the soil in the cylinder and making contact with the reaction plate is performed while maintaining the chosen total stress on both upper and lower faces of the soil. A hydraulic ram as shown in Figure 2.5(a) mounts directly on the perspex top section after removal of the pipe and tap and closure of the outlet. The ram is extended almost to full stroke when it bears against the underside of the bottom reaction plate. 'G' clamps are used to fix the composite cone and block sections together to avoid leakage from the reservoir if the plates are allowed to move apart. Ram pressure is then increased to deliver the total stress to the upper soil surface on removal of the top nuts to the long holding-down bolts on the consolidation cell. A small increase in below-piston pressure allows the piston to begin raising the soil at a constant rate. Bearing contact is made between the composite top cone flange and the reaction plate legs after approximately 20 minutes. Total stress at the piston face remains constant throughout the operation suggesting a constant cell

wall/soil and cell wall/piston friction. Cell piston pressure is then reduced to equal the soil consolidation stress once again and the ram pressure is released with the ram being removed to refit the apex pipe and tap. Pressures are allowed to equilibriate over 24 hours. Surplus wall grease and water at the exposed 1 mm face of the soil is removed to avoid signal transfer through the cell body. For the same reason, the film of water covering this face is removed before testing. Also any electrical conductance to the receiver was avoided by earthing the cell wall. Acoustic tests may then be performed over a period of 32 hours while the soil remains in the stable condition.

The ram operates at up to 1000 kPa of fluid pressure which delivers any chosen total stress up to 140 kPa at the upper soil surface. Since there is no total stress measuring facility at the upper soil boundary the stress here, as delivered by the ram, is calculated from the ram pressure value, allowing for a very small piston friction loss. Ram pressure is provided by an adapted soil consolidation cell. Hydraulic fluid half fills the pressure chamber above the piston and a PDCR 22 (Druck Ltd) pressure transducer is fixed into the top plate using a screw-in sleeve similar to that provided for the PDCR 22 in the acoustic cell. The piston is locked in position and the air pressure over the fluid is increased by a compressed air supply. A hole through the piston allows fluid to transfer to the ram under pressure to provide the ram thrust.

It will be shown in the section on the acoustic system that it was necessary to carry out tests on chosen liquids for calibration purposes. Since liquid could not provide the required support to the top section during the decoupling procedure, equipment was constructed to allow the top to be suspended from the reaction plate. The sling device is shown in the photograph of Figure 2.5(b) of the acoustic cell which is set-up for acoustic tests on the calibration liquids. A support plate fits

horizontally around the block section and below the pressure plate. Two mild steel studs with lock nuts are then used as tie rods between the two ends of the support and the two ends of a bar laying over the lower reaction plate. The composite cone and block sections are fixed together with 'G' clamps (without the water reservoir and burette connection in place). The whole top section is then adjusted to fit centrally above the cell chamber before the tie nuts are tightened carefully to bring the top sections against the reaction plate assembly in precisely the same position as for the soil tests. Overtightening and distortion of the pressure plate is avoided by tightening to the point where the deflection gauge at the pressure plate is returned to datum. This gauge will be discussed in connection with soil depth measurements.

2.2.6 Precise soil depth measurement (LVDT and deflection gauge)

This section, together with section 3.3 later, will deal with the precise measurement of transducer separation and signal transit time respectively. These two concerns will be dealt with thoroughly since the accuracy with which they are measured is crucial to all the methods of obtaining sound speed used in this research study. Also the validity of the resulting sound speed calculation must be firmly established in order to separate a true sound speed response from a fluctuation in accuracy.

Figure 2.5(a) indicates the elevated position for measuring the precise depth of soil that will be used to compute sound speed. The cell chamber, piston and the various top section units are marked so that each unit will be orientated in the same manner each time the cell is assembled for testing. This ensures that the calibration and setting of the linearly varying displacement transducer (L.V.D.T.) and the deflection gauge will produce consistent accuracy in measuring the soil depths for each test.

2.2.6.1 Special calibration for the LVDTs

Both consolidation cells are fitted with type DCR/100 MM/s L.V.D.T.s (Sangamo [Schlumberger] Ltd.). The specifications consist of a 0.3% linearity and a 2.06 mV/V/mm sensitivity at a load impedance of 20,000 ohms and a stroke length of ± 100 mm. Since linearity is poor, the application of a constant calibration factor to convert from mV to mm travel would not provide sufficient accuracy for the soil depth measurement.

As linearity could not be improved, a calibration table was drawn-up to make the conversion to an acceptable accuracy of ± 0.025 mm. Calibration was carried out by fixing the LVDT to a lathe to record horizontal movement to an accuracy of ±0.005 mm. The LVDT was provided with a stabilized voltage supply type L30 (Farnell Instruments Ltd) which was set at 10 volts as measured by a 5 digit, voltmeter type MA5D (BBC GOERZ METRAWATT). This voltmeter is retained at 5 digit accuracy by periodical checks using a more sophisticated voltage calibration meter type 404s (Time Electronics Ltd). At intervals of precisely 5.00 mm, over the full stroke of 200 mm, the voltmeter supplied a reading to within 0.0001 volts in the range from -2.0 to +2.0 volts. Reversing the direction of the stroke and repeating measurements indicated that the voltmeter readings were unchanged and that the tables relating stroke position to voltage produced repeatable values. This procedure was followed again 12 months after the original calibration and showed no significant changes.

2.2.6.2 LVDT assembly

The different arrangements of fixing the LVDTs to the two consolidation cells meet their individual operational requirements. On Cell 2 the LVDT is held vertically by a clamp bolted to the table top. The extending pointer of the LVDT projects downwards onto the surface of a kicker plate that is

attached to the piston push rod below the cable outlet slot and extends outwards just beyond the table legs. This kicker is made from 15 mm duralumin plate with the central region in plan, cut out in order to reduce self-weight loading and avoid movement at the kicker/push rod clamp. Cell 1 is fitted differently since the piston level at the reaction plate stage is much higher than Cell 2, because of the proposed soil depths. The LVDT is clamped vertically to the mid-height table cross member. Its extending pointer projects upwards to the underneath of a short kicker plate clamped to the piston push rod below the cable outlet slot.

2.2.6.3 Setting the LVDT's for soil measurement

Before the test programme was commenced, the LVDT positions in the clamps were adjusted so that the voltage calibration reading, which corresponded to the 0.00 mm stroke position, occurred when the transmitting and receiving transducers were in face to face contact. This position was achieved by using a 20 mm deep brass spacer for Cell 1 and a 65 mm spacer for Cell 2, since these depths are the chosen soil thicknesses for each cell. Both ends of the spacers are circular with both tops being equal in diameter to the transmitting transducer's araldite face (68 mm), and both bases equal to the diameter of the receiver's araldite face (40 mm). The sides are tapered between ends and the end faces are ground precisely to parallel planes. Micrometer readings recorded the distance between planes to within 0.001 mm.

For the adjustment procedure, the top sections were held against the reaction plate using the sling device all as described in section 2.1.5. The spacer was set on top of the receiver and within the stainless steel receiver walls, bearing wholly on the araldite face, to avoid bridging effects. Below-piston pressure was increased to a level which would apply the chosen soil total stress over an area mid-way between the top and bottom end face areas of the spacer. A small allowance was made for piston seal

loss. The piston rose very slowly to bring the top face of the spacer in contact with the transmitting transducer face also without bridging across its stainless steel walls.

Pressure was maintained between the transducer faces while the LVDT position was finely adjusted in the clamp to give a mV reading which corresponded exactly to the spacer thickness. The arrangement therefore replicated the test conditions where the same thickness of soil would be compressed at approximately the same face stress. However, the risk of overloading or damage to the brittle araldite surface of the transducers because of the rigid spacer contact prevented the regular use of this setting procedure. Releasing the below-piston pressure, and manually bringing the faces into touch contact by rotating the swell back stop, indicated a repeatable -0.02 mm error in the measured soil depth due to the omission of soil stress on the transducer faces. It was therefore decided that all further pre-test adjustment checks on the soil depth measuring equipment should be carried out safely by bringing the faces together (using the spacers) in touch contact only and applying a correction for stress due to elastic deformation. The exact point of touch contact was decided by using a beam produced by a high-intensity fibre optic light source directed between the spacer and transmitting transducers faces, onto a dark surface behind. The LVDT position was set at the precise piston position at which the light source disappeared from the surface. This procedure produced repeatable results for the piston position and led to adjustments in the LVDT position between tests in the following programme of less than 0.01 mm. Since the laboratory was temperature controlled and thermometer records indicated variations of only $\pm$ 0.25 °C, no temperature corrections were necessary. The resulting adjustments were therefore probably necessary because of creep deformation in the transducer material, as will be discussed later.

2.2.6.4 Gauge displacement measurement of the reaction plate assembly

In both adjustment procedures described, allowance is made for any deflection arising from the stressing of the reaction plate and joist section. A deflection gauge with divisions of 0.01 mm is held by a wall bracket so that its extending pointer is directed vertically downwards onto the upper surface of the pressure plate part of the composite block section. The wall bracket shown in Figure 2.5(a) is substantial to avoid disturbance to its precise position. It is formed from 25 mm x 25 mm, 3 mm gauge mild steel box section, welded to a 10 mm mild steel wall plate and is fixed into a masonry wall by 8 mm diameter expanding bolts. This gauge is set to a zero displacement datum for the condition of no upward thrust, and it records up to 0.10 mm of upward displacement during the application of a 25 kPa total stress on the soil. This displacement provided a gauge datum correction for use in the earlier comparison, to convert from the soil depth measured without total stress to that measured for spacer touch contact only.

2.2.6.5 Additional measures

A similar temporary deflection gauge arrangement, set up to measure table top displacement under load, confirmed that no further soil depth correction due to base movement was required.

The 10 volt supply for the LVDTs is provided by the stabilized voltage unit used for calibration on the lathe. This supply voltage is checked and adjusted using the voltmeters already described before each LVDT reading is taken by the BBC voltmeter and quoted within ± 0.0005 volts. It is performed for both setting-up procedures and test. The LVDT chart recorder connection caused an additional electrical impedance in the circuit to the voltmeter which leads to a significant change in the voltage displayed and a

corresponding difference in the soil depth measurement. Hence all the calibrations, setting adjustments and following tests involved measuring the soil depths after first disconnecting the chart recorder.

The above process of measurement ensures that the system can provide soil depths to an accuracy of ± 0.025 mm.

2.2.7 Construction of the acoustic transducers

Figure 2.6(a) illustrates the construction method of both transmitting and receiving transducers. Acoustic aspects will be detailed in the section on the acoustic equipment, except for the discussion here which concerns the choice of the plasticell material, since it is considered in context with its mechanical behaviour.

Plasticell (Permali Ltd) is supplied to the building industry as a thermal insulation material. It is a relatively rigid, closed-cell, P.V.C foam and was found to provide a reasonable level of signal energy reduction for use as a barrier to attenuate sideways and backwards transmission to, or from, the ceramic elements. Although only a small depth of the material is contained in the receiver, the three transmitters have between 46.5 and 121 mm and are therefore more susceptible to displacement under load. Compression tests at 1 MPa for 7 days on plasticell with a density of 100 kg/m^3 indicated no significant elastic deformation. Some plastic deformation occurred but was only due to the exposed fractured cells in the end faces collapsing under load. For this reason the plasticell was fixed into the transmitters and receivers under load in an effort to avoid further deformation during soil tests.

Absorption tests in water at 500 kPa indicated an immediate penetration of 0.02% by volume which was once again attributed to the fractured surface cells, and was also obviated by compressing the plasticell during transducer construction. Absorption over 5 days thereafter was negligible. However, as a precaution against penetration of water into the transducers the thin araldite protection layers were channelled at the outside edge and the araldite/steel interface sealed by an 'o' ring.

The electrical contacts with the ceramic elements were provided by using fluxless silver solder to connect a thin insulated wire to the top surface and another to the underside, leading both through a hole drilled in the plasticell to the cable outlet. At the outlet point a plastic coupling and seal waterproofed the back of the transducers to avoid accidental damage during handling. The wires, element (plus metal extensions) and plasticell block were arranged in place in the stainless steel body before pouring in araldite (Ciba-Gigy Ltd) and then using a vacuum to expel free gas from the resin. Once the araldite had hardened, the exposed surface was ground flush with the end face of the stainless steel walls.

2.3 OTHER EQUIPMENT IN THE MECHANICAL SYSTEM

2.3.1 Hydraulic pressure (A/W interface, filter and regulator)

Figure 2.6(b), part A, shows the system that may be used to supply hydraulic pressure to the below-piston chamber in the acoustic cell. The air pressure is normally provided from a 600 kPa pressure reservoir tank supplied by an air compressor. For the initial compression test of Cell 1 a nitrogen gas bottle was used to provide pressures up to 2000 kPa. Type F51004A filters (Norgren Ltd) are used to remove contaminants and fluid before entry to a Manostat air pressure regulator (John Watson and Smith Ltd) fitted with a Norgren dial gauge. The air/water interface (Wykeham Farrance Engineering Ltd) supplies water, at the regulated pressure, to the consolidation cell.

A similar arrangement of the equipment in part A is shown in part B, and can be used to provide back pressure to the soil in the cell when it is required. Otherwise the outlet from the burette tubes is held below water with a reservoir surface height which corresponds to the mid soil height in the consolidation cell for atmospheric pressure.

2.3.2 Loading and unloading (Flow restrictor)

The flow restrictor device is shown in Figures 2.6(b), part A, and 2.7(a). It is a development of Lee (1979) which has been further utilized in the one-dimensional fast consolidation cell by Sills et al (1985). For the purpose of this research, however, the flow restrictor was used to restrict flow to the below-piston cell reservoir rather than at the drainage outlet. This arrangement allowed the device to be used in the loading operation to provide:

(i) Slightly more spherical bubble shapes due to some reduction in consolidation periods.

(ii) increased bubble sizes due to reduced pore water pressure levels within the soil, since less free gas will be dissolved into the water and removed by drainage when the pore water pressures are lower.

(iii) more uniform structural development from top to bottom of the soil sample due to a more uniform distribution of consolidation stress.

The response shown in Figure 2.7(b) illustrates how the above conditions are met. Total stress and pore water pressure are measured at the undrained face by the piston pressure transducers for Cell 1 using a 20 mm sample depth of soil with a gas fraction less than 0.005 (98% degree of saturation). Assuming a zero pore water pressure at the drained face (upper soil surface), smaller and less divergent pore pressures exist throughout

the sample than would exist without the flow restrictor fitted. This results in more uniform consolidation stresses, and therefore structure, throughout the soil; thus meeting condition (iii). The overall reductions in excess pore water pressure contribute to meeting condition (i) and, combined with shorter consolidation periods, that of condition (ii) also. For the unloading operation, below-piston pressure is totally released in steps down to a residual of around 10 kPa over a period of 12 hours, whereupon the flow restrictor device is applied in conjunction with a vacuum as shown in part A of Figure 2.6(b). Care is taken to avoid applying the vacuum for a greater period than necessary and causing sample stretching. Repeated removal of the vacuum, and allowance for the pressures to equilibriate each time, allows the total stress to be returned to atmospheric level without observed sample damage.

As explained in section 2.2.1, the purpose of vacuum application to the flow restrictor is to counter the residual pressure caused by the piston/cell wall and soil/cell wall friction in order to return the soil sample to atmospheric pressure. If the soil is abruptly removed from the cell without reducing the residual pressures, a sudden unloading of the soil results in a further cause of fracture which has been observed at the same stage in tests using consolidation cells with perspex walls. This sudden release causes an immediate equivalent drop in the pore water pressure throughout the soil and a resulting expansion of gas within the pockets. It is this expansion of gas which is thought to be the cause of sample rupture and, by a similar process, the cause of structural damage to deep water gassy sediment core samples which have been removed to a condition of atmospheric pressure. Silty clay soils of low permeabilty do not allow the immediate flow of pore fluid in the region of the gas pockets caused by the expanding gas. This leads to a localised build-up of pressure and results in failure surfaces being interlinked between pockets of greatest pressure.

2.3.3 Phase volume measurement (Burettes)

50 cc capacity burette tubes are installed in the volume change measuring equipment shown in Figure 2.6(b) in the manner of the type WF12520 system (Wykeham Farrance Ltd). It is possible to measure volume change to an accuracy of ±0.025 cc.

Volume change measurement is performed after discharging the gas collected at the cone apex in the manner described in section 2.1. Thus, having removed the effect of the discharged gas ,the water phase volume change of the soil is measured at the burettes. Gas phase volume change is then calculated as the difference between the total sample volume change, measured by piston displacement, and the water phase volume change. The structural parameters, such as gas fraction and degree of saturation can then be assessed for any stage in the test by measuring the condition of the sample after the test and backcalculating using the phase volume changes.

Because of the gas pressure changes in the sample, gas phase volume change cannot be measured simply from the discharged gas in the cone. As a result of an increase in total stress, free gas compresses to a reduced phase volume and the consequent rise in gas pressure, above atmospheric level, causes a further reduction as gas dissolves into the surrounding pore water. It is largely this dissolved gas which discharges from the soil in the drainage water and comes out of solution when returned to the atmospheric pressure of the top cone reservoir. Therefore, total gas volume within the soil specimen cannot be predicted from stage measurements of the free gas collected in the cone, since they are not equal to the changes in volume of the soil's gas phase. The measurement of gas fraction and degree of saturation of the sample removed from the cell is performed by three methods in the various tests described in this research study. The pycnometer test is perhaps the simplest and most common method used, but inaccuracies may

occur when measuring gassy soil (as will be discussed in section 4.2.7). It is therefore only used as a comparison for the results supplied from the B.S.D. analysis (also to be described in the later section).

A more accurate method than the two mentioned above, is used in the consolidation rate tests of section 2.4.2 and the cyclic loading tests of section 2.4.3 (to be described). This method entails the measurement of total sample water volume from the loss in weight due to oven drying. The total solids volume is assessed using the density and mass of the dry soil and, finally, gas volume is given as the difference between the total sample volume and the sum of the water and solid phase volumes.Total sample volume is known from the cell dimensions and the height measured by the accurately calibrated LVDT already described. The method could not however be adopted for the later research tests, since sub-sampling for the required size distribution analysis prevented use of the whole sample.

2.3.4 Data recording (Chart recorder and voltmeter)

The mV outputs of the LVDTs on both cells are recorded on a type 460, 4-channel chart recorder (BBC Goerz Metrawatt) in order to indicate trend, not level, since soil depth is assessed more accurately using the voltmeter. Using this record, and also pore water pressure readings, the end of primary consolidation can be easily determined. The soil was left under pressure for a further 72 hours for each test in the main programme to be sure that it had reached an equilibrium state before raising it to the reaction plate level for acoustic testing.

2.4 MECHANICAL CONSIDERATIONS

2.4.1 The choice of confinement pressures (σ_1 and P_o)

The consolidation cell was designed to operate at pressures up to 1.6 MPa which allows the replication of most common gassy soil in situ confining pressures. Gassy soils at up to 60 m below a mudline submerged by up to 50 m, are found in river, lake, harbour and river delta environments. These maximum stress conditions are reproduced in the cell by applying 1.6 MPa of total stress (σ_1) and a back pressure (P_o) of around 1100 kPa, which provides a consolidation stress ($\sigma_1 - P_o$) of 500 kPa.

However, in order to provide the spherical bubble shapes crucial to the correlation of bubble sizes with acoustic properties, it was necessary to restrict total stress to 25 kPa for this initial research study. Also back pressure was restricted to atmospheric level since bubble sizes, measured after the soil is removed from the cell, have to be relevant to the sizes which exist while the soil is in the loaded condition for the acoustic test. (It is not certain that the bubble sizes will remain unaltered on removal of a back pressure). These considerations and later discoveries are discussed in more detail in the following pages, since the constraints suggested will be relevant to any future work using this test equipment on gassy soil , and possibly to other researchers who are developing similar apparatus.

2.4.1.1 The bubble shape constraint on total stress (σ_1)

Visual examination of the shape of bubble pockets in the soil showed that, when the consolidation period exceeds the period of bubble formation (less than 36 hours) the pockets are elongated perpendicular to the direction of applied stress. The use of a consolidation stress of 25 kPa together with

reductions in the period of consolidation (to be discussed in section 2.4.2), reduced the diametral aspect ratio to unity. Above this stress, the ratio increased so that bubbles could no longer be idealized as spheres. This idealization is important for both the valid use of the B.S.D measurement process and for the interpretation of the acoustic response, since there would be an indeterminate effect on the theoretical and practical acoustic results due to flattened bubbles.

2.4.1.2 The back pressure constraint (P_o = 1 atmosphere)

The measurements of parameters such as bubble size and gas fraction depend on the measurement of gas pocket structures established under the confining pressures when the soil is removed from the cell. Any disturbance to the size and shape of these pockets, due to the timing and sequence of unloading the sample confining pressures, is therefore a source of error. The evidence of disturbance is apparent in gassy soil core samples that have been taken in deep water environments and have been brought to the surface at atmospheric pressure. Also the back pressure samples described later in section 4.3 exhibit fractures around the bubbles due to gas expansion. It is therefore reasonable to avoid the risk of this source of error for the research study by adopting only an atmospheric level of back pressure.

2.4.1.3 The acoustic transducer, face-displacement constraint on total stress ($\sigma_1 < 550$ kPa)

During the cell pressure tests of section 2.3.1.2 the face of the 20 to 40 kHz transmitting transducer was permanently displaced by 0.5 mm due to the compression of the plasticell. This value of plastic deformation greatly exceeded the value indicated during the separate loading tests on plasticell (see section 2.1.7). Speculation as to the cause of this suggests that the

plasticell supplied for this transmitting transducer and for the 40-95 kHz transducer was in fact a less dense variety (55 kg/m^3) than the material tested and also the material supplied for the 95-200 kHz transducer. The lighter material has a compressive strength of only 550 kPa, but has the same absorption and has an improved attenuation level. This resulted in a total stress (σ_1) constraint of 550 kPa for the two lower range transducers but an improved acoustic performance.

The recessed face on the 20-40 kHz transducer was corrected by grinding down the stainless steel walls to finish flush with the outer surface of the araldite. An annular shaped plate was constructed in anodised duralumin with a thickness precisely equal to the reduction in transducer wall length. Using the plate as a spacer between the back of the transducer and the top section pressure plate ensured that the araldite face was returned to its original level when assembled ready for the soil test.

2.4.1.4 The volume change measurement correction and constraint on total stress ($\sigma_1 \leq 100$ kPa)

Section 2.3.3 described the process of phase volume change measurement in order to backcalculate values of structural parameters such as gas fraction and degree of saturation. However, some allowance must be made for the effect of cell volume change due to the elastic strain of the equipment and the creep and absorption behaviour of the perspex window section. The results of a series of tests to provide the values of these corrections also exposed the need to apply a maximum total stress constraint for the test programme.

Calibration tests were carried out to assess the volume changes at different stress levels for the cells and burette assemblies. A pressure of 500 kPa

was applied to the volume change burettes and cell top section. Figure 2.8(a) shows the burette tube volume change (curve(i)) measured between the paraffin/water interface of the right hand side tube and the closed outlet of the left hand side tube and curve (ii) shows the cell volume change.

The curves illustrate similar profiles at different levels. Curve (ii) may be conveniently separated into an immediate response of around 13.5 cc and a further long term response of 3 cc. The immediate volume change is contributed to by the elastic expansion of the equipment and, to a lesser extent, by the compression of water and the displacement of the transmitting transducer face. Long term behaviour is a result of creep and absorption in the perspex. This effect is clearly shown by curve (iii) which was obtained by replacing the perspex top section by an identical duralumin section. The overall immediate volume change is reduced by around 2 to 3 cc and there appears to be no long term change thereafter because of the effective elimination of the level of creep and absorption that was due to the perspex. Full immediate recovery of volume change occurs, unlike the residual shown in curve (ii).

The curve (ii) test was repeated and the results presented in curve (iv). This illustrates the degree of repeatability in performance, and therefore the level of accuracy of the cell volume change correction figure that is relevant to a soil consolidation stress of 500 kPa. It is equivalent to using atmospheric back pressure with the perspex top section, since perspex creep and absorption effects under pressure are removed by using the duralumin top cone. Taking curves (ii) and (iv), that are approximately 2 cc apart, as the upper and lower bounds, suggests a $\pm$ 1 cc level of accuracy in the assessment of the volume change correction. If this level of inaccuracy is present in the assessment of gas volume change in Cell 1, it would lead to a significant cumulative error in backcalculating the structural parameter values.

Further tests at 100 kPa and 25 kPa, using the duralumin top section, are shown in Figures 2.8(b) and 2.8(c) respectively and suggest ±0.25 cc and ±0.15 cc correction accuracy. This provides a cumulative backcalculation accuracy in the degree of saturation value of ±0.5% and ±0.3% over four steps. Hence a total stress (σ_1) of 100 kPa and below allows acceptable parameter measurement accuracy when used in conjunction with an atmospheric level of back pressure. This is necessary to avoid the further reduction of consolidation stress ($\sigma_1 - u_w$) and also to remove the problems of creep and absorption in the perspex that are caused by above atmospheric pressures in the top section hydraulic reservoir.

2.4.2 Slow consolidation and non-homogeneity of the soil samples

This section discusses how the problem of the non-homogeneity of the soil sample was resolved to avoid producing spurious acoustic results, because of structural inconsistencies.

It was found that 160 mm of soil slurry, at a bulk density of 1280 kg/m^3 and a moisture content of 184%, took over 300 hours to consolidate using a load of 135 kPa. Pycnometer moisture contents taken from the extruded soil sample revealed an average 9% increase from sample base to top, in the centre, and an average 15% increase at the side walls. This suggested that the poor rate of consolidation and soil homogeneity was caused by considerable soil/wall resistance, since a repeated test, using a perspex cell wall material, avoided similar problems. Adhesion resistance, at the honed surface, is created by the suction effect caused by two smooth surfaces compressed together, between which there is a thin film of fluid. The nature of the resistance to shear at this interface is the same as that developed at the surface of a pile in cohesive soil and assessed by shaft bearing capacity.

A new cylinder top section with total stress transducers was used to measure the effect of the wall resistance. It was found that a total stress of 100 kPa caused stresses of only 30 and 15 kPa at the centre and circumference of the top face respectively. Therefore, the silicone grease, used to cover the walls in previous experiments, was replaced by a much heavier, non-soluble waterpump grease (Castrol Ltd). Primary consolidation periods were considerably reduced, and further moisture content tests indicated sample homogeneity where radial and vertical variation was within $\pm$0.8%.

A further test of the homogeneity of the soil is discussed in chapter 4 which concerns the vertical variation of gas fraction and B.S.D.

2.4.3 Cyclic loading to investigate transmitter replacement during testing

To extend the range of frequency over which pulse signals could be successfully transferred through the soil, the transmitting transducers were constructed to allow interchange during a soil test. Acoustic tests can therefore be carried out using all three on a single soil sample. This entails two additional unloading and reloading operations to change the transducers. They must be carried out in a manner which reduces the possibility of creating significant structural change in the soil medium. A cyclic loading test was performed to provide the data necessary to assess this.

A 160 mm depth of soil slurry, at a bulk density of 1280 kg/m^3 and moisture content of 183.8%, was consolidated in three load increments to a total stress of 135 kPa and an atmospheric level of back pressure. Two unload and reload operations up to 100 kPa were performed in triple decrement and triple increment sequencies, each time allowing the pressures to

equilibriate within the soil. Void ratios and degrees of saturation were then backcalculated using the methods described in section 2.3.3

Figure 2.9(a) shows the variation of voids ratio with load. In two loading cycles the variation in voids ratio of 0.08, between 65 and 100 kPa, is perhaps a little too great to assume that no significant structural change will occur in the soil over the full transducer interchange operation. However, an examination of each of the two sets of corresponding unload and reload values of void ratio at 65 kPa reveals a difference in both cases of less than 0.01 (0.7%). It is likely therefore that reloading up to 65 kPa rather than 100 kPa would have in this instance, created a variation of less than 0.015 over the two cycles. This level of structural change would probably mot be significant enough to cause a material inconsistency between the three stages of the test, although the degree of overconsolidation necessary to provide this amount of change may cause the acoustic data to be more relevant to the maximum load condition. In any event, it would appear that the transducer interchange operation is viable for the chosen test programme load of 25 kPa if the sample is first overconsolidated to 50 kPa, and then reduced to the level of 25 kPa for unload and reload cycles. However, the effect on bubble shape due to the increase in load would need to be investigated.

Figure 2.9(b) shows gas fraction versus load data from the same test. Intermediate burette data from the first unloading operation is not available to plot gas fraction. However, an examination of the second unload and reload cycle at the 65 kPa load point of interest for this test reveals a variation of 0.004 (7%), which corresponds to a change in degree of saturation of only 0.5%. This variation is perhaps only marginally acceptable in view of the importance of the gas content on the acoustic response of the soil, although behaviour will be dominated by bubble size rather than gas fraction.

Although the cycle loading study has shown that it is possible to interchange acoustic transducers during a test, the test programme to be reported here did not adopt the operation. The investment of further time in the study of cyclic loading at the proposed 25 kPa level, and in test period extensions for adopting the interchange, would, in return, provide acoustic data over a greater frequency range and would allow data corroboration where transducer frequencies overlapped. It is therefore recommended for a further research programme using this equipment.

2.4.4 Elevated residual pore water pressure measurements

Pore pressure measurements, recorded by the two Gaeltec transducers in the piston, showed the same elevated residual values in the consolidation period tests of section 2.4.2 and the cyclic loading tests of section 2.4.3. Figure 2.10 illustrates pore water pressure data from the initial tests of section 2.4.2. Although the end of primary consolidation is indicated by the settlement versus time record, the Gaeltec transducers indicate a residual excess pressure. Such a response is described by Nageswaran (1983) and is attributed to free gas bridging across the face of the transducer with the menisci supporting a pressure differential at the gas/water interface. The pressure, measured at any stage in a test, is therefore a function of the radius of curvature of the menisci and the water pressure. Since both transducer housings are apparently susceptible to the collection of gas, it would be misleading to rely on resulting measurements to interpret pore water pressure.

CHAPTER 3 - DESIGN AND OPERATION OF THE ACOUSTICAL SYSTEM

3.1 AN OUTLINE OF THE OPERATION

3.2 THE MEASUREMENT EQUIPMENT
- 3.2.1 Compression wave transducers (Piezo-electric ceramics)
- 3.2.2 Signal transmission
  - 3.2.2.1 The square wave (SW) pulse transmitter
  - 3.2.2.2 The broadband voltage spike transmitter
  - 3.2.2.3 The continuous wave (CW) transmitter
- 3.2.3 Signal recovery
- 3.2.4 Signal analysis

3.3 THE METHODS OF MEASUREMENT
- 3.3.1 Sound speed by the Leading Edge Method
- 3.3.2 Sound speed by the TTC Method
  - 3.3.2.1 The basic theory
  - 3.3.2.2 Support to the theory, and application
  - 3.3.2.3 Initial proving tests
  - 3.3.2.4 Calibration tests to provide the TTC database
  - 3.3.2.5 Accuracy
- 3.3.3 Sound speed by the FT Method
  - 3.3.3.1 Waveform preparation, and the Fourier transform
  - 3.3.3.2 The theory
    - 3.3.3.2.1 To find the cumulative phase angles
    - 3.3.3.2.2 To find the value of the correct phase displacement at the chosen frequency
    - 3.3.3.2.3 To find the value of the PSDC
    - 3.3.3.2.4 To find sound speed
  - 3.3.3.3 Proof of the method
  - 3.3.3.4 Accuracy
- 3.3.4 The FT Method for attenuation
  - 3.3.4.1 The theory
    - 3.3.4.1.1 Use of a calibration liquid to allow for apparatus loss
    - 3.3.4.1.2 To find attenuation
  - 3.3.4.2 Accuracy

3.4 ACOUSTIC CONSIDERATIONS
- 3.4.1 Beat signal waveforms in gassy soil
- 3.4.2 Indirect signal transfer
- 3.4.3 Other acoustic systems
  - 3.4.3.1 Sound speed by the CW Reference Point Method
    - 3.4.3.1.1 Point identification by the spike reference marker
    - 3.4.3.1.2 Point identification by two peak-tracing methods
    - 3.4.3.1.3 Point identification by amplitude modulation
  - 3.4.3.2 Sound speed by the sine wave pulse
  - 3.4.3.3 Attenuation by waveform envelope measurement

3. DESIGN AND OPERATION OF THE ACOUSTIC SYSTEM

3.1 AN OUTLINE OF THE OPERATION

After pressures have equilibriated, following the consolidation and de-coupling processes described in Chapter 2, compression wave acoustic tests are performed on the soil sample. Three separate methods were used in the test programme to provide sound speed data, and one for attenuation, at frequencies within the range 10kHz to 1MHz. In all cases, signals are transferred through the soil between a pair of piezo-electric ceramic transducers in each of the two concurrently operated consolidation cells. The transducers are designed to respond to a square wave pulse from a power drive module (transmitter) over a range of frequencies by providing a signal with a characteristic frequency equal to the frequency of excitation. These signals are used in two methods of obtaining sound speed by transit time measurement. The transducers also respond to a very short, half cycle voltage burst by providing a broadband signal which is recorded for treatment by Fourier analysis to provide the third set of sound speed results and also the attenuation data.

For the research programme, Cell 1 contains the higher frequency range transmitting transducer (40 - 95kHz) in conjunction with the 20 mm consolidated soil depth, while the lower range transducer (20 - 40 kHz) is used in Cell 2 for the 65 mm soil depth. It was possible to extend the individual frequency operating ranges of the transducers beyond the quoted values, in some cases up to the previously stated limits of 10kHz to 1MHz, since they also provided reduced power beyond the design ranges. The required soil depths in each cell were found by successively reducing soil thickness until a signal of sufficient strength and regularity was received through a sample of maximum gas fraction. Despite dividing the same prepared soil sample between cells, structural parameters of the consolidated soil in the two cells were significantly different and provide

two independent sets of data rather than the intended separate frequency ranges of complementary data. These relatively short depths are an indication of the very great attenuative property of gassy soil in comparison with saturated soil and also of its dispersiveness. The difficulties experienced and the resulting limitations on the frequency range of results is caused directly by these properties and by the inherent problems with transmitting transducers which are required to respond over a range of different excitation frequencies when matched with soils exhibiting an extremely large range of acoustic impedances.

Figure 3.1 shows the layout for the acoustic system. The three power drive modules for signal transmission are options to provide the various signal excitations for the systems to be described in this chapter, whereas the remaining equipment is common to all the acoustic systems used. Post amplification is used to boost the received signal, and the waveform amplitude is controlled to avoid "saturating" the bandpass filter. A tight bandpass is used on the filter to depress unwanted frequency components and improve the regularity of the signal collected on the digital transient recorder. The BBC microcomputer transfers the received waveform to a display on the monitor and a signal averaging routine improves signal to noise ratio before analysis. Position and phase measurements are then carried out on the pulse signal waveforms for the two transit time methods, whereas the waveforms received from the voltage burst signals are recorded to disk and transferred to the main frame computer for Fourier analysis. Both signal types are recorded by dot-matrix printer. The traditional method of measuring sound speed using a pulse signal depends on using the time delay between transmission and reception with the point of reception being defined by the "leading edge" of the received pressure amplitude waveform. (This is regarded as the point at which amplitude begins to deviate from the stable condition as a result of transmitter excitation.) It will be shown later why the Leading Edge Method is not suitable alone for

use on the gassy soil test material but may allow useful observations when results are compared with those from the other two methods.

The second method, developed specifically for this research, to overcome the difficulties concerning dispersion, attenuation and transducer related problems, is referred to as the Transit Time Correction (TTC) Method. It provides the most accurate data but over a smaller frequency range. The pulse transmitter is used and the method relies on the accurate definition of the received signal phase position. Velocity is obtained by correcting for phase shifts using a calibration material to provide a true soil transit time over the measured soil depth.

The third method adopts the voltage burst transmitter to create a wideband frequency spectrum. Waveforms are provided for the soil and for a calibration material and are converted to Fourier transforms after sending to the mainframe computer. Phase angles for the soil and calibration material are converted to the same datum using a phase difference from the TTC method. Sound speeds can then be calculated from variations to this phase difference. The method produces sound speeds over a wide frequency range and is referred to here as the FT Method. Attenuation data is also provided by the corresponding set of Fourier transforms.

On completion of these measurements, the soil is unloaded and removed for structural analysis.

3.2 THE MEASUREMENT EQUIPMENT

3.2.1 Compression wave transducers (Piezo-electric ceramics)

Designs of the three transmitting transducers, and single receiver, were supplied by C.P. Engineering Services who also assisted in their construction. The basic design aim consisted of the transfer of a pulse

signal into a range of soils to provide a waveform of maximum pressure amplitude at a pronounced centre frequency for all frequencies in the range 20 to 200 kHz. For design purposes the gassy soil test medium was assumed to have an acoustic impedance of 0.3 to 1.5 ($x10^6 kg/m^2 s$), an attenuation of 1 to 20 dB/cm and a depth of around 75 mm and the three transmitting transducers were given frequency ranges of operation of 20 - 40, 40 - 95 and 95 - 200 kHz. In practice, the frequency ranges were increased well beyond these narrow confines by varying signal excitation and soil depth and by applying different methods of measurement in order to secure the best combination in the range and accuracy of results. Also these arrangements accommodated an extended range of soil conditions for the research tests which varied in impedance from 0.3 to 2.56 ($x10^6 kg/m^2 s$) and in attenuation from 1 to well above 20 dB/cm.

The internal arrangement of the transducers has already been shown in Figure 2.6, and section 2.2.7 has dealt with their construction and associated mechanical behaviour under test conditions. Table 3.1 gives the dimensions of the sections which have been chosen after consideration of the above design parameters. The metal extensions reduce the damping action on the band of frequencies excited by the power drive module. Therefore each transducer can respond to a range of frequencies of excitation. The plasticell air brick material enclosing the element and metal extensions reduces the sideways signal transfer by 4.5 dB/cm as measured using Pundit attenuation equipment (C.N.S. Electronics).

The diameter (D) of the active face of each transducer was fixed by applying the following constraints:

$$1.27\lambda < D < \sqrt{(2H\lambda + \frac{\lambda^2}{4})} \qquad (3.1)$$

This ensures that all frequencies, within the range of the transducer, should be above a certain minimum, f_{min}, (the left hand side constraint) and the receiver should remain beyond a certain point in the beam pattern (the right hand side constraint). These limits are explained as follows where (λ) is wavelength and (H) is the transducer face separation.

Since (λ), in the left hand side of equation 3.1, is set to the wavelength of the lower limit of the frequency range of each transducer in turn, then the corresponding values of (D) will ensure that all frequencies of operation for the three transducers will be above the values of (f_{min}). (f_{min}) is the frequency above which the reactive output of the transducer (susceptance) decreases significantly in proportion to the resistive components (conductance) and becomes comparatively stable. Hence there is a more efficient transfer of energy into the soil, rather than the disordered pattern of spreading energy below (f_{min}). Figure 3.2 may now be used to explain the right hand side constraint. A plane wave propagation pattern extends over the Fresnel Zone (Near Field) to a point where energy begins to radiate over the Fraunhofer Zone (Far Field). The optimum position for the receiver is in the Far Field. This is so since, within the Near Field, there is a variation in path length between those signal rays along the centre line between the transducer faces and those rays from the extremity of the transmitting transducer face to the centre of the receiver face. This raypath disparity may result in a combined signal phase shift. However, the phase shift effect is corrected to a certain extent by using a calibration material in the same arrangement, when using phase position measurement of transit time.(This will be discussed in section 3.3). The optimum receiver position is therefore a result of the maximum value of (D) being set by applying the right hand side of equation 3.1 which limits this disparity in lengths to $\lambda/4$ for the chosen transducer frequency ranges, provided the receiver remains outside the range of the Near Field. In practice, because

of very high attenuation strengths in the soil, this Far Field position constraint could not be always observed for the research tests. This is discussed further in context, within section 3.3 dealing with the methods of measurement.

Each of the transmitting transducers was designed to transfer maximum power to the soil over the given effective face area of radiation at 100 volts (peak to peak) input. Also the risk of non-linear wave propagation due to exceeding optimum power output at a low impedance interface is avoided. The araldite bond strength between the element and metal masses also imposed a limit on the designed output level.

The calculated output power versus frequency response for each of the transmitting transducers is shown in Figure 3.3 (C.P. Engineering Services) for three values of acoustic impedance. In general a fairly flat response over the frequency range of interest is predicted for the less gassy soil of $1.5 \times 10^6 kg/m^2 sec.$ which gradually deteriates into a trough between two peaks of power at the limits of the frequency range as impedance decreases as the soil becomes more gassy. In practice significant power response has been found to extend beyond both upper and lower frequency limits of design for the less gassy soil, using the intended square wave pulse excitation, and some extension has been found for the more gassy soils using the wideband voltage spike.

3.2.2 Signal transmission

There are three power drive modules which provide the transducer excitations for the tests described in this thesis.

3.2.2.1 The Square Wave (S.W.) pulse transmitter

This consists of a combined power supply and counter unit with separate drive and power amplification. A six way switch allows selection of the pre-set pulse lengths over the range 35 to 210 μs. Pulse repetition frequency is adjustable between D.C. and 5kHz with pulse frequency variation between 10 and 412 kHz, using two stages.

A square wave is produced, as shown in Figure 3.4(a), which can be varied in voltage amplitude from 0 to 100 volts (peak to peak) using a power supply of up to 25 watts r.m.s. This produces a frequency spectrum, in the signal propagated from the transducer face, that contains a strong characteristic component at the drive module frequency with significant off-centre components. A diagram of the low frequency end of the spectrum is shown in Figure 3.4(b) to illustrate this feature, whereas Figure 3.4(c) is a diagram of the typical signal waveform received through a non-dispersive medium. Although, with saturated soils, the leading edge remains sharply defined at all frequencies within the range of each transducer, high attenuation and transmission related interference generally obscures this point for gassy soils.

The transmitter provides an external trigger for the oscilloscope and transient recorder at zero time delay for each pulse transmission. A cycle delay switch, on the trigger, allows the delay to be increased in steps up to 9 cycles when measuring sound speed by the TTC method.

3.2.2.2 The broad band voltage spike transmitter

The spike excitation for the transducers is provided by a type PA1011 flaw detector unit (Baugh and Weedon Ltd). By applying resistances to the output, the unloaded spike signal can be reduced to the 100 volts x 0.25 μs

pulse shown in the diagram of Figure 3.5(a). This provides a received signal for which an example frequency spectrum is shown in Figure 3.5(b) and a waveform in Figure 3.5(c) when transferred through a non-dispersive liquid.

3.2.2.3 The continuous wave (C.W.) transmitter

The transmitter consists of a separate amplifier and waveform generator. The waveform unit generates a sine wave of amplitude up to 100 volts (peak to peak) and a frequency range of 0.05 Hz to 500 kHz. A simultaneous square wave output is used to provide a single half cycle voltage spike of around 0.2 μs, that is adjustable between 0 and 50 volts. The single spike is superimposed onto the sine wave at a given peak amplitude point as a marker reference and the combined signal amplitude is then limited to 100 volts (see Figure 3.6). Spike repetition can be varied in steps of between one and a hundred cycles. The frequency spectrum of the received signal, at the point where the spike is applied, indicates the dominant CW frequency with a broad band of frequencies varying in strength according to the spike to CW power ratio. The received waveform through non-dispersive liquid varies from a regular CW sine wave for zero spike voltage to a sine wave which is very irregular in the region following the spike position, for maximum spike voltage. An example of this waveform is shown later and is discussed in section 3.4.3.1.1.

3.2.3 Signal Recovery

The basic aim of the signal recovery equipment illustrated in Figure 3.1, is to record a high resolution image of the received signal waveform with reduced signal to noise ratio and well defined leading edge or phase position. This must be achieved without introducing spurious effects,

caused by the recovery equipment, that cannot be calibrated out by the following signal analysis.

Pulse signals transferred through non-dispersive liquids have reasonably regular waveforms which can be improved slightly by attenuation of off-centre frequency components using the type 3100A bandpass filter (Krohn-hite Ltd). Dispersion in a gassy soil medium causes the initially ordered components, that create the transmitted pulse waveform, to be displaced in phase. The received signal regularity becomes disrupted and is therefore significantly improved by using the bandpass filter. This attenuates those components which are further in frequency from the centre since these are likely to be phase shifted the most, through dispersion.

The filter has a 24 dB/octave attenuation slope with an 80 dB limit, over the frequency range 10 Hz to 1 MHz. Upper and lower bandpass controls are set at the centre frequency of transmission for all the research programme tests. This ensures that the characteristic frequency component is not phase shifted although off-centre components are affected by $\pm$ 180^{o} over a factor of 10 times increase in frequency. It is therefore essential, in all tests where phase position is being measured, that the periods of the received signal waveform conform to the frequency of transmission on which the bandpass is centred.

Optimum efficiency is provided by adopting a two-stage gain in voltage amplitude through the post amplifier and bandpass filter combination. The first stage of the differential amplifier is constructed to give a x10,000 magnification before the signal is transferred to the bandpass filter and back for the second stage to provide the overall x50,000 gain. This avoids attempting to filter signals of low amplitude. It also avoids the further magnification of unwanted frequency components, such as noise, to saturation

level where the combined signal exceeds amplitude operation limits for the amplifier unit or the transient recorder. This would cause unnecessary signal distortion and phase shift. Therefore a type D83 oscilloscope (Telequipment Ltd.) is used to display the output from the amplifier to check for waveform distortion and to avoid exceeding the 20 volt input limit to the transient recorder. It is also used to display the transmitted signal in order to ensure consistency between tests.

The gain is adjusted in such circumstances by a unit comprising variable resistors which are arranged to avoid causing signal phase shift. This unit also removes a contribution to signal related interference from the multiple reflections travelling along the receiving transducer output cable because of the electrical impedance mismatch between receiver and amplifier. Variable resistors in the unit can be adjusted to balance the impedancies to the point where this particular interference reduces to a minimum on the waveform displayed at the oscilloscope.

The amplified and filtered signal is then collected by the transient recorder, type DL 910 Datalab (Data Laboratories Ltd). It provides an analogue to digital conversion of the received signal waveform at a rate of 20 MHz - fast enough for the pulse repetition rate of transmission. The waveform is defined by a sampling window with a time base of 4096 samples, at a rate of 0.1 μs to 10 μs per sample, and a voltage amplitude of 256 data points over a total height of 0.1 to 20 volts. This provides a transit time measuring accuracy of ±0.05 μs. Triggering of the sample start time is achieved externally by the trigger point on the square wave pulse transmitter, the marker on the CW transmitter or the reduced output level from the spike transmitter.

A BBC B series micro-computer (British Broadcasting Corporation) is interfaced with a Datalab standard parallel TTL binary digital output. The

interface (Campus Computer Consultants) connects to the 1MHz output supply rail (BUS) and is operated by simple commands in BASIC computer language. Software on EPROM is arranged in machine code to access the digitized received signal waveform in real time. 2048 samples are transferred to the computer to display any 1024 sample width on a high resolution monitor type V7001/05B (Philips Ltd). A totalizing method of noise reduction by signal averaging is carried out by the computer before displaying the waveform. Waveform data is collected at the pulse repetition rate and cumulative amplitudes are divided by the number of signals chosen (50 for the Leading Edge and TTC methods and 200 for the FT methods).

3.2.4 Signal analysis

Software is provided in BASIC language to control a variety of functions dealing with the waveform analysis, storage and retrieval performed by the microcomputer.

The vertical and horizontal display scales can be set so that two vertical cursors can be positioned anywhere to provide time base (as referenced from the sample start time) and amplitude co-ordinates of the cursor points on the displayed waveform. This is essential for the measurement of transit time when using the SW pulse transmitter and locating the received signal waveform commencement point for the Leading Edge Method.

Measurement of the phase position of this received pulse waveform on the monitor is performed by simultaneously projecting onto the display a continuous sine wave pattern. The model CW is adjusted in period, amplitude and phase until the two waveforms are exactly in phase and correspond precisely to the transmitted centre frequency. Phase position of the CW is displayed in degrees as referenced from the sample start point of the authentic pulse signal. This provides the device by which the true transit

time can be calculated in the TTC Method. Periods and phase positions can be adjusted in steps much smaller than the maximum resolution of 0.1 μs per sample for signal waveform collection by the transient recorder. Any region of the 2048 samples from the recorder can be expanded to full width display on the monitor to examine the waveforms, and the degree of fit, in more detail.

For record purposes the waveforms for all signals used in the research tests have been saved on a dot matrix printer type RX-80 (Epson Corporation) at a resolution of 640 dots per 8-inch display width. Cursor co-ordinates, and CW period, amplitude and phase are included in the printout of the waveforms. The received signal waveforms from tests using the spike transmitter, are recorded on floppy disk. The disk software includes the conversion of the waveform, stored in binary, to ASCII mode which is then transferred to the main frame computer using a file transfer package called KERMIT (Lancaster University). The main frame computer generates data and hard copy (plots) using the FT Methods. Fourier transforms are provided for the soil and calibration material together with plots of sound speed and attenuation versus frequency.

3.3 THE METHODS OF MEASUREMENT

3.3.1 Sound speed by the Leading Edge Method

The SW pulse transmitter is used to develop the transducer response described in section 3.2.2.1 and to provide the received signal waveform shown in Figure 3.4(c). This waveform is recovered, displayed on the microcomputer monitor and analysed using the equipment and software described in section 3.2.3 and 3.2.4. Measured transit time (from the pulse transmission start time to the leading edge of the received signal) is recorded at varying frequencies from f_{min} to the maximum which is

successfully conveyed through the soil in each concurrently operated cell. In order to improve definition of the leading edge point of the received signal waveform, the input voltage amplitude scale on the transient recorder is adjusted to maximum gain (since input 'saturation' of the Datalab 910 does not affect leading edge position).

The measured transit time is corrected by subtracting delays caused by the equipment used in the acoustic system. Measurements of delay established that the apparatus comprising the system described in sections 3.3 and 3.4 did not cause significant delay to the signal leading edge position. Previous systems had to be discarded when found to impose triggering delay. Only the travel time delay caused by transmitting and receiving transducers was found to be significant enough to warrant the application of a correction. Delays were in excess of ± 0.05 μs resolution achieved for the measured transit time using the signal analysis system described. In order to provide values for each transducer combination, distilled water and glycerol were used in the cell to generate two separation versus time curves by measuring pulse transit time over several transducer separations up to 200 mm. The sound speeds of the glycerol and the water were taken from the gradients and were used to compute the true transit times for the given separations. These true transit times were subtracted from the measured times to provide the separation versus transducer delay curves shown in Figure 3.7. This method of plotting the data provides an accurate measurement of transducer transit time delay at the zero separation point, at which the water and glycerol lines intersect. As the lines are not vertical, this indicates that the measured sound speeds are slightly incorrect. An adjustment of these speeds to bring them vertical is unnecessary, since the zero separation point is still valid. The delays are 2.20, 6.38 and 12.85 μs ($\pm$ 0.02μs) for the 95-200, 40-95 and 20-40 kHz transducers respectively. Hence sound speed is computed by using these values to correct the measured transit times recorded in the test programme

together with the accurate measurements of soil depth provided by the system described in section 2.2.6.

An assessment of the accuracy of the Leading Edge measuring system is provided in Table 3.2 for the two soil depths of 20 mm and 65 mm in Cells 1 and 2 respectively. The accuracy of measuring depth ($\pm$0.025 mm) is taken from section 2.2.6 and that of transit time ($\pm$0.05μs) is taken from 3.2.3 to give overall accuracies in sound speed of $\pm$7.5 and $\pm$2.3 m/s for a saturated soil of sound speed 1500 m/s.

No similarly calculated values, using the Leading Edge method have been entered in Table 3.2 for gassy soils of reduced sound speed since they would be misleading for several reasons. The reasons are mentioned here since they will be relevant to all in situ and laboratory sound speed measurements made using the standard leading edge technique for gassy soils and since the results presented here need to be interpreted with these considerations in mind.

Poor signal to noise ratios, caused by the equipment operating at maximum path length in order to optimise sound speed accuracy, create an uncertainty in defining the true leading edge point of the received waveform. Reducing the path length, and therefore the signal loss, to improve signal to noise definition, increases error bands to a level above the likely trend in sound speed variation with frequency. Also, where transducers are designed for operating over a band of frequencies in a range of soil acoustic impedancies, it is impossible for all signals to be propagated into all media at peak power. The problem of reduced power at the receiver is further aggravated by an initially slow rate of rise for the waveforms from gassy soil (rise time being the duration from the leading edge to the maximum voltage amplitude).

Signal related interference is also a problem. It is significant in leading edge definition for systems which exhibit poor signal to noise ratios and is therefore present in this system for gassy soil media. The main sources of this interference are through transmitter breakthrough and indirect signal induced oscillations in the post amplifier. By keeping the transmitter remote from the cell receiver and signal recovery apparatus, breakthrough is reduced to a minimum. The post amplifier oscillations were reduced by designing a unit for use with this system and then damping the vibrations to a minimum amplitude. However, these attempts, together with the impedance matching adjustments to the receiver cable (described in section 3.2.3) were not enough to remove the problem entirely.

Finally, the dispersive nature of gassy soil causes the components of frequency, indicated in the frequency spectrum of the pulse signal, to be conveyed with different transit times. Hence the first arrival may not correspond to the frequency component which triggers the delay time start point on the transient recorder and may not be the centre frequency of transmission. It is therefore impossible to predict the first arrival frequency for all signals over a given test range and unlikely that there will be any major variation in the corresponding sound speeds since the first arrival may be the same component which is present in all frequencies of transmission.

A further problem of equipment induced signal delay can be ignored in relation to this work since it was caused by the bandpass filter and remedied by removing this unit for the sequence of research tests. However, it is a problem that may affect other laboratory or in situ tests on gassy soil using bandpass filters. Tests in Cell 1 at 40 and 90 kHz, using distilled water, revealed corresponding increases in transit times of 0.8 and 8.2 μs that may possibly arise from some combination of the off-centre bandpass phase shift of the signal components present in the rise period of

the waveform, together with poor leading edge definition. This may be supported by the evidence that no phase difference occurs in a similar comparison of with and without bandpass filtering when using a continuous sine wave without significant off-centre frequency components.

In summary, this system is acceptably accurate for measuring the sound speed of saturated soils, but the additional sources of unquantifiable errors discussed in this section become more significant with increasing gas content. Therefore the results from this method may be used where they are obtained for soils of very low gas content (around 0.003 gas fraction) to interpret the acoustic response of the soil. However, for soils of significant gas content, these results do not give reliable, independent information. They may be interpreted by using the correct results from the other two sound speed methods in order to try and quantify the effects of the sources of errors discussed here.

3.3.2 Sound Speed by the TTC Method

The SW pulse transmitter and signal recovery technique referred to in the Leading Edge Method of section 3.3.1 is also used in the TTC Method. In addition, this system makes use of the bandpass filter, the cycle delay switch on the SW pulse transmitter (described in section 3.2.2.1), and the CW curve fitting technique (described in section 3.2.4) in order to determine phase position rather than leading edge.

3.3.2.1 The basic theory

The basic theory will be presented first and then discussed in more detail together with its practical application.

Figure 3.8 shows four waveform diagrams, where (a) is the signal propagated from the transmitting transducer into the soil and (b) is the signal that would be collected at the receiver without incurring the delay due to transferring through the soil. The remaining pair (c,d) are collected at the receiver after transferring through the medium. Waveform (a) illustrates the zero time datum, for the transient recorder sample period, being triggered at a specific cycle start point using the cycle delay switch. This point is selected individually for each signal frequency and test medium and marks the beginning of the section of waveform where the frequency of transmission becomes established following the early part of the rise period.

Waveform (b) indicates a phase shifting of the selected point in waveform (a). The delay caused by this phase shift is referred to as the Transit Time Correction (TTC) and combines all the sources in the total system which contribute to the final phase position of the received signal waveform displayed on the monitor, except that of the transfer medium itself. However, the value of this TTC varies with both signal frequency and transfer medium and must be calculated from measurements on a calibration material, as described below.

Waveform (c) illustrates the waveform received after transfer through a calibration material provided by a liquid of the same acoustic impedance as the soil under test. The delay from the datum to the equivalent cycle start point used in waveform (a), and taken from the monitor display, is referred to as the Measured Transit Time (MTT_1). Similarly, waveform (d) resulting from the same signal transferred through the test soil, produces a measured delay of (MTT_2). Both waveforms (c) and (d) are assumed to be phase shifted by the same degree, giving equal TTC values since both the signal frequency and the acoustic impedancies of the two transfer mediums are equal.

It is possible to measure the sound speed of the calibration material separately using the Leading Edge Method since it is non-dispersive and does not create the problems referred to in section 3.3.1. The True Transit Time (TTT_1) for this medium can then be calculated using the path length, that is relevant to the (MTT_1) value and is measured as section 2.2.6. Hence the value of TTC can be found from:

$$TTC = MTT_1 - TTT_1 \qquad 3.2$$

and the value of (TTT_2) in the equivalent soil can be found from:

$$TTT_2 = MTT_2 - TTC \qquad 3.3$$

since TTC is assumed common to both media. Sound speed for the soil is then simply calculated using the measured soil path length.

A data bank of TTC values has been obtained using equation 3.2 at pre-arranged frequencies over the operating range of each transducer. This has been done for each of several materials which were chosen since their values of acoustic impedance are uniformly distributed over the range of values of the soils to be tested. The soil test programme employs the same pre-arranged signal frequencies and so the corresponding TTC values are provided from the databank by interpolation between pairs of calibration impedancies at each of these frequencies.

3.3.2.2 Support to the theory and application

The point at which phase position is measured for this method is important since the initial and latter sections of the received waveform are not at

the frequency or phase of the middle section. The early part of the rise section does not always conform to the centre frequency of transmission since the transducer face cannot respond instantly to the level of excitation delivered to the ceramic element. This rising waveform is therefore assembled from those frequency components which more quickly respond efficiently by propagating into the medium.

The latter part of the waveform is phase shifted due to the influence of multiple and cell wall reflections. Multiples result from a proportion of energy in the direct signal being reflected from the face of the receiver due to an acoustic impedance mismatch at this interface. It then similarly rebounds between transmitting and receiving transducer faces. Wall reflections are propagated by side lobe power at the extremity of the Near Field as illustrated by the diagram of Figure 3.2(c) earlier, showing the locus of power typical of this type of transducer. Evidence of both wall and multiple reflections at the receiver are presented later in this chapter in connection with CW signal tests. Their effect is such that when the direct and reflected waves of equal frequency meet at the receiver, the resulting combined signal is also of the same frequency, but of different phase, to both components. (This feature has been demonstrated using a twin-channel oscilloscope to display two out-of-phase signals of the same frequency which were then combined by a 'summing' device). This particular effect on the waveform phase position cannot be calibrated out. The delay point at which the first multiple, or wall reflection, arrives at the receiver is calculated from the geometry of the compression chamber, the near field dimension and the sound speed values from the Leading Edge Method for both soil and calibration media.

The cycle start point is therefore chosen by displaying the received waveform on the computer monitor and overlaying it by a continuous sine wave pattern of the same frequency, to locate the earliest point at which the

transmission frequency becomes established. This point is then used as a trigger to generate the test-signal demonstrated in the waveforms of Figures 3.8(a) to (d) and the CW pattern is again overlayed on (c) or (d) to locate the precise equivalent point on the received waveform. The CW is adjusted in amplitude and phase until it fits with the 'middle' section, away from the regions affected by rise or reflections. Use of the CW to locate the equivalent point improves accuracy since the position is continuously defined over the full extent of the middle region. Therefore the total number of whole and part cycles from the zero delay time (triggered at the chosen transmitted cycle start point) to the corresponding equivalent point in the received waveform is converted to microseconds at the transmitted frequency to provide the value of MTT. Figure 3.8(e) gives an example taken from a negative-going received signal printout for a gassy soil, with the model CW fitted to obtain the MTT as shown. The model CW fits both the middle and end regions of the pulse waveform. This is because the first multiple reflection is greatly attenuated by its additional two way travel through the gassy soil and therefore does not cause a measurable phase shift when combined with the direct signal.

The assumption that waveforms (c) and (d) are equally affected by the TTC phase shift delay arises from an examination of the contributory factors influencing the phase position of the middle sections of the received signal waveforms (other than the effect of transfer though the medium).

Phase shifts at both the transmitting and receiving transducer interfaces with the soil cause frequency dependent variations in the received signal waveform position. These phase shifts are determined by the ratio between the resistive (conductance) and reactive (susceptance) components of the energy at the interfaces which is, in turn, dependent on the acoustic impedance of the medium at the faces of the transducer. The variations of both conductance and susceptance with frequency are mostly small within the

operating ranges of the transmitting and receiving transducers in the two cells. Hence the variation of the ratio between the two, and therefore the waveform position, over the relatively small steps in test frequency is fairly uniform and continuous. Only an occasional transitional region of frequencies interferes with the uniformity, and no TTC values or MTT readings are taken within such areas for calibration and soil tests.

Further contributions to the final received signal waveform phase position develop within both transmitting and receiving transducers. The travel time delays caused in the transfer of the signal through the transducers, between face and ceramic element, are recorded in section 3.3.1. They are constant, rather than frequency dependent, unlike the phase position delays caused by multiple reflections which rebound between the transducer front, or rear, face and element. The received signal waveform output to the printer, shown in Figure 3.9(a) provides evidence of the existence of such multiples. For the required resolution, a 2 volt, 1 μs wide spike was used in Cell 1, that produced a predominantly 500 kHz received waveform through distilled water. The figure illustrates at least four signal arrivals at approximately 7 μs intervals following the first direct signal arrival. Since multiples across the medium, or wall reflections, were predicted to occur at intervals in excess of 40 μs, and neither shear nor surface waves are compatible with the time difference, the signal arrivals are assumed to be internal transducer multiples. This is supported by an examination of the geometry and component speeds of the signal over the (40 - 95 kHz) transducer body, as shown in Figure 3.9(b). It can be seen that the 6 - 8 μs two-way transit time between the ceramic and the back face of the araldite, or the back face of the transducer, is close to the measured interval, unlike the signal reflected from the araldite front face. The signal waveform propagating from the ceramic element will therefore ultimately be a combination of direct and multiple component excitations of equal frequency and its phase position will therefore be frequency dependent. A further waveform phase

position effect is produced by the phase difference associated with the way that the transmitting transducer initially responds to the excitation provided. Not all component frequencies making-up the combined signal waveform will start to respond in phase at zero time. This will produce an inherent phase position relationship at zero time that will be common to the waveforms propagated when using both soil and calibration media.

The final contribution to phase position is made by the signal recovery equipment that was found to cause a zero to 2.5 μs phase shift delay over the frequency range 40 to 460 kHz. These five sources of phase deviation are therefore combined under the single value of phase position correction (TTC). Since they are jointly unaffected by other than signal frequency and the acoustic impedance of the material at the transducer faces, then the TTC values in the waveforms of Figures 3.8 (c) and (d) should be equal.

The consequences of two problems in the application of the TTC method can be largely overcome as follows. Firstly, the initial selection of the appropriate TTC value from the databank at the required signal frequency can only be made by using an acoustic impedance provided from a sound speed measured by the Leading Edge Method. Since this is inaccurate for gassy soils, a process of iteration is employed involving the reselection of TTC values from updated impedance results ultimately supplied by sound speeds from the TTC method. Secondly, in addition to the absence of databank TTC values at some frequencies, further data loss occurs in the TTC method from discarding soil MTT values at certain frequencies where there is a 'beat' effect in the signal waveform.

Beat frequencies arise from two, or more, dominant frequency components contained in the signal arriving at the receiver. When they are relatively close in frequency they combine to cause maximum voltage amplitude where the waveforms of both components are in phase, and minimum amplitude where they

are least in phase. This produces a waveform envelope which peaks and troughs at regular intervals referred to as the beat frequency. An example record of this waveform is shown in Figure 3.9 (c) taken from one of the research tests. The beat peaks are clearly reducing with time since the contributory components both decay exponentially. This waveform envelope is not consistent with other signal arrivals such as reflections and can therefore only be explained in terms of beat effects. The factor which concerns the application of the TTC method is that the frequency of the combined beat waveform may be significantly different to those of the two components, and hence the signal transmitted. It is therefore susceptible to phase shift from the bandpass filter when the filter is centred on the transmitting frequency.

Beat signals will be discussed later in this chapter (in section 3.4.1) since the occurrence of such dominant frequency components indicate a special acoustic response between the gassy soil and the transducers that are used in many in situ or laboratory tests. The origin of the two component frequencies which provide the beat effect for the soil waveform will be described in detail. However, in order to develop a means of dealing with the effects of such components and their resulting beat waveforms for the TTC method, a series of tests was performed to measure filter phase shift from several combinations of component frequencies and amplitudes.

Two sine waves, provided from separate CW waveform generators, were displayed on the two-channel oscilloscope and combined by the 'summing' facility. Table 3.3 shows the component and combined signal frequencies with their amplitude ratio. The last two columns indicate the shift in phase position of the combined signal waveform as a result of the bandpass filter being centred on the frequency of component 1 and then component 2. Errors in the penultimate column would be typical of TTC tests on 'beat'

waveforms in which the transmission frequency component was smaller in amplitude than the other component present and therefore further in frequency from the combined received signal. The last column shows more acceptable errors which are equivalent to a transmission frequency component larger in amplitude than the other component present and therefore closer in frequency to the combined received signal. From the 100/150 kHz worst case combination chosen for Table 3.3 a less than 5% difference in frequency causes an error within ± 0.25 μs. It is therefore a requirement of the TTC Method test, that, where transmission and filtered received frequencies are different, those signal waveforms should not be used. Hence it is necessary to examine all the beat waveforms in the TTC Method to select those of unequal frequency that must be discarded. In practice differences of greater than 1% can be easily detected.

The continuous sine wave pattern is used in the selection process by adjusting its frequency until cumulative periods match in transit time over the middle region of the beat waveform. The signals that are discarded have been phase shifted by an unmeasured amount that cannot be allowed for by calibration techniques. Also phase shift cannot be avoided by centering the bandpass on the received frequency, since the particular transducer/gassy soil response then produces another off-centre bandpass frequency which is again phase shifted. However, the problem of the combined regions of data loss which result from discarding beat signals is not too disruptive in the test programme and is alleviated to some extent by producing infill results from the FT Method.

3.3.2.3 Initial proving tests

In order to test the validity of the TTC Method of measuring sound speed, Cell 1 was used first with distilled water and then with glycerol. Varying frequencies and path lengths were used to provide the results shown in Table

3.4 and the values of MTT, TTT and TTC were found by using the methods, described in sections 3.2.2.1 and 3.2.2.2.

By comparing those TTC values in Table 3.4 denoted by an equal number of asterisks, it can be seen that, despite changes in path length, the values are reasonably constant for a given signal frequency. The four frequencies, chosen in the range from 53 to 450 kHz, all show a constant value of TTC to within $\pm$ 0.2 μs. Also it is considered that this apparent level of consistency could have been improved by a more discerning application of the model CW fitting technique. This test was repeated for glycerol and similarly produced consistent results. It can therefore be assumed that since TTC values are constant for each combination of frequency and transfer medium, for all path lengths, then the correct TTT and sound speed can be computed from given TTC and MTT values using equations 3.2 and 3.3.

3.3.2.4 Calibration tests to provide the TTC database

Initially, five calibration liquids were chosen from published sound speed (c) and density (ρ) levels which produced uniformly spaced acoustic impedances (ρc) in the range (0.5 - 2.61 x 10^6 kg/m^2s) relevant to the soils to be tested. Density and Leading Edge Method tests on these liquids then provided actual values. Table 3.5(a) and (b) show the measured TTC values of each liquid at the chosen steps in frequency within the operating ranges of the transducers in Cell 1 and 2 respectively. They have been found by adopting the TTC Method, culminating in the use of equation 3.2.

Examination of Table 3.5(a) reveals that the differences of the TTC values between columns at a given frequency are always substantially less than 1 μs. This ensures that any interpolation between the TTC values of the different acoustic impedances represented by the media will always be well

within ±0.5 μs. Table 3.5(b), for Cell 2, however does not always indicate such small differences. Further test results to provide intermediate figures using methanol and ethylene dibromide (of impedances 0.908 and 2.403 $x10^6 kg/m^2 s$,respectively) were discarded since the araldite transducer faces were found to be softened, presumably by interaction with both chemicals. No materials could be found to replace either medium. However, for the research tests, no interpolation between columns was necessary for Cell 2 because the acoustic impedances of the four soil samples were close to hexane, ethylene glycol and glycerol. Also, since the araldite re-hardened after two days and TTC calibrations repeated for water produced the same results, it was assumed that no permanent damage had been caused to the transducers and that the TTC database was still valid.

In order to check that the same TTC value could be produced by a transfer medium of equal impedance, but of significantly different sound speed and density, a final sequence of TTC tests was performed using olive oil. Although the published properties of olive oil suggested that it had an equal impedance to distilled water ($1.483 \times 10^6 kg/m^2 s$), measurements as a result of the tests revealed that it was slightly less ($1.348 \times 10^6 kg/m^2 s$). However, the TTC results for olive oil, as shown in the additional column of Table 3.5(b), are generally close to the results for distilled water and also to the values produced by interpolating between the column values either side of the oil.

3.3.2.5 Accuracy

The most significant effect on sound speed measuring accuracy for the TTC method arises from the definition of the TTC value. As seen from section 3.3.2.3, the value of TTC for the research tests can generally be placed well within error bands of ±0.5 μs. An allowance of ±0.07 μs should also be

made for the possible error in the soil MTT due to the slight phase shift caused by the beat effect. This level of error is indicated in Table 3.3 where it is shown that a 110 kHz transmitted signal may undergo a 1% change in frequency to 109 kHz. Greater values of delay in the table need not be considered since the beat signal selection process discards signals of frequency change greater than 1%.

The final contribution to the level of error in transit time measurement is made from the model CW curve-fitting process for both the calibration material (TTC measurement) and the soil (MTT measurement). Twice the ± 0.025 μs level of accuracy attained for the process is allowed which provides a total transit time measurement accuracy for the TTC method of 0.62 μs. Therefore, using the path length accuracy of ± 0.025 mm, sound speed can be calculated within the error bands shown in Table 3.2.

Although the error bounds stated for a very gassy soil of 350 m/s, are acceptable at $\pm$ 4.2 m/s and ± 1.3 m/s for Cells 1 and 2 respectively, the errors for a saturated soil of speed 1500 m/s are less reasonable. Here the error bounds on sound speed using the Leading Edge Method are superior at ± 7.5 m/s and $\pm$ 2.3 m/s. In summary the TTC Method results should always be used with the levels of accuracy given in Table 3.2 in mind, but should be supplemented at the low gas content limit by the Leading Edge Method results.

3.3.3. Sound speed by the FT Method

The broad band voltage spike transmitter is used to develop the transducer response described in section 3.2.2.2 and to provide the received signal waveform shown in Figure 3.5(c). This waveform is recovered and displayed on the microcomputer monitor using the equipment and software described in section 3.2.3. It is then transferred to the main frame computer using the

process described in section 3.2.4 for analysis using Fourier transforms. One waveform is taken for each of the two cells containing soil. This is repeated for a calibration medium which possesses the same value of acoustic impedance as the soil.

The waveform records are taken at a transient recorder sampling speed (s), of either 0.1 or 0.2 μs per sample, for a constant number of samples (N=2048). These sampling speeds ensure an accurate conversion from an analogue to digital waveform record so that all frequency components can be correctly represented by the Fourier transform. Tests at 0.1, 0.2 and 1.0 μs per sample confirmed that no significant variation in the corresponding transforms occurred between the first two rates, and the third was entirely different because of the inadequate sampling speed.

3.3.3.1. Waveform preparation and the Fourier transform

The waveform data section is displaced from the middle of the record to the beginning so that the leading edge point coincides with the first sample of the record. This is carried out on both the soil and the corresponding calibration records so that there will be no phase angle displacement between the two due to the different zero datum to leading edge delay periods. Such a difference would cause a phase shift of (a/T) for each frequency point in the Fourier transform where (a) represents the time displacement and (T) the period of the frequency point (Bracewell, 1978). First arrival time at the receiver is calculated for either a multiple or wall reflection (as described in section 3.3.2.2) and the corresponding point in the digitized waveform record is noted. To complete the waveform preparation the amplitudes of all sample points, after this first reflection arrival point, are reduced to zero voltage. This avoids the influence of additional component power from other than the single direct signal. Retaining the full 2048 complement of sample points and ending with a large

number of zero voltages, 'smooths' the Fourier transform to avoid an erratic variation which would otherwise be caused by an abrupt curtailment of the signal record at the reflection arrival point.

A computer program has been written to provide a discrete Fourier transform of each waveform record using the voltage amplitudes of the waveform sample points as real parts and zero for the imaginary ones, for the required complex input data. The transform provides the voltage amplitudes, in terms of real (V_R) and imaginary (V_I) parts of 2048 discrete component frequencies contained in the broad band received signal waveform. This data can provide the amplitudes and the phase angles of each component which, in turn, can be used to produce attenuation and sound speed results at all the discrete frequencies.

The intervals of frequency are defined by (1/NS) MHz, where (S) is in microseconds, and the range by (1/S)MHz. (Only the first half range from zero to (1/2S) is used, since the second half of the data is complementary.) Interval size and range for the 0.1 and 0.2 μs/sample recording rates are therefore 4.883 kHz, 10 MHz and 2.441 kHz, 5 MHz respectively. Phase angles for each component frequency are defined by:

$$\text{phase angle} = \tan^{-1}\left(\frac{V_I}{V_R}\right) \qquad 3.4$$

The phase angles produced from a single waveform for a given medium are all referenced from the same datum. Since equation 3.4 produces a zero phase angle at the zero frequency component, this datum is taken as zero frequency.

3.3.3.2 The theory

It will be shown that the phase angle data derived from the soil and its calibration liquid can be correlated together since all phase delay influences (except from transferring through the medium) are common to both. This correlation will be used to generate sound speeds for the soil at the corresponding intervals of frequency. However, before this can be done, a Phase Shift Delay Correction (PSDC) must be found which, when used in the correlation, applies the correct phase angle between the zero frequency datum points of the two sets of data. The effect of imposing a phase displacement between the two datum points is similar to that provided by the delay difference (a), in section 3.3.3.1. Therefore each soil frequency component is displaced in phase by the proportion $(\frac{PSDC}{T})$ which ensures that its amended phase angle is referenced from the same datum as the calibration medium.

The value of the correction is found after selecting a frequency component from the phase angle data (referred to as the coincident point) at which the TTC Method has already provided a reliable measurement of sound speed for the soil and calibration medium. The correct phase angle displacement between the two can then be calculated for this frequency. It is used, with the change in phase angle displacement that occurs between the frequency and the zero datum, to find the correct phase angle difference at datum (PSDC). This is explained in detail with the aid of diagrams.

Figure 3.10 illustrates possible phase position displacements of the individual frequency components generated by the broadband response to the spike transmitter, using example frequencies (10, 20 and 40 kHz) for particular transfer media. The time displacement due to all influences, other than that caused by transfering through the media, is referred to as

the Spike Transit Time Correction (STTC) and this is assumed constant for a given frequency and material acoustic impedance. It originates from exactly the same sources described in section 3.3.2.2. which combine to form the TTC delay and is merely different in value because of the displacement caused by the particular way that the transmitting transducer responds to the spike excitation rather than the SW pulse.

The displacements of the signal components from 'zero time datum' in Figure 3.10 are therefore relevant to the displacements of both the soil and calibration materials where they are unaffected by transfer through the medium itself. Phase position displacement (STTC), from the zero frequency datum, is shown here to vary uniformly with frequency since this will be shown to be the correct relationship. (However, the actual relative values of STTC are not pertinent to the eventual sound speed calculation by the FT Method).

As a result of transfer through the medium the broad band frequency components are further displaced in phase position. Sections (a) and (b) of Figure 3.10 illustrate the total (or cumulative) phase position displacements (tc) and (ts) in time delay for the calibration material and soil, respectively. In section (a) they are due to the phase shift imposed by the apparatus (STTC) and, in section (b), by a combination of the apparatus and transfer through the soil. The relative positions of the frequency components in section (a) are the same as at datum since the additional true transit time (TTT) is common to all frequencies for a non-dispersive medium. This is not the case for the soil in section (b).

Therefore the apparent phase position difference between the two media at any component frequency can be described by the difference between (ts) and (tc). If these are expressed in terms of degrees of cumulative phase shift

($degs_f$ and $degc_f$) at that component frequency (f) instead of time delay, then:

$$\frac{degs_f - degc_f}{360} = \frac{TTT'_s - TTT_c}{T_f} \qquad 3.5$$

where TTT'_s is the apparent TTT of the soil, and TTT_c is the TTT of the calibration medium. The former is referred to as 'apparent' since it must be amended by the PSDC value to give TTT_s. (T_f) is the period of the component frequency (f). Both sides of the equation denote phase displacement as the proportion of a cycle.

Since the value of STTC is contained in both (degs) and (degc) it must cancel out in the expression (degs-degc) and therefore does not need to be found.

3.3.3.2.1 To find the cumulative phase angles (degc and degs)

The values of the cumulative phase angles (degs) and (degc) are found from summing the rotational displacements caused by generating all the preceding incremental phase angles from the zero reference datum to the frequency of interest. The phase angles for the calibration materials used in the research test cause (degc) to increase by fairly constant amounts (20° to 70°) as frequency increases in intervals of 2.441 or 4.883 kHz. Since it can be seen from Figure 3.10 that (STTC) must vary as (tc), because TTT is constant, this shows that the previous assumption in illustrating a uniform variation for (STTC) in diagram (a) is correct. This uniformity enables cumulative phase shift to be assessed, without risk of error, by using a phase rotation diagram. It therefore assists in the interpretation of

rotation when repeating this process for the soil, as soil produces a less uniform rate of increase in the cumulative phase angle.

Figure 3.11 (a) shows the rotation diagram which may be produced to find the cumulative phase angles (degc) of a calibration medium. The figures in the phase angle column are provided directly from equation 3.4 where positive angles are referenced from zero datum, in an anti-clockwise direction, up to the +180° mark, and negative angles are referenced from zero in a clockwise direction to -180°. The first component is marked (o) and represents the zero datum frequency. Succeeding components are numbered up to (6) and are marked on the phase rotation diagram in broken radial arrows indicating their phase position. The circular arrows indicate the direction that the phase displacements are increasing in, and the range over which the increase is made from datum. A positive clockwise sign convention is used since although a positive anti-clockwise convention provides the same value of (degs-degc) but of opposite sign, it produces largely impossible values of sound speed for the soil. Corresponding (degc) values are indicated in brackets next to the component phase angles.

It is possible that the direction of rotation for the soil may reverse for a particular component as shown in Figure 3.11 (b). This reversal may be allowed when the cumulative phase angle due to reversal remains closer to the predicted cumulative phase angle than the angle produced by continuing rotation in a positive direction. This predicted value is calculated by adding the average change in the cumulative phase angle over each interval in component frequency to its previous value. Figure 3.11 (b) indicates the reversal from component 3 to component 4 and shows that the actual position of 4 is at a smaller displacement from the predicted position by the reversal (I), than by continuing in the usual direction (II).

3.3.3.2.2 To find the value of the correct phase displacement at the chosen frequency (coincident point)

Using equation 3.5 and substituting the correct value of TTT_s for the apparent one, and the correct phase angle displacement (ϕ_f) at the coincident point frequency, gives:

$$\frac{\phi_f}{360} = \frac{TTT_s - TTT_c}{T_f} \qquad 3.6$$

Here the values of TTT_s and TTT_c can be found by using the sound speeds produced by the TTC Method and the path lengths used for the waveforms collected in the spike excitation tests. Hence the value of (ϕ_f) can be found.

3.3.3.2.3 To find the value of PSDC

The value of the change in the phase angle displacement (ϕ_{fo}) that occurs between the zero frequency datum and the chosen coincident point frequency is:

$$\phi_{fo} = degs_f - degc_f \qquad 3.7$$

Hence the correct phase angle difference at datum (PSDC), in terms of phase time delay (in microseconds), is:

$$PSDC = (\phi_{fo} - \phi_f) \frac{T_f}{360} \qquad 3.8$$

3.3.3.2.4 To find sound speed

A computer program has been written which provides the values of ($degs_f$) and ($degc_f$) using the theory of section 3.3.3.2.1. for each of the component frequencies (f). Equation 3.5 is then used to generate the apparent true transit times (TTT'_s) that are corrected by adding the PSDC algebraically at each frequency for the TTT_s values. Sound speed versus frequency data are then provided from these values by using the soil path length.

3.3.3.3. Proof of the method

The FT Method of producing sound speed is based once again on the assumption that the STTC values are the same in materials of equal acoustic impedance. Since this has been corroborated for the TCC values in the test with olive oil reported in section 3.3.2.4 and the initial proving tests described in section 3.3.2.3, it can also be assumed to be true for the STTC values. This assumption is made since the theory behind the contributions to the combined TTC values (see section 3.3.2.2) is common to both TTC and FT systems.

3.3.3.4. Accuracy

An assessment of the accuracy of the FT Method of measuring sound speed has been made by using the degree of fit of the Fourier transform. Initial programming work entailing the inverse of the Fourier transform and reconstruction of the waveform indicated a degree of fit within approximately $\pm$ 0.1% (where fit was taken as the sum of the amplitude errors as a proportion of the sum of the amplitudes). It was therefore assumed that the phase and cumulative phase angles are all within $\pm$ 0.1% giving TTT_s

accuracies of ±0.6% and ±0.3% for Cells 1 and 2 respectively (using Table 3.2 for TTT_c and equation 3.5 for the combined TTT_s accuracies). These percentages are converted to time (ΔT) and shown in Table 3.2 for the overall sound speed accuracy of the FT Method. The values indicated under the heading 'WITHOUT TTC' are the errors due to the FT method only. Those indicated by the heading 'WITH TTC' also contain the inaccuracies of the TTC method as a result of making use of a sound speed value at the coincident point found by that method.

In summary, the basic accuracy of the FT Method is reasonable for gassy soils, even when influenced by the added errors of the TTC Method. However, since the accuracy for saturated soils is not as acceptable, the results from the Leading Edge Method again may be used, when interpreted in the light of their shortcomings, to contribute to the overall record.

Two aspects of the method can only be assessed qualitatively. Firstly, the effect of the abrupt curtailment of the signal, as described in section 3.3.2.2., cannot be readily assessed without separate tests with the transducers installed in a large tank to delay substantially the reflection arrivals. However, it is considered to be common practice by many acousticians using Fourier transforms for removing unwanted end effects. Secondly, the calibration material used has a constant acoustic impedance value and therefore cannot always match that of the soil at all the components of frequency that are contained in the signal waveform. Since no values of STTC are available, some idea of error may be gained from the TTC values of Table 3.5 which generally vary within ±1.5 μs at each frequency. A 1.5 μs variation in transit time would lead to a further source of error in sound speed for gassy soil of ±9.6 m/s and ±3.0 m/s for Cells 1 and 2 respectively (and ±170.7 and ±52.5 m/s for saturated soil). The variation of sound speed for the research tests, however, generally indicate very

small ranges of acoustic impedance with correspondingly small additional inaccuracies. Hence, the Table 3.2 figures may remain largely unaltered.

3.3.4 The FT Method for attenuation

The Fourier transforms which are used to produce phase angles in the FT Method for sound speed described in section 3.3.4. are also used to produce attenuation results at the same component frequencies. Therefore the apparatus and procedure used in obtaining the soil and calibration transforms, described in the introduction of section 3.3.3., and in section 3.3.3.1, are relevant to this method.

3.3.4.1 The theory

The theory assumes that the loss of energy of each signal component using a soil test medium is equal to the loss which occurs using a liquid test medium of the same acoustic impedance plus the scatter and absorption loss due only to transferring through the soil. This transfer loss in the soil is described as the soil's attenuation and the above statement assumes that the transfer loss in the calibration liquid is insignificant in proportion to that of the soil. The loss when using a calibration liquid, referred to in the statement, is therefore assumed to be entirely due to the sources jointly considered as apparatus loss.

3.3.4.1.1 Use of a calibration liquid to allow for apparatus loss

The energy diverted away from the propagating wave front by reflection is a form of 'apparatus loss'. The reflections are due to the mismatch of acoustic impedances at the interfaces of various materials in the transducer and at the soil face. Contributions are also made from damping within the transducers and as a result of the level of susceptance at the soil faces.

Apparatus loss is therefore assumed to be common to both soil and calibration mediums for the research tests.

However, beam spreading effects are not common and may be significant in reducing the intensity of the signal received. They may therefore be considered in the same way as energy loss to the signal. Side lobe power, as shown in Figure 3.2, is not fully developed until the extremity of the near field where it radiates so that wave intensity is reduced by the inverse of the square of the propagated distance. For beam spread loss to be common to both test mediums, the receiver must be placed at the same number of wavelengths from the transmitting transducer when performing the calibration test as it was previously for the soil. However, for a dispersive medium, such as soil, the wavelength of each frequency component is different and prevents the selection of a suitable single path length.

For the research tests, a path length has been chosen to be approximately equal to the soil path length for both the cells. The difference in spreading loss is assumed to be a second order effect in comparison to the soil attenuation loss and is therefore neglected. This assumption is made since the level of increases in attenuation, due to the presence of gas in the soil, is much greater than that of the corresponding disparity in wavelengths in the media that causes the variation in spreading loss. Experiments have been performed which confirm this. Different calibration path lengths (5, 20, 60, 200 mm) were used to provide attenuation versus frequency data for the research tests and do not show significant differences in either attenuation or pressure amplitude of the respective transforms.

The dispersive quality of the soil also creates a variation in the degree of acoustic mismatch at the transducer/soil interfaces. Loss of signal energy due to reflection from the interface back towards the ceramic element cannot

therefore be equal for both soil and calibration tests over the full range of the frequency components received. However this effect can also be shown to be of second order significance by calculating the loss, for example, due to a change in sound speed from 750 m/s to 1500 m/s.

Using an equation assembled from the theory of Rayleigh (1877), loss due to reflection (L_R) is:

$$L_R = 10 \log_{10}[(1 + R)^2 \quad \frac{\rho_2 \, c_2}{\rho_1 \, c_1}] \qquad 3.9$$

where the variables are defined for equation 1.4. The corresponding difference in loss for sound speed varying within the chosen range is less than 1 dB.

3.3.4.1.2 To find attenuation

The transforms, which are initially generated in terms of the real and imaginary parts (V_R and V_I, see section 3.3.3.1) are converted to provide the vector resultant (V) where, for each frequency component:

$$V = (V_R + V_I)^{1/2} \qquad 3.10$$

Attenuation (α) can then be expressed as:

$$\alpha = \frac{10}{L} \log_{10} \left[\frac{V_s}{V_c} \right]^2 \qquad 3.11$$

where (V_s) and (V_c) are the vector resultants for the soil and its corresponding calibration medium respectively, (L) is the path length through the medium and (α), for these experiments, is measured in dB/cm.

In order to ensure that the Fourier transform data for the soil and calibration waveforms are comparable, the individual voltage reductions caused by the gain adjustment unit (see Section 3.2.3) are measured for each of the two media and used to increase the input waveform amplitudes to their correct voltage levels. This allows the correct ratio of (V_s/V_c) to be used in equation 3.11

3.3.4.2 Accuracy

The accuracy of the transform procedure is ± 0.1%, as described in section 3.3.3.4, which allows attenuation results to be calculated to within $\pm 2 \times 10^{-5}$dB. However, the two additional aspects of accuracy which were assessed qualitatively for the FT Method of sound speed (section 3.3.3.4) are also relevant for attenuation. The comments concerning the abrupt curtailment of the signal also apply here and the errors due to the soil's dispersive quality (causing variations in acoustic impedance and wavelength) has been dealt with in the previous section. Since these later considerations are of greater significance in terms of accuracy, the figure quoted above is not applicable.

A further potential source of error is avoided by discarding only a very small quantity of frequency component results. As shown in Figure 3.5 (b) several of the troughs in the curve of the Fourier transform are at the noise level, as indicated by the curve amplitude beyond the frequency limits of the received signal. Troughs occur in both soil and calibration transforms, not necessarily at the same frequency components, where the

signal is close to zero voltage amplitude ($V \simeq 0$). At these frequencies, use of the ratio ($\frac{V_s}{V_c}$), in equation 3.11, is meaningless.

Data produced from such results may develop peaks and troughs in the attenuation versus frequency curve that are random in level and unrelated to the test medium properties. Sound speed data at these trough frequencies should also be discarded but do not interfere with the results at other frequencies. Each phase angle is a separate measure of a frequency component relative to the zero datum frequency. It does not depend on the phase angles of previous, or later, components.

3.4 ACOUSTIC CONSIDERATIONS

3.4.1 Beat signal waveforms in gassy soil

Beat waveforms were introduced in section 3.3.2.2 in order to discuss their phase shift effect on the TTC Method of measuring sound speed. In this section the origin of the beat waveform will be discussed since it is provided by a specific reaction between the gassy soil and the compression wave transducers.

Figures 3.12 (a) and (b) show diagrams of the typical frequency spectrum associated with a received SW pulse signal through a non-dispersive liquid at transmission frequencies ($f_{t(a)}$) and ($f_{t(b)}$) respectively. The broken line in each diagram represents the level of soil attenuation versus frequency above which the remaining energy of the components make up the frequency spectrum collected at the receiver. This curve is hypothetical, although it can be seen from the results of the research test (and the theory of Anderson) that steeply rising attenuation with increasing

frequency may be expected for gassy soils. Also the position of this curve is a consequence of the frequencies of bubble resonance.

The shaded regions of both figures represent the way in which two frequency components t_1 and t_2 may dominate the frequency spectrum of the received signal. Whereas the frequency of transmission contributes one of the dominant components in Figure (a), both components are contributed by off-centre transmission frequencies in Figure (b). The response of Figure (b) was found in tests using large depths of gassy soil where received beat waveforms were often at frequencies well below those transmitted. This feature supports the theory that for gassy soil the attenuation cut-off (as indicated by the dashed lines in Figure 3.12) can be so abrupt as to exceed the rate at which the component peaks increase over the first half of the range of the spectrum frequency even for the SW pulse signals at below 100 kHz transmission.

Although no corresponding Fourier transforms have been developed using SW pulse transmitter excitation for both gassy soil and calibration media to prove that single dominant frequencies may result from soil attenuation, actual transforms are shown from the spike excitation system. Figure 3.13 (a) and (b) show the Fourier transforms of a signal waveform received through hexane and through gassy soil respectively. These correlate to the Figure 3.12 initial frequency spectrums for the SW pulse signals shown before the effects of soil attenuation, and the remaining spectra, above the broken lines, after attenuation. Dominant frequency components exist at approximately 47 and 60 kHz (with a smaller addition at 25 kHz). The attenuation versus frequency plot produced from the FT method of attenuation shown in Figure 3.13 (c) indicates that attenuation does increase sharply over the region between 40 and 100 kHz which encompasses the two soil peak amplitude frequencies. Figure 3.13 (d) shows the beat waveform which

results from the frequency component domination of the transform in Figure (b). The envelope exhibits a beat frequency of very approximately 20 kHz, whereas the combined signal frequency is around 50 kHz, which is a result of the dominance of the components shown in Figure (b).

This transducer/gassy soil response of providing dominant components of frequency below that transmitted, in the form of a beat waveform, provides a simple method of indicating the probable presence of very gassy soil. It may be used in place of, or to confirm, sound speed and attenuation tests instigated purely to locate such soil.

3.4.2 Indirect signal transfer

Several tests have been performed on gassy soil and various liquids which can be used to identify the sources of the various contributions made to the combined signal collected at the receiver. It was necessary to identify the contributions to ensure that no spurious events influence the response to be measured by the methods described in section 3.3. It was this preliminary investigation which identified the presence of the signals circumventing the direct route by travelling via the cylinder wall to the receiver and led to the development of the reaction plate assembly for decoupling. Such signals cannot be identified when using liquid media of low attenuation but, when using gassy soil, the low amplitudes of the circumventing signals become significant in comparison to the much reduced direct signal amplitudes.

Initial tests, before the reaction plate assembly was considered, were carried out without elevating the soil in the cell, using the SW pulse transmitter, the (40-95) kHz transducer and a 69 mm depth of gassy soil. Waveforms collected at the receiver were dominated by the circumventing signals. This was assumed because a reducing path length resulted in an increasing sound speed. Confirmation of this was achieved by elevating the

soil within the cell in increments while recording the received waveform at certain stages as shown in Figures 3.14 (a) to (e). The waveforms are therefore a result of the stage decoupling of the indirect contributory signals. The combined received waveform envelope was successively reduced by four significant events: separation of the pressure plate with the cell wall (b), the long holding-down bolts with the pressure plate (c), the block section quadring with the cell wall (d), and separation of the top vyon filter with the cell wall (e). The variation in amplitudes of the waveforms is a result of both the displacement in arrival times and the phase relationships between several equal frequency signals arriving after taking a variety of different routes around the cell. However, it can be seen from the sequence of figures that there is an overall trend to a reduction in amplitude of the waveform envelope, signifying a reduction in the number of indirect signals being received as a result of signal decoupling.The final waveform indicates that the direct signal route through the soil is not providing any contribution at the receiver. It is probable that, at these relatively high frequencies and path lengths the signal is attenuated to an amplitude below noise level.

The function of the reaction plate assembly in decoupling the transmitting transducer from the cell chamber is therefore essential. Further tests were performed by using the system modified by introducing the reaction plate assembly. This revealed the presence of surface waves (Rayleigh or Love waves). Figures 3.15 (a) to (f) show diagrams of the signal component waveforms that it is postulated may contribute to the actual received signal (g). The continuous sine wave (a) is caused by the oscillations of the signal recovery equipment described earlier. It is illustrated at very low amplitude similar to the direct signal waveform (b), the first multiple reflection (c) and the wall reflection (d) also described earlier in the chapter and assessed by assuming a speed of 300 m/s. The reduced amplitude became apparent due indirectly to a discovery concerning the decoupling of

the remaining signals. Removal of the water film and displaced solids discharged against the exposed 1 mm face of the soil, by the soil elevation procedure, decouples almost all the received signal (g), to leave a very low amplitude waveform envelope consistent with combining (a) to (d) only.

Waveforms (e) and (f) have been drawn in envelope position and amplitude so that when they are superimposed in phase they generate (g) exactly. This has been done in order to assess the construction of the circumventing signals which contribute to (g), and is possible since no phase changing, consistent with out of phase combinations, is apparent throughout waveform (g). Signal (e), since it arrives well before the soil direct signal, must travel through a medium of greater sound speed. Its arrival time coincides with that calculated for a surface shear wave travelling at approximately 3000 m/s around the metal/soil interface between transducers (plus the transducer body delay time). Waveform (e) is drawn by reproducing the first nine cycles of (g). Since only 9 cycles are transmitted in the pulse, (e) is completed by assuming exponential decay. Subtracting amplitudes (e) from (g) provides (f) which also has a 9 cycle pulse before decay commences. The origin of a signal such as (f) is unknown, although, since it can be decoupled by cleaning the exposed surface of the soil, it must be a surface wave travelling around the chamber. Also, its further delay in arrival after (e) can be attributed to the lower sound speed of a shear wave, reduced further by partially travelling through soil. The absence of early arrivals signifying surface waves in Figure 3.14 may be due to a voltage scale effect. This may be substantiated by the fact that no direct soil signal is evident.

Therefore the procedure of decoupling the surface waves is adopted in further tests at shorter soil path lengths. These have shown that no further sources of indirect signals contribute to the waveform collected by

the receiver of an amplitude comparable to, or even below, that of the direct signal.

3.4.3 Other acoustic systems

This section deals with the examination of cw signals used for measuring the acoustic response of gassy soil. Although the systems are so far unsuccessful in providing reliable sound speed and attenuation results, discussion of the consideration given and the work carried out may contribute to the efforts of other researchers in resolving the difficulties experienced in measuring the acoustic properties of gassy soils.

3.4.3.1 Sound speed by the CW Reference Point Method

This system is the same as the TTC Method of measuring sound speed described in section 3.3.2 except in its use of the CW transmitter detailed in section 3.2.2.3. Zero time datum on the Datalab is triggered by the spike reference point on the signal from the CW drive module. The corresponding point on the received signal waveform is identified and the MTT value recorded by using the model CW fitting software to fix its position accurately. True transit time, and therefore sound speed, can be calculated by applying the TTC value appropriate to a CW signal in a calibration liquid of the same impedance.

There are several advantages in using a CW signal instead of an SW pulse. The signal operates at a constant high voltage amplitude for maximum soil penetration whereas the pulse signal length and rise period seldom allow a build-up of the same level before the signal decays. Also the received CW waveform is generally smooth and regular in shape similar to that transmitted. Unlike the SW pulse signal, the CW propagated into the soil has a narrow band of frequencies over which the dispersive effect is small.

This enables useful CW signals to be propagated through large depths of soil, unlike those of the SW pulse. Figure 3.16 (a) shows a CW transferred through 138 mm of gassy soil. Its voltage amplitude is proportionally much greater than the waveform received from the SW signal and located centrally in Figure (b). The pulse is comparable in level to the oscillating waveform caused by the signal recovery equipment which can be seen either side of the pulse waveform. It shifts the phase and obscures the pulse beyond usefulness. Also, there are no beat waveforms using the CW signal because the characteristic frequency, propagating from the transmitting transducer, alone dominates a very narrow band signal. Therefore no difficulty arises over the choice of whether a received waveform is valid or not.

There are two disadvantages in using the CW. The first is the difficulty in identifying the point on the received signal which corresponds to the spike reference point. Procedures to overcome this problem will be described in the following sub-sections and the results will be used to investigate the level of phase shift caused by multiple and side wall signal reflection which is the second disadvantage.

3.4.3.1.1 Point identification by the spike reference marker

A voltage spike is superimposed onto the CW as described in section 3.2.2.3 in order to identify the reference position on the received waveform from the resulting disturbance at that point. Figure 3.17 (a) shows spike disturbances on a received signal record through gassy soil. The CW and spike marker voltages used are 22 and 31 respectively, since smaller spike sizes do not penetrate through large soil depths and retain sufficient voltage amplitude. CW frequency and spike repetition rate are 20.4 kHz and 30 cycles and the bandpass filter was removed from the system. The reduced sampling rate used to show the repeated waveform disturbance pattern is not fast enough to reproduce precisely the waveform from digital form, since

some high frequency components cannot be recorded. However the record does indicate a variety of frequencies present, because of the large bandwidth of the spike signal, in addition to the dominant CW. Using the filter on this signal with a tight bandpass setting at the transmitted frequency restores a regular CW received signal without the waveform disturbance of higher frequencies. Increasing the amplitude of the transmitted CW to 40 volts and resetting the passband to 15 and 25 kHz, as shown in Figure 3.17 (b), allows some disturbance through to mark the spike position without causing the irregularity of waveform (a).

It is therefore shown that the spike position may be used to define the reference position in the received signal waveform, without filtering, which will identify the required CW peak for MTT measurement performed using a tight bandpass. Two significant problems, however, prevent the use of this method to locate the reference point. Firstly, since the test medium is dispersive, the high signal frequency components of the spike may have a significantly different transit time to the CW signal and could cause the wrong peak to be identified. Secondly, the broadband spike may contain strong component signal frequencies equal to, or close to, the CW frequency. This would cause an error in the MTT value due to the resulting phase shifts or beat waveforms. The problems may be resolved by reducing the relative voltage amplitude of the spike marker to a level where a Fourier transform may indicate the presence of only a few frequency components of significant power. CW transmission can then be avoided at these component frequencies. No further work, however, has been carried out concerning this final proposal.

3.4.3.1.2 Point identification by two peak tracing methods

The equipment and approach of section 3.4.3.1.1 is adopted here but the power level of the spike marker is reduced to zero and only the CW is

transmitted through the soil. This revised approach has the advantage of using the CW co-ordinated spike position to trigger the sampling time record on the transient recorder without generating any spike signal components into the soil. Two methods are used to provide a corroborated identification of the correct reference peak on the CW without disturbing the signal.

Firstly the SW pulse signal is used to obtain an approximate transit time by the Leading Edge Method and a peak is identified which provides the nearest TTT to this value (using the TTC method). Secondly, corroboration of this TTT value is achieved by identifying the correct peak at the minimum frequency of transmission and using the oscilloscope display to avoid losing the identity when drive module frequency is gradually increased to operating level. Minimum frequency can be used successfully since cycle periods are large, which causes an incorrect choice of peak to produce an impossible sound speed.

By commencing tests in both cells at the low frequency limit it should be possible to avoid peak identification error by increasing test frequencies in small enough intervals where the actual transit time does not vary more than a cycle period over the interval. The TTC results to be shown later indicate that true transit time varies less than cycle period for intervals of 2.5 kHz up to 400 kHz for all the soils used.

Tests were carried out in an attempt to prove this system in the same way as that used in section 3.3.2.3 for the TTC Method. These consisted of TTC measurements with the CW signal in water over different path lengths. Table 3.6 gives the results and indicates that the TTC values are not constant whatever the transducer separation value. Later tests using the spike transmitter in varying depths of different liquids generally indicate an amplitude enhancement pattern at the positions where multiple reflections

between transducer faces are received. It is therefore assumed that continuous multiple reflections, when using the CW transmitter, cause phase shifting to the direct signal and therefore phase position dependency on transducer face separation. Similar phase shifting will not occur in gassy soil, since the multiple and side wall reflections are attenuated to a much greater extent than in non-dispersive liquids.

The phase shifting problem only concerns the TTC calibration measurements. In order to remove the reflection effects from the received signal waveform a signal analysis technique would have to be developed. This may make use of estimates of the voltage amplitude and phase of each multiple CW in order to reverse their effect on the direct signal waveform. No work has been carried out however on this particular proposal.

3.4.3.1.3 Point identification by amplitude modulation

Other signal forms such as the amplitude modulated CW have been considered for use in the same manner as the CW and spike marker signal and rejected for the same reasons. This signal is a CW waveform envelope that peaks and troughs at given cycle peaks within a chosen number of cycles. The combined signal bandwidth is much greater than that caused by the standard CW signal and therefore the additional frequency components may result in the problems suggested in section 3.4.3.1.1.

3.4.3.2 Sound speed by the sine wave pulse

Use of the SW pulse transmitter results in the stimulation of additional high frequencies in the transducer response due to the sharpness of the drive model waveform. Adopting the SW pulse for measuring sound speed by the TTC and FT methods may cause unnecessary waveform irregularity in the received signal due to dispersion. A sine wave pulse producing a signal of

less bandwidth was tested in parallel to the SW pulse using gassy soil. There was very little improvement in the received waveform regularity over the range 0-100 kHz, showing that the dispersion of high frequency components was not a problem in receiving clear signals for large depths of gassy soil. The major cause of such irregularity is therefore assumed to be the additional oscillations caused by the signal recovery equipment (referred to in section 3.4.2) where they are comparable in voltage amplitude to the direct signal.

3.4.3.3 Attenuation by waveform envelope measurements

The basic CW signal may be used for both dispersive and non-dispersive media using the method of measuring attenuation. Use of the logarithmic ratio of received signal voltage amplitudes provided by soil and calibration materials at each frequency of transmission provides a simple method of measuring attenuation. However, for pulse signals and treated CW signals the amplitude and shape of the waveform envelope, due to a dispersive medium, is to some extent a function of the relative phase positions of the contributing frequency components. This is illustrated by beat waveforms from the SW pulse which achieve a first peak amplitude and position dependent on where the frequency components become in-phase in relation to their individual peak amplitudes. In these circumstances relative off-centre frequency power and corresponding phase position may incorrectly influence the magnitude of the soil envelope amplitude and therefore the measurement of attenuation.

CHAPTER 4 - THE BUBBLE SIZE DISTRIBUTION (BSD) MEASURING SYSTEM

4.1 AN OUTLINE OF THE OPERATION

4.2 THE BSD TECHNIQUE

- 4.2.1 Sample preparation
  - 4.2.1.1 Drying
  - 4.2 1 2 Resin impregnation
- 4.2.2 Imaging
- 4.2.3 The measurement of planar size distribution
- 4.2.4 Conversion from a planar size to a spherical size distribution
- 4.2.5 Statistical considerations
  - 4.2.5.1 Re-arranging single bins into grouped bins
  - 4.2.5.2 The number of images
- 4.2.6 The structure of gassy soil
- 4.2.7 The example test results

4.3 THE INFLUENCE OF CERTAIN PARAMETERS ON BSD AND GAS FRACTION

- 4.3.1 The influence of variations in the preparation of gassy soil
- 4.3.2 The effect of varying confining pressures
- 4.3.3 The effect of different dewatering techniques

4. THE BUBBLE SIZE DISTRIBUTION (B.S.D.) MEASURING SYSTEM

4.1 AN OUTLINE OF THE OPERATION

The importance of bubble size and gas fraction in dominating the acoustic response of gassy soil is discussed in section 1.3.1. Therefore a method has been developed which measures gas fraction and B.S.D. of the soils used in the research programme in order to correlate these parameters with acoustic behaviour. After the mechanical and acoustical work of sections 2.1 and 3.1 have been completed the soil is removed from both cells and sub-sampled ready for analysis.

The general technique can be used to measure the total void, gas void or particle size distribution in both gassy and saturated sediments provided the void spaces, or particles, can be approximated to spheres. In this study only the measurement of gas voids is required. Resin-impregnated specimens are provided from the sub-samples and mounted to use in a scanning electron microscope (S.E.M). Images are passed to a computer where a noise reduction technique improves resolution before the pictures are stored on hard disk for B.S.D. analysis.

An averaged planar size distribution is obtained from the SEM images by computerized measurement of the resin-filled void regions on the monitor display as distinguished by luminance intensity. Conversion from the planar to a spherical size distribution is then carried out by a statistical method of probability.

Results are presented to illustrate the consistency and accuracy of the measurement technique as a whole and finally, observations are made regarding the structure of the laboratory gassy soil which may be relevant to an in situ sea bed gassy soil. A separate section then deals

with several tests performed to investigate the influence of certain effects on B.S.D.

4.2 THE B.S.D. TECHNIQUE

4.2.1 Sample preparation

Samples are taken from gassy soil consolidated to stresses in excess of 25 kPa. They are therefore stiff enough to avoid other than very localised deformation when cut out using a taut steel wire. Specimens of 23 mm diameter and 10 mm depth are cut to fit into moulds of 25 mm diameter and depth.

4.2.1.1 Drying

Green-Kelly (1973) discusses the distortion, synthesis, alteration of clay minerals and the substantial shrinkage due to various methods of drying soil. However, a new process is described by Fitzpatrick (1984) called vapour phase replacement which has not been seen to suffer significantly from any of these problems. This method allows the soil fabric to be preserved intact as the pore fluid is slowly exchanged with acetone vapour. A desiccator is used with increasing concentrations of acetone in water (at percentages of total volume of 1, 2, 4, 8, 14, 20, 30, 40, 50, 60, 70, 80, 90, 100) below a gauze on which stand the wet samples in the 25mm diameter dry moulds. One day is allowed for each concentration. The 100% acetone is changed each day until there is no layering when the liquid is removed from the desiccator and mixed with petroleum spirit. Layering would indicate the presence of water from the soil since acetone dissolves in petroleum spirit, but water does not.

4.2.1.2 Resin impregnation

The choice of a suitable resin was made by two considerations: the atomic number disparity between the resin and that of the soil, and the ability of the resin to permeate the soil under a high vacuum. A polyester resin proved useful in largely providing the required contrast in atomic numbers to give easy distinction between soil particles and resin-filled voids. To resolve the difficulty of penetration it was necessary to reduce the viscosity of the chosen polyester resin using a thinner which would then need to be removed by evaporation to allow curing. Fitzpatrick describes a process by which relatively large single samples of a clay soil can be impregnated with resin to provide thin specimens. The method was adapted for gassy soil and for processing as many as twenty specimens at a time using the apparatus shown in Figure 4.1. Figure 4.1(a) shows a feeder arm fitted with a spherical bowl to hold the resin mixture. It can be rotated through 360° on a vertical axis through a desiccator neck to locate each sample pot in turn using the arrangement shown in Figure 4.1(b). 150 cc of acetone and 150 cc of polyester resin are mixed before adding 3 cc of catalyst. The mixture is let into the soil specimen pots using the feeder arm tap below the mixture reservoir. This operation is conducted under a high vacuum within the desiccator which is applied by connecting a vacuum pump to the feeder arm branch. Each specimen is covered to a depth of 10 mm before the vacuum is removed. Particular attention must be given to gassy silty clay soil specimens in regard to the speed of application and removal of the vacuum. Ruptures of the soil structure in the region of gas pockets have been observed in samples which have been subjected to rapid pressure changes during resin impregnation. The sudden reduction of desiccator pressure causes an immediate, equivalent drop in the pore fluid pressure throughout the specimen and a resulting expansion of any gas within the pockets. Rupture may then occur in the manner described

in section 2.3.2, dealing with the effects of a sudden unloading of soil in the consolidation cell. In order to avoid specimen damage, an arbitrary period of 30 minutes is chosen for the gradual application of the full vacuum to allow pore fluid flow and gas expansion without rupture. Other soil samples which have different values of permeability may require greater, or lesser, periods. The 30 minute period is also used to raise the desiccator pressure back to atmospheric following impregnation. The specimens are then put into a fume cupboard for 3 days after which most of the acetone will have evaporated off. Topping-up of the moulds is carried out using a mixture without acetone. Seven days in an oven at 25°C followed by 3 weeks at 40°C is usually enough to evaporate the remaining acetone and harden the resin. The samples are then cut in half and ground down using silicon carbide paper at gradually decreasing coarseness to grade 1200.

4.2.2 Imaging

An SEM system was developed which obtained an averaged planar size distribution in the format required.

The samples were prepared for the SEM using a type 12E6 high vacuum carbon evaporator system (Edwards High Vacuum Ltd) to provide a conductive carbon coating several Ångstroms thick. Colloidal Silver type 1206 (Polaron Equipment Ltd) is used to provide a conductive strip from the sample surface to the 25 mm diameter brass mounting stub to which the specimen is glued. A typical prepared specimen is shown in figure 4.2 which may provide a video image as shown in figure 4.3.

The video imaging system is described by E.D. Boyes et al (1983) and utilizes a Jeol JSM 35 S.E.M. (Jeol Ltd) interfaced with a Micro Consultants Interlect-200 computer. The advantage of using an S.E.M.

rather than an optical microscope is that it discriminates between distinct phases characterized by significant differences in the major elements since it depends on the sensitivity to mean atomic number. Hence the resin phase can be analysed separately from the background phase of the solid soil matrix (or vice versa). Advantages of using calibrated predominantly back scattered electron images are: good spatial resolution due to a reduced excitation volume, much higher cross sections compared to x-rays and better geometrical detection efficiency of signals. The system provides a conversion of the S.E.M. image to a digital video framestore image memory giving a continuously updated image display or video recording at TV rate. Using the Interlect-200, each of the multiple framestore units has 512 x 512 x 8 bit memory locations and can be stacked (to 16 bits) for greater depth, or width or height (to 2048, for example, 1024 x 1024).

Routines are provided for noise reduction, optimization of the luminance intensity and storage of up to 38 of the selected images to a hard disk type RL02 K-DC data cartridge (Digital). Noise reduction is carried out by spatially resolved time averaging during acquisition of the S.E.M. images to the video in order to enhance the signal to noise ratio. Pixel luminance intensity over the area of the image can be plotted as the histogram in Figure 4.4(a) showing frequency on the vertical axis versus luminance intensity on an intensity scale of 1 to 255. Adjustment of intensity level of the S.E.M. images can be made while observing effects on the continuously updated video image. In this way the bi-modal phasing effect in the histogram can be enhanced in order to secure a sharper cut-off in intensity level between the resin (first peak) and soil matrix (second peak) to provide the means of separating the area to be analysed later, on those images stored to disk. The cut off point, that distinguishes the end of the resin phase in Figure 4.4(a), occurs at around 85 units on the intensity scale. Image storage to disk can be

carried out by first freezing the video image at the desired luminance intensity and signal to noise ratio. Since there is no image corruption due to the recording process, the image which is stored provides the same facilities of luminance discrimination and pixel spacing as when first transferred from the S.E.M. to the video monitor.

It is necessary to calculate the scaling between the object size of the specimen and the video image to obtain feature sizes and then to check this conversion by using a micro grid S.E.M. specimen which is stored to disk using the same process. Exact areas in pixels can then be converted to the diameters in pixels of the equivalent circle areas and hence to the diameters in microns. In the test results to be shown, the specimen object area is approximately 3 mm x 3 mm and this converts to a 500 x 500 pixel planar module. Measuring data is stored in groups or bins, by radius size starting from 0 to 1, 1 to 2, 2 to 3 pixels up to 99 to 100 pixels. The chosen scaling for the test therefore dictates a measurement range of approximately 12 to 1200 microns diameter. It is therefore possible to obtain at least 12 images from each prepared specimen and to cover adequately the range of void spaces of interest that may be from 25 microns diameter to the maximum void size present (less than 1000 microns diameter in these tests). Obviously, scaling may be varied to suit the range of sizes of interest with high magnification limited only by the resolution of the S.E.M. and low magnification, by the smallness of the specimen area or microscope aperture boundaries. Should the number of bin sizes not be sufficient to include the full range desired, then options include expanding the number of bins available, which increases processing time, or measuring the same specimen at two or more scales and integrating the results.

In order to achieve a representative planar size distribution, S.E.M.

images of the prepared specimens are taken over a strict grid pattern (with no spacing between image boundaries.)

4.2.3 The measurement of planar size distribution

Measurements of the areas of the void spaces displayed in the images are carried out using the Interlect-200 computer to combine a number of standard image processing routines in a convenient form. Images are recalled from disk for observation and measurement. Because of the differences between the scan length in the display monitor of the S.E.M. and the square format of the framestore, the image needs to be corrected by scaling appropriately in one direction in order to re-establish the square pixel image points. The vertically elongated enclosures of Figures 4.3 and 4.4 recover their true aspect ratios in this process and are therefore made more circular. Since the luminance value of pixels imaging resin is lower than that of pixels imaging soil a luminance threshold is then set by the operator below which all pixels are subsequently deemed to be inside resin filled space, corresponding to void space in the original soil. The program (which has been developed from that partially implemented by Gill (1983) then automatically counts these pixels, working line-by-line through the picture, assigning each pixel counted either to an already noted void space (from the previous or current line) or defining a new void space as appropriate. During this process any noise of one or two pixels extent is suppressed, rather than counted. At the end of the pass corrections are made for void spaces which touch the edges of the frame being measured. Then they are sorted into size groups both by number of pixels (total area) and by equivalent circle diameter. This last figure, together with the total area measured, is accumulated and averaged over the required number of images. The planar measurement process incorporates the use of a boundary treatment to deal with those resin-filled spaces which touch the edge of

the image and whose overall shape and size is therefore unknown. After the line by line scan of the complete image, those resin areas which contact the image boundary are deleted from the number versus size group record obtained. The number of resin areas in each diameter category (x) is then expressed in terms of an area of measurement within the broken line of Figure 4.4(b). In this way, those areas with a centroid outside the broken line are deleted from the record and those within are included. Therefore, on average, the total area deleted from measurement within the broken line boundary (shaded region I) equals that total area included from outside the boundary (shaded region II) and in this way a fair assessment is made for the number of resin areas per unit of measurement area. The planar measuring system also offers size distribution by area should it be required for use with a different material where perhaps the enclosures to be measured could not be idealized as circles or spheres.

Crystals which share approximately the same atomic number as the resin, and are assumed to be biotite, are present in all the silty clay soils tested in this thesis. An optical microscope examination, which easily discriminates between the black crystals and the opaque resin, is performed on each B.S.D sample to confirm that the crystals are smaller than the resin areas being measured and will not therefore be confused with them.

4.2.4 Conversion from a planar size to a spherical size distribution

Each observed void in the planar size distribution may be only a section of a larger diameter sphere. It is therefore necessary to perform a conversion from the observed planar size distribution to the probable spherical size distribution. This is achieved by computing a probability distribution for each sphere diameter which denotes the probability of

that sphere being observed in a smaller section for each of the size categories below it. For each sphere size the probabilities sum to unity. The distributions are then assembled into a matrix. Mathematical theory used in formulating the distributions and assembling the matrix is essentially similar to Wicksell (1925) whose theory is supported in a design-based proof by Jensen (1984).

Therefore in matrix form the equation to solve becomes:

$$\{PN\} = [M_1] \{VN\}$$

where {PN} and {VN} are vectors of size equal to the number of diameter categories chosen for the measurement.

{PN} contains the numbers of observed circular areas within a standard area module for each size category.

{VN} contains the numbers of spheres within the standard volume module for each size category, and is unknown.

$[M_1]$ is a square matrix of dimension equal to the number of size categories and contains the probability distributions. The matrix equation is then arithmetically converted to planar and volume fractions rather than numbers which alleviates problems in computing solutions using planar size data with very large and small numbers together. This gives:

$$\{PF\} = [M_2] \{VF\}.$$

The analytical solution of the matrix equation to obtain {VF} causes the occurrence of negative values for some volume fraction categories of

size. It is assumed that the nearest realistic solution to the analytical one will be obtained by not allowing elements of {VF} to become negative. Hence a 'best fit' solution is computed using an iterative process to minimise the sum of the modulus of errors caused by imposing the non-negative constraint.

4.2.5 Statistical considerations

Two particular points in the process will be discussed here since they affect the experimental results presented later.

4.2.5.1 Rearranging single bins into grouped bins

Experimental results from the planar measurement of gassy soil specimens indicated a problem in the arrangement of the bin sizes by radius and this problem could well be common to other materials. Since the planar distribution data is arranged in 100 bin diameters set at increments of 1 pixel radius it is not uncommon to find isolated occupied bins amid several empty bins. It is likely that the best fit procedure adopted within the planar to spherical size conversion process will reduce these occupied bins to empty, since they will not fit the calculated probability distribution. Therefore the experimental planar data needs to be conditioned by grouping bins to reduce the problem to a minimum. The particular soil specimens used for the experimental presentation produced planar size data where large numbers of measured voids existed in the small bin sizes and few scattered numbers existed in the large bin sizes. Groups were therefore formed by initially using single bins from 1 pixel radius upwards providing 13 bins, then combining 2 single bins to provide a further 6 grouped bins, then combining 3 single bins to provide a further 4 grouped bins, and so on up to combining 8 single bins. The 100 single bins are therefore rearranged into 34 grouped bins. A system

of input data grouping can be tailored to meet the typical distribution problem posed by the condition of the planar data from any material under examination. However, the effect on the presentation of the final results and the ability to analyse such results must be prime considerations in using any regrouping system. The success of the grouping system used here in improving the 'best fit' for the conversion process is illustrated in the following technique.

In order to compare the accuracy of the 'best fit' planar to spherical size conversion, an analytical reconstruction of the planar size distribution is backcalculated from the spherical size distribution output. A comparison between the planar input data and the reconstructed planar data then measures the success of the re-grouping of bins and the accuracy of the conversion in general since the actual input data can be compared bin to bin with the converted, and backcalculated, input data. A typical comparison between raw planar and reconstructed planar distributions is shown in Table 4.1. Differences are due to points of non-uniformity in distribution of the sizes in the planar data which cause difficulties in fitting the probability distribution that provides the conversion to spherical data. Otherwise the conversion is an exact fit.

4.2.5.2 The number of images

It is clear that the choice of the number of images to represent a specimen is critical in providing the exact range of sphere sizes present. The largest planar diameter observed is the largest spherical diameter obtained in the conversion. Hence the largest sphere size known to be present in the specimen material must be observed at least once at its maximum section to create a spherical size distribution containing the true maximum diameter.

To increase the probability of measuring the actual spherical diameter of the largest sphere present in a 500 pixel module the following method can be used. A lengthy examination of oven-dried samples must be carried out under an optical microscope to find the largest size of sphere present in the specimen material. When this size has been established the probability of it occurring on at least one image at its maximum section can be assessed for a given number of images representing a 500 pixel cube module. If each image represented a planar section of the 500 pixel cube module then a section would be taken on average every S_s pixels in spacing where:

$$S_s = \frac{500}{N_i} \quad \text{where } N_i = \text{number of images.}$$

Hence, on average, a section will occur within the range $\pm(S_s/2)$ pixels from the spherical diameter (D_b) (where D_b is the largest sphere diameter established within the specimen).

From the geometry of Figure 4.5, it can be seen that, on average the observed diameter will vary between (D_b') and (D_b) over the spacing S_s. If there is a significant difference between (D_b') and (D_b) then (N_i) may be increased accordingly. If the maximum diameter observed in the group of specimens is then not close to the largest spherical diameter established it may be because there are on average less than one of these sizes within each 500 pixel cube volume of soils. (Or simply to keep up an average of one size per module some groups may contain that size and others may not). Should this sphere size occur often throughout the material, but less than once per module, its volume fraction, relative to a 500 pixel cube module, may still be significant. A minimum significance level must therefore be decided below which the void fraction of a sphere size will be ignored. This significance level can

be expressed as a minimum volume fraction and the cubic dimension calculated to provide this volume fraction for the occurrence of one sphere only. The figure of 500 pixels can now be replaced by the revised cubic dimension in the above process and (N) calculated to provide on average at least one occurrence as close to the maximum section diameter as required. The figures used in the calculation for the soil sample chosen to demonstrate the B.S.D process are:

significance level = 0.00593
Maximum established diameter = 650 microns (i.e. D = 108 pixels) giving:
D'_b = 101 pixels

Therefore, on average, the worst case measured value of (D'_b) still allocated the largest established sphere to the correct grouped bin.

Since there was always a large number of the smallest circles present in each planar image observed from the specimen material, no approach was necessary for dealing with the minimum spherical diameter.

4.2.6 The structure of gassy soil

Before looking at the example test results it will be useful to consider the structure of gassy soil. Since the foregoing conversion from planar to spherical sizes depends on an idealization of the void spaces as spheres it is necessary to inspect the framework of a gassy soil to decide whether this is acceptable.

Figure 4.6(a) is an S.E.M. image taken from an oven-dried sample which has been prepared by gold coating to provide the conductive surface. It is from a fracture surface of a gassy soil of 80% degree of saturation and represents what is considered to be a gas filled void structure (the

diameter is 6μm) surrounded by a saturated soil matrix. The particular gas filled void structure in Figure 4.6(a) is not typical in size as will be shown later. It is the product of deliberate and extensive search for the smallest possible gas pocket in this type of gassy soil, and it is unlikely that a significant volume of gas is contained in these non-typical sizes. It does however represent a compact view of the typical bubble particle structure for the purpose of illustrating gas pockets. Figure 4.6(b) further illustrates this saturated soil matrix construction around the wall of a larger bubble pocket of approximately 300 μm diameter where interparticle voids are less than 10 μm diameter.

As discussed in Chapter 1, gas content may be modelled in either the large bubble or compressible fluid conditions. Figure 4.6 is an illustration of the former model and, as will be seen later, the test results imply that gas is contained predominantly within relatively large void spaces analagous to this particular model. The larger spheres contained in Figure 4.3 are therefore assumed to be gas pockets and since they are reasonably circular in planar view when the sample is sectioned at varying angles, these pockets are idealized as spheres.

4.2.7 The example test results

The spherical size distribution contains voids which are either water-filled or gas-filled. A method of distinguishing between water and gas filled voids is suggested by the following analysis of tests carried out to illustrate the B.S.D system.

Figure 4.7 presents the results of tests on four separate soils, the details of which are recorded in Table 4.2. The samples are identified by the different periods that their respective zeolite contents were exposed to methane impregnation at a constant pressure of 200 kPa.

Sample 0 was fully saturated. Samples 2, 12 and 17 hours contained the same solids and water content as sample 0 and were prepared at the same consolidation stress (of 500 kPa). The sample provided by an impregnation period of 17 hours contains the most gas while the samples of 2 and 12 hours contain less, as indicated in the 'Gas Void Fraction' columns of Table 4.2. Since data provided from the smallest two bin sizes are perhaps inconsistent due to single pixel noise level on the video images it is prudent to neglect volume fractions within bin 1 and 2 and to align void fractions at bin 2 level for all the four specimens as shown on the figure. A threshold diameter which distinguishes between gas-filled voids above and water-filled voids below is drawn in at bin 14 consistent with the following criterion:

(i) Soil 0 is fully saturated and should therefore contain no gas voids. It has a relatively small range of measured sizes ending at bin 14 (198.4 μm). An optical examination revealed that this size range is made up from only interparticle void spaces and biotite crystals. This range might be expected to be present in the saturated soil matrix of soils 2, 12 and 17 but at reduced fractions (i.e. the saturated matrix of a gassy soil must be smaller in volume than a saturated soil of the same overall volume). This hypothesis fits in well with a comparison between the curves since the profiles 2, 12 and 17 follow slightly below that of 0 over the range of sizes contained in 0.

(ii) The two distinct profiles within the gassy soil curves meet at bin 14. The abrupt change in the average volume fraction per bin could easily be explained by a change in the structure of the void spaces. The only apparent change in structure of the voids is the change from the normal interparticle matrix structure to larger spherical enclosures which are assumed to be

gas pockets. It should be noted that if the grouped bin B.S.D. results in Figure 4.7 are converted to a single bin plot the latter sections of the curves will not be approximately straight but will be curved parabolically. However the two sections of the curves will still provide the abrupt change in profile at 173.6 to 198.4 micron diameter.

(iii) The influence of the methane impregnation period on gas content can be seen in the gassy soils B, C and D over the range of sizes greater than those in bin 14. The distribution is similar, but the range is greater for the soils of higher gas content. This suggests that greater methane impregnation periods lead to increased bubble size ranges only, and not increased gas fractions in all bubble sizes at sizes upwards from bin 14.

(iv) Independent pycnometer measurements on the soil indicate that the gas contents of each specimen are such that if all the gas was contained in only the largest voids then the threshold diameter would be close to that of bin 14 as shown in the 'Pycnometer' column of Table 4.2. The pycnometer gas void fractions are consistently lower than those obtained by B.S.D. Later analysis of the pycnometer method has indicated that this method yields low gas contents for gassy soil specimens unless triaxial samples are used which remain within the thin rubber membrane, to prevent degassing when submerged in water. It is this observed loss of gas which causes the apparent low value of the measured gas fraction.

The above consistency in marking the threshold diameter serves as a further check on the accuracy of the measurement process as a whole. A

further series of tests with four samples varying the methane impregnation pressure for constant periods has yielded similar results to those presented.

This method therefore provides a reliable and acceptably accurate method of measuring general spherical shapes within a material matrix with less time and effort involved than for the more traditional serial sectioning technique.

4.3 THE INFLUENCE OF CERTAIN PARAMETERS ON B.S.D AND GAS FRACTION

Several tests were performed using the B.S.D measuring process to record the effects of variations in soil preparation and consolidation procedure. The results are used to supplement the information provided by Nageswaran (1983) concerning the preparation and characteristics of laboratory gassy soil and to discuss the influence of certain parameters on the B.S.D and gas fraction of both laboratory and in situ gassy soils. Except where stated to the contrary, the gassy soil samples are prepared as described in chapter 1 at a zeolite content of 17% by weight, and are impregnated with methane at a pressure of 200 kPa for 17 hours. A histogram for one of two standard samples appears on each figure (except 4.8(g) and (i)) at the relevant total stress, where 'Standard 1' is for the test groups at 500 kPa and 'Standard 2' is for 100 kPa. Also, the individual samples on each figure are identified by the parameter that is being varied from the standard condition. For example, in the previous case of Figure 4.7, this parameter is the methane impregnation period. The samples in the group are therefore identified as 2, 12 and 17 hours.

4.3.1 The influence of variations in the preparation of gassy soil

Figure 4.8(a) presents the results from two gassy soil samples of varying methane gas pressure, 100 kPa and 200 kPa, and a constant impregnation period of 17 hours together with a fully saturated sample. As for the previous test, of Figure 4.7, samples were consolidated to a total stress of 500 kPa at atmospheric back pressure. The increasing methane pressure causes a corresponding increase in total gas fraction and bubble size range. Although the variation in periods for Figure 4.7 and pressures for Figure 4.8(a) produce the same increase in bubble size, methane pressure variation is shown to have a greater effect on gas fraction than period variation. This indicates that, by controlling methane pressure, it is possible to produce a group of soils of very different gas content but similar bubble size range.

In order to see if the same observations could be made for a relatively low degree of soil consolidation the tests were repeated at a total stress of 100 kPa and at atmospheric back pressure. Figures 4.8(b) and (c) present the results for varying methane periods and pressuresrespectively and use a new saturated soil control sample, also at 100 kPa. It is found that, as before, neither the variation of pressure nor period have much effect on the bubble size range. However, unlike the 500 kPa results, period variation between 12 hours and 17 hours has a greater effect on gas fraction than pressure variation from 35 kPa to 200 kPa.

The effect of using different proportions of the total zeolite content that is saturated with methane is investigated by performing two further tests. Methane-saturated zeolite contents of 15% and 60% are compared to the 100% content of Standard 2. All samples were prepared at the standard 17 hours and 200 kPa methane impregnation period and pressures.

Figure 4.8(d) indicates a gas fraction increase consistent with an increasing quantity of methane in the mixture. However the reducing bubble size range indicates that greater bubble sizes result from smaller quantities of methane. Since this effect is not consistent with the trend in B.S.D produced by reducing methane content, as a result of reduced impregnation periods and pressures, it may be a dispersal effect. The smaller amount of zeolite that is fully methane-saturated, dispersed in pockets further apart, may result in a tendency to produce larger bubbles if they no longer, for example, experience any inter-bubble polarity effects which may attract or repel. It may be the inter-bubble polarity that helps to produce the uniform distribution of gas bubbles always associated with the formation of laboratory gassy soil. It may also be an effect of the zeolite content on the soil properties, such as the Atterberg limits, or the effective friction angle (ϕ'), and could also be due to the separate influences of using either the soil slurry or distilled water, to saturate the methane-saturated zeolite and the dry zeolite, respectively.

4.3.2 The effect of varying confining pressures

The use of different total stresses in the previous tests provides further information concerning the effects of consolidation. A reduction in soil consolidation produces substantial increases in maximum and minimum bubble size and gas fraction, as can be seen by comparing the Standard 1 curve on the 500 kPa figures and Standard 2 on the 100 kPa figures. (Both curves are produced from samples using a 200 kPa methane pressure for a period of 17 hours). It is shown in the work of Thomas (1987) that greater total stresses lead to higher gas pressures. This causes a greater amount of gas to dissolve into the water and drain out of the soil, reducing the soil's gas content.

Low gas fractions may also be caused by the reducing radii of curvatures of the menisci (shown in Figure 1.1(c)) as a result of the solid particles becoming more densely packed during consolidation and the developing gas pockets may be less able to enlarge by deforming the much stronger surrounding soil matrix. The tighter curvatures allow the menisci to contain free gas at greater pressure and therefore in smaller volumes. This latter explanation is supported by the fact that both maximum and minimum bubble sizes are smaller in Standard 1 than in Standard 2 and therefore that all bubbles appear to be proportionately reduced in volume. This result provides corroboration for the statement in Chapter 1 that bubble size is dependent on the in situ soil confining pressures. However it does not indicate whether size is dependent on total stress (σ_1), on consolidation stress (σ_1-u_w), or is influenced by pore water pressure (u_w) only, or not at all.

In order to investigate the effect of a varying hydrostatic head of water on the B.S.D of a gassy soil undergoing consolidation, two further tests were performed at different back pressures 100 kPa and 400 kPa, applied at the burette tube outlet point. Table 4.3 lists the confining pressures adopted for the two samples which are shown in Figure 4.8(e) with Standard 2 and SAT from the previous test. All samples are at a constant value of (σ_1- u_w), and methane impregnation periods and pressures remained the same. An increasing back pressure was found to reduce both the bubble size range and the gas fraction, although the soil structure may be responding to the variation of total stress rather than simply pore water pressure. However, it can be seen that the reduced total gas fraction and maximum bubble size of the sample at a back pressure of 400 kPa can be produced by a soil at the higher total stress of 500 kPa despite the absence of back pressure. This suggests a gas volume and bubble size dependency on total stress rather than the respective proportions of back pressure and consolidation stress.

Local fractures were observed around gas bubbles in the specimens subjected to back pressure. This was assumed to be caused by a too rapid release of pressure at the burette outlet causing the type of localised matrix failure discussed in section 2.3.2 due to the expansion of the gas pockets.

A further test was carried out to investigate varying total stress at constant back pressure. Table 4.4 and Figure 4.8(f) show the confining pressures and B.S.D curves used in the comparison. The increase in total stress from 200 kPa to 300 kPa, both at the same back pressure, indicates no change in bubble size range but a significant reduction in gas fraction. Although Standard 2 is not at the same back pressure it produces an increased gas fraction and bubble size range consistent with a decrease in total stress. These results therefore support the total stress dependency suggested by the earlier analysis of Figure 4.8(e).

All the previous tests reported in this chapter have been performed on soils consolidated in perspex-walled cells where wall/soil friction has not been significant. However, the question of the homogeneity of the soil specimens consolidated in the acoustic cells is considered in the curves of Figure 4.8(g) where friction effects are excessive without the use of heavier grease as discussed in section 2.4.2. This figure produces the results of sub-samples taken from the top (TOP 1 and TOP 2) and from the bottom (BOTTOM 2) of a soil specimen consolidated at 100 kPa to a thickness of 108 mm.

A further sub-sample from the bottom was discarded due to its poor degree of fit in the conversion to spherical sizes as discussed in section 4.2.5.1. The inhomogeneity of the soil specimen is demonstrated by the variation in maximum bubble sizes and gas fractions between the histograms. Top samples differ slightly in gas fraction and bubble size,

probably as a result of the radial variation caused by the wall adhesion. The differences between the average of the top samples and the bottom indicate a fairly substantial reduction in gas content of around 20%, and a similar percentage reduction in maximum bubble size. This supports the evidence of inhomogeneity suggested by the moisture content difference over a soil sample depth of 160 mm reported in the earlier section. The structural effect is probably once again a result of the variation in total stress. On this occasion it varies with sample height as a result of soil/wall adhesion.

4.3.3 The effect of different dewatering techniques

Finally, a comparison is made in Figure 4.8(h) between specimens of the same soil sample which have been de-watered by two different processes. The specimens were both provided from the mid-height of a soil sample consolidated in Acoustic Cell 1, using heavy grease to avoid excessive wall adhesion and inhomogeneity problems. The OVEN and VAP histograms are produced by oven drying at 105 °F, until sample weight loss became negligible, and by the vapour phase replacement technique of section 4.2.1.1, respectively. Approximately 10% reduction in gas fraction and 15% reduction in maximum bubble size is indicated for the shrinkage of OVEN in excess of any volume change suffered by VAP. This result corroborates the work of Fitzpatrick (1984) who suggests that vapour phase replacement for clay soils avoids the excessive shrinkage effects of other drying techniques.

CHAPTER 5 - THE RESEARCH TESTS

5.1 TEST PROCEDURE

5.2 THE BSD RESULTS

5 THE RESEARCH TESTS

5.1 TEST PROCEDURE

Four experiments were conducted, each using the two concurrently operated cells. The soil samples were prepared as described in section 1.4 where the proportions of methane-saturated zeolite used in each experiment are as listed in Table 5.1. Standard impregnation periods and pressures (17 hours, 200 kPa) were adopted throughout. Samples E53-1 to E53-2 were produced by using very low methane proportions in order to provide detailed acoustic results over the very low gas content soils for which the theory of section 1.3.1.3.1 predicts a dramatic fall in sound speed.

Each of the soil samples were consolidated at a vertical stress of 25 kPa, with back pressures at atmospheric level, using the proceedure outlined in section 2.1. Acoustic tests were carried out and followed by a BSD analysis, as outlined in sections 2.1 and 4.2. Gas fractions (n_g), from the results of the BSD analysis, are recorded in Table 5.1. These figures are used to backcalculate values for the total void fraction (n) from:

$$n = \frac{e_m + n_g}{1 + e_m} \qquad 5.1$$

where (e_m) is the matrix voids ratio (e_m was supplied by the pycnometer measurement of a saturated soil at the same confining pressure and found to be 1.66). Bulk density (ρ) was calculated from equation A2 (Appendix A) where published gas density (ρ_g) = 0.662 kg/m^3, measured mineral density (ρ_m) = 2689.7 kg/m^3 and measured water density (ρ_w) = 1020 kg/m^3. Finally degree of saturation (S_d) and void ratio (e) were calculated using the expressions:

$$S_d = \frac{(n - n_g)\ 100}{n} \qquad 5.2$$

$$e = \frac{n}{1 - n}$$

5.2 THE BSD RESULTS

Figures 5.1 and 5.2(a) to (h) present the BSD histograms for the eight soil samples described in Table 5.1. Two types of histogram are shown for each sample. The first type in Figure 5.1 presents cumulative gas fraction versus grouped bin size using the previously described grouping arrangement of section 4.2, where the imaging scale is amended from 6.2 to 9.2 μm/pixel. This form of display provides a method of comparing the total gas contents between samples over regions of sizes. Since the grouping causes a weighting effect that confuses the visual appreciation of the distribution of gas, the second type of histogram in Figure 5.2 presents gas fraction versus single bin size. It also uses non-cumulative gas fraction which further enhances the appreciation, since areas under the histogram now reflect actual, rather than weighted, proportional distribution. The histograms of Figure 5.2 are produced by sharing the group gas fraction equally over the range of single bin sizes (each of 18 to 19 microns) covered by that group. This provides the estimated average contents, rather than the measured contents of each individual bin. The range of sizes comprising interparticle voids and biotite crystals have been deleted from the figure using the criterion described in section 4.2.7. For the four samples of lowest gas content, where the histograms could not so easily be separated into two sections of different gradient, those voids formed by gas were separated out by subtracting the histogram of the corresponding saturated soil.

Examination of the plots in Figure 5.1, in conjunction with Table 5.1, illustrates the pattern of an increasing gas fraction (0.00357 to 0.198) as a result of an increase in the proportion of methane-saturated zeolite (2.5 to 100 %). A similar pattern is illustrated in Figure 4.8(d) of Chapter 4 with sample proportions from 15 to 100%. However, the levels of both gas fraction and bubble size for the 15% proportion are much higher than E53-1 and E53-2, at 17%. This may be due to the additional loss of gas in the latter samples during consolidation, because of the weaker matrix that may allow some gas to leave by fracture.

Possibly as a result of the additional loss of gas in the soil, samples E53-1 and E53-2 are only marginally more gassy than E51-1 and E51-2 that may also have experienced a proportional reduction in gas fraction. Otherwise it may be simply the effect of a rather arbitrary relationship between methane saturated zeolite and soil gas fraction. The trend of an increasing maximum bubble size as a result of an increasing methane/zeolite proportion, however, is contrary to the behaviour shown in Figure 4.8(d) where samples are at a higher consolidation stress. The reaction that stimulated larger maximum sizes to be produced for more dispersed amounts of zeolite, as reported in section 4.3, therefore appears to be present in well consolidated soil at 100 kPa but is not evident in soil at 25 kPa. Also, it is of interest to note from Figure 5.1 that the minimum bubble size ranges from 130 to 160 μm for the low gas content samples (E51 and E53) and from 220 to 260 μm for three out of the four high content samples (E50 and E52). Furthermore, a constant minimum size can be found for the samples of Figure 4.8(d) and, since gas fractions are all high, it is assumed that the minimum corresponds to a 'high gas content minimum'. Re-examination of this series of tests (Figure 4.8, (a) to (f)) reveals that there is a single high gas content minimum of 198 μm diameter for all the samples consolidated to 500 kPa, and a value of around 320 μm for all the soils in five of the seven

figures of the soils consolidated to 100 kPa, regardless of impregnation periods and pressures and also cell back pressures. It is also apparent from Table 5.1, that the gas fractions of the Cell 1 samples are generally greater than those of Cell 2, despite originating from the same soil slurry mixture and consolidation procedure (E52 being the single exception). This is once again assumed to be due to the difference in consolidation periods, caused by using unequal sample depths. It is not entirely counteracted by the reduction in time due to the additional bottom face drainage of Cell 2.

A comparison between the results for Cell 1 and 2 over the four experiments provides further information about the behaviour of gas in soil. Cell 1 generally produces bubbles of the same minimum bubble size as Cell 2, but generally of a larger size (E52 being the exception again). Since there is more free gas available there must be a statistically greater opportunity for larger bubbles to develop. However, both the E50 and E53 experiments provide BSDs which indicate large bubble contents not in proportion to the smaller increases in gas fraction.

It can be seen from a comparison of histogram gradients in Figure 5.1 that regional distributions of gas in the Cell 1 and 2 samples are always fairly similar. An examination of the histograms of Figure 5.2 shows that the similarity is brought about by a general feature common to all samples. Each histogram exhibits an accumulation of gas at the lower end of the bubble size range and a more scattered presence at the upper end.

CHAPTER 6 - ACOUSTIC RESULTS - SOUND SPEED (At resonance)

6.1 FOURIER TRANSFORMS

6.2 EXPERIMENT RESULTS

6.2.1 The high gas content samples of experiment E50

6.2.2 The moderately high gas content samples of experiment E52

6.2.3 The low gas content samples of experiment E53

6.2.4 The lowest gas content samples of experiment E51

6.3 THEORETICAL RESULTS

6.4 THE INFLUENCE OF PARAMETER VALUES ON SOUND SPEED (At resonance)

6.4.1 Variation of the ambient hydrostatic pressure

6.4.2 Variation of the reciprocal specific dissipation function

6.4.3 Variation of the matrix elastic moduli

6.5 EXPERIMENT/LITERATURE SOUND SPEED COMPARISON (At resonance)

6 ACOUSTIC RESULTS - SOUND SPEED (At resonance)

Chapters 6, 7 and 8 will deal with the presentation and analysis of results for sound speed (at resonance), attenuation and sound speed (below resonance), respectively. Also Chapter 6 includes the Fourier transform results while Chapter 8 deals with reflection loss (below resonance only) and shear wave speeds in order to extend the available range of data over a more complete field of research. By using Chapter 6 to estimate the frequency at which resonance effects begin to be apparent in each soil sample, it is possible to extract those measured sound speeds that are relevant to Chapter 8 for the 'below resonance' case. Each of the three chapters will provide experiment results followed by an attempt to correlate these with the corresponding BSD figures in section 5.2. Theoretical results will then be presented and compared with the experiment results and finally, experiment data will be compared with measurements in the literature.

Any summaries and conclusions will be dealt with where they are appropriate.

6.1 FOURIER TRANSFORMS

Fourier transforms are dealt with separately since they provide the basis from which both the following sound speed and attenuation results are derived using the FT Method. They are also a useful visual indicator of the acoustic response of each individual gassy soil sample, when used in conjunction with the non-dispersive result of the calibration medium, to illustrate deviation from the transmitted signal.

Figures 6.1 (a) to (g) show the Fourier transforms (see section 3.3.3.1), of the received spike waveforms in each of the tests (except for E50-2).

Type (i) are for the soil and type (ii) for the calibration media. They are plotted in terms of the vector resultant of the real and imaginary components of the transform, versus frequency. The discrete frequency components are at intervals of 2.441 kHz using the 0.2 μs/sample waveform recording speed.

The frequency range over which sound speed and attenuation results are calculated for the FT method, is controlled by the range of the signal received through the soil, as indicated by the extent of the soil transform for each sample. Soil amplitudes and frequency ranges are greatly reduced in comparison with those of the calibration media for the more gassy soils, Figures 6.1 (a) and (b). Each sample acts as a filter which attenuates certain frequencies more than others due to the sources of signal loss described in section 1.3.1.3. It will be shown in Chapter 7 that these reductions are caused by attenuation levels several orders of magnitude higher than for a saturated soil. Therefore, this response is due to the dominant effects of bubble resonance rather than those mechanisms of non-resonant absorbtion and scatter loss also present in a saturated soil, which are considered to vary approximately linearly with frequency. A comparison of each pair of transforms (i) and (ii) indicates the severity of the frequency range restriction to signal penetration in soil due to the presence of increasing amounts of gas in the group of soils tested. Those frequencies beyond the upper limits of the soil transforms have been reduced in amplitude below noise level. This illustrates the nature of the difficulty discussed earlier in section 3.1 concerning the measurement of sound speed in gassy soils at other than very confined frequency ranges, since higher frequencies will not penetrate even the shortest of path lengths.

Apart from the general reduction in strength of all low frequency signals and the marked effect on high frequencies it can be shown from the high

gas content samples of Figure 6.1 (a), (b) and (c) that, on a smaller scale, certain frequencies are passed through the soil while those close-by are more attenuated. This causes the small scale peaks and troughs of Figure 6.1 (a,i) for a soil of gas fraction 0.198, and the single peaks at 45 kHz and 23 kHz in Figure 6.1 (b,i) and Figure 6.1 (c,i) for gas fractions 0.082 and 0.115, respectively . It can be shown from their corresponding calibration transforms, when replotted on the same frequency scale, that the signal transmitted into the soil is comparatively uniform across the frequency range of the soil transform. This therefore indicates that the peaks and troughs in the type (i) transforms are caused only by the attenuation of the soil, which, because of the strong frequency dependence, is due to the influence of bubble sizes on absorption and scatter loss at resonance. The variation is therefore influenced by bubble sizes in the same manner as shown in the scatter loss tests of Silberman (1957) using bubbles in water. It should therefore be possible to correlate this strong frequency dependent response to the resonance of certain bubble size groups that contain significant gas fractions. A correlation of sound speed and attenuation results with corresponding BSD histograms will therefore be examined in the following chapters.

The soil transforms of Figure 6.1 (d,i), 6.1 (e,i) and 6.1 (g,i) for low gas fractions 0.00511, 0.00407 and 0.00357 respectively, all demonstrate similar variation to that of the corresponding calibration medium shown in the type (ii) transforms. Little effect due to resonance is indicated here. This is probably because there is insufficient gas content in any bubble size for resonance to dominate the overall response which is therefore composed of matrix absorption loss and the scatter from bubble interfaces that are enhanced at resonance. However, the result of Figures 6.1 (f), (i) and (ii), indicate total signal loss in the soil at frequencies above 550 kHz, and substantial reductions between 300 and 550

kHz. This additional rate of loss was initially considered to be the result of the commencement of scatter effect on an increasing frequency. It can be seen from the work of Silberman (1957) with water that scatter loss will occur at bubble interfaces for signals with a half wavelength less than the bubble diameter. However this may not be the case here, since the 300 kHz frequency has a half wavelength of 2.17 mm at a sound speed of 1300 m/s (taken from the TTC result of section 6.2). This would suggest normal scatter effects on bubbles of 2 mm diameter and larger, but none are shown in the BSD histogram. Therefore, resonance effects are finally considered to be the cause of this loss, and Chapter 7 investigates the correlation between Anderson's computed resonance frequency and the attenuation results. This may indicate some connection between bubble size and loss in Figure 6.1 (f). It seems unlikely, however, since broadly similar size distributions in the above three low gas content samples do not indicate the dramatic variation associated, in theory, with resonance effects.

6.2 EXPERIMENT RESULTS

The sound speed results for each of the four experiments are illustrated in Figure 6.2 (a) to (d). Data for both Cells 1 and 2 are included on each plot since the soil samples are provided from the same mixture and, as shown in section 5.2, they are relatively similar in BSD. All eight samples are represented by the results from the leading edge, TTC and FT methods of measurement as described in 3.3.1 to 3.3.3 (with the exception of the FT results for E50-2 since no spike signal could be received through the soil). Also marked is the TTC/FT coincident point where the TTC sound speed result is used to generate values from the FT method. As it was necessary, for comparison, to present several curves on each figure, certain curves will not be referred to until much later in the chapter.

6.2.1 The high gas content samples of experiment E50

The Leading Edge method results in Figure 6.2 (a) are restricted in range to those signals which provide a received frequency equal to that transmitted. Due to the difficulty in defining the true leading edge position, for the reasons discussed in section 3.3.1, transit time could only be estimated within $\pm 2\mu s$ and $\pm 7.5\mu s$ for E50-1 and E50-2 respectively and appeared to be constant within these error bars over the measured frequency range. Both curves are therefore shown at the constant average sound speed values of 448 ± 23 m/s and 322 ± 13 m/s. This confirms the belief that a single frequency component, present in all the signals transmitted, is consistently the first arrival at the receiver. In a comparison between the sound speeds of these two single frequency results, it is perhaps unusual for the lesser gas content of sample E50-2 to produce a lower sound speed than E50-1. Since this result may also be indicated by the TTC method data, the response appears to be valid and may be due to the differing influences of bubble size between the two samples.

The data points from the TTC method shown in Figure 6.2(a) to (d) provide relatively smooth curves which, because of the individual treatment of each data point, indicates a satisfactory level of consistency for the method. Since the two frequency ranges shown in Figure 6.2(a) are both restricted and do not overlap, it is not possible to infer comparisons between sample responses solely from the TTC data. However, the curve from the single FT method contribution for E50-1 indicates that the two samples may have a consistent sound speed profile. From the coincident point at 44 kHz, the curve traces the E50-1 TTC profile at decreasing frequency for a short section before eventually meeting the E50-2 curve.

The leading edge curve may now be used to examine the consistency of results from the three methods and also between the two soils. Since it is accurate at only the first arrival component frequency, then there is only one point on the curve that is correct. As very high frequencies are attenuated out by soils of high gas content, this single frequency may be within, or close to, the frequency range of the TTC curve. As the FT curve is consistent with the TTC curves for both samples E50-1 and E50-2 and coincides with the leading edge curve at 25 kHz, it is probable that both TTC curves also coincide at this point. This suggests that the first arrival frequency at which sound speed is correct for the leading edge curve of E50-2 is 25 kHz and that the results from each of the three methods are consistent for both samples in indicating an increase in sound speed of around 200 m/s between 20 and 40 kHz. Applying a similar approach to the E50-1 curves indicates that the first arrival frequency, at which the leading edge curve is correct, is 60 kHz, since it is here that the TTC curve coincides. It is of interest to note that the FT curve also indicates that the leading edge curve of sample E50-1 may have a first arrival frequency at which the sound speed is correct, since it also crosses the leading edge curve at 36 kHz.

The sound speed response may now be examined in relation to the BSDs of the two samples. Firstly it is useful to refer to the earlier Figure 1.4(a). This indicates that in theory there is an abrupt increase in sound speed at the resonance frequency (f_o) of the single-sized bubbles of radius (r) in soft soils. This point will be referred to as the 'transition point' between the 'below resonance' and 'at resonance' conditions. Referring back to Figure 6.2(a), it can be seen that a possible 'transition point' for both samples E50-1 and E50-2 occurs around 20 kHz (giving f_o = 20 kHz). Since the two samples contain a range of bubble sizes, it is not clear which bubble diameter may be

dominating resonance effects in the soil at the 'transition point' frequency. Two possibilities are investigated here.

The first assumes that the effects are caused by the largest bubbles in the distribution, since the first bubbles to resonate as signal frequency increases from the 'below resonance' position, are the largest as their diameters are closer in size to the wavelengths than those of the smaller bubbles. From Figures 5.1(a) and (b), the average diameter of the largest bubble is 1746 μm for both samples. The second assumes that resonance at the 'transition point' is dominated by the accumulation of gas content at the small bubble end of each histogram, as discussed in section 5.2, rather than by the more dispersed larger bubbles. Here the bubble radius will be referred to as the 'peak gas content bubble size' which, from Figures 5.2(a) and (b), occur at 312 and 422 μm diameter for samples E50-1 and E50-2. respectively.

It is suggested by Anderson (1974) that the product of the resonance frequency and the bubble radius ($f_o r$) is a constant for a given soil. Therefore, assuming that at the 'transition point' (f_o) is 20 kHz for both samples, then the large bubble option provides an ($f_o r$) value of 1746 Hz.cm and the 'peak gas content bubble size' provides 312 and 422 Hz.cm for samples E50-1 and E50-2, respectively. It may be of interest to note that these ($f_o r$) results may be adopted to provide values for the resonance frequencies of all the bubble sizes in each sample, using either option.

6.2.2 The moderately high gas content samples of experiment E52

The leading edge method results in Figure 6.2(b) are shown as constant average sound speeds of 475 ± 50 m/s and 403 ± 22 m/s for E52-1 and E52-2 respectively. Comparative values are consistent with the expected speed

versus gas fraction relationship unlike the previous experiment, E50, since the larger gas content of E52-2 has a lower sound speed (by 72 m/s). This is also confirmed by the TTC method results which indicate a difference of around 100 m/s, and also the FT method results which show very similar sound speed profiles for the two samples, between 30 and 100 kHz at a separation of around 100 to 150 m/s. The first arrival frequency component for the E52-1 Leading Edge method results should be between 42 and 54 kHz, since all three methods produce the same sound speed, whereas for E52-2 it appears to be much lower in frequency, at around 15 kHz.

Both samples indicate low speeds consistent with very gassy soil samples and, as expected, provide slightly higher speeds than the greater gas content samples of experiment E50 for frequencies below resonance. However, for frequencies 'at resonance', the speeds of both samples reduce to below those of experiment E50. Therefore resonance effects in the samples of experiment E50 are causing speed to increase at a greater rate than those of E52. This is a result of bubble size rather than gas fraction. The decreasing sound speed with increasing frequency shown by both the E50 samples may be consistent with theory if it were only a minor reduction associated with the trough, at the foot of the steep incline produced at resonance, as shown in Figure 1.4 (a).

Since the positions of the 'transition points' for E52-1 and E52-2 are expected to be outside the range of the experiment results, no data can be provided for the values of $(f_o r)$.

6.2.3 The low gas content samples of experiment E53

Since the low gas content samples were chosen specifically to define the dramatic drop in sound speed due to only a small amount of gas, it

is expected that tests E51 and E53 will provide speeds from the saturated soil level to that of a soil with significant gas fraction. In Figure 6.2 (c) the Leading Edge method results are close to the sound speed of a saturated soil (around 1500 m/s) for both samples and are therefore consistent with soils much less gassy than the previous two experiments. They are presented as constant average sound speeds of 1506 ± 13 m/s and 1495 ± 8 m/s for samples E53-1 and E53-2 respectively. Since the sound speed for gassy soils above resonance frequency represents the speed of waves propagating through only the saturated soil matrix, then it must be assumed that the first arrival component frequency for both samples is above resonance. As the curves only coincide with the TTC method results at above 200 kHz then the first arrival cannot be below this frequency. It is assumed that the matrix of the gassy soil has the same structural parameters of shear modulus, bulk density and bulk modulus as a saturated soil. Therefore, taking an average of the two Leading Edge method results, the sound speed of a fully saturated soil is taken to be 1501±16 m/s.

The continuity of the TTC method results for both samples is broken by a middle region of frequency over which no data was obtained and therefore the two sections have been joined using a straight line. The apparently erratic variation of sound speed for sample E53-1 above 200 kHz is different to the smoothly varying curves of the previous experiments, E50 and E52, and also E53-2 here. Although variation is within the ±70.34 m/s measurement error bars, suggested by Table 3.2, it does not appear to be random, since each peak and trough is defined by several data points in an apparently co-ordinated arrangement. This feature appears to be relevant to the acoustic response of a saturated soil, since the region above 200 kHz varies about a constant sound speed fairly close to 1500 m/s. Similar sound speed fluctation at the saturated soil level will be shown in the results of the final experiment.

Data from the FT method for E53-1 does not agree well with the TTC results over the central frequency region but is close at each end. However, an approximate transition point is indicated at around 20 kHz which produces an ($f_o r$) value of 458 Hz.cm for the 458 μm diameter large bubbles shown in Figure 5.1(e). No accumulation of gas appeares at the small bubble end of the distribution in Figure 5.2(e), and therefore no ($f_o r$) value is calculated from a 'peak gas content bubble size'. However, it is worth noting that the ($f_o r$) value of 458 Hz.cm produced from the largest bubble size, is of the same order as those values produced from the 'peak gas content bubble sizes' in earlier samples (E50-1 and E50-2). Further examination of the BSD in Figure 5.2(e) reveals that there may be an accumulation of gas at the large bubble end of the histogram, at around 425 μm. If so, the corresponding value of ($f_o r$) of 425 Hz.cm for E53-1 may be interpreted as being from a 'peak gas content bubble size'.

TTC results for E53-2 indicate a sound speed level above that for E53-1 projected over the same frequency. This is consistent with their relative gas fractions. The profile of the FT method curve is possibly not consistent with the theory of the minor sound speed trough at the transition point, since the reduction between 20 and 90 kHz, of around 500 m/s, is probably too great. However, the sound speed does show signs of increasing after the fall at frequencies above 100 kHz, although no prediction of the transition point may be made.

6.2.4 The lowest gas content samples of experiment E51

The final Leading Edge method results of Figure 6.2 (d) are constant at an average of 1489 ± 7.5 m/s and 1503 ± 2.3 m/s, and the general comments made for those of experiment E53, apply here also.

The TTC and FT Method results for sample E51-1 closely concur over most of the range of results. They indicate that sound speed at the low frequency end may fall between the levels of the two samples of experiment E53 which would be consistent with the gas fractions of the three soils. At 400 kHz, the sound speed has almost reached the predicted 'above resonance' saturated soil response. The projected frequency for this would be at around 800 kHz, well after that of E53-1 which has a greater gas content and a larger maximum bubble size. Below 80 kHz the TTC and FT method curves diverge, providing an upper and lower bound sound speed at 50 kHz, of 1090 and 680 m/s respectively. Taking a mean between the two over 50 to 80 kHz would provide a 'transition point' at 80 kHz (the foot of a steep incline in the curve). The stimulation of a resonance response here, by large bubbles will therefore produce an ($f_o r$) product of 1540 Hz.cm, for a diameter of 385 μm. Alternatively, the peak gas content produces 548 Hz.cm for a diameter of 137 μm.

Sample E51-2 displays a similar fluctuation to the above resonance, saturated soil response of E53-1. Both the TTC and FT method curves fluctuate about a 1650 m/s average, some 150 m/s above that indicated by the Leading Edge method. Since the sample contains some gas, this sound speed response is expected to be the result of resonance. Therefore, sound speed may not reach the constant saturated soil value for above resonance, until beyond the 800 kHz upper limit of the FT data range. There is some evidence, between 180 and 800 kHz, of a trend towards this level which may be predicted to occur at around 1.5 MHz. The elevation of sound speed above 1500 m/s, for frequencies below 1.5 MHz, may be explained by the post-resonance frequency peak shown in Figure 1.4 (a). Some evidence of similar elevations above the speed in saturated soil for samples E53-1 and E53-2 is shown in Figure 6.2 (c), whereas the curves of the high gas content samples of tests E50 and E52, and also sample E51-1, do not appear to extend to the 'above resonance' frequencies.

6.3 THEORETICAL RESULTS

Equation 1.2 is used to provide equivalent theoretical data over the same frequency range as the experiment results. The parameter values used are listed, with their sources, in Table 1, Appendix B and are relevant to the eight soil samples of the research tests. It should be noted here that the high gas content samples of experiments E50 and E52 exceed the gas fraction limit suggested by Spitzer (1943) for applying the theory from which equation 1.2 has been produced (as discussed in section 1.3.1.2). Since the value of dynamic (G) was not measured, two predictions were made from separate sources in the literature that should provide reasonable upper and lower bound levels of sound speed.

The first estimate of 130 MN/m^2 is taken from the dynamic (G) measurements by Smith (1973) and Hamilton (1971) on saturated sediments of varying classification. The corresponding value of (G') is estimated as shown in Table 1, Appendix B. Equation 1.2 then makes use of Gassman's dynamic (K) as described in section 1.3.1.2 for the first sound speed bound. The second estimate of (G) follows from Jardine, Symes and Burland (1984) and is used in conjunction with an estimate of the corresponding value of (K), for this value of (G), from Wheeler (1986) to provide the second sound speed bound. Jardine et al found from triaxial cell tests for small strains of 0.01%, that:

$$500\ Cu_{sat} < G < 1000\ Cu_{sat} \qquad 6.1$$

where (Cu_{sat})is the undrained shear strength of a saturated soil. Using a value of 75 kN/m^2,for (Cu_{sat}),an approximate value of (G) from above is 50 MN/m^2. Although the tests concern static stress/strain behaviour, the levels of strain are perhaps more consistent with the dynamic pressure wave propagation of sound signals of strain 0.01 to 0.001% and should

therefore provide a reasonable lower bound value of (G) for the required dynamic behaviour.

Figures 6.3 (a) to (h) provide the theoretical sound speed versus frequency curves where (i) and (ii) use the upper and lower bound values of (G) and (K) respectively. Curve (i) on each figure produces a more acceptable peak value of sound speed, comparable with that of Anderson's (1974) harbour mud shown in figure 1.4(a), whereas curve (ii), for the high gas content experiments of E50 and E52, show unrealistic peak values. It will be shown in section 6.4 that it is the reciprocal specific dissipation function (Q), in equations A9 and A10 (Appendix A), that is causing the high peak values in both curves, since a reduction in this term causes damping to increase and provides more acceptable revised peak levels. By allowing the values of (Q) to remain unaltered, the levels of the elastic moduli,(G) and (K), may be adjusted to provide a better correlation with the experiment results before finally applying the best combination of values of (G), (K) and (Q). However, in order to make this initial comparison between theoretical data and the experiment results, no adjustment of (Q) has been made to obtain the results in Figures 6.3 (a) to (h), since at this stage it may have adversely affected the objectivity of the comparison.

The theoretical results of curve (i), for each sample, have been plotted on the corresponding graphs of Figures 6.2 (a) to (d) for the experiment results, since they utilize the slightly more direct method for predicting (G) and (K). It is confirmed by the theoretical curves, that the frequency range of experiment results generally embraces the constant sound speed 'below resonance' section, and the initial part of the 'at resonance' section. However, the transition points between periods, produced by the theoretical results, are generally at frequencies greater than those indicated from the experiment results. This means that the

soil is actually responding to resonance at lower frequencies than current theory predicts.

Table 6.1 lists the theoretical frequencies of resonance for each of the bubble sizes of the 8 soil samples calculated using equation A8,Appendix A. The diameters are those of E50-1, although the remaining samples have only slightly differing diameters because of minor variation in image sizes during the BSD process. It therefore follows that the sample resonance frequencies at each bubble size are also not precisely equal, unlike the ($f_o r$) product of 9085 Hz.cm which remains constant. In an effort to demonstrate the effect of bubble size on the transition point position, the BSD of each sample has been plotted on Figures 6.2 (c) and (d) using proportional gas fraction at the corresponding resonance frequency of the bubble diameter. It can be seen from Table 6.1 that the largest bubbles of the samples shown in Figures 6.2 (a) and (b) have resonance frequencies just outside the range of the plots, and therefore a note is made to this effect.

Generally the apparent locations of the 'transition points' in the theoretical sound speed curves are reasonably close to the theoretical resonance frequencies of the largest bubbles. This confirms that, in theory, the transition points may approximately indicate the size of the largest bubbles present in the soil. However, the experiment results of section 6.2, which are summarized in Table 6.2, indicate that the large bubble sizes do not provide a reasonably constant value for ($f_o r$), whereas the 'peak gas content bubble sizes' do. Since only three values are given here, further evidence is required to confirm that it is the resonances of these bubbles that are controlling the positions of the 'transition points'. Such evidence is provided by including in Table 6.2 the ($f_o r$) value of 425 Hz.cm for E53-1, referred to in section 6.2.3. This increases the number of sample contributions of the same order to

four from 'peak gas content bubble sizes'. The average value of ($f_o r$), (taken from values in the left hand section of Table 6.2) is therefore 427 Hz.cm for these soils at a consolidation stress of 25 kPa. Also, further evidence will be provided in section 7.1, where the attenuation results indicate that it is the 'peak gas content bubble size' that causes the onset of resonance effects as frequency increases.

If a database of ($f_o r$) values is generated for a range of consolidation stresses it may be possible to predict the 'peak gas content bubble size' of a gassy silty clay soil'. However, it would be necessary for further tests at other consolidation stresses to establish whether this product remains constant over a similar range of gas contents.

Although the theoretical ($f_o r$) products and transition point positions do not agree well with the experiment results, sound speed levels both below and at resonance show the same trend in much reduced speeds, that are dependent on the soils gas fraction. Both the high gas content experiments, E50 and E52, indicate very low speeds for below resonance frequencies while the low gas content samples of E53 and E51 are generally less comparable at other than above resonance frequencies.

6.4 THE INFLUENCE OF PARAMETER VALUES ON SOUND SPEED - (At resonance)

The effects of varying the values of ambient hydrostatic pressure, reciprocal specific dissipation function (Q) and elastic moduli (G) and (K) will be investigated using equation 1.2 for sound speed. The objective is to use the calculated level of parameter dependence for the theoretical sound speed response, to predict the effect on the actual response. The degree by which the theoretical dependence relates to the actual case should be acceptable, since the basic profile predicted by theory is essentially the same as found by experiment; differences in

sound speed level and frequency should not be crucial, since only relative variability is being studied here. Also, in this section, values of these parameters will be suggested that provide a better correlation between the theoretical and experiment curves in Figures 6.2(a) to (d)

6.4.1 Variation of the ambient hydrostatic pressure P_o)

Figure 6.4 presents the sound speed versus frequency response of sample E50-1, using equation 1.3 for values for (P_o) of 1 and 100 atmospheres. As earlier in section 6.2 , the curve which is denoted by (i) is provided using the values of (G) and (K) from Hamilton (1971) and Gassman (1951) while (ii) denotes the curves provided using (G) and (K) from Jardine et al (1984) and Wheeler (1986). The values of the gassy soil parameters (G), (K), (n), (r_1), (ρ_g), (ρ_w) (c_g) and (S_p) will all change as a result of increasing the back pressure on sample E50-1 and causing a reduction in volume of the free gas content. Since the sound speed response is dominated by the volume of gas and the size of bubbles, it will be substantially affected by the reducing volume as back pressure, and therefore total stress, increases. As the effect of gas fraction and bubble size is discussed elsewhere in this section an attempt has been made to isolate the effects of increases only in pressure, caused by the pressure head. Therefore (n) and (r_1) are left constant in equation 1.2, while (P_o) is varied. Also (G) (K) and (ρ_w) are assumed to remain constant since (G) and (K) here are saturated soil moduli and the effects of changes in (ρ_g), (c_g) and (S_p) due to increases in (P_o), are incorporated in the expression for (X) in equation A6. This study therefore compares the sound speeds of separate soils of equal gas fraction, BSD and porosity, that may exist in different depths of water. It should not be confused with a comparison of the sound speed response of a single soil sample progressively back-pressured. In all other

respects, the values and techniques used to calculate sound speed remain as described in section 6.3.

In case (i), peak sound speed reduces by only 1% between a (P_o) of 1 and 100 atmospheres whereas the softer soils depicted by case (ii) indicate a 17% increase over the same variation in (P_o). At frequencies below and above resonance, no change in sound speed occurs for a 0 to 100 atmosphere change in (P_o) for case (i), although for case (ii) variation is as much as 8% for below and almost zero for above. It is therefore apparent that gassy sediments with a matrix described by the moduli of case (i) may exhibit the same sound speed response irrespective of their depth below the water surface (up to at least 1000 m), and sediments of case (ii) may show only a small increase. This is not however surprising, since both the theory used in deriving equation 1.2, and the values of (G) and (K) of both cases, are essentially the large bubble model of a two-phase material consisting of gas pockets in a saturated soil matrix. Effective stress for a saturated soil remains unchanged with the introduction of a standing water head, and therefore (G), (K) and (ρ) for the matrix also remain largely unchanged. It is the second order effect of the increase in (G) (K) and (ρ) for the gas phase, that brings about the small level of variation in the combined elastic response. This is not the case for the compressible fluid model, where the combined elastic response is dominated by the fluid phase that is most affected by the pressure head. For this model there is a significant sound speed dependence of (P_o) as will be shown in Chapter 8 on the 'below resonance' theoretical results for a compressible fluid.

For the low gas content sample of E51-2, no significant sound speed differences were found for either case over the same change in (P_o).

6.4.2 Variation of the reciprocal specific dissipation function (Q)

This parameter is the inverse of the damping constant (d), as defined in Appendix A and discussed in section 1.3.1.3. Figure 6.5 presents the sound speed versus frequency response of sample E50-1 from equation 1.2 using constant values for (Q) of 1 and 4. This is compared with results using the calculated value of (Q) from the equation of Appendix A. The (Q) value of approximately 1 is suggested by Anderson for stiffer ocean sediments although he maintains that, for soft harbour muds, a slightly higher figure may be more appropriate. (Q=4) was found to produce a reasonable mid-point result between Q=1 and the calculated value. Finally, the upper limit of (Q) is provided by the calculated value used in equations A9 and A10 (Appendix A) which varies with bubble size and signal frequency to provide the sound speed curves shown in Figure 6.3(a). The previous case(i) and (ii) values of (G) and (K) are again used to represent the theoretical bounds of sound speed.

(Q=4) can be seen to produce a similar peak result to the harbour mud of Figure 1.4(a). Comparing the results from (Q=4) and the calculated value of (Q) for case (i), shows that speeds below resonance are increased by 20% and, above resonance, are equal. The (Q=4) value therefore significantly improves the correlation between the theoretical and experiment sound speeds discussed in section 6.3. There is also a small improvement in the correlation of transition point position, since the 'transition point' and, to a lesser extent, the peak point occur at lower frequencies in comparison with the curve from the calculated value of (Q).

Reducing (Q) still further, to the value of 1 has an adverse effect on the correlation, since, although below resonance sound speed remains unchanged from the (Q=4) result, above resonance levels are reduced by

23% below the accepted level for saturated soil. Also no peak occurs, and therefore the 'at and above resonance' response resembles the predicted profile of the stiffer ocean sediment shown in Figure 1.4(a).

Therefore the value of (Q=4) has been found to allow the most successful correlation between theory and the experiment results for the given conditions. However, it will be shown in the following section on varying the values of the elastic moduli, that the calculated value of (Q), together with revised values of (G) and (K), will provide a better combination of parameters for this correlation.

Further tests at other consolidation stresses, for various soils over the same range of gas fraction, would provide a data base of (Q) values, should the theory to experiment correlation remain acceptable in each case. This would ultimately allow equation 1.2 to be modified by the appropriate value of (Q) to predict the sound speed response of any gassy soil, providing the values of the required parameters are available, and are reliable.

6.4.3 Variation of the matrix elastic moduli (G and K)

Figure 6.6 provides the sound speed results for sample E50-1 at varying values of elastic moduli for the saturated soil matrix, using equation 1.2.

Figure 6.6(a) illustrates the response due to a constant value of (G), at 130 MPa, and varying values of (K), at 1.404, 3.650 and 14.038 GPa. Since, in practise, the value of (K) cannot vary independently of (G) in soils of the same classification, gas content and consolidation stress, this investigation presents a purely hypothetical case for sample E50-1. However, this exercise will demonstrate the effect of dependence on (G)

in relation to a comparison of sound speed response for different soils. Also, since there is some uncertainty in the theoretical moduli values adopted in this study, it will provide a quantitative method of assessing the validity of the chosen values by the comparison between the resulting theoretical and experiment curves.

The curve with square symbols is provided by the standard case (i) (G) and (K) values, presented previously in Figure 6.3(a). Increasing the value of (K) is seen to cause an unacceptable increase in the peak sound speed level and frequency position, a propitious reduction in speed below resonance and no change at well above resonance. The converse is true for a decrease in (K) at peak, and below, resonance positions. Therefore neither case suggests a value of (K) which would improve the overall correlation between the values of theory and experiment.

Figure 6.6(b) illustrates the predictions due to a constant value of (K) at 4.221 GPa, and a varying value of (G) at 50, 130 and 500 MPa. The above comments on the objectives of this investigation apply here also. The curve with square symbols is again provided by (G) and (K) values closest to the standard case(i) of Figure 6.3(a). An increase in the value of (G) produces a reduction in peak sound speed, a delay in peak position frequency and an increase in below resonance speed. The converse is true for a decrease in (G). Here the curve of triangular symbols for G = 50 MPa produces a lower below resonance sound speed together with a lower frequency transition point position, to provide a better correlation with the experiment results of E50-1.

Finally a revised prediction has been made for the matrix (G) and (K) values again using Wheeler (1986). Extrapolation from his triaxial test results for a saturated soil at a consolidation stress of 200 kPa, provides a value for the shear modulus of 2 MPa. Further reference to

Jardine et al (1984) suggests that the shear moduli applicable to a strain of 1% would have to be increased by 10 times to represent the value relevant to a strain of 0.01%. Hence a conversion from the value of (G) for the triaxial test to the value indicated for an acoustic test is achieved by increasing Wheeler's value by 10 times, to 20 MPa. The theory of Wheeler was then used to obtain the corresponding value of (K), of 3570 MPa. These revised moduli values are used with the various values of (Q) suggested in section 6.4.2, to investigate the best combination of (G), (K) and (Q) values. The most successful result was provided by the calculated value of (Q) that is shown in Figure 6.2(a), denoted as 'revised theory' It can be seen that, for sample E50-1, the correlation between the theoretical and experiment results is reasonable for both below resonance sound speed and for the transition point frequency position. Using the same combination of parameter values for the remaining experiments gives similarly improved results. The values of the dynamic elastic moduli (G) and (K), of the matrix, are therefore found to be approximately 20 and 3570 MPa respectively, for all the research test samples at 25 kPa. Similarly the value of the reciprocal specific dissipation function relevant to all the samples is found to be that of the calculated value (Appendix A).

6.5 EXPERIMENT/LITERATURE SOUND SPEED COMPARISON - (At resonance)

Figure 6.7 presents the experiment results described in section 6.2, with those from the literature described in section 1.3.2, and additional references where gas fractions are uncertain and signal frequencies are generally low.

Results from all eight soil samples are presented and noted by the specimen number, then the process by which the speed was measured and finally the value of gas fraction. The data taken from the literature is

noted initially by reference and finally by gas fraction, if known. The laboratory measurements of Kepkay (1977) on soft silty clay with a gas fraction of around 0.2 indicate an unusually high sound speed, as discussed in section 1.3.2, in comparison with sample E50-1 of similar gas content. This sound speed result is extended over the frequency range shown since the signal bandwidth used was 3 to 100 kHz. The results of Edrington and Calloway (1984) are from measurements in soft clay at a gas fraction of 0.00065 and a signal bandwidth of 0.05 to 20 kHz. Here the sound speed is similar to that of sample E53-1, with a gas content of 0.00511, but vastly different to sample E51-2 of 0.00357. The sound speed of the soil therefore seems more appropriate to a soil of gas fraction around 0.005 to 0.006 - an order of magnitude greater than quoted.

Hochstein (1970) uses a bandwidth of 100 to 200 Hz, well below the range of data presented here, as indicated by the reference arrow. The measured sound speed is relevant to a silty clay of approximately comparable density and gas fraction to sample E51-2. The sound speed result is again more applicable to a higher gas content soil of gas fraction around 0.08. Jones et al (1964), does not produce figures for gas content to allow a comparison with the experiment samples. The two separate ranges of their results for soft-mud, taken at a signal bandwidth of 0.2 to 3.2 kHz, suggest that gas fraction is above 0.2 for the 46 to 123 m/s values and around 0.0036 for the 1564 to 1656 m/s speeds. The remaining data from Press and Ewing (1948), Worzel and Drake (1959), Levin (1962) and Jones et al (1958) are taken using low signal frequencies and uncertain gas fractions. Their sound speeds may be accommodated by gas fractions of 0.004 to 0.2, as indicated by the experiment results.

In general, therefore, the comparable data from the literature is insufficient to assess the degree of correlation with experiment results. It is possibly the problems and inaccuracies involved in assessing in situ gas fractions that may have lead to the shortage of data.

CHAPTER 7 - ACOUSTIC RESULTS - ATTENUATION (At resonance)

7.1 EXPERIMENT RESULTS

7.1.1 The high gas content samples of experiments E50 and E52

7.1.2 The low gas content samples of experiments E51 and E53

7.2 THEORETICAL RESULTS

7.3 THE INFLUENCE OF PARAMETER VALUES ON ATTENUATION

7.3.1 Variation of the ambient hydrostatic pressure

7.3.2 Variation of the reciprocal specific dissipation function

7.3.3 Variation of the matrix elastic moduli

7.4 EXPERIMENT/LITERATURE ATTENUATION COMPARISON

7 ACOUSTIC RESULTS - ATTENUATION

7.1 EXPERIMENT RESULTS

The attenuation values for each of the four experiments are found using the FT method, described in section 3.3.4 and are presented in Figure 7.1 (a) to (d). Data for both Cells 1 and 2 are included on each plot, except for Figure 7.1(a) where no spike signal was received through the soil in Cell 2 (test E50-2).

7.1.1 The high gas content samples of experiments E50 and E52

All three samples E50-1, E52-1 and E52-2 shown in Figures 7.1(a) and (b) indicate high levels of attenuation as a result of their large gas contents. Individual values are consistent with their relative gas fractions, with average losses of 25, 20 and 8 dB/cm for E50-1, E52-1 and E52-2, respectively. All three samples indicate an underlying trend of increasing attenuation with frequency. Although E50-1 shows a dramatic increase in rate at around 50 kHz, the samples of experiment E52 may indicate only a slight change at about 45 kHz. It will be shown from the plots referred to in the next paragraph, that this increased rate from around 45 kHz continues above the 80 kHz limit of Figure 7.1(b). Once again the increased rates may be interpreted as more pronounced resonance effects which may result from an accumulation of gas at the small bubble end of the BSDs. As expected, no correlation exists between these frequencies and the transition points from the sound speed data, since Figure 1.4(b) suggests an earlier attenuative response to resonance than is provided by the sound speed of Figure 1.4(a).

The more localized trend in variation of all three samples indicates a reduction in attenuation at between 40 and 50 kHz. This may also be bubble size dependent, since it may be caused by the absence of gas in

each of the BSDs between 700 and 780 microns diameter. The association between radius and frequency would provide an ($f_o r$) product of 1700 Hz.cm.

Finally, an observation can be made concerning the level of attenuation at above those frequencies over which experiment results are presented in Figures 7.1(a) and (b). It can be seen from the Fourier transforms of Figure 6.1(a) to (c), that the signals through soil are attenuated to below noise level between the upper frequency limits of the soil (the type(i) transforms) and the upper limits of the calibration media (the type(ii) transforms) for each sample. Therefore, if attenuation versus frequency data is provided for this range of frequencies, in the same manner as that used to provide Figures 7.1(a) to (c), the new curves generated would indicate minimum levels of attenuation. Hence, at each frequency, the true attenuation of the gassy soil samples must be at, or greater, than the levels illustrated by the curves. Figures 7.1(e) to (g) illustrate these curves where the low frequency sections are the same as the corresponding plots of Figures 7.1(a) to (c) and the sections above these are marked as 'minimum possible values only'. In general, attenuations are indicated which are at least the same order of magnitude as the low frequency sections, therefore illustrating how the effects of resonance dominate into higher frequencies.

Since the low gas content samples do not generally have soil transforms of significantly reduced frequency range, the above treatment is unnecessary.

7.1.2 The low gas content samples of experiments E51 and E53

The attenuation results for experiments E53 and E51 are provided in Figure 7.1(c) and (d). All these samples, except for E51-2, show high

values of attenuation inconsistent with the comparatively low levels of gas content, but similar to the high gas content values of experiment E50 and E52. As for section 7.1.1, individual values are consistent with their relative gas fractions, with broad average losses of 19, 15, 8, 0 dB/cm for E53-1, E51-1, E53-2 and E51-2, respectively. The zero level here indicates that the soil of sample E51-2 is no more attenuative than the glycerol calibration liquid.

The lowest gas content samples, E53-2 and E51-2 show little variation in loss and suggest that attenuation is nearly constant at all frequencies within an accuracy of 1 dB/cm. Conversely, samples E53-1 and E51-1 show considerable localized variation and some overall variation. E53-1 begins to increase gradually in attenuation at around 340 kHz, possibly indicating more significant resonance. Here the greater response in attenuation, due to resonance, occurs much later in frequency than on sound speed where, for this sample, the transition point is 30 kHz.

Sample E51-1 has a very non-typical attenuation curve compared with the other samples. It has a zero attenuation trough at 170 kHz, the same frequency as the non-zero trough of sample E53-1. This may therefore indicate a bubble size influence, since the BSDs of both have a shortage of gas between 260 and 380 microns diameter. The corresponding ($f_o r$) product is 2720 Hz.cm.

A similar approach to that used in section 6.3 concerning resonance effects caused by the largest bubble, or 'the peak gas content bubble size', of a soil may also be applied to the attenuation results. Although samples E53-2 and E51-2 do not indicate an increased rate of rising attenuation with frequency, the remaining four samples provide a relatively constant value for the ($f_o r$) product for 'peak gas content bubble sizes' rather than largest sizes. (No experiment data is

available for E50-2, and E53-1 does not have a significant peak gas content). Table 7.1 presents the results for both cases where, for peak gas content bubble sizes, the average value of the product is 980 Hz.cm. Again, further tests would need to be performed at different consolidation stresses to establish whether the product remained constant for a given stress. This may establish a useful data base of product values for predicting bubble size, that could be used to corroborate results from the same approach used on sound speed. It should be noted however that, because there is a factor of two difference between the average ($f_o r$) value found from sound speed results and that found from attenuation, the 'peak gas content bubble radii', which are common to both, are prescribed different resonance frequencies. No reason has been found for this.

Finally, a reasonable correlation is achieved by comparing the corresponding curves for the experiment results of sound speed and attenuation shown in the set of Figures 6.2 and 7.1. In the majority of cases, the curves in both figures indicate a similar degree of response, as frequency varies, to both gas fraction and the apparent effects of bubble resonance, in terms of level and variation. This is true for both the low gas content samples of this section and for the high gas content samples of section 7.1.1.

7.2 THEORETICAL RESULTS

Equation 1.3 is used to provide equivalent theoretical data over the same frequency range as the experiment results. Parameter values are again those referred to in section 6.3 on sound speed and are listed in Table 1, Appendix B. They are also relevant to the eight soil samples and, as for sound speed, it should be remembered that the high gas content samples exceed the gas fraction limit suggested by Spitzer (1943) for

applying the theory used in equation 1.3 (as discussed in section 1.3.1.2).

Figures 7.2(a) to (h) provide the theoretical attenuation versus frequency curves where curves (i) and (ii) use the upper and lower bound values of (G) and (K), respectively (from Table 1). As for the theoretical sound speed results, the peak curve values appear unrealistic for the high gas content samples of experiment E50 and E52. Again it will be shown later how the damping constant (d) in equation A9 and A10 (Appendix A) may be adjusted to reduce both peaks to a more reasonable level. As for the theoretical sound speed values, the curves of Figure 7.2 have been provided using the original calculated value of (Q) to retain objectivity in the comparison with experiment results.

The theoretical results of curve (i) for each sample, have been plotted on the corresponding graphs of Figure 7.1(a) to (d) for the experiment results. Theoretical curves again confirm that the frequency range covered by the experiment results generally embraces the lower frequencies of resonance effects. Also, for all but E53-2 and E51-2, the underlying trends of gradual, and then more significant increases in attenuation, are predicted reasonably closely by the theoretical curves. As for sound speed, the BSD of each sample is plotted on Figure 7.1(c) and (d) using proportional gas fraction at the corresponding resonance frequency of each bubble size and again using (f_o) values from Table 6.1. The correlation with the positions of increased attenuation rate, in the theoretical curves, confirm that they occur due to the additional influence of resonance, since they are close to the low frequency end of the plotted BSD. As these positions for the experiment curves are generally close to the theoretical, they also correlate with the plotted bubble resonances.

Although the underlying curve variations agree well with experiment results, the levels of attenuation predicted by theory are, in the majority of cases, around 20 dB/cm lower. The next section will investigate the effect of varying the parameter values in order to arrive at a more successful prediction of the actual attenuation response from theory.

7.3 THE INFLUENCE OF PARAMETER VALUES ON ATTENUATION

The effects of varying the values of ambient hydrostatic pressure, reciprocal specific dissipation function and the elastic moduli, are investigated here using equation 1.3 for attenuation. This analysis will provide data for predicting the dependence of the actual attenuation response on these parameter values. As for the sound speed case, since the basic profile predicted by theory is essentially the same as found by experiment, theory may be used to indicate the trend in variation rather than specific levels of attenuation at certain frequencies. Also, the results are used to indicate the parameter values which produce a closer fit of predicted to actual data.

7.3.1 Variation of the ambient hydrostatic pressure (P_o)

Figure 7.3 provides the attenuation versus frequency curves of sample E50-1 for values of (P_o), 1 and 100 atmospheres, using equation 1.3. Again, curve (i) uses the (G) and (K) values from Hamilton (1971) and Gassman (1951) while the curves denoted by (ii) use those of Jardine et al (1984) and Wheeler (1986). Also, the comments made in section 6.4 are relevant here, as this section compares the attenuation of separate soils of equal gas fraction, BSD and porosity that may exist in different depths of water.

In case (i), there is approximately a 1% decrease in attenuation due to the 1 to 100 atmospheres increase in back pressure. For case (ii), pre-peak and peak attenuation increase by up to 3%, while post peak reduces by this amount for the same increase in (P_o). It is therefore apparent that gassy sediments, which have fairly stiff matrix elastic moduli as case (i), may exhibit the same attenuation response irrespective of their depth below the water surface (up to at least 1000 m). Sediments of case (ii), however, with less-stiff matrix elastic moduli, may exhibit a 3% variation. This suggests that the elastic moduli, gas fraction and BSD of the soil, that may vary as a result of large depths of submergence, are more significant than the consequent effect of an increase in gas pressure.

For a low gas content sample, E51-2, no significant differences for either case (i) or (ii) were found over the same variation in (P_o).

7.3.2 Variation of the reciprocal specific dissipation function (Q)

Figure 7.4 provides the attenuation versus frequency curves for sample E50-1, using varying values of (Q) in equation 1.3. For two trials, (Q) was kept constant at 1 and 4, and for the third the calculated value (from Appendix A) was used, as Figure 7.2, varying with bubble size and signal frequency. The case (i) and (ii) values of the elastic moduli are again used here.

None of the curves resemble the harbour mud result illustrated in Figure 1.4(b). However, reducing the value of (Q) from its calculated level to a constant value of either 1 or 4 reduces attenuation at 100 kHz, for both case (i) and (ii), by between 5 and 25 dB/cm. It can be seen from Figure 7.1(a), that the theoretical value needs to be increased by 25 dB/cm at this point to equal the experiment response. Also, the position

of increased attenuation rate of the theoretical curve is changed, in frequency, away from that indicated using the calculated value of (Q) that agrees well with the underlying trend in variation of the experiment results. Therefore, as with sound speed, it is the calculated values of (Q) that have been found to allow the most successful correlation between theoretical and experiment results for a gassy soil at a consolidation stress of 25 kPa. This result should be tested for different consolidation stresses before adopting the equations of A9 and A10 for (Q) in order to predict attenuation for a range of soils.

7.3.3 Variation of the matrix elastic moduli (G and K)

Figure 7.5 gives the attenuation results for E50-1 at varying values of the matrix elastic moduli (from equation 1.3). Comments concerning the hypothetical nature of the investigation for the sound speed case of section 6.4.3 are also valid here.

Figure 7.5(a) provides the response due to a constant value of (G) at 130 MPa and varying values of (K), at 1.404, 3.650 and 14.038 GPa. The curve with square symbols represents the case (i) standard (G) and (K) values used in Figure 7.2(a). Increasing the value of (K) results in a unrealistically high value overall for attenuation while reducing (K) provides an overall reduction. However, the low value of (K) increases the difference between experiment and theoretical results at 100 kHz by a further 5 dB/cm from the standard case(i).

Figure 7.5(b) illustrates the result due to a constant value of (K) while (G) is given the values 50, 130 and 500 MPa. The curve with square symbols again represents the standard case(i) values for (G) and (K). Increasing the value of (G) this time reduces attenuation overall but increases the disparity between experiment and theoretical results at 100

kHz. A decrease in (G) to 50 MPa reduces the difference from around 25 to 5 dB/cm, although peak attenuation is made increasingly unrealistic. Also the position where the attenuation rate significantly increases, is reduced in frequency to improve further the correlation using the 50 MPa figure for (G).

Finally the revised prediction for the values of (G) and (K), adopted in the sound speed section 6.4.3, and used in conjunction with the calculated value of (Q), again provides the most successful comparison with the experiment results of test E50-1. The curve is shown in Figure 7.1(a) as the 'revised theory'. Further trials with the other samples also provide similarly improved results.

Therefore the value of the matrix dynamic elastic moduli, (G) and (K), are confirmed to be approximately 20 and 3570 MPa respectively for all the research test samples at 25 kPa. These values when used with the calculated value of (Q), (Appendix A), provide the most successful combination of parameters for the correlation between the theoretical and experiment results.

7.4 EXPERIMENT/LITERATURE ATTENUATION COMPARISON - At resonance

Figure 7.6 presents the experiment results described in section 7.1 with those from the literature. Results from four experiment samples are presented and noted by the specimen number and the gas fraction, whereas those from the literature are labelled with their reference only, since no gas contents are recorded.

The Nyborg et al (1950) measurements are taken on loose Hagerstown silt loam in the laboratory, after entraining air. They range from 26 to 74 dB/cm over frequencies from 10 to 35 kHz. Using the results of the

research tests to indicate possible gas contents for the silt, suggests that their soils could have a gas fraction from 0.2 to well above this level. However, since the unconsolidated loam silt is likely to have lower values of elastic moduli than E50-1, the levels of gas content may be reduced in proportion as shown by the effects of Figures 7.4 and 7.5(b). This may also be relevant to the 17 to 24 dB/cm results from the unconsolidated laboratory muds of Wood and Weston (1964), that contain entrained gas, and which otherwise indicate a gas fraction of 0.1 to 0.2. Anderson et al (1971) reports the much lower value of 0.13 dB/cm at 40 kHz in mud from Lake Austin, that may be of similar classification and consolidation to the soils of the research tests; if so, gas fraction here may be between 0.0036 and 0.0040.

CHAPTER 8 - ACOUSTIC RESULTS - SOUND SPEED (Below resonance)

8.1 EXPERIMENT RESULTS

8.2 THEORETICAL RESULTS

8.3 THE INFLUENCE OF PARAMETER VALUES ON SOUND SPEED (Below resonance)

8.4 THE SOUND SPEED OF BULK SHEAR WAVES

8.5 LOSS DUE TO REFLECTION (Below resonance)

8 ACOUSTIC RESULTS - SOUND SPEED (Below resonance)

8.1 EXPERIMENT RESULTS

Figure 8.1 provides the below resonance sound speed results, shown as separate data points for each of the 8 test samples. Sound speed is plotted against gas fraction, since it is expected that there will be no variation with frequency below resonance. The eight values have been selected by examining Figure 6.2(a) to (d) for the 'at resonance' case and taking the speed at which the curve appears to level to a constant value at the low frequency limit (shown arrowed on each figure). This approach is made since, as discussed in sections 6.2 and 6.3, the 'transition points' between the 'below' and 'at resonance' conditions appears to occur within the frequency range of the results in each test. Therefore, in all tests, a constant level of sound speed is assumed to exist at around the 10 kHz limit.

As seen from sections 6.2 and 7.1, the sound speed and attenuation response of sample E51-2 is that of a saturated soil, although it has a measured gas fraction of 0.00357. A consistent trend is indicated by linking the data points of all four low gas content samples that firmly establishes the validity of the E51-2 result. This suggests that gassy soils respond as saturated soils when they have a non-zero gas content that is below a certain minimum level. The minimum gas fraction thus appears to be between 0.003 and 0.004.

The sound speeds of the high gas content samples, from E51-2 to E50-1, also indicate a fairly consistent trend but at a reduced rate of decrease. Sound speed eventually falls to as low as 250 m/s, which is well below the 446 m/s speed in methane gas only. It is therefore shown from these experiment results that it should be possible to predict the gas fraction of soils consolidated to a vertical stress of 25 kPa from

sound speed data below resonance frequency. Further tests at other consolidation stresses, over the same range of gas contents, would confirm whether this is possible at all stresses and whether the results can be used to predict both gas fraction and consolidation stress for the given soil classification. This would further indicate whether direct acoustic probe measurements would be useful in determining sea-bed gas contents in order to be able to predict strength and stiffness characteristics using data such as Wheeler (1986).

8.2 THEORETICAL RESULTS

Equation 1.1 is used to provide equivalent theoretical data over the same range of gas fractions as the experiment results. Four different sources are used for the values of the elastic moduli, (G) and (K) which are listed in Table 8.1(a) to (d). The values of bulk density for the eight samples are common to all four of the above combinations, and are those values from the BSD analysis recorded earlier in Table 5.1.

The first two sources for the elastic moduli are the upper and lower values used by Anderson (1974) as discussed in section 1.3.1, which are developed from compressible fluid and suspension theory, respectively. The second two sources are the upper and lower bound values suggested from the work of Wheeler (1986) and Jardine et al (1984). The lower bound values of (G) and (K) for each sample are extrapolated from Wheeler's triaxial test results at a consolidation stress of 200 kPa, to a stress of 25 kPa, as referred to in section 6.4.3. These values are therefore representative of static loading at large strains. For the upper bound case, the values of (G) and (K) appropriate to a strain of 0.01% are used, as also adopted in section 6.4.3 for sound speed and 7.3.3 for attenuation to provide the 'revised theory' curves of Figure 6.2(a) and 7.1(a) respectively. In calculating the corresponding values

of (K) here, to use with those of (G), the theory of Wheeler makes use of the 'large bubble model' discussed in Chapter 1.

Figure 8.1 shows Anderson's upper and lower bound curves as broken lines. Both 'compressible fluid' and 'suspension' models provide the same rapid decrease in sound speed for a very small increase in gas fraction (up to 0.003). Thereafter the variation is small. For the upper bound curve, the rapid decrease is a direct results of the abrupt loss in the soil's bulk stiffness, as defined by (K) in equations A3 and A4 (Appendix A). This is due to the presence of free gas in the pore water, that dramatically reduces the value of the 'compressible fluid' bulk modulus (K'_w) in equation A5. For the lower bound curve, the same rapid decrease in the bulk stiffness of the suspension is caused by the sudden inclusion of a gas phase volume, in equation A1, that is several orders of magnitude less stiff than the water and gas phases.

Conversely, the upper and lower bound curves of Wheeler and Jardine et al shown as unbroken lines in Figure 8.1 illustrate the behaviour of the 'large bubble model' in providing more gradually varying values of both (K) and (G) as a result of greater sample gas fractions. Here the gas is held in pockets which are largely supported by the surrounding matrix of saturated soil and so the overall soil stiffness is not drastically affected by having larger or more numerous enclosures.

The data points from the experiment results exhibit a similar abrupt fall in sound speed at low gas content as Anderson's two curves and the lower bound curve of Wheeler and Jardine et al. However, for large gas content samples, both the trend and level of the results follow the pattern predicted by only the upper bound curve of Wheeler and Jardine et al. It is therefore apparent that the latter curve offers a reasonably successful prediction of speed below resonance over all but extremely

small gas fractions. Here it seems that the elastic wave equation may only be appropriate with suitable bulk values of (G) and (K). For gas fractions less than 0.0036, the levels of (G) and (K) are required to remain constant at the values of the saturated soil matrix, whereas for gas fractions immediately above 0.0036 the moduli need to vary rapidly for small increases in gas content.

Further validation of those values of elastic moduli predicted from the work of Wheeler and Jardine et al, is given by comparing the sound speeds of sample E50-1, calculated by using the separate theories of the two conditions - 'below resonance' and 'at resonance'. The below resonance sound speed, found using the theory for the 'at resonance' condition (equation 1.2) is within 50 m/s of the sound speed predicted using the 'below resonance' condition (equation 1.1). An equivalent comparison using the case(i) values of elastic moduli from Hamilton (1971) and Gassman (1951), described in section 6.2, provides a much greater disparity of around 300 m/s, and must therefore be unrepresentative of the soils stiffness in general.

A further comment may be made concerning the Wheeler and Jardine et al values, in regard to the influence of bubble size on below resonance speed. Although the upper bound values of (K), predicted using Wheeler's theory, are not dependent on bubble size, the values of (G) may be, since they are extrapolated from triaxial test results. Therefore the less successful correlation for the low gas content samples may also be a result of the effect on the value of (K) of bubble size, rather than just gas fraction, since the maxima, minima and ranges shown in the BSDs for these samples are significantly less than for the high gas content samples.

8.3 THE INFLUENCE OF PARAMETER VALUES ON SOUND SPEED - (Below resonance)

Below resonance, sound speeds are primarily dependent on the values selected for the elastic moduli. Also, the effect of a varying (P_o) causes a change in sound speed by its effect on the soil's consolidation and therefore its (G) and (K) values. Since the effects of varying the values of the elastic moduli have been discussed in the previous section concerning the four models, it may be useful here to indicate by how much the values of (K) may vary as a result of changes in (P_o) and the effect on the corresponding values of sound speed. Of the four models, only the Anderson upper bound theory considers the value of (P_o) which changes the bulk modulus of the compressible fluid (K'_w) in equation A5, and therefore the values of (K) for the gassy soil.

Table 8.2 contains the values of (K) as (P_o) varies through 1, 5 and 100 atmospheres giving the curves shown in Figure 8.2. The change in (K), and therefore sound speed, for (P_o) values of 1 and 5 atmospheres, is only significant for gas fractions less than 0.015. However the variation for P_o) values between 5 and 100 atmospheres is significant for all gas contents, causing increases in speeds of 60 m/s to around 800 m/s from the highest to the lowest sample gas contents. Although these results will not be the same as for the more favoured values of (G) and (K) taken from the work of Wheeler and Jardine et al, they may provide some indication as to the possible level of variation in speed as a result of the effect on (K) only. The order of magnitude of variations in the value of (G), as a result of changes in (P_o), are suggested by Wheeler (1986) and are likely to be of much lower magnitude than those of (K).

The change in sound speed as a result of the variation of the third parameter, that of (ρ) in equation 1.1, is proportionately much smaller

than that caused by the elastic moduli and will not therefore be discussed. Finally, more tests at other consolidation stresses may determine whether new values of (G) and (K), found from Wheeler and Jardine et al, are again appropriate for soils over the same range of gas contents, in order to provide sound speeds which correlate with the experiment data.

8.4 THE SOUND SPEED OF BULK SHEAR WAVES

The bulk shear wave speed (c_s), for an elastic solid of homogeneous and isotropic behaviour, is:

$$c_s = \sqrt{\left(\frac{G}{\rho}\right)} \qquad 8.1$$

This equation is used to provide the theoretical curve of shear wave speed versus gas fraction shown in Figure 8.3, where the values of sample bulk density (ρ) have been taken from Table 5.1 and the predictions from Wheeler and Jardine et al for the shear modulus (G) have been taken from Table 8.1(c). For the saturated soil condition, the revised value for the matrix shear modulus (20 MPa), from Wheeler and Jardine et al, has been used with its corresponding bulk density (1648 kg/m^3) for the saturated soil condition.

The shear wave curve varies, approximately linearly, by only 11.34 m/s from a saturated soil condition to that of the most gassy of the test samples. For comparison, a compression wave curve is also shown using the upper bound case predicted from Wheeler and Jardine et al, (Figure 8.1). This curve is provided from the same (G) and (ρ) values as the shear wave curve together with a corresponding bulk modulus (K). The comparatively low degree of variation of the shear wave with gas fraction indicates that probes, that incorporate shear wave measuring apparatus,

are unlikely to indicate the presence of gas from sound speed results. However, a probe which measures compression wave sound speeds below resonance should more easily detect the presence of gas and should also provide an indication of the volume. The contrasting degrees of variation of the two wave types are a result of the considerable changes in (K), on which the value of the compression waves are largely dependent, and the small variations of (G) on which the shear waves depend.

8.5 LOSS DUE TO REFLECTION - (Below resonance)

No direct tests have been carried out in this study on the reflection and refraction at mudlines formed from gassy soil, and no corresponding theory is available at least for the 'at resonance' condition. However, theoretical results can be presented for the 'below resonance' condition, since they can be provided by using the bulk density, compression wave sound speed and attenuation results already obtained in this thesis. Results will be relevant to seismic profiling work, where signals react with offshore water/sediment mudlines of various sediment gas contents.

Curves of the reflection coefficient (R) are calculated using the theory of MacKensie (1960) and are shown in Figure 8.4. Whereas the simple Rayleigh equation (1.4) concerns only those signals which propagate in a direction normal to an idealized liquid/liquid mudline interface, MacKensie theory incorporates the effects of varying the grazing angle (the acute angle between the direction of the incident signal and the mudline). It also extends the simple liquid/liquid interface model, to allow for sediment absorption loss, by defining the wave number for the sediment as complex. Both his in situ measurements, and those of Muir et al (1979), show reasonable correlation with MacKensie's theoretical values. The sound speed (1532.3 m/s) and bulk density (1.025 kg/m^3) of

the salt water are taken from the velocity ratios of Table 1 and the densities of Table 2 from Hamilton (1971), since they are relevant to average continental shelf conditions overlying silty clay sediments. Values chosen for the saturated sediment are 1502.5 m/s (measured) and 1648 kg/m^3 (calculated as section 5.1).

The low gas content sample, E53-2, indicates a similar sign reversal at the zero reflection coefficient to that exhibited by the saturated soil curve, whereas sample E53-1, with slightly more gas, shows the same trend as the large gas content soils, E52-1 to E50-1. It is because of the influence of even small amounts of gas on sound speed and attenuation, that the reflection coefficient is very sensitive to gas content. Also, the range of variation from the saturated soil curve to the most gassy of the soils, E50-1 is much greater than that shown to exist by MacKensie over the range of saturated soils from clayey silt to sand.

Figure 8.5 shows curves of loss due to reflection calculated from equation 3.9, using the coefficient (R) provided from Figure 8.4 for the saturated soil, and for the gassy soils of large gas content, (E50-1), and small, (E53-1).

The absence of a critical angle, below which all energy is reflected, is typical of a silty clay, since the sound speed is generally less than for the overlying water. This is generally not the case for more granular soils, such as sands and gravels. Loss for E53-1 is only significant below a grazing angle of 40°, whereas for E50-1, loss is greater than 2.5 dB at 90° and rises to 6 dB at 40° (the angle limits within which most seismic profiling devices may operate). Therefore, considerable signal energy is lost penetrating a gassy soil mudline. However, such losses are small in comparison to those which occur due to attenuation, as the

wave propagates through the soil after transmission across the mudline (E50-1 gives 24.25 dB/cm, at 10 kHz).

The reduced velocities of gassy soil have a further effect on the overall energy loss for a signal in seismic profiling work. Beam spreading loss accounts for a considerable proportion of the overall loss and is affected by a refraction at the mudline interface related to the ratio of velocities across the interface. An allowance for this is made in the expression for beam spreading loss from the work of Brekhovskikh (1960):

$$L_{BSL} = 10 \log_{10} \left\{ \frac{1}{\left(R_w + \frac{R_s}{N}\right)^{1/2} \left(R_w + R_s \left[\frac{\cos^2 \theta_1}{N \cos^2 \theta_2} \right] \right)^{1/2}} \right\}^2 \qquad 8.3$$

where (Θ_1) and (Θ_2) are the angles of incidence and transmission, which are related by Snell's law; (R_w) and (R_s) are the transmission distances through water and sediment for a signal source at a given height above the mudline and a sediment penetration depth below the mudline, (N) is the refractive index ($\frac{c_1}{c_2}$).

Beam spreading loss is proportional to the square of the distance of propagation through the water and the sediment. However, for non-normal incidence at the mudline, (Θ_2) is less than (Θ_1) as a consequence of $c_2 < c_1$ - (Snell's law). Therefore, as gas content increases and (c_2) reduces, the sediment transmission distance, necessary to achieve a given depth below mudline, also reduces.

This results in an overall reduction in spreading loss due to the reduced propagation distance. Figure 8.5 shows the three curves calculated using equation 8.3 which demonstrates the reduction in beam spreading loss

(around 5 dB) as gas fraction increases from zero in the saturated soil to 0.198 in the gassy soil. Both source height and penetration depth are taken as 50 m, which results in approximately equal overall losses for each soil type when the losses due to reflection and beam spread (with refraction) are summed for grazing angles above 40°.

CHAPTER 9 - CONCLUSIONS AND RECOMMENDATIONS

9.1 CONCLUSIONS

9.2 RECOMMENDATIONS

9 CONCLUSIONS AND RECOMMENDATIONS

9.1 CONCLUSIONS

The equipment, described in Chapters 2 and 3, has been used to provide acoustic data on gassy and saturated soils to an acceptable degree of accuracy. Two proceedures referred to as the TTC and the FT methods, have been devised specifically to overcome the difficulties in interpreting the results of tests on gassy soils. Also, the traditional Leading Edge method has been shown to provide sound speeds that do not correspond to the characteristic frequencies of transmission. Eight tests have been performed at a consolidation stress of 25 kPa, on soils that have gas fractions between 0.00357 and 0.198. Sound speed and attenuation measurements were found to vary within the limits of 1600 m/s to 250 m/s and 0 to 40 dB/cm, respectively, over frequencies within the range of 10 kHz to 1 MHz.

A process has been devised to measure each sample gas fraction and bubble size distribution. This method has been used to correlate the gas content of the test soils with their acoustic response. It has also been found that the product of the transition point frequency (between the sound speed conditions of 'below' and 'at resonance') and the diameter of the dominant bubble size group, is constant for the range of soils tested. This is also the case for attenuation, where the transition point used is the frequency at which the measured attenuation increases significantly in rate. Both products may be used to predict the dominant bubble size of similarly prepared soil samples of different gas content from their acoustic response. The measured sound speeds below the transition points are influenced by gas contents, not bubble size, and can therefore be used to predict the gas fraction of similarly prepared soils.

Expressions for sound speed and attenuation from current theory have been tested against the experiment results. This has shown that equation 1.2, (derived from the theory of bubble dynamics in water) for the 'at resonance' condition, provides a reasonable prediction of the level and overall trend in the variation of sound speed. Results are within ±100 m/s for the large gas fraction samples over 0.08, despite exceeding the restriction to gas content suggested by Spitzer (1943 - see section 1.3.1.2). However, the equivalent expression for attenuation, equation 1.3, provides results which are consistently 20 dB/cm below measured data, although the overall trend of variation is similar. For the condition of 'below resonance' sound speed, experiment results are shown to follow the behaviour of wave propagation in a homogeneous elastic solid (equation 1.1) for soils of gas fraction greater than 0.005.

Generally, it has been found that the 'at resonance' response is dominated by the soils gas content, the bubble size and the elastic moduli of the saturated matrix. These are determined by the availability of free gas and the depth at which the soil exists below the water surface and the mudline. It is therefore possible to predict the acoustic response of similar soils consolidated by the same stress from the experiment results or, to a lesser degree of accuracy, from theory, providing accurate values are used for the above parameters. It has been found that in regard to the soils that have been tested, the matrix elastic moduli for both the 'at resonance' and 'below resonance' conditions are predicted accurately from the work of Wheeler (1986) and Jardine et al (1984). Conversely, the in situ measurements of Smith (1973) and Hamilton (1971) appear to be almost seven times these values. This may be due to either the difficulty in predicting in situ values, or that the in situ soils are not similar in classification and consolidation to the laboratory soils.

It has been shown by the correlation of speeds below resonance that the 'large bubble model' described in Chapter 1 is generally more successful than the 'compressible fluid' response suggested by Anderson (1974). However, at gas fractions below 0.00511, and bubble diameters below 400 μm, the response was found to deviate from that described by the elastic wave equation in conjunction with the large bubble model. Below a gas fraction of 0.004 the acoustic response indicated was that of a saturated soil.

9.2 RECOMMENDATIONS

Further tests need to be performed to reproduce a range of in situ sediment confining stresses so that the above observations may be confirmed in general. If successful, a data base will be available to predict the gas fraction and dominant bubble size of silty clay sediments from the in situ measurements of an acoustic probe and an estimate of the condition of consolidation.

Correlation of these results with theoretical curves will establish whether the values of the elastic moduli can be predicted consistently by the work of Wheeler and of Jardine et al for all confining stresses. Also a more rigorous derivation of the expressions for sound speed and attenuation 'at resonance' needs to be attempted to establish a firmer basis for the above correlations.

Finally, the study should be extended to cover the full range of soil categories that may contain discrete gas bubbles. This should be performed in parallel with an examination of the engineering properties, similar to the work of Wheeler (1986) and Thomas (1987) on silty clay soil.

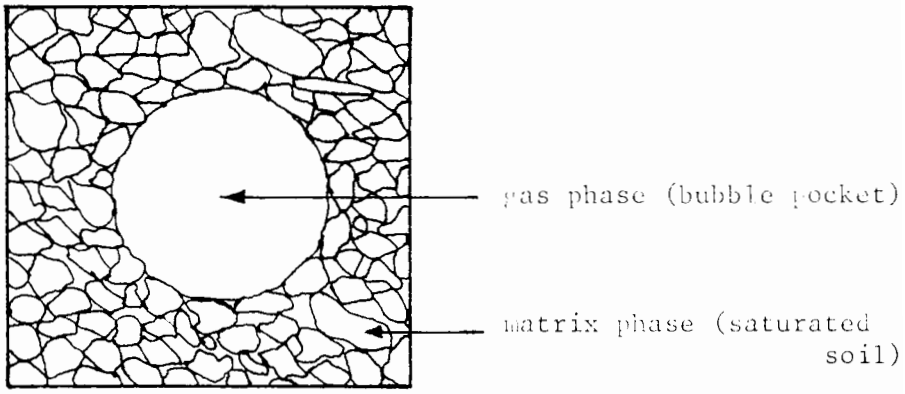


Figure 1.1(a) - THE LARGE BUBBLE MODEL

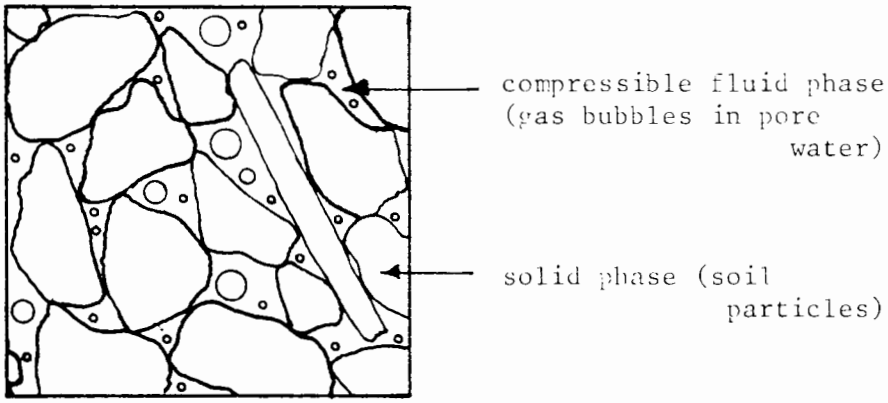


Figure 1.1(b) - THE COMPRESSIBLE FLUID MODEL

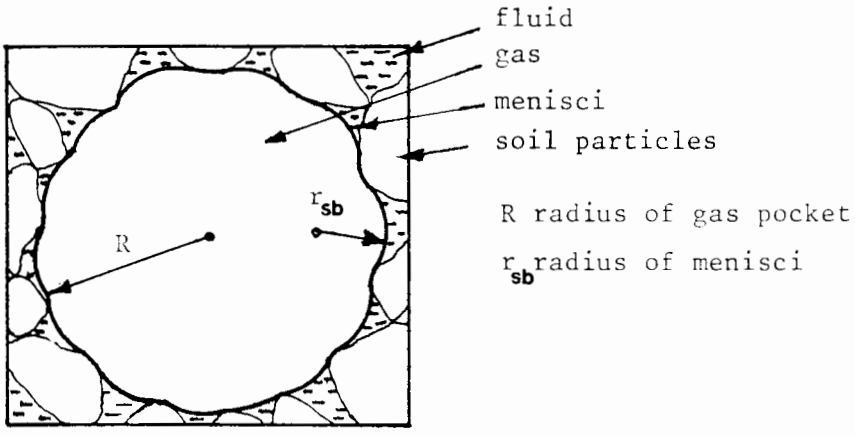


Figure 1.1(c) - BUBBLE CURVATURE



Figure 1.2(a)-
gassy soil (core
sample from muddy sand,
North Sea, Fannin, 1979)

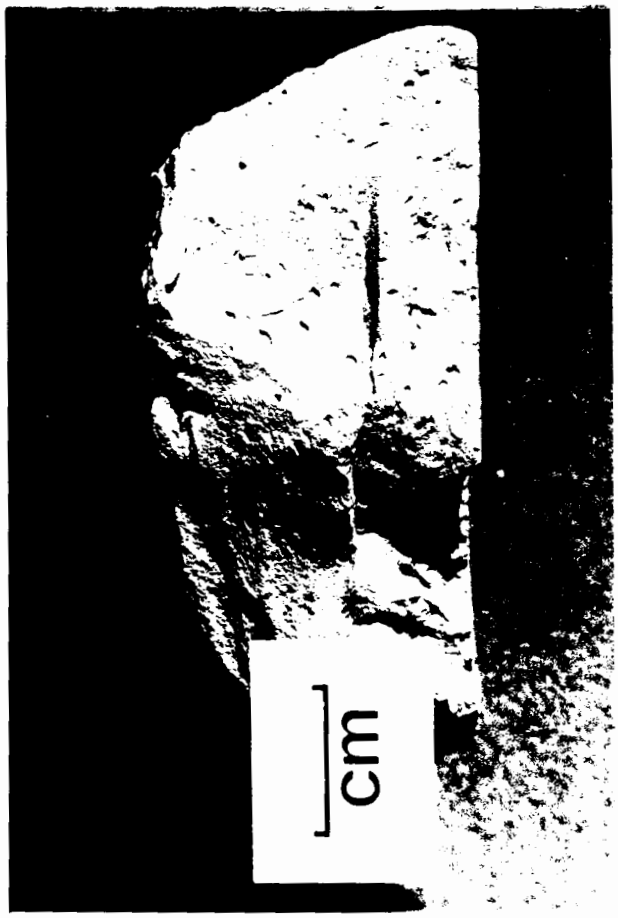


Figure 1.2(b)-gassy soil(dried specimen
from core sample,Bristol Docks)

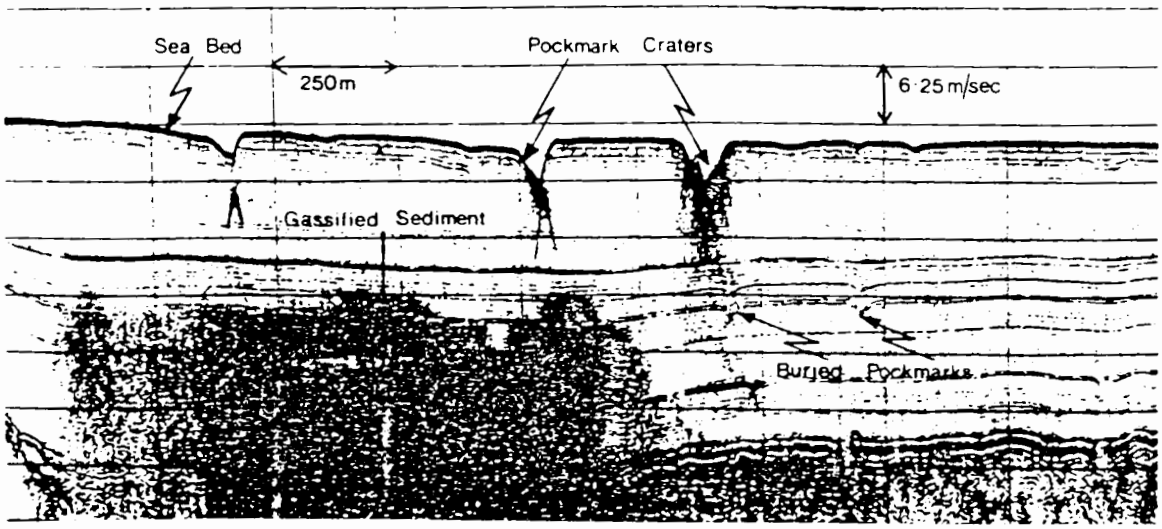


Figure 1.3-Acoustic blanking(North Sea, Fannin, 1979)

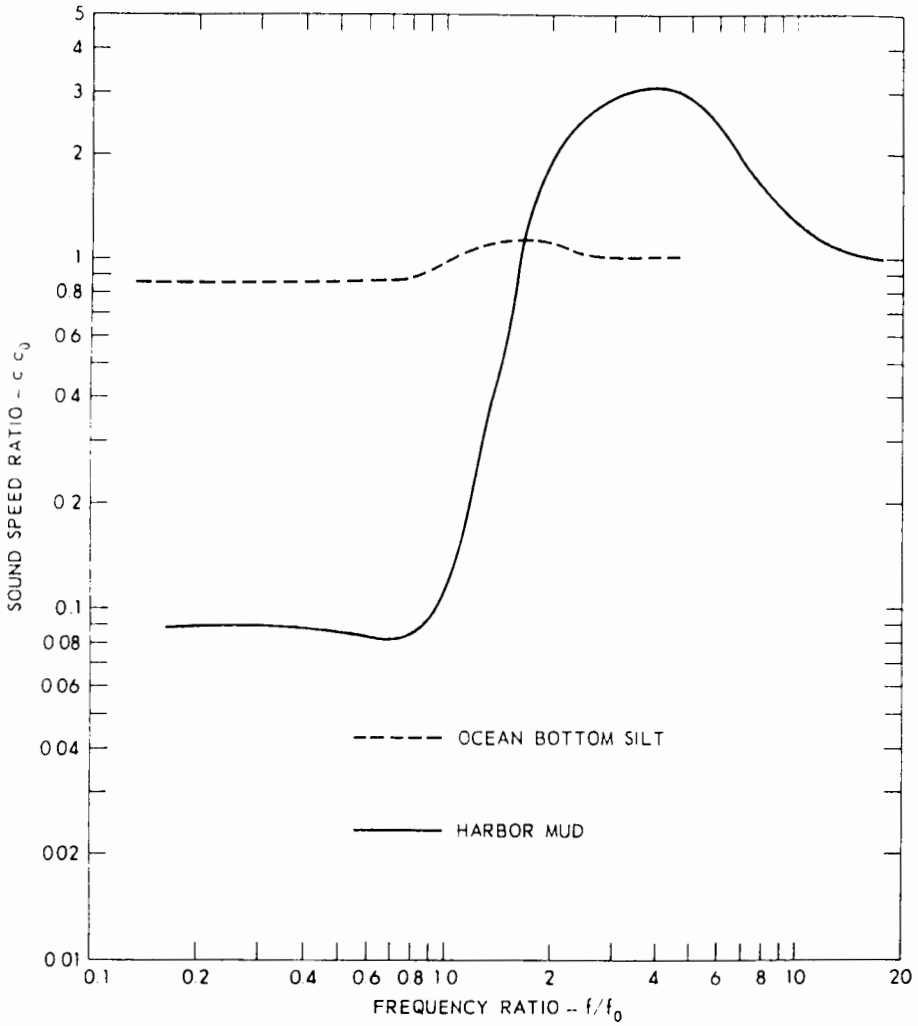


Figure 1.4(a)-Sound speed versus frequency (Anderson, 1974) Porosity, density and shear modulus are: silt- 0.68, 1550 kg/m³ and 2.5 GPa
mud- 0.75, 1400 kg/m³ and 1 MPa

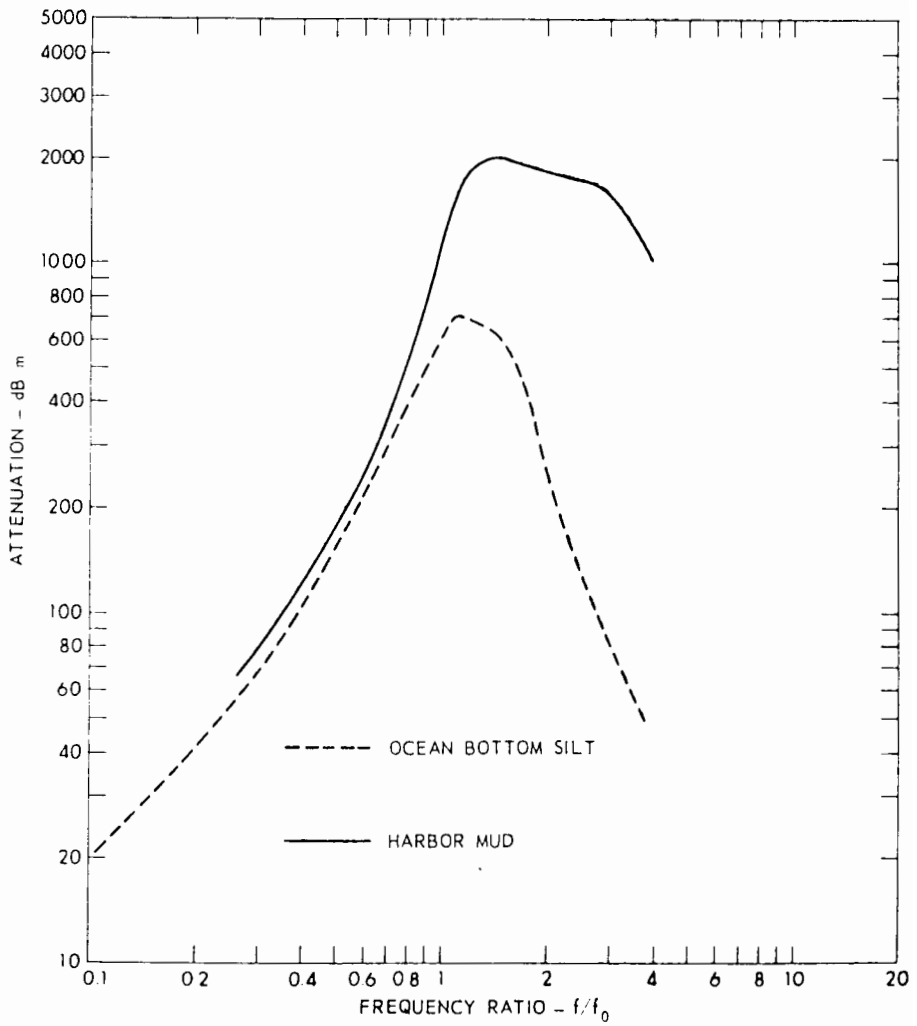


Figure 1.4(b)-Attenuation versus frequency (Anderson, 1974) Porosity, density and shear modulus are as for Figure 1.4 (a).

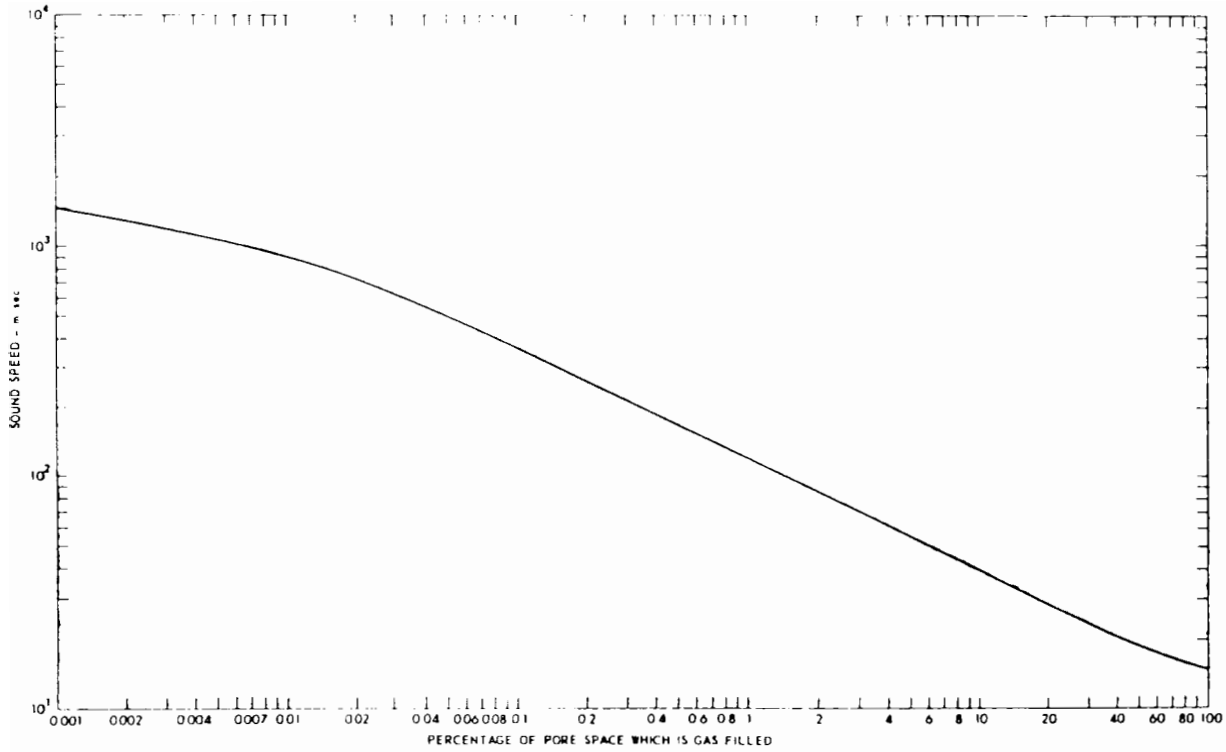


Figure 1.4(c)-Sound speed versus gas fraction (Anderson,1974)



Figure 1.5-Laboratory gassy soil (gas fraction 0.12, sample depth 3cm.

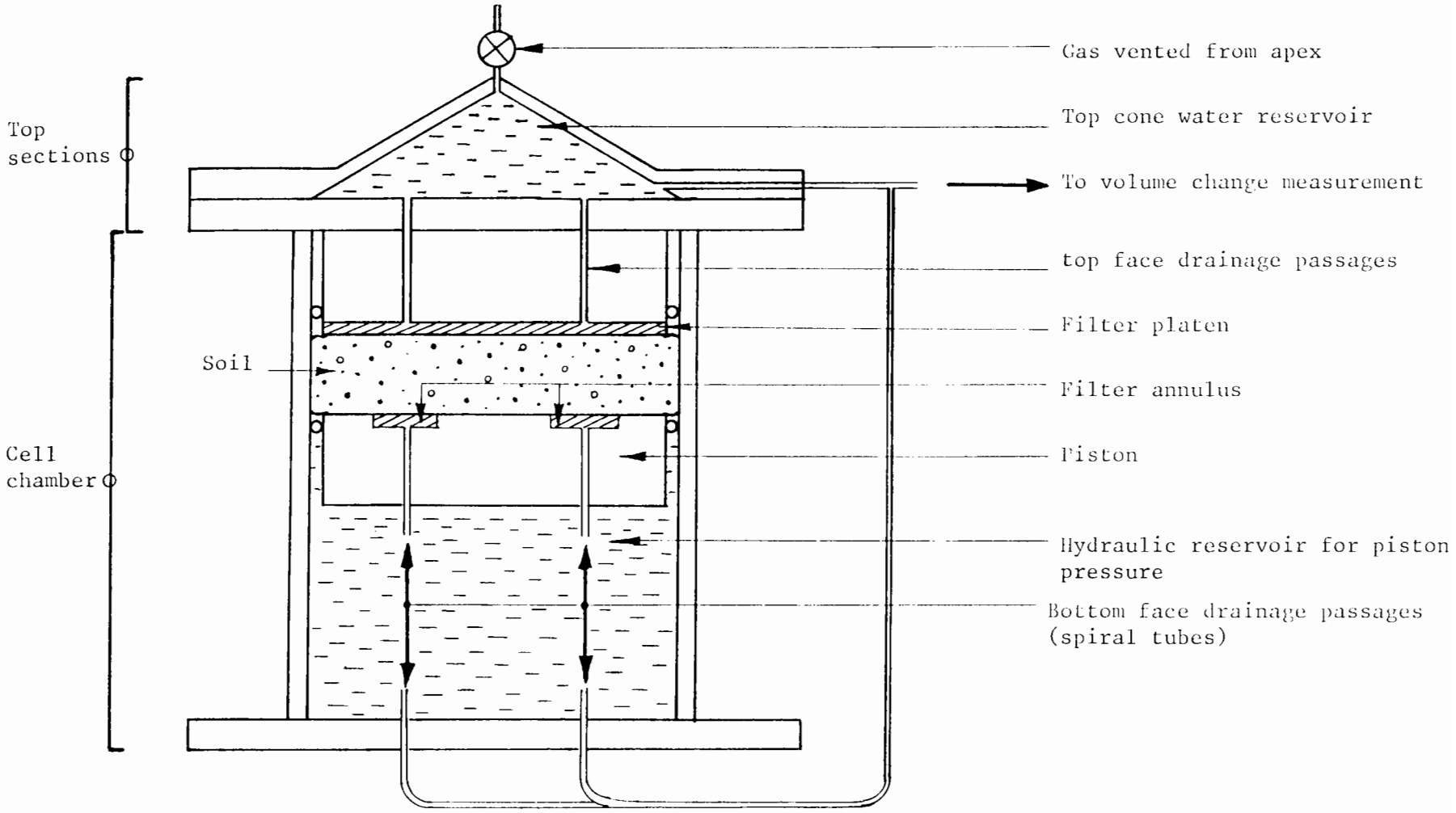
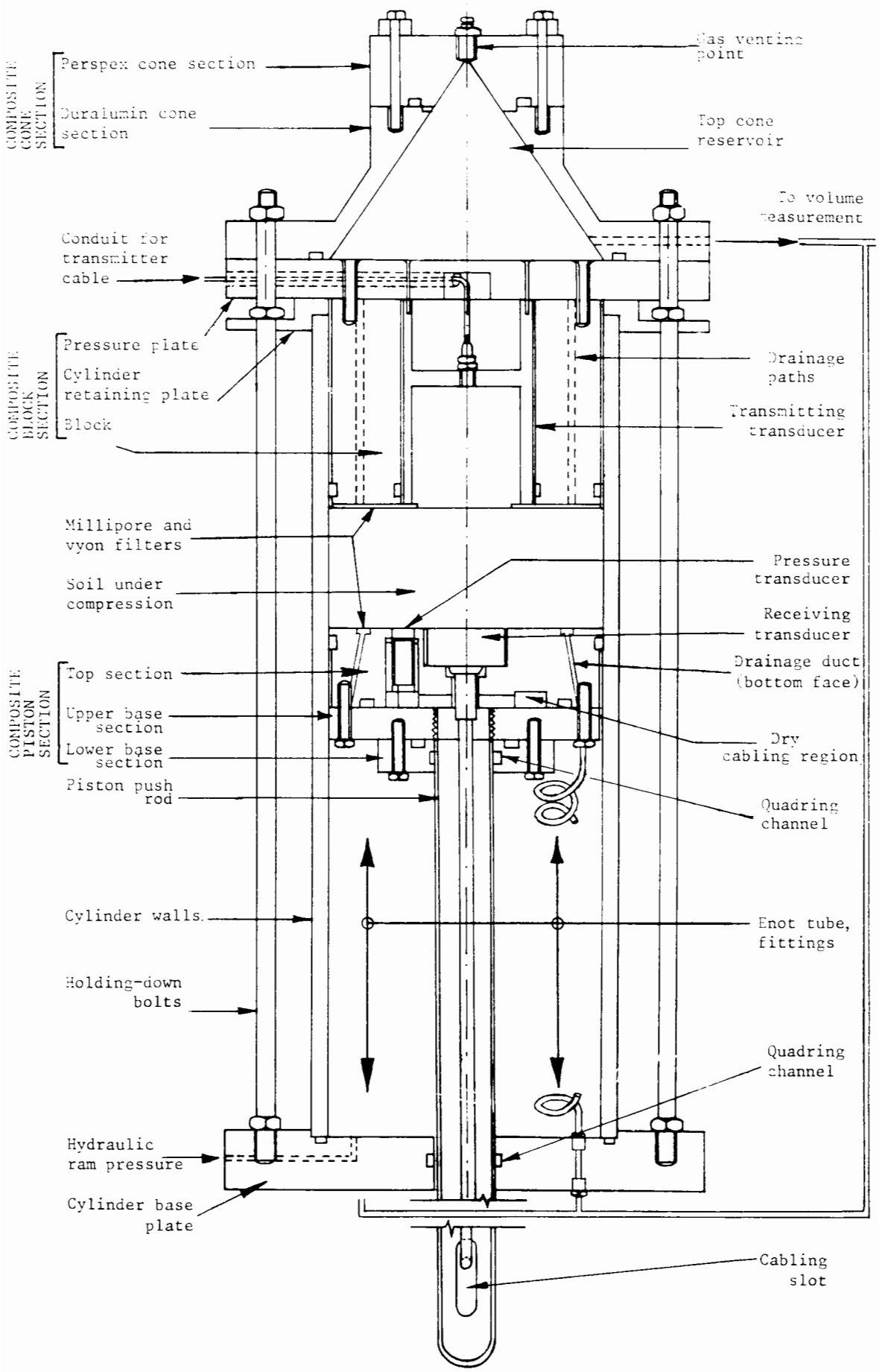


Figure 2.1(a) - Outline diagram of cell 2

Figure 2.1(b) - The acoustic consolidation cell (Cell 2)



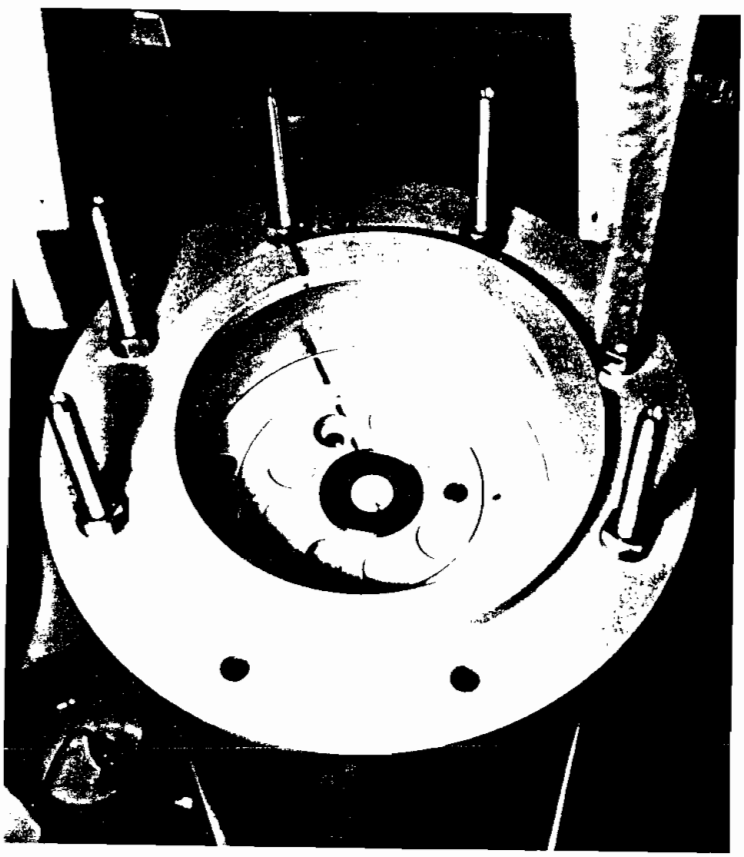


Figure 2.2 -View of piston top face (down cylinder)-Cell 2

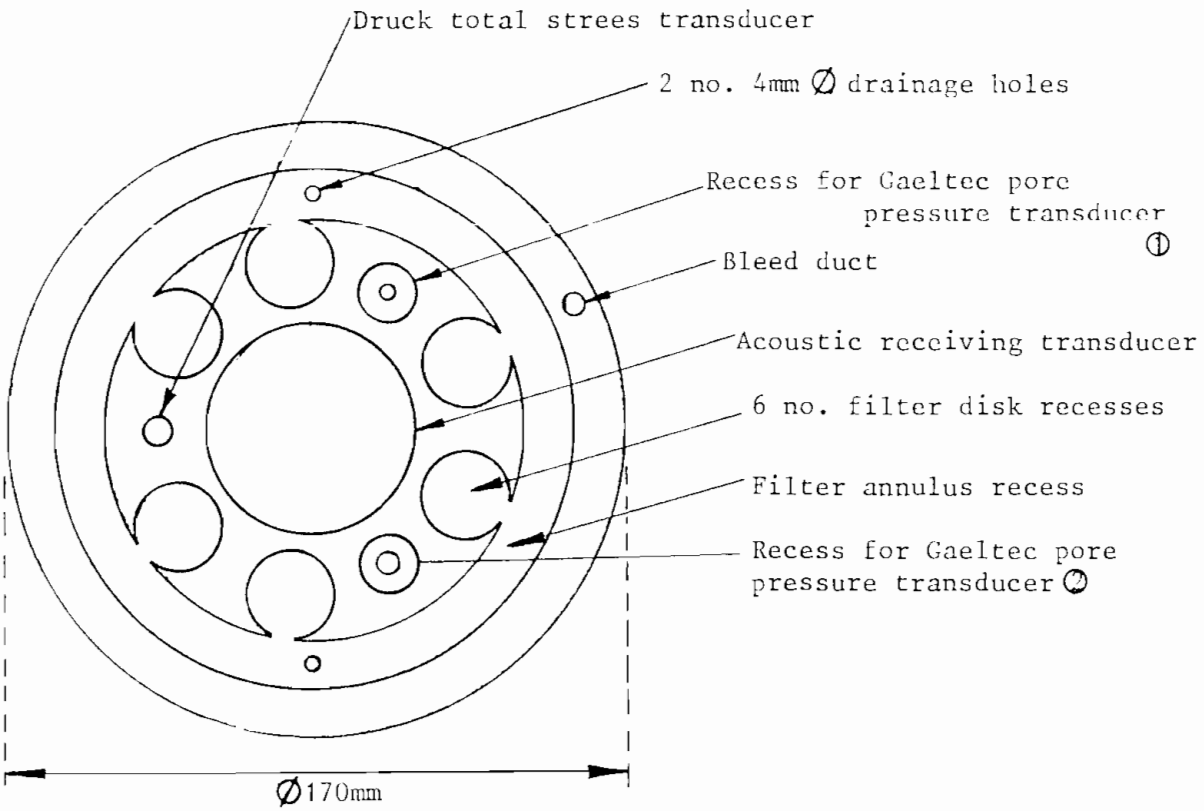
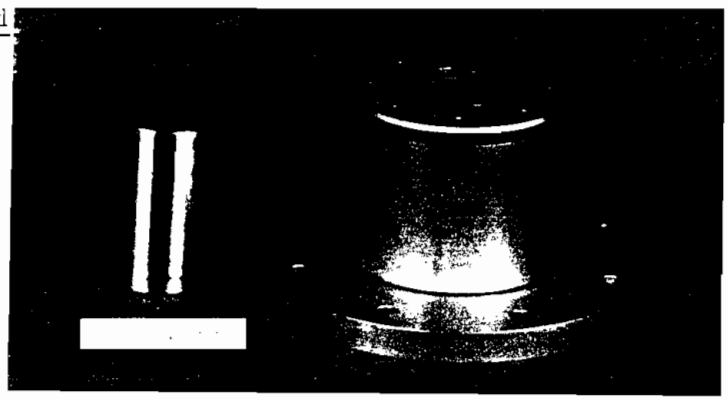


Figure 2.3 - Piston face (Cell 2 only)

Figure 2.4-Top plate and transmitting transducer



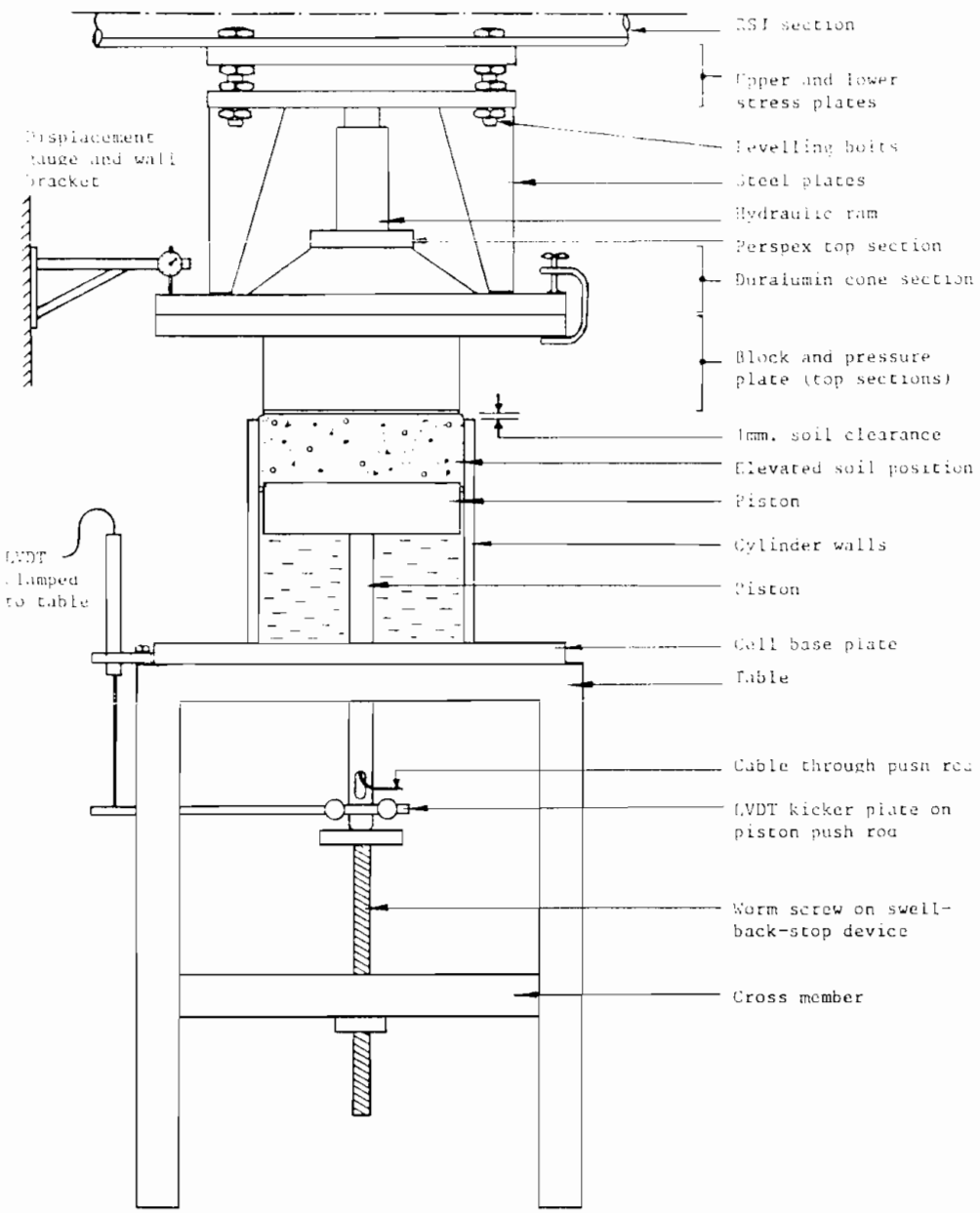


Figure 2.5(a)-Elevation to the reaction plate assembly

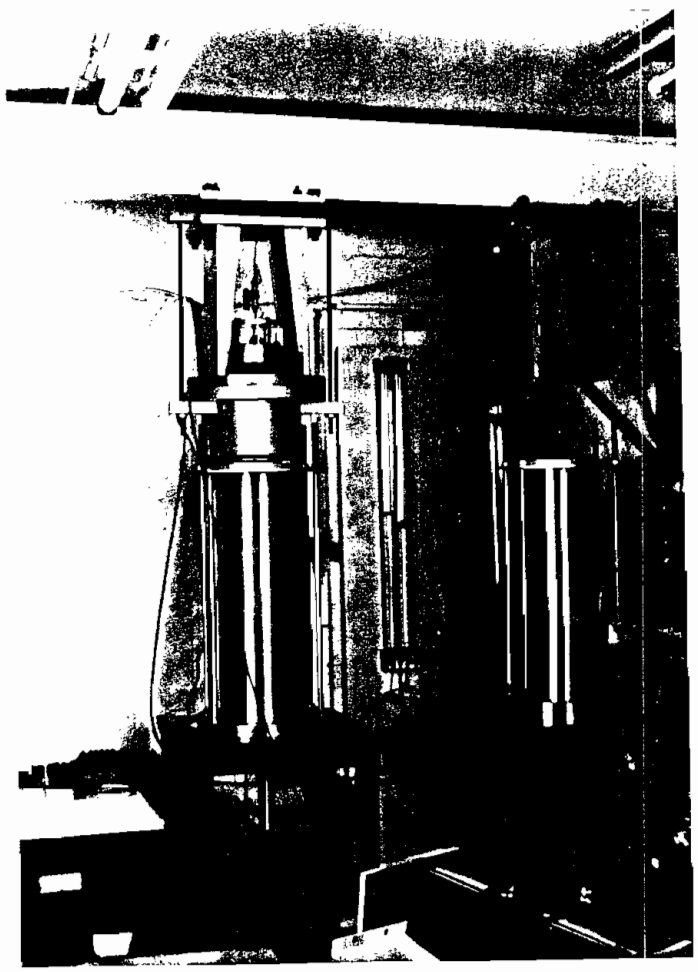


Figure 2.5(b)-The acoustic cell and sling device

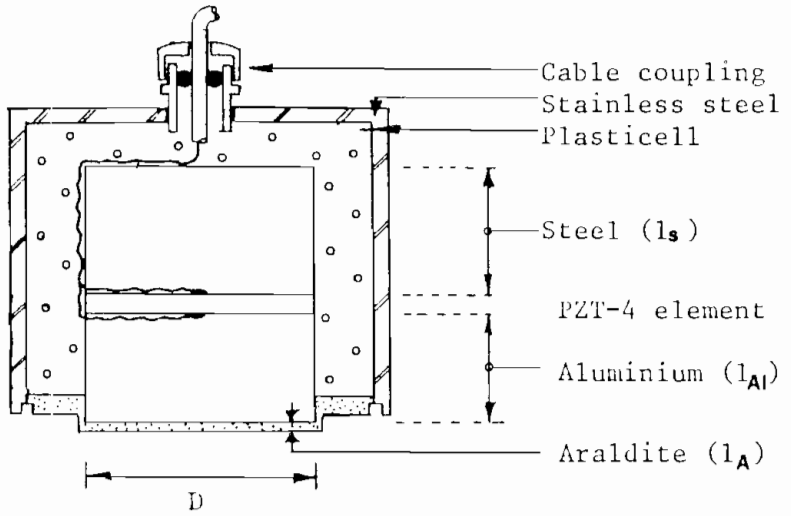


Figure 2.6(i) - Transmitting transducer

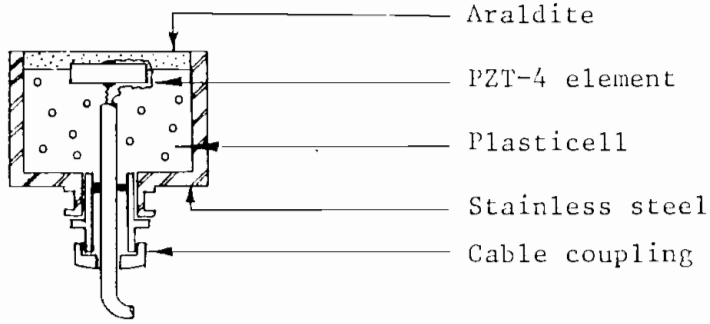


Figure 2.6(ii) -Receiving transducer

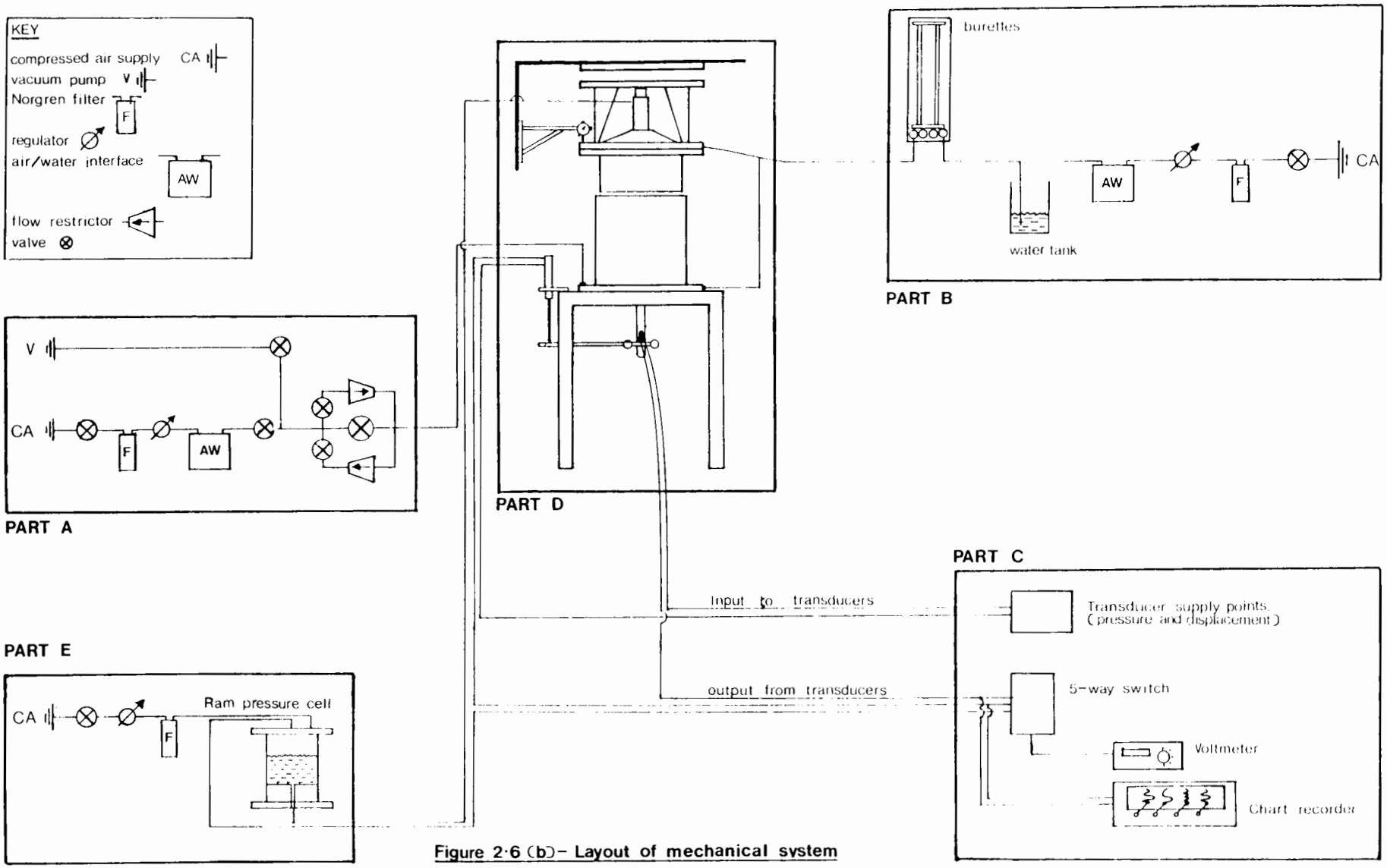


Figure 2·6 (b) – Layout of mechanical system

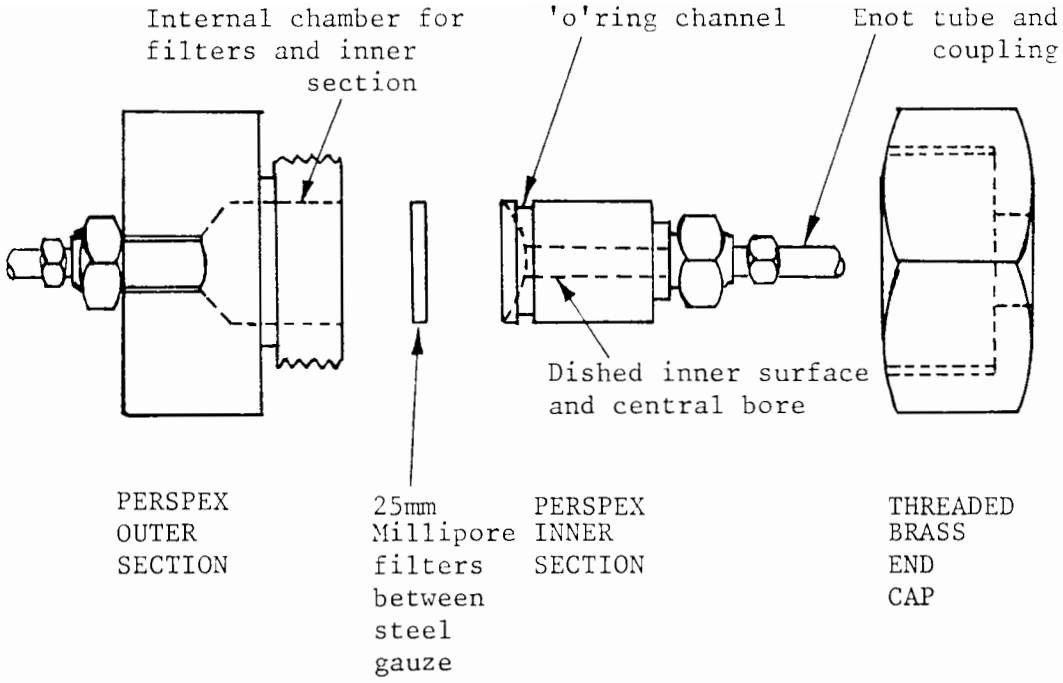


Figure 2.7(a) - Flow restrictor device

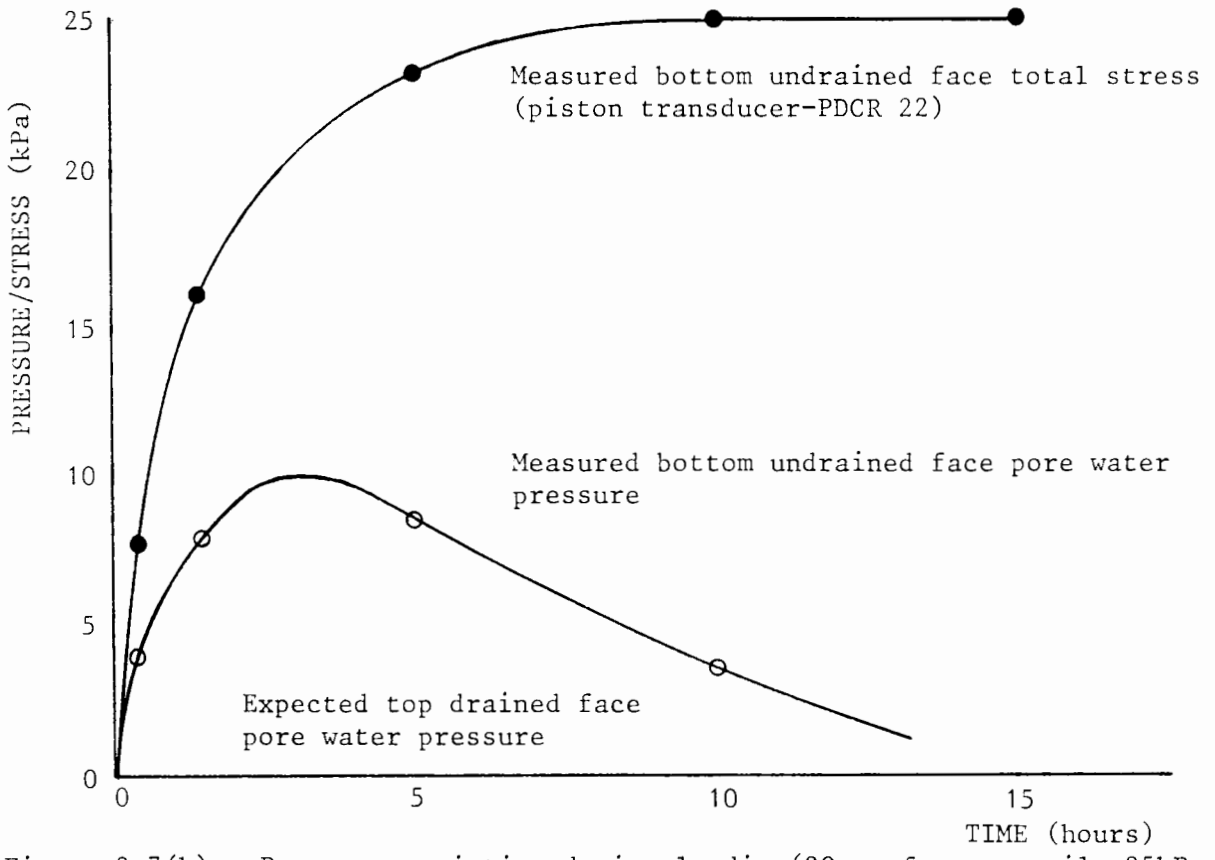
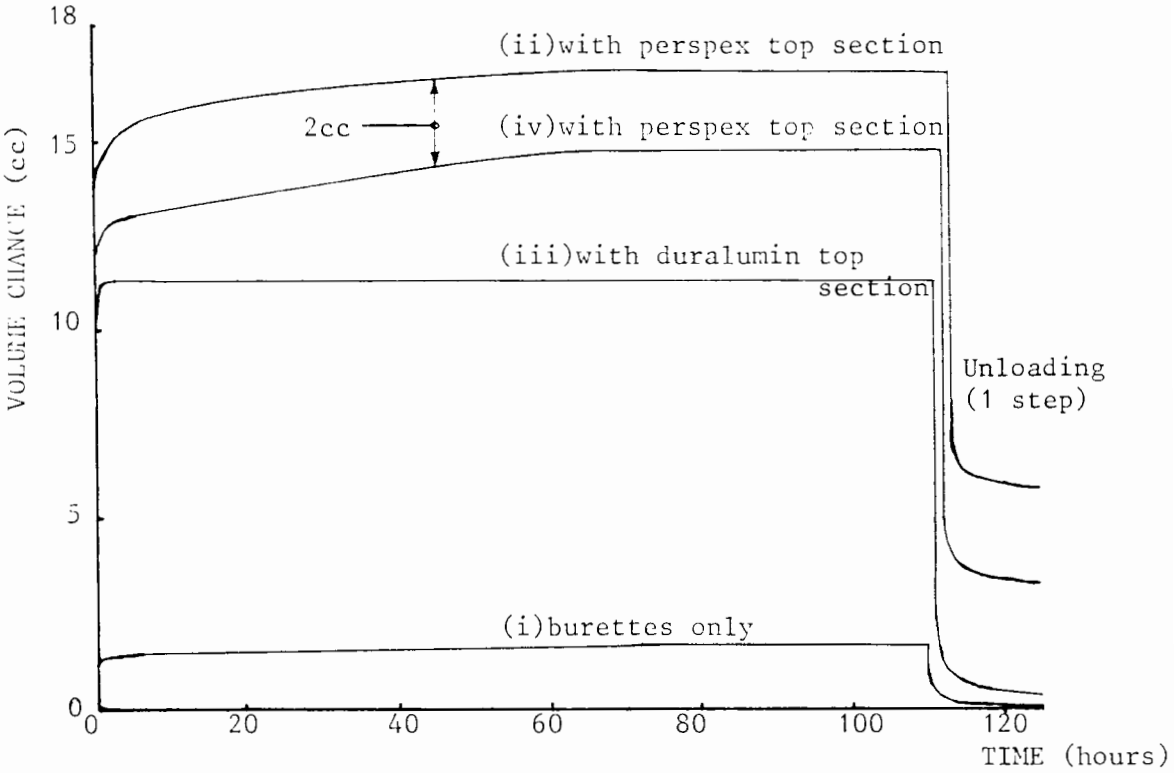
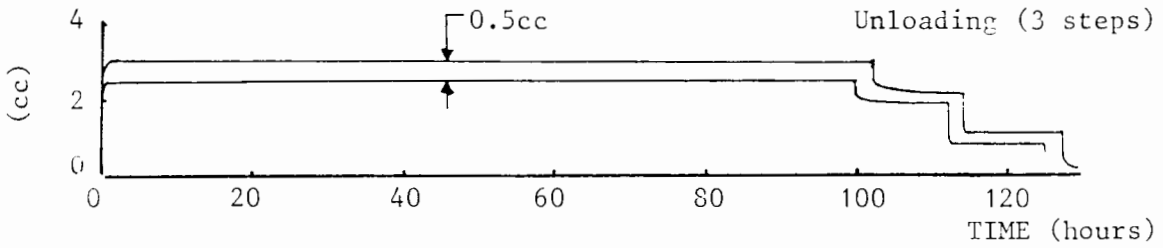


Figure 2.7(b) - Pressure variation during loading(20mm of gassy soil; 25kPa consolidation stress; Cell 1 only; below piston flow restrictor, fitted with 36 no. Millipore filters of 0.025μm pore size.)

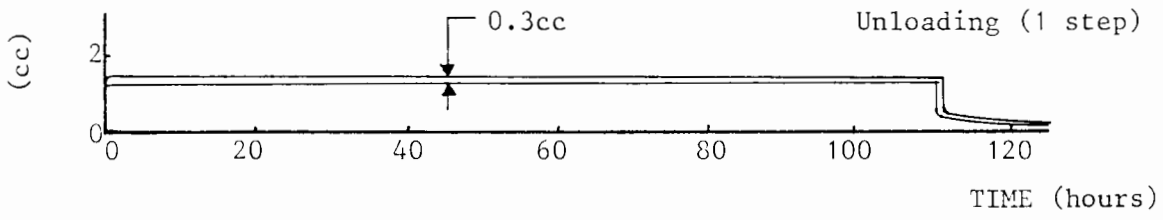
Figure 2.8-Volume change of cells and burettes



(a) Cell 1 and burettes at 500kPa (Tests TNG 15V,VI,VII)



(b) Cell 1 only at 100kPa -Repeatability with duralumin top section (Test TNG 15VIII)



(c) Cell 2 only, at 25kPa -Repeatability with duralumin top section(Test TNG 46)

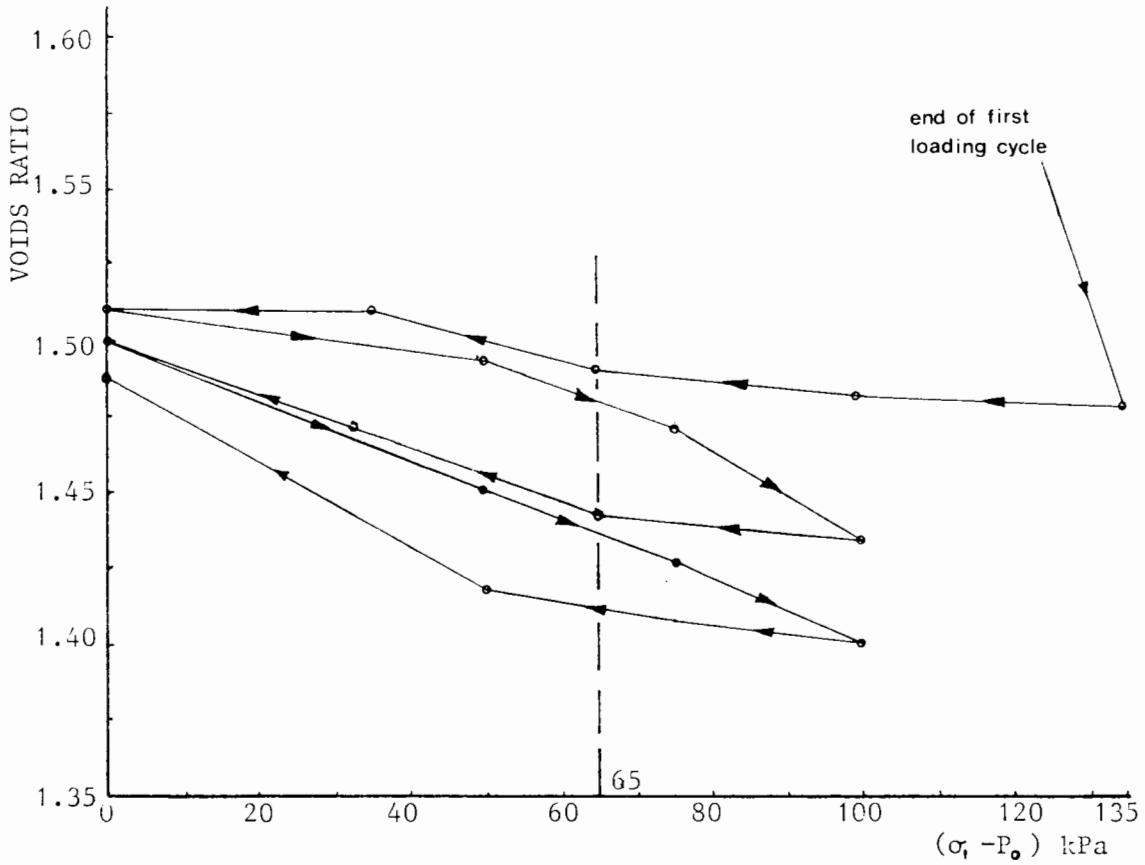
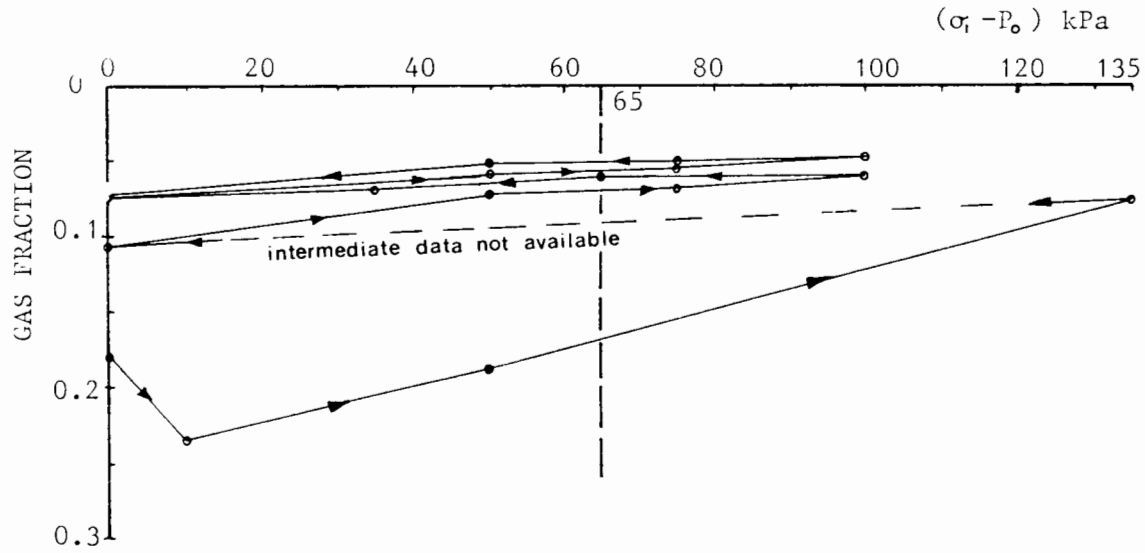


Figure 2.9-Cyclic loading tests (Test TNG 18B,C)

(a)Voids ratio versus load



(b) Gas fraction versus load

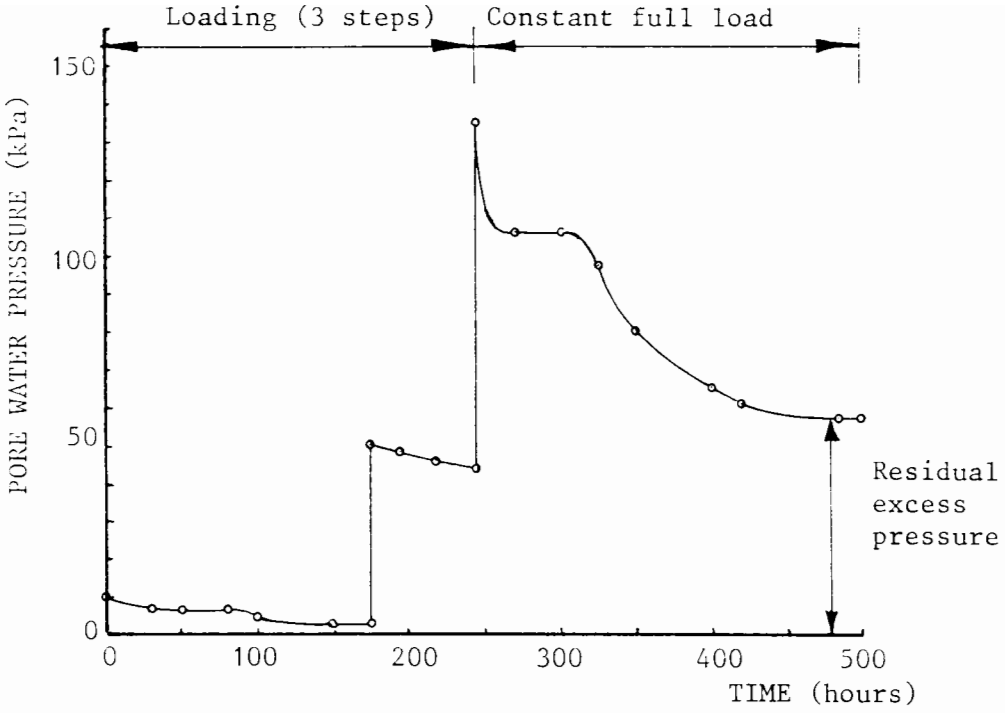


Figure 2.10-Pore water pressure versus time (Test TNG 18B)

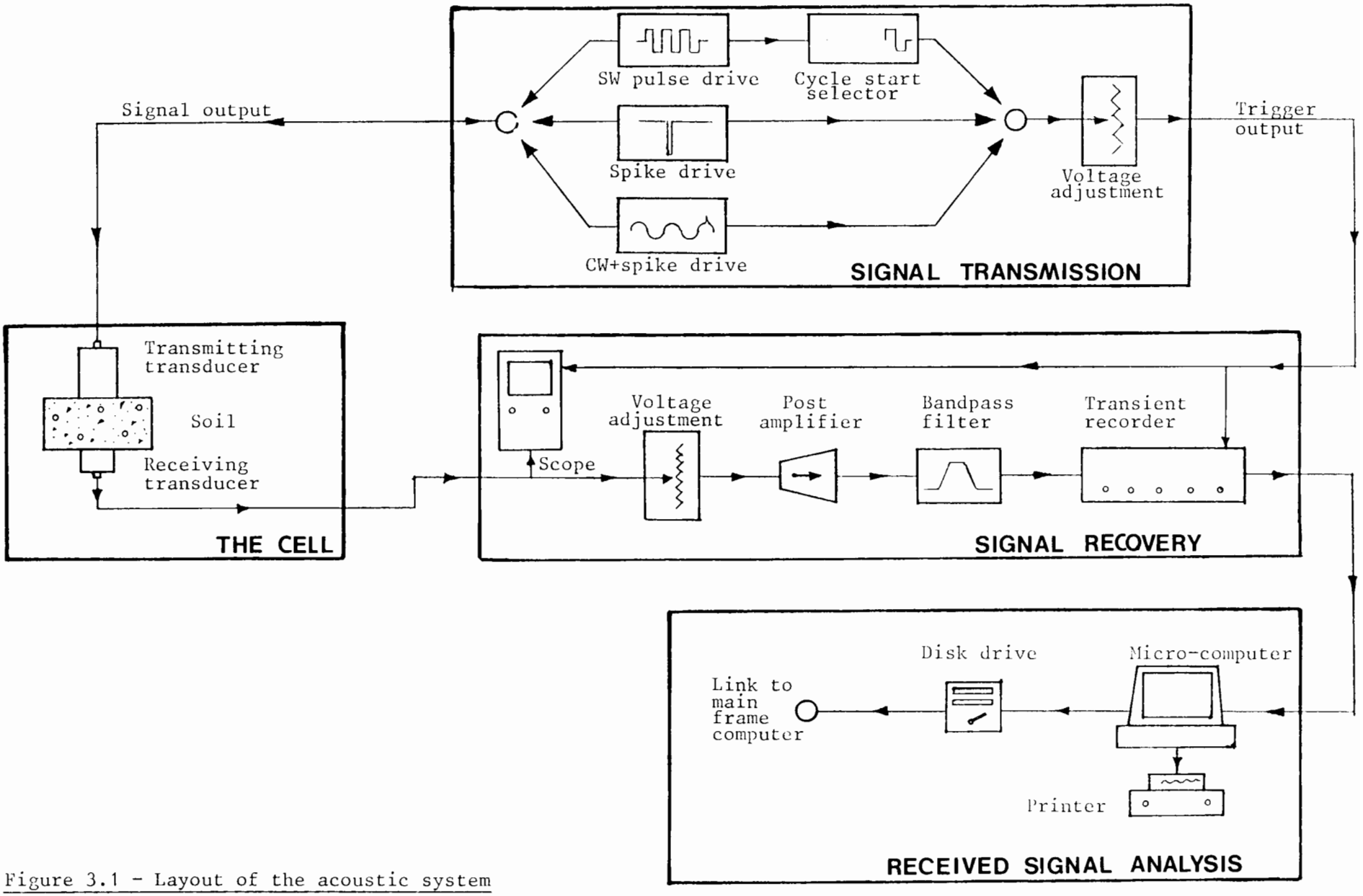
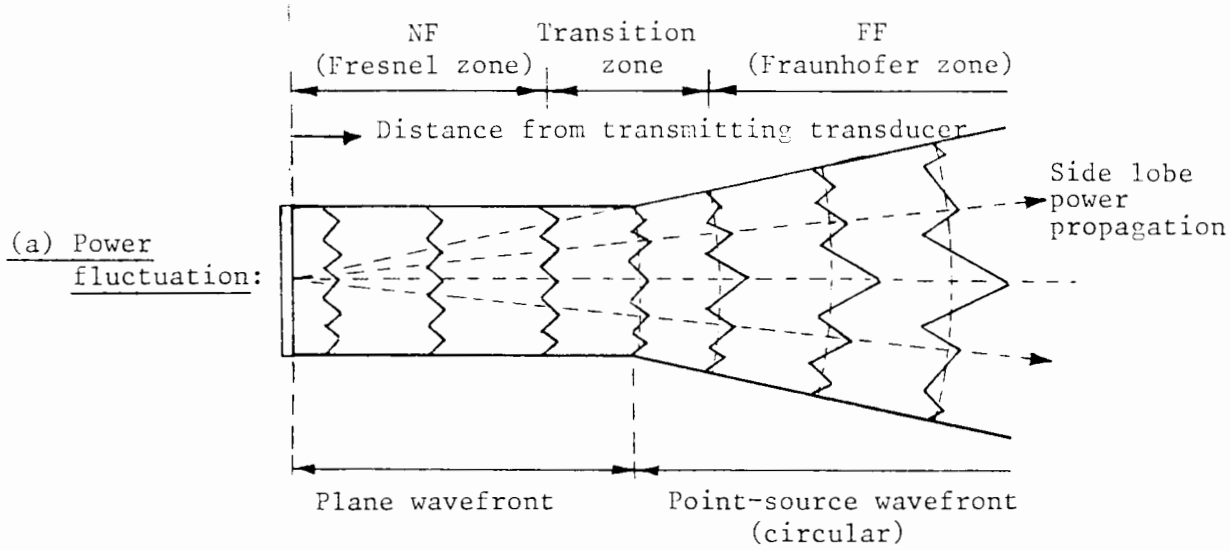
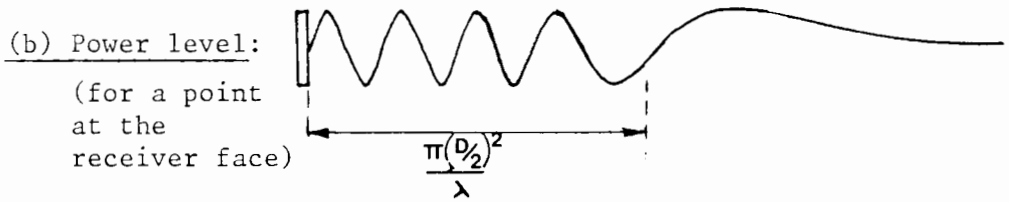


Figure 3.1 - Layout of the acoustic system

Figure 3.2 - Near and far field beam patterns of a plane wave source





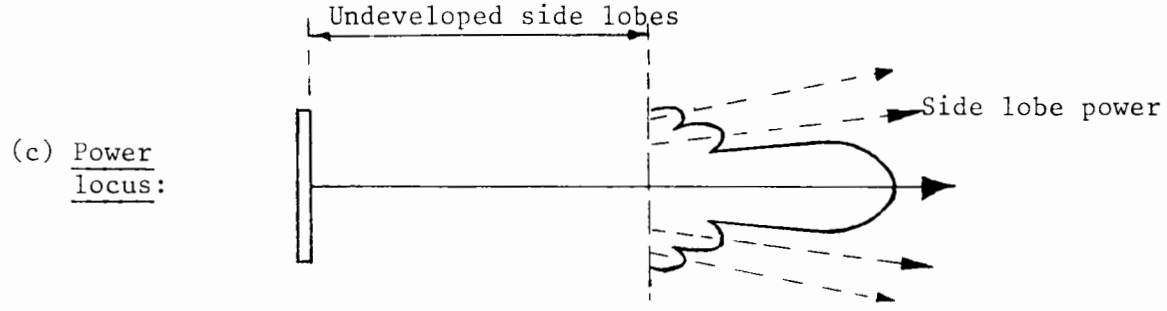
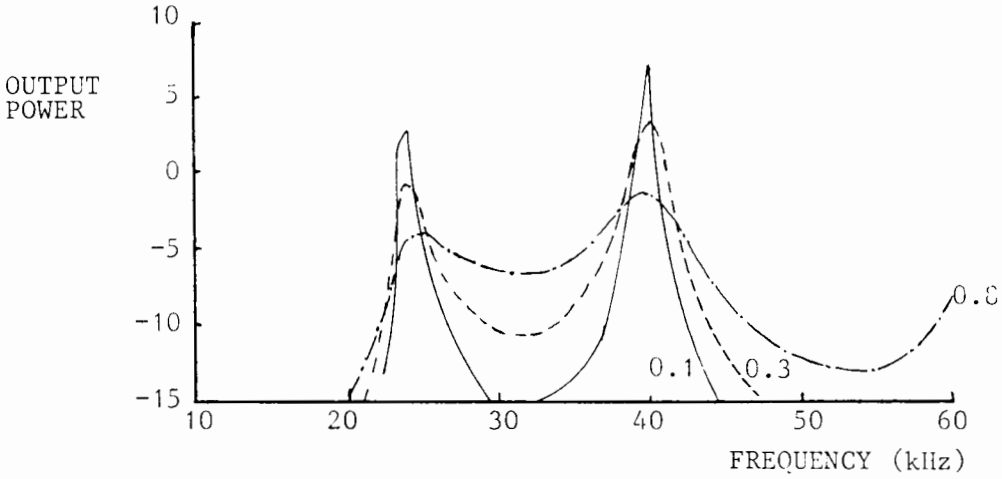
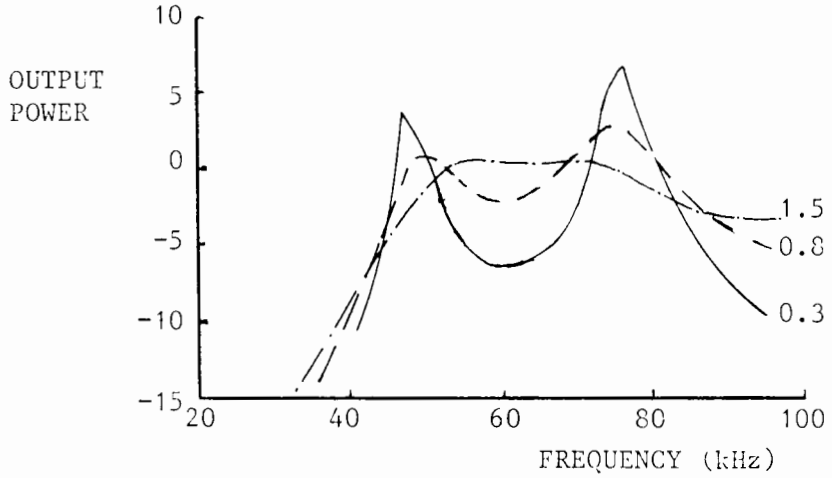


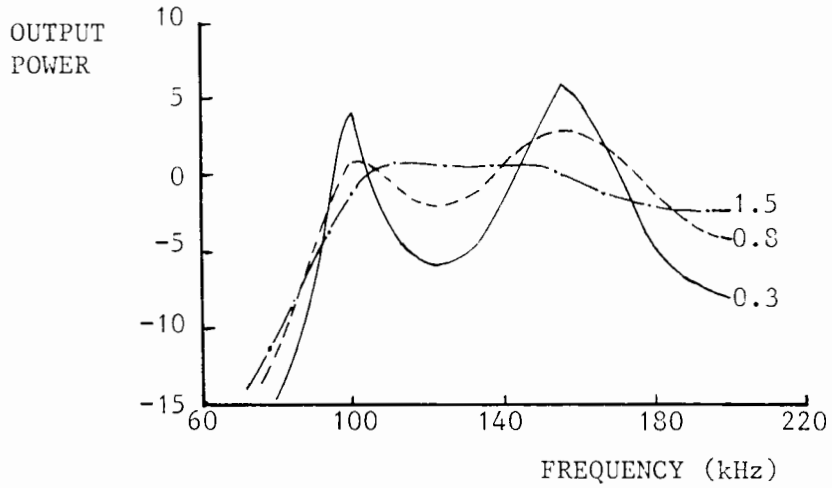
Figure 3.3 - Transducer output power versus frequency.
Note 1-Units of output power are 1dB re 1 watt per $(100\text{volts})^2$ input.
Note 2-Each curve represents a particular acoustic impedance (Units are 10 kg/m^2s).



(a) Transducer (20-40)kHz



(b) Transducer (40-95)kHz



(c) Transducer (95-200) kHz

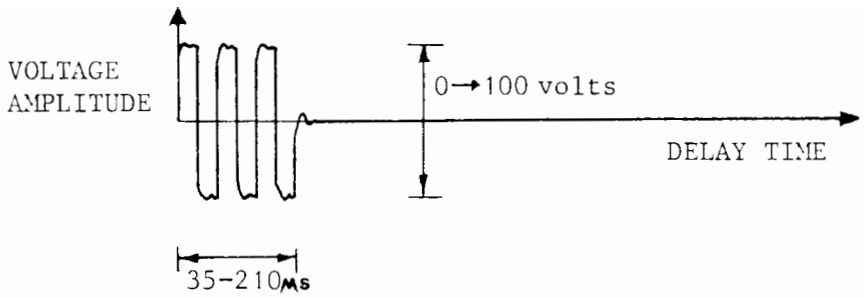


Figure 3.4(a)Diagram showing the typical SW pulse input to the transducer (100 kHz; transducer under load)

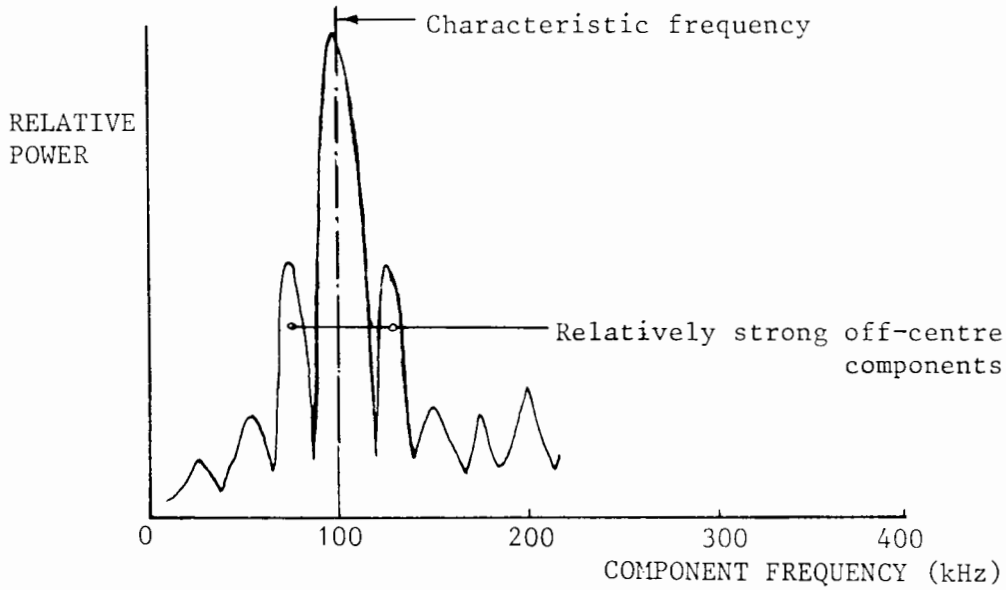


Figure 3.4(b) -Diagram representing the typical relative strength of off-centre frequency components in a spectrum of the signal propagating from a transmitting transducer (100kHz)

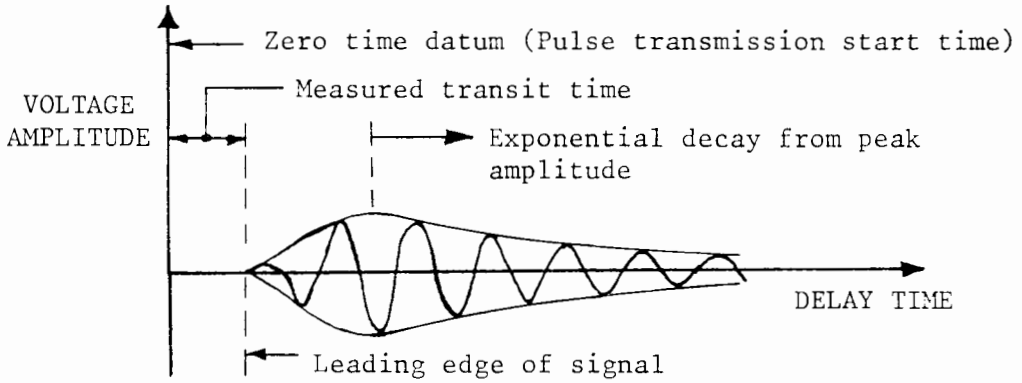


Figure 3.4(c) - Diagram showing typical received signal waveform through a non-dispersive liquid (100kHz; No reflection or beat frequency interference)

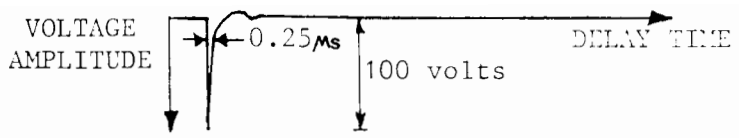


Figure 3.5(a) - Waveform of the spike signal (Unloaded output of power drive module)

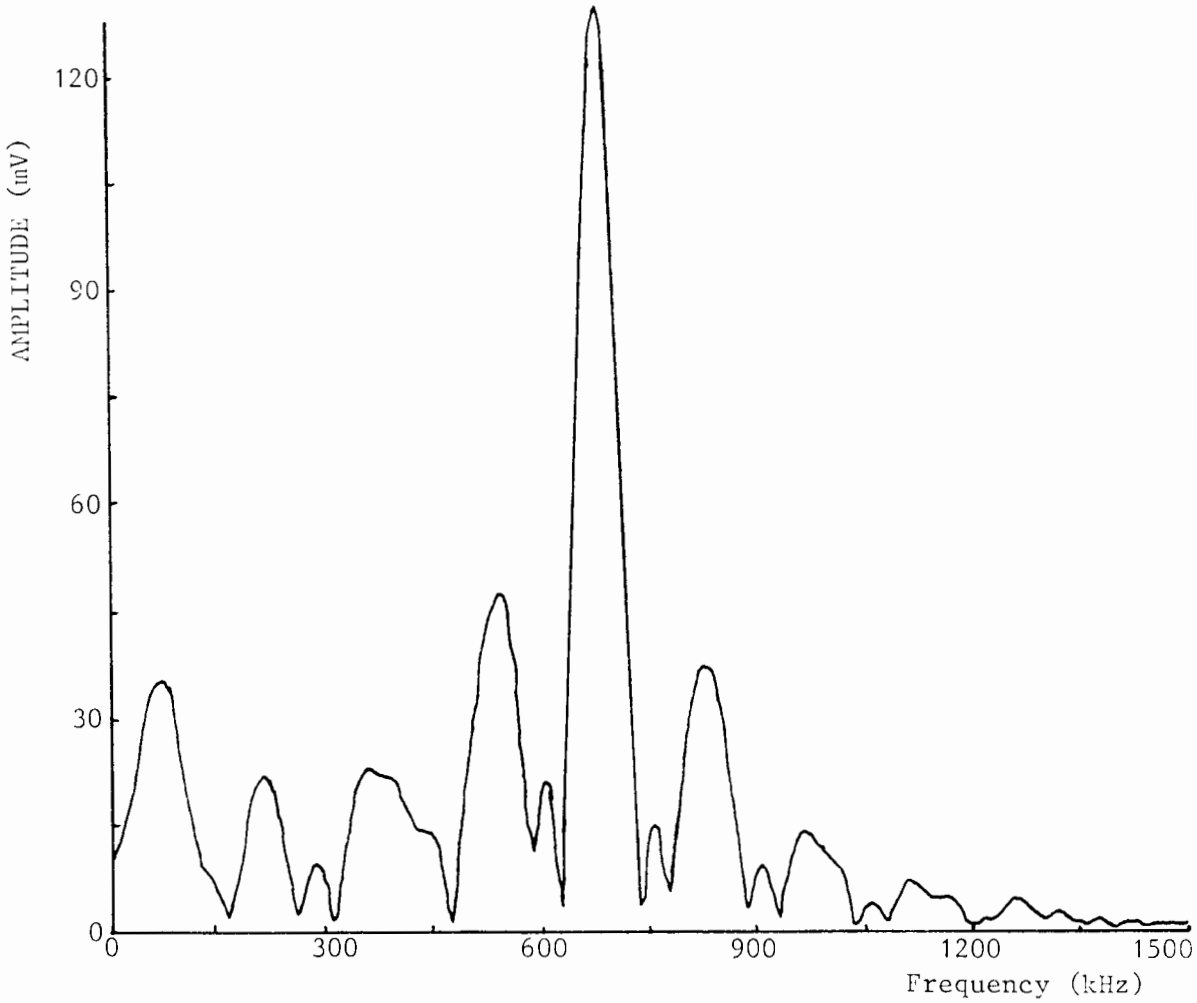


Figure 3.5(b) - Frequency spectrum-spike signal input to receiver (glycerol; Cell 1;Test TNG 51(C2011).)

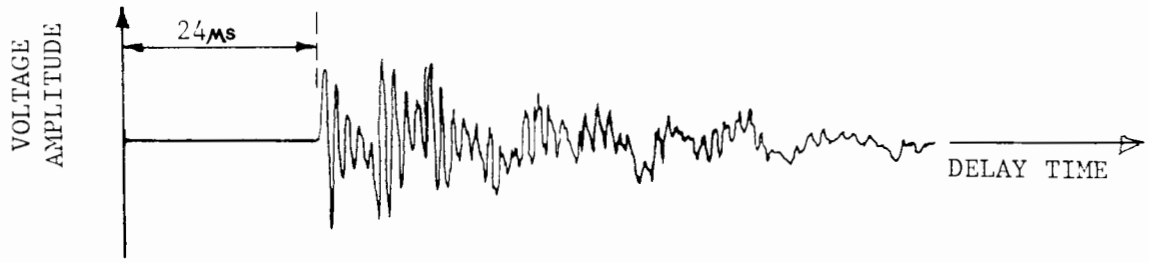


Figure 3.5(c) - Received signal waveform of spike (Spectrum as 3.5(b))

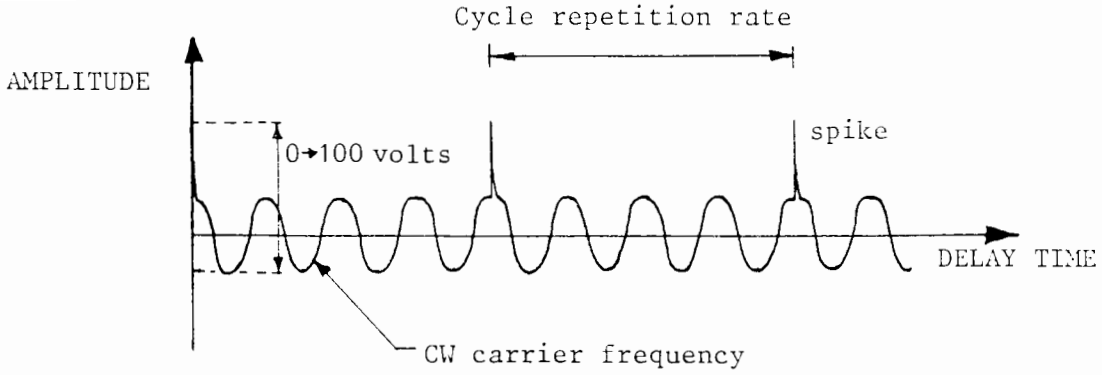


Figure 3.6 - Waveform of CW plus spike signal (Unloaded output of power drive module

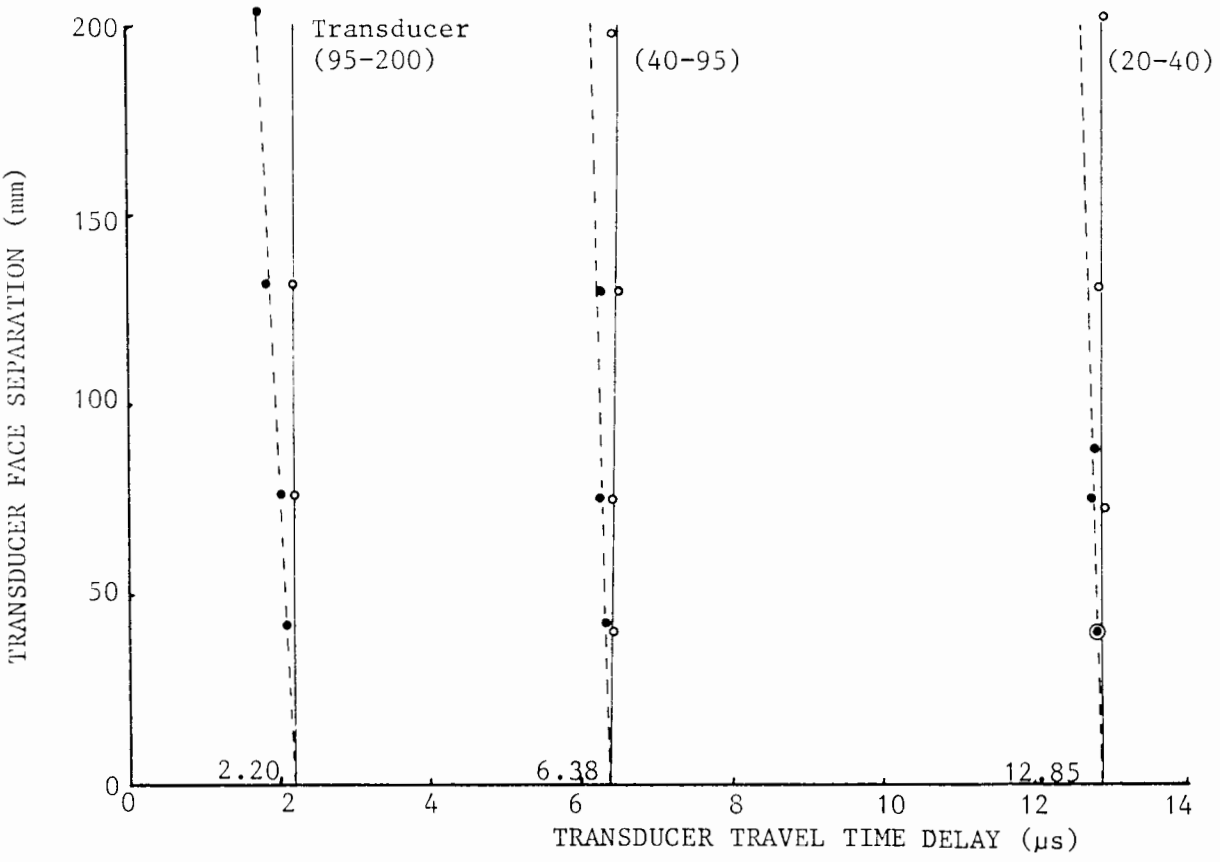


Figure 3.7 - Transducer travel time delays (Test TNG 17C)

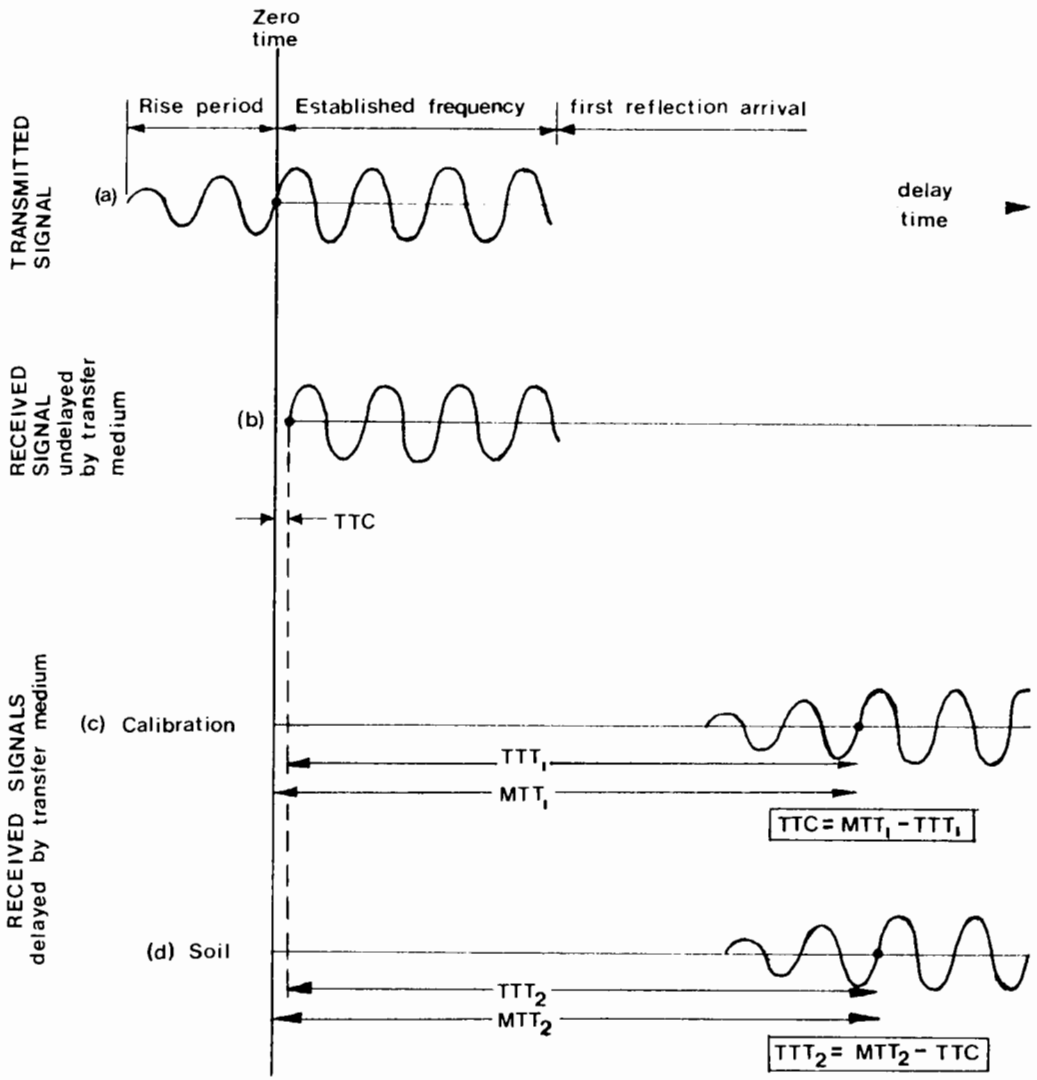
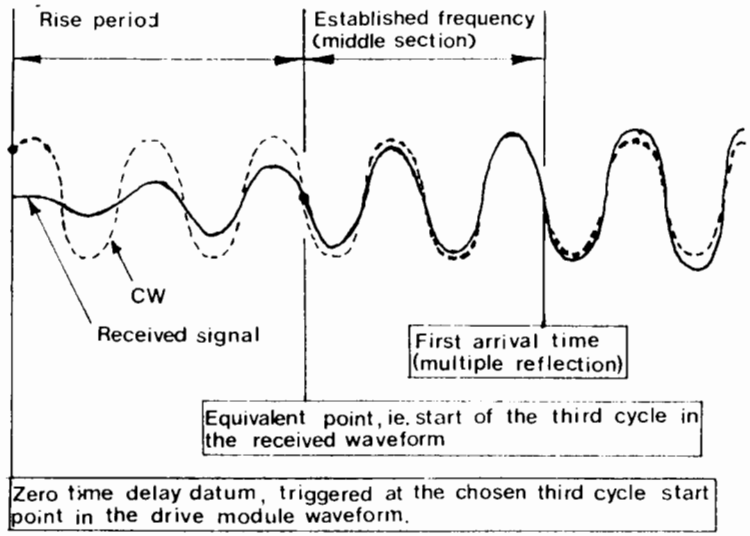


Figure 3·8(a,b,c,d) – The transit time correction system



2no. CW cycles + part cycle (181°).
Total delay, at 15·63 μs per cycle = 39·12 μs
Hence: MTT = 39·12 μs

Example sound speed calculation:

TTC at 64 kHz, from Table 3·5(a) = 11·97 μs
TTT from equation 3·3 = 27·15 μs
Hence, for a soil depth of 20·272 mm,
sound speed = 746·67 m/s

Figure 3·8(e)-Example CW curve fitting to obtain MTT (Test TNG 51(W), 64 kHz, trigger at start of cycle 3)

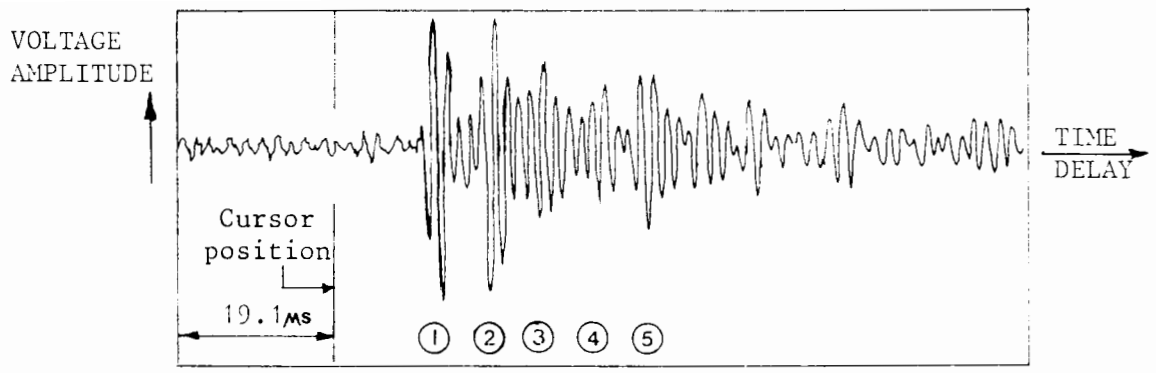
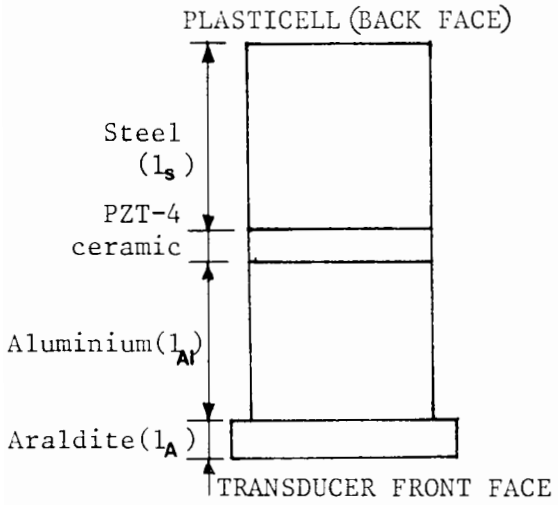


Figure 3.9(a) - Multiple reflections in the received signal waveform (Cell 1)



Aluminium:
l_{Al} = 2.04cm
t_{Al} = 4.0ms
at 5150m/s
$2t_{Al}$ = 8.0ms

Araldite:
l_A = 0.95cm
t_A = 4.7ms
at 2041m/s
$2(t_A + t_{Al}) =$
15.8ms

Steel:
l_s = 1.76cm
t_s = 3.35ms
at 5250m/s
$2t_s$ = 6.7ms

where:
t_{Al}, t_A, t_S = transit times in the three materials

Figure 3.9(b) - Multiple reflections within the body of the transmitting transducer (Cell 1)

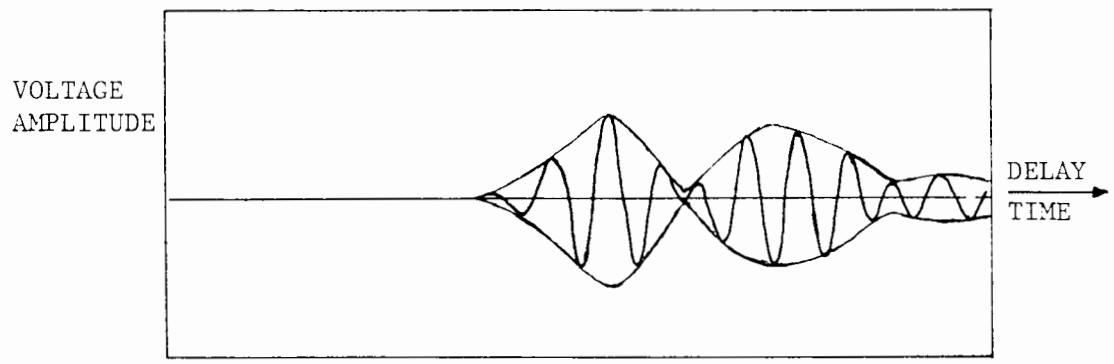
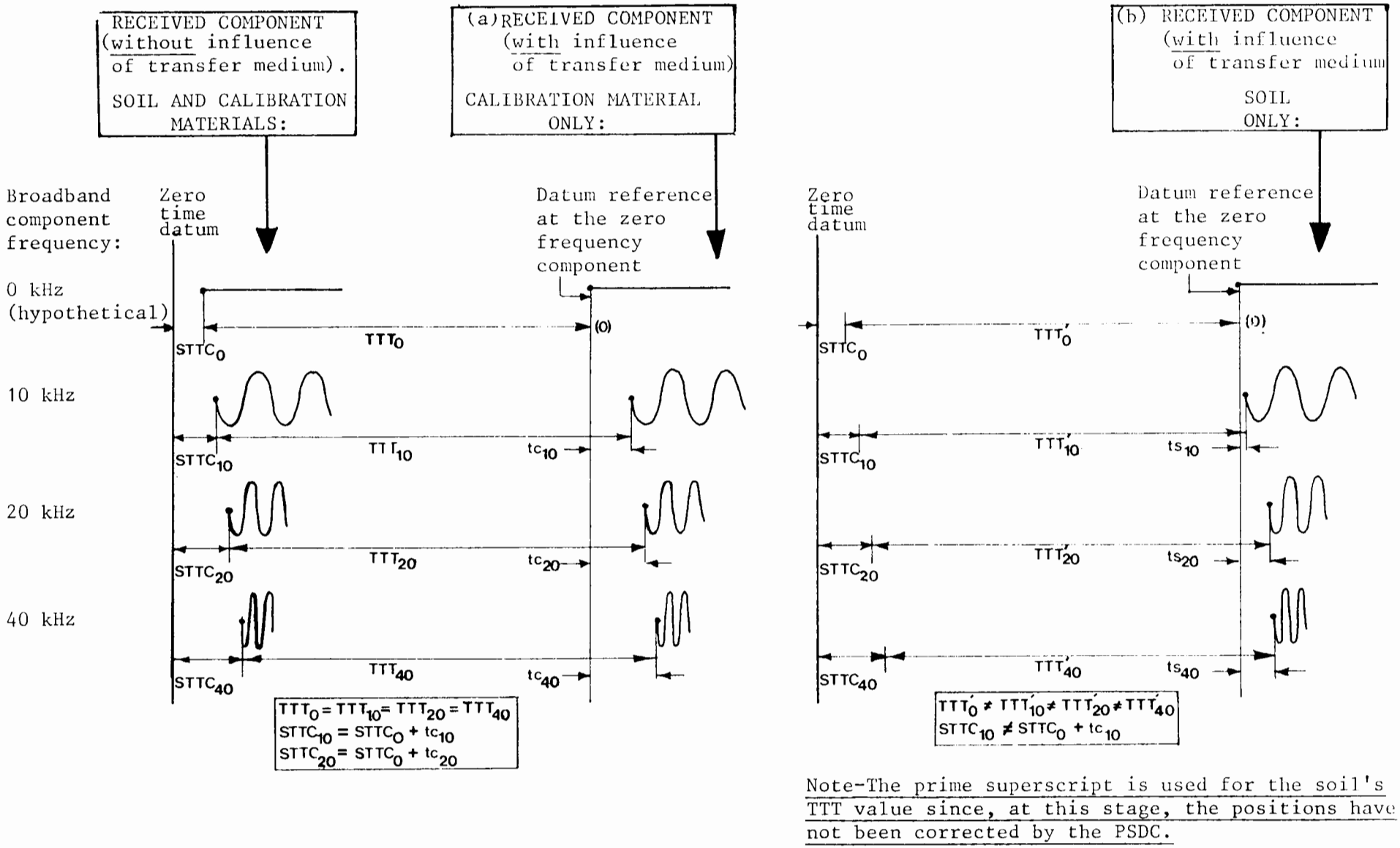
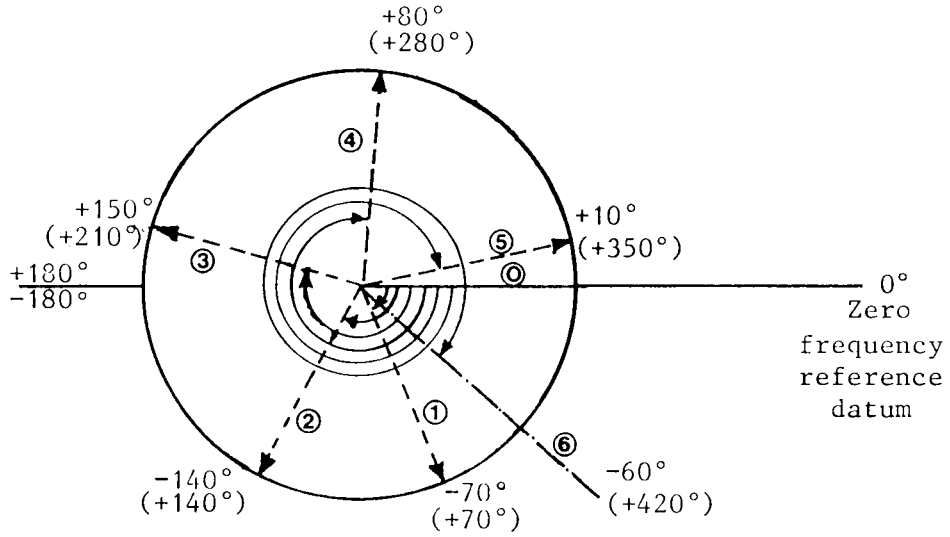


Figure 3.9(c) - Example of a beat waveform (38kHz transmitted; 30kHz received; 7.5kHz beat; Test TNG 52(W2); Cell 2; gassy soil)



Note-The prime superscript is used for the soil's TTT value since, at this stage, the positions have not been corrected by the PSDC.

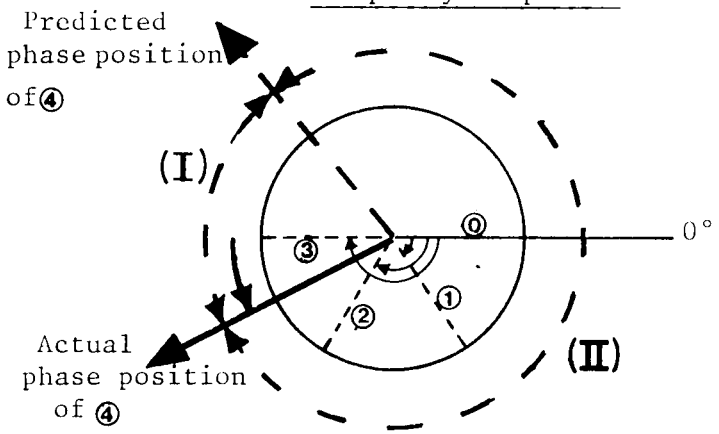
Figure 3.10 - Phase position displacement from datum - FT Method



No. of frequency components	Phase angles (equation 3.4)	Cumulative phase displacement
0	0°	Degc ⓪ = 0°
1	-70°	Degc ① =+70°
2	-140°	Degc ② =+140°
3	+150°	Degc ③ =+210°
4	+80°	Degc ④ =+280°
5	+10°	Degc ⑤ =+350°
6	-60°	Degc ⑥ =+420°

Figure 3.11(a) - Phase rotation diagram for cumulative phase displacement.

Figure 3.11(b) - Reverse rotation of a frequency component



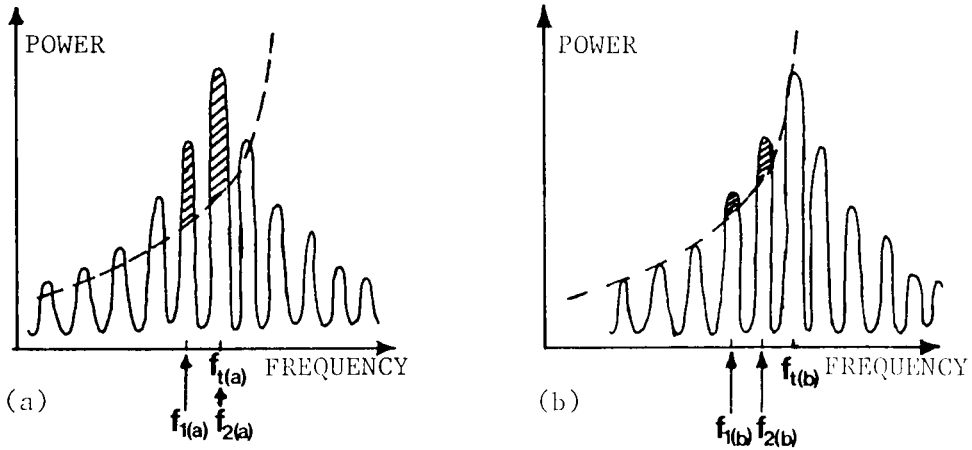
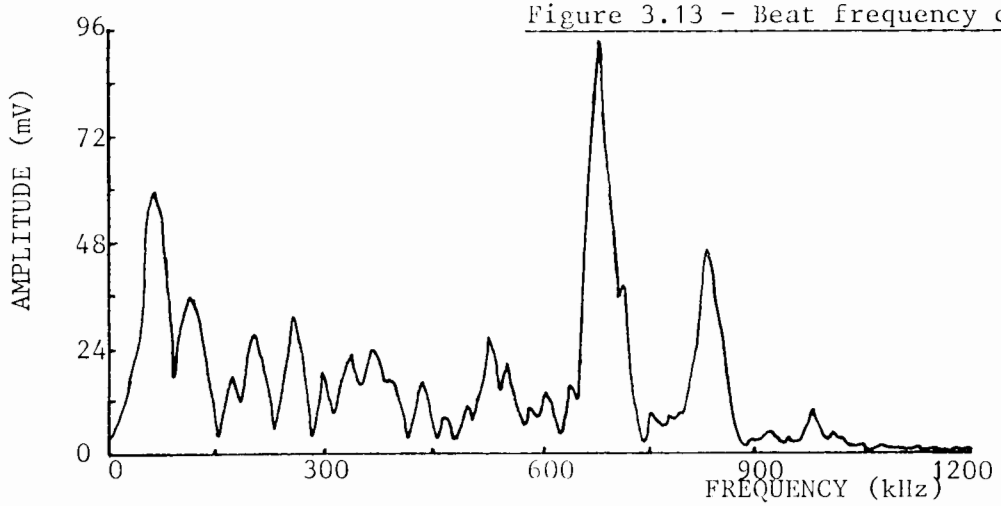
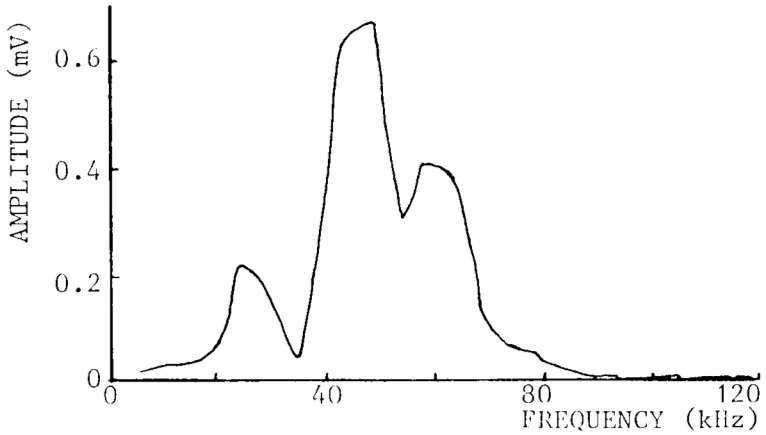


Figure 3.12 - Beat frequency components (Gassy soil)

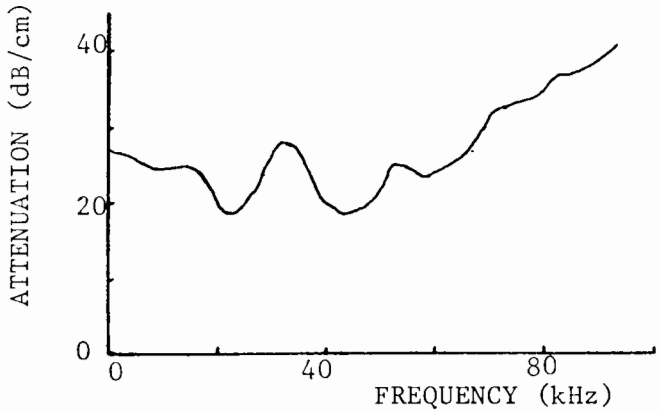
Figure 3.13 - Beat frequency components for a gassy soil



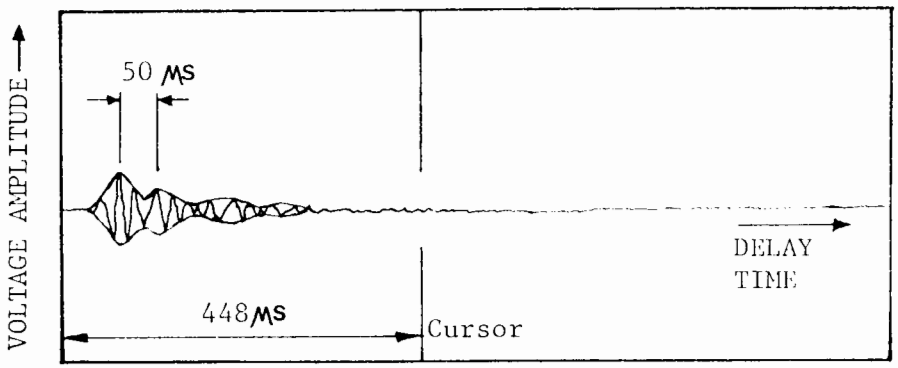
(a) Fourier transform of a wave form received through 20mm of hexane (Spike signal Cell 1; Test TNG 50(C20).)



(b) Fourier transform of waveform received through 20mm of gassy soil(Spike signal; Cell 1;Test TNG 50(S10).)



(c) Attenuation versus frequency from (a) and (b) above (Test TNG 50(S10/C20).)



(d) Received signal (beat) waveform producing the transform in (c) above (Test TNG 50(S10).)

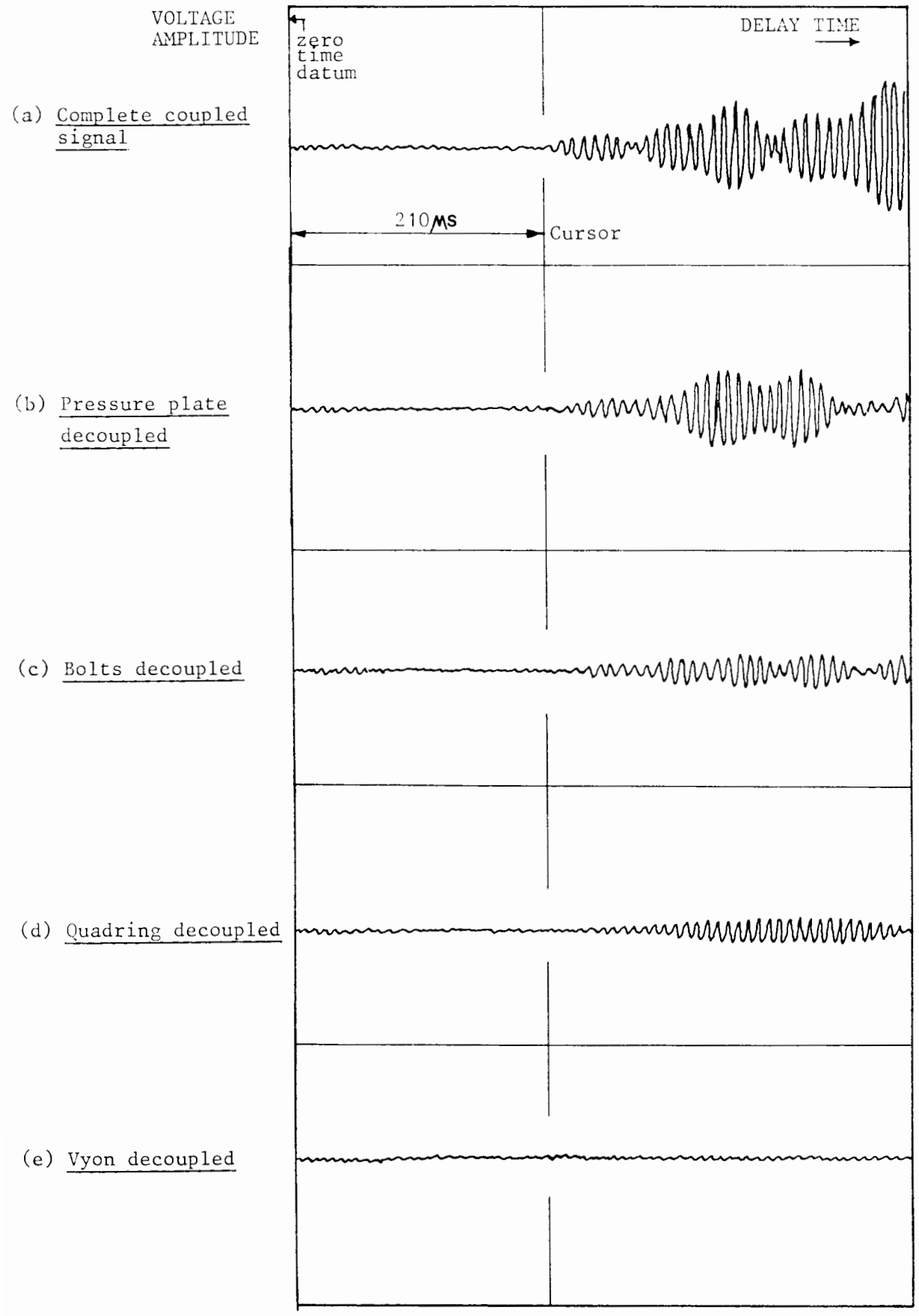


Figure 3.14 - Actual received waveforms during staged decoupling, not using the reaction plate assembly (SWpulse transmission; 110kHz;69mm of gassy soil; 80% degree of saturation; 15kPa consolidation stress; Test TNG 29.)

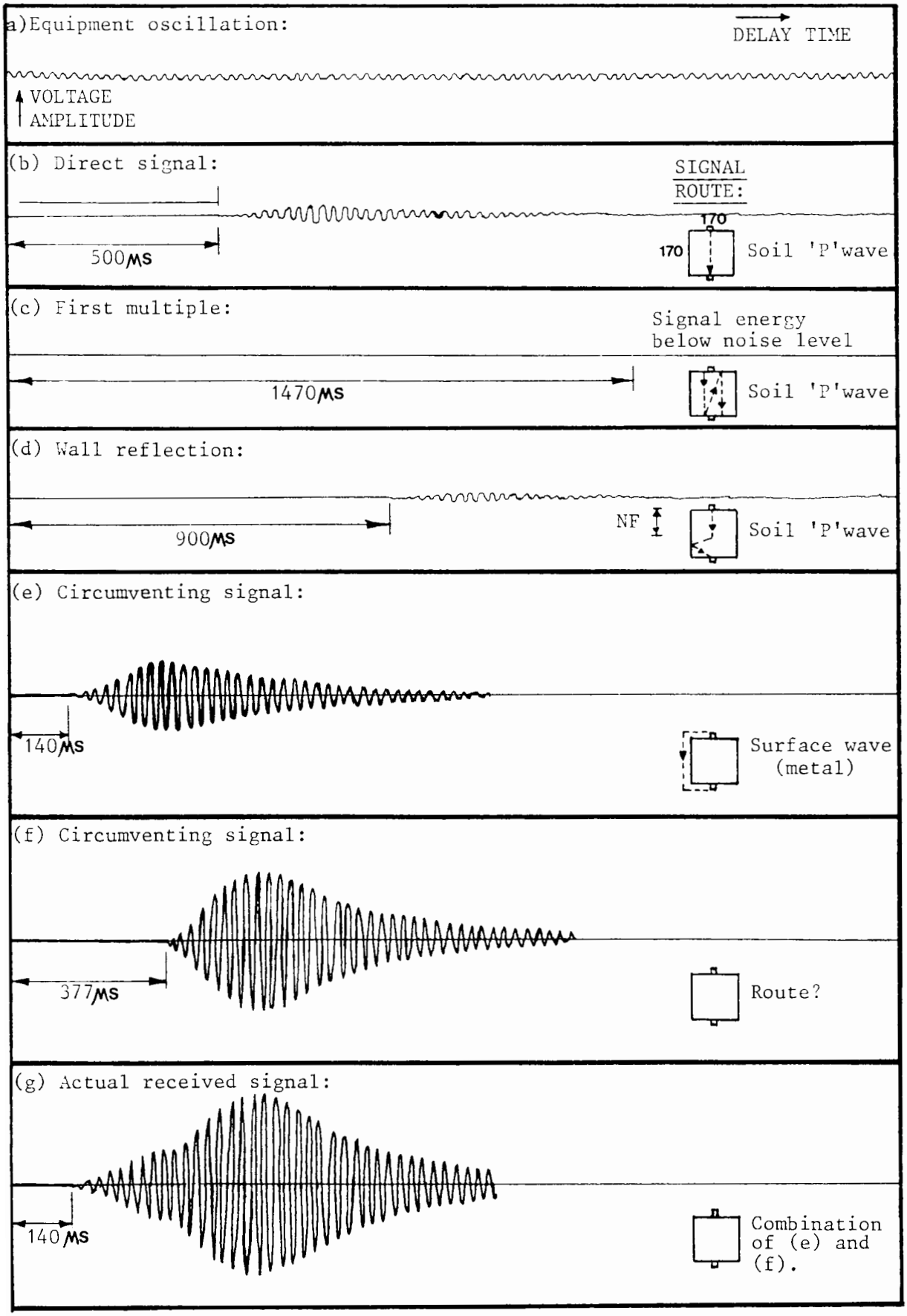
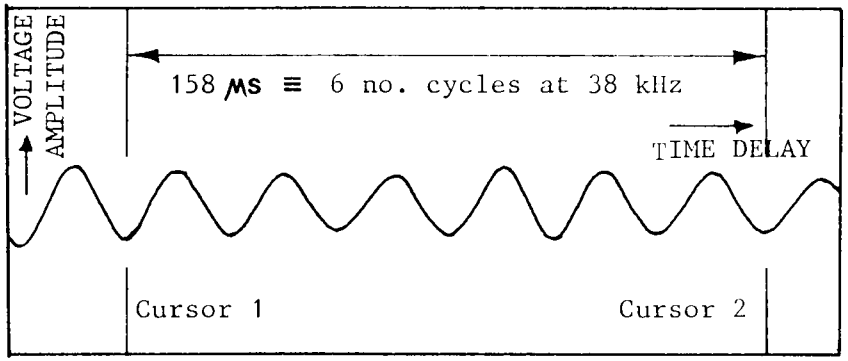
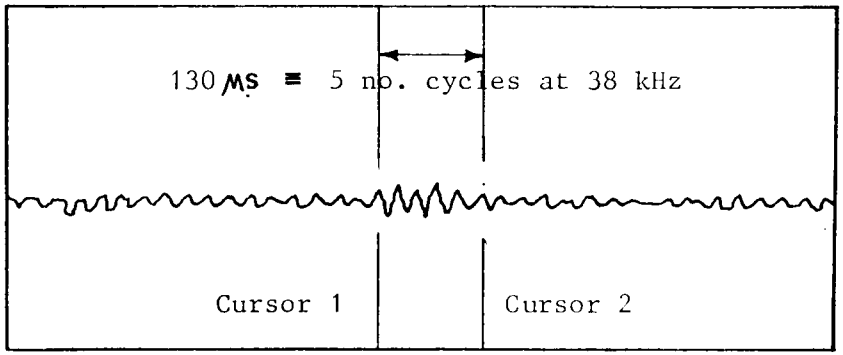


Figure 3.15 - Contributions to the collective signal at the receiver (SW pulse transmission; 38kHz; 170mm of gassy soil; 80% degree of saturation; 25kPa consolidation stress; Test TNG 36.

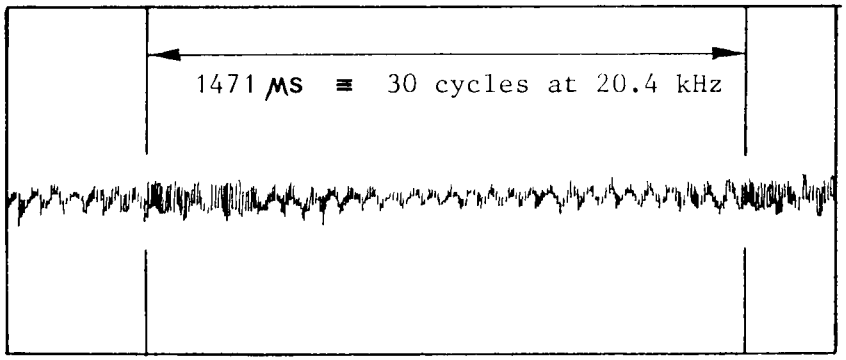


(a) 60 volt CW signal (Scale 0.2 μs /bit)

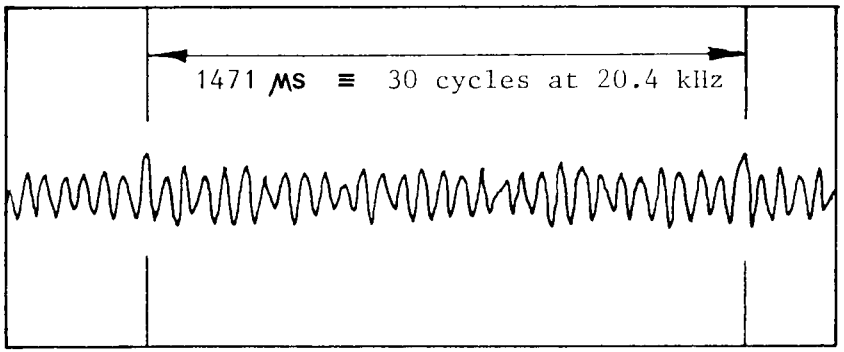


(b) 60 volt SW pulse signal (Scale 0.1 μs /bit)

Figure 3.16 - Relative penetration of signal types (38kHz; 138mm of gassy soil; 80% degree of saturation; 25kPa consolidation stress; Test TNG 36)

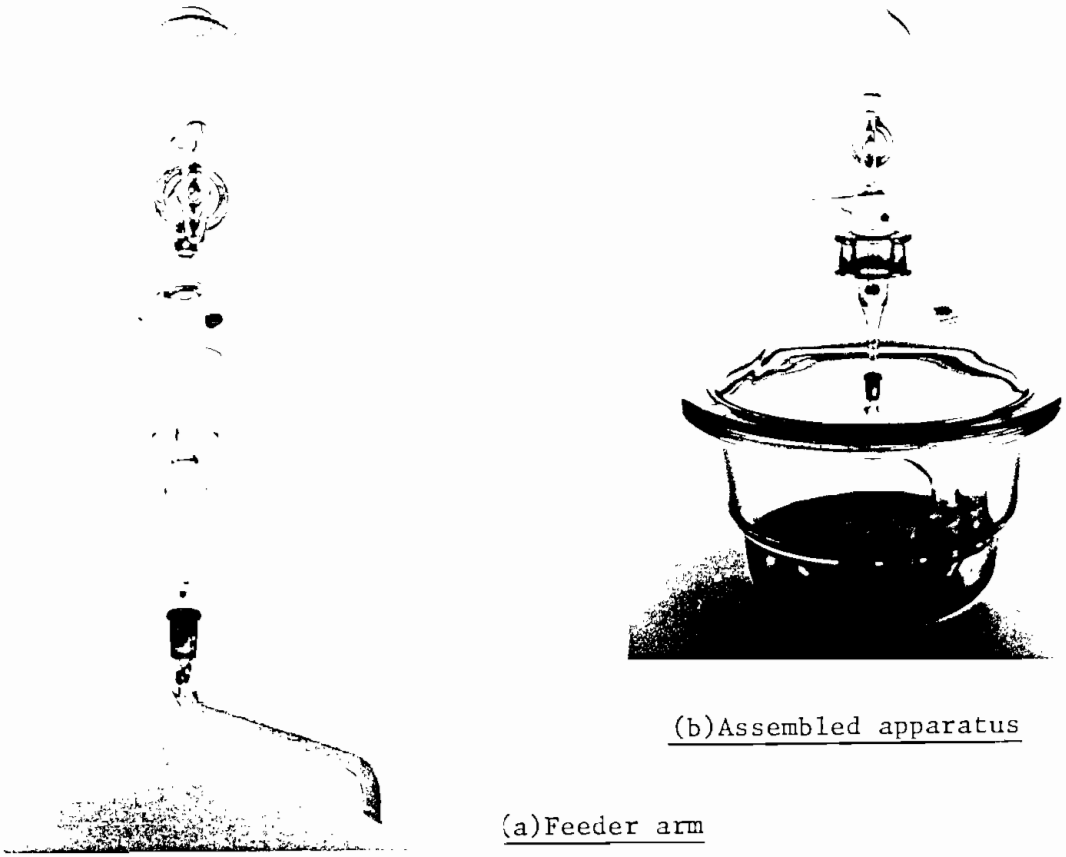


(a) No bandpass filter (Spike disturbance at cursor points)



(b) Passband at 15/25 kHz

Figure 3.17 - Received waveform records of the CW PLUS SPIKE MARKER system (20.4 kHz CW; 30 cycle spike interval; 170mm of gassy soil; Test TNG 36)



(b)Assembled apparatus

(a)Feeder arm

Figure 4.1 - Resin impregnation apparatus

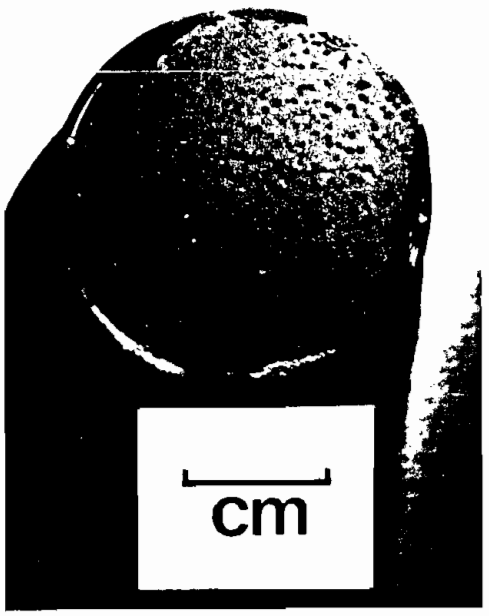


Figure 4.2 - SEM sample (mounted and carbon coated



Figure 4.3 - SEM video image of a gassy soil specimen

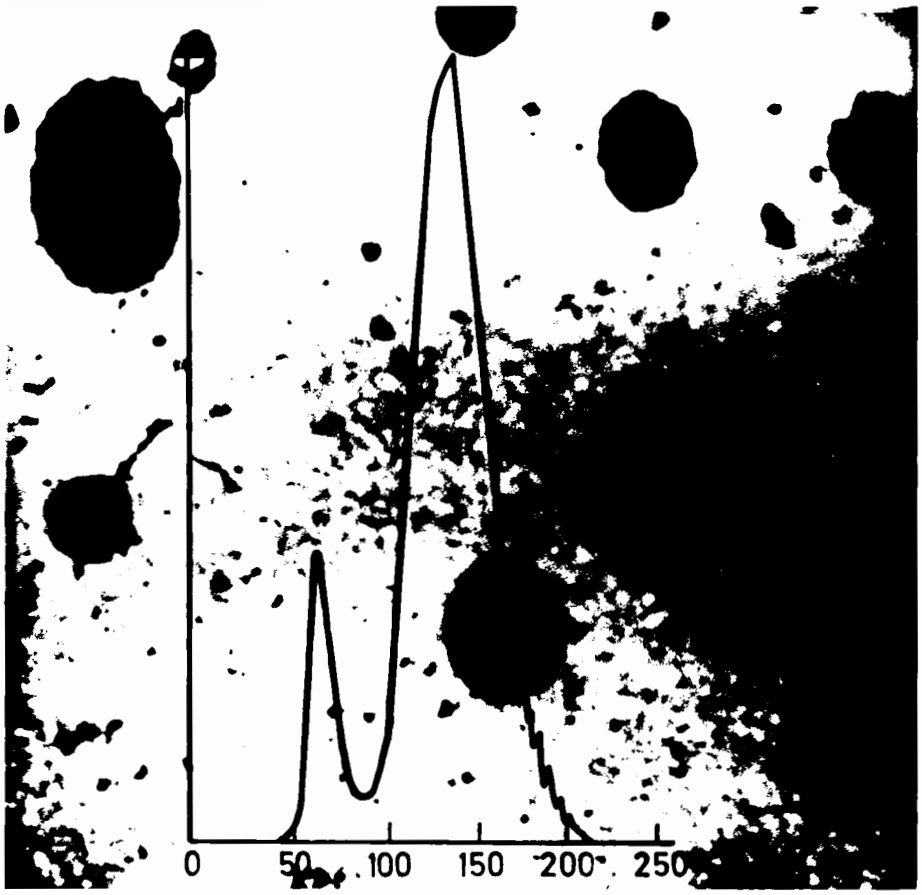


Figure 4.4(a) Frequency versus luminance intensity (SEM specimen of a gassy soil

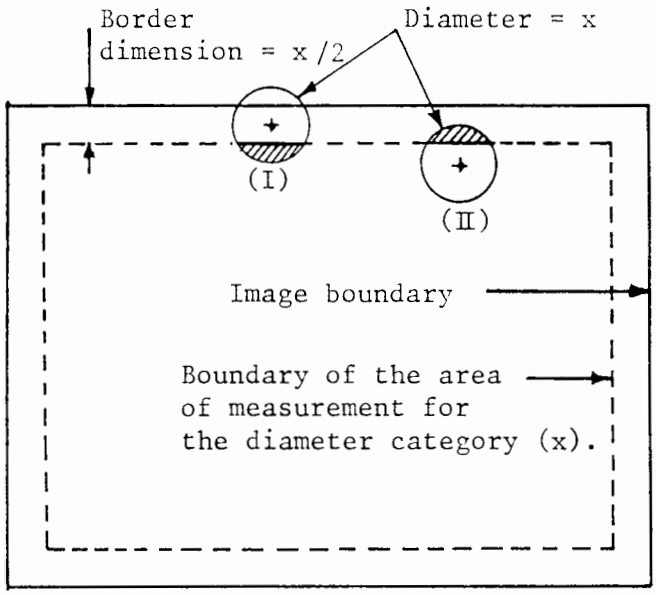


Figure 4.4(b) - Boundary treatment for SEM images

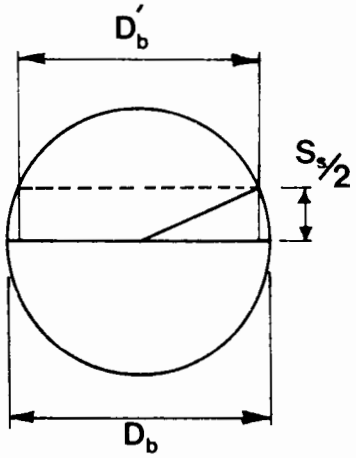


Figure 4.5 - Measurement accuracy of the largest sphere diameter



Figure 4.6(a) - SEM image of a single gas void (6μm Ø)



Figure 4.6(b) - SEM image of the wall of a gas void (300μm Ø)

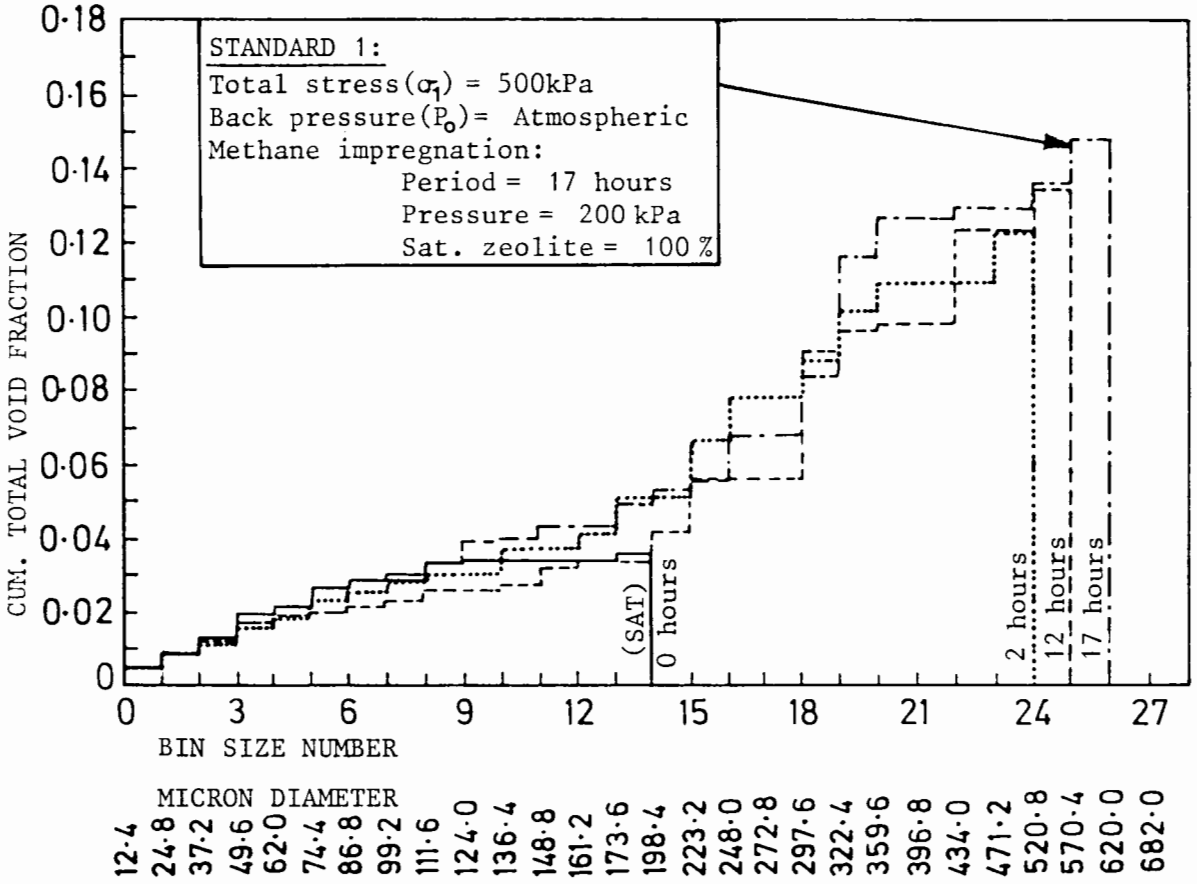
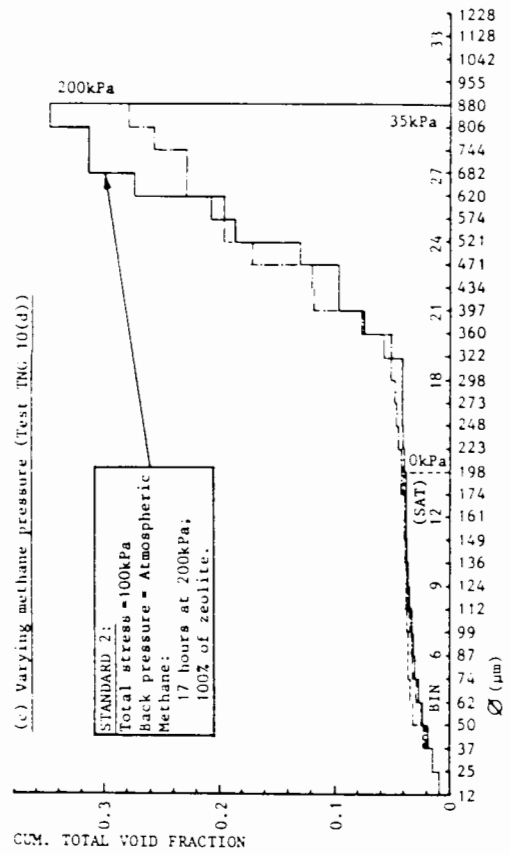
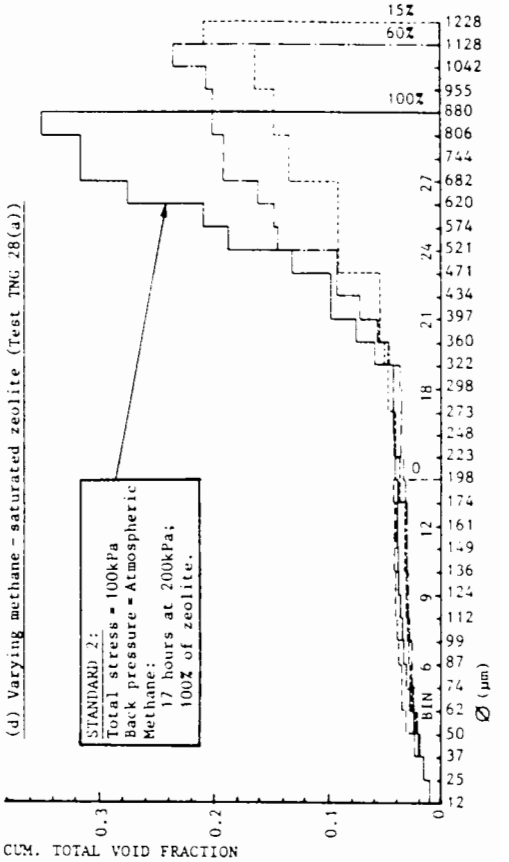
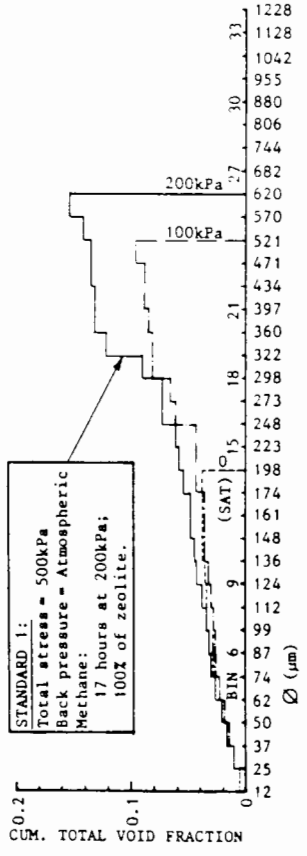


Figure 4.7 - Varying methane periods (Test TNG 10(a))

FIGURE 4·8 - BSD CURVES







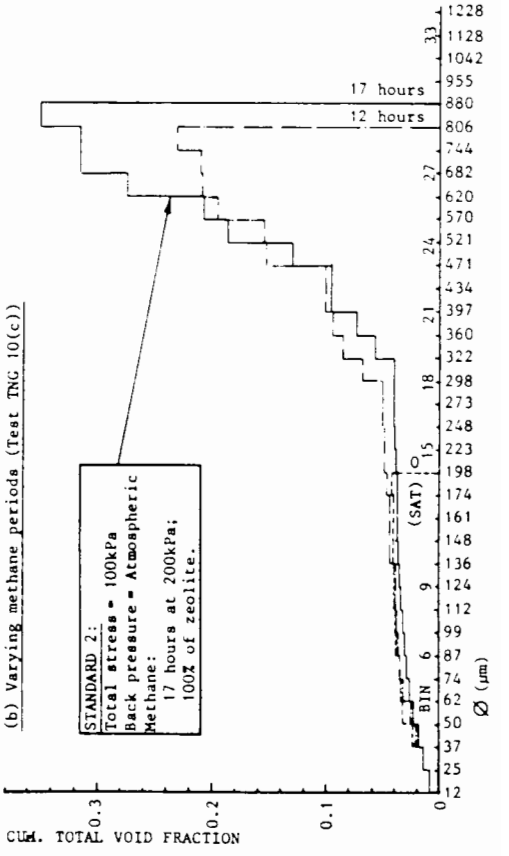
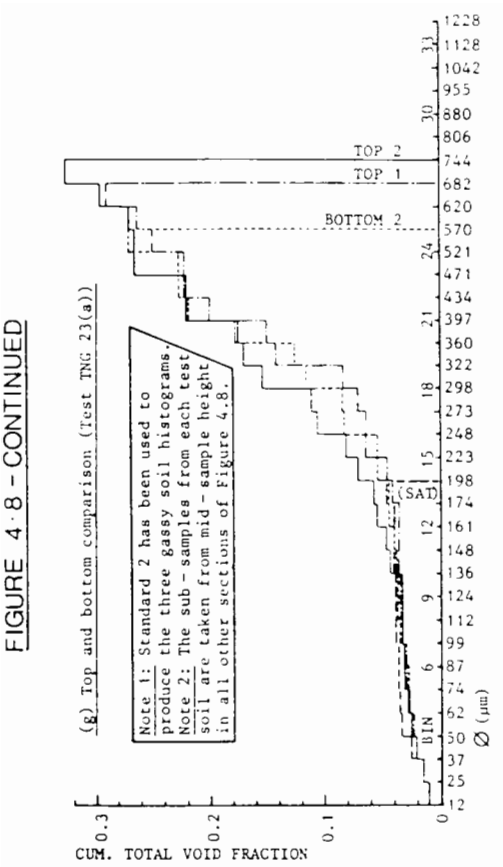
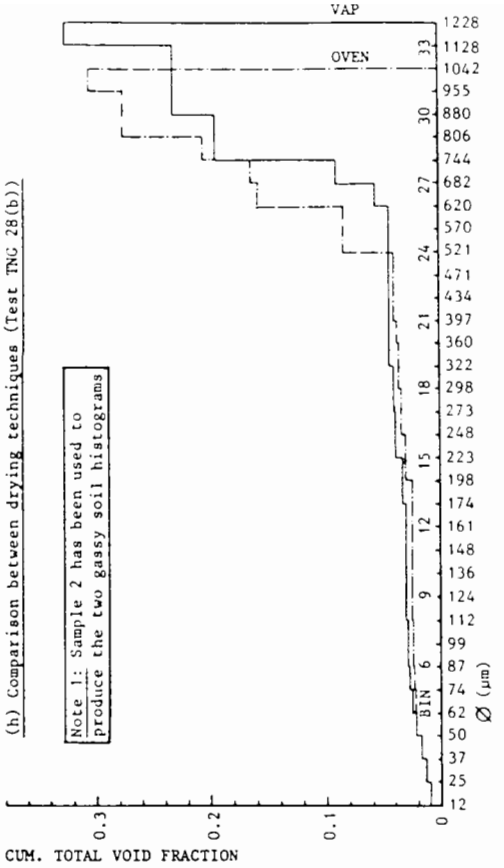
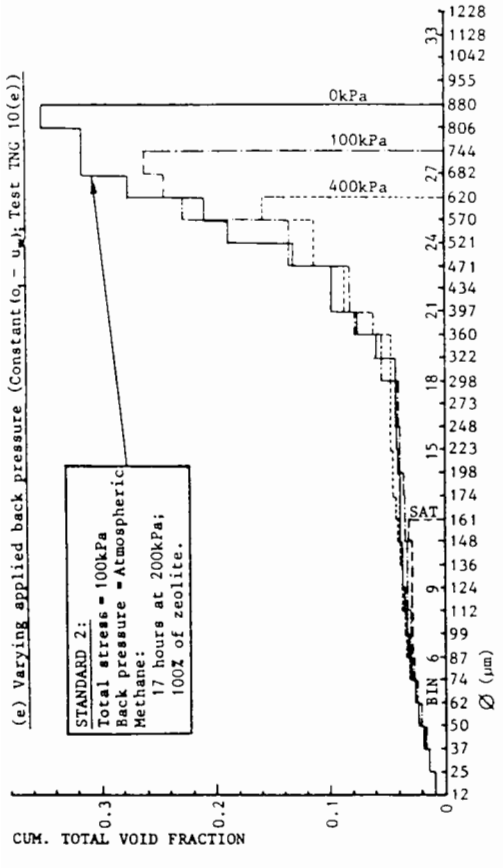
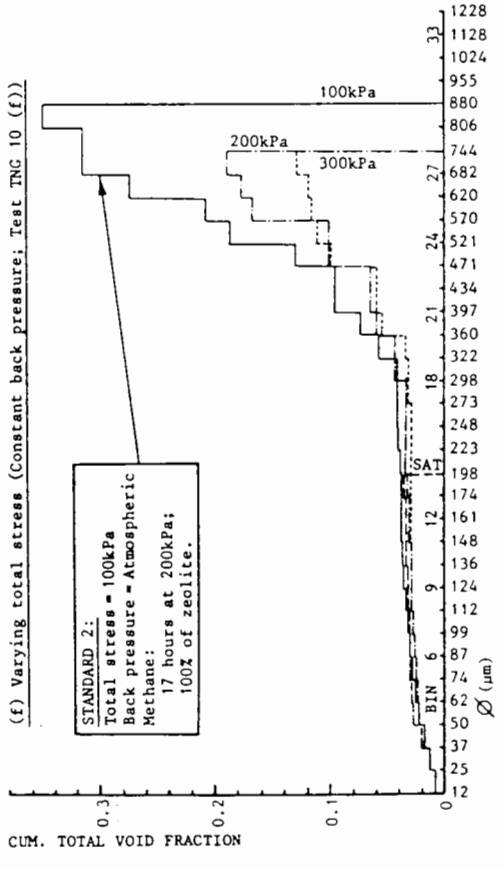


FIGURE 4·8 - CONTINUED









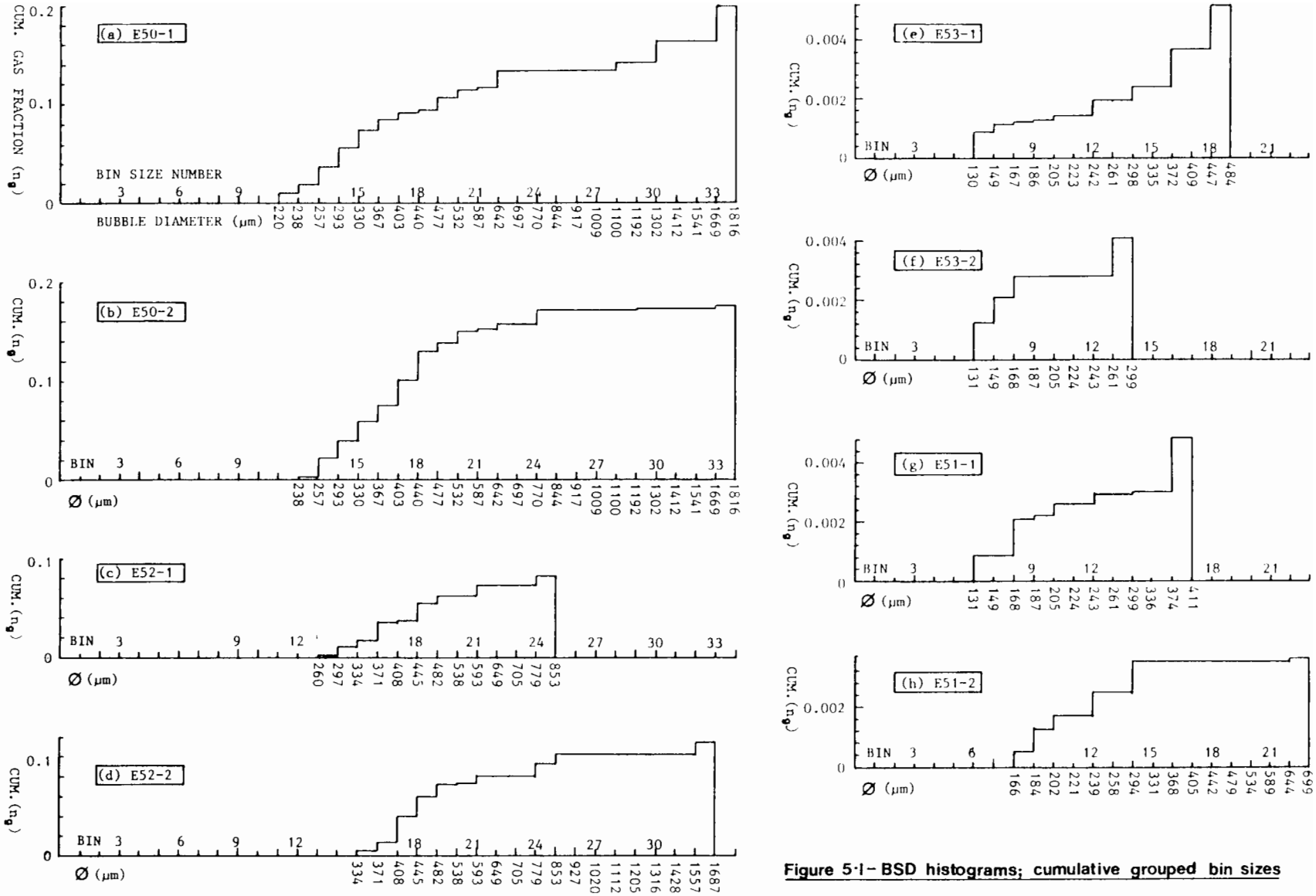
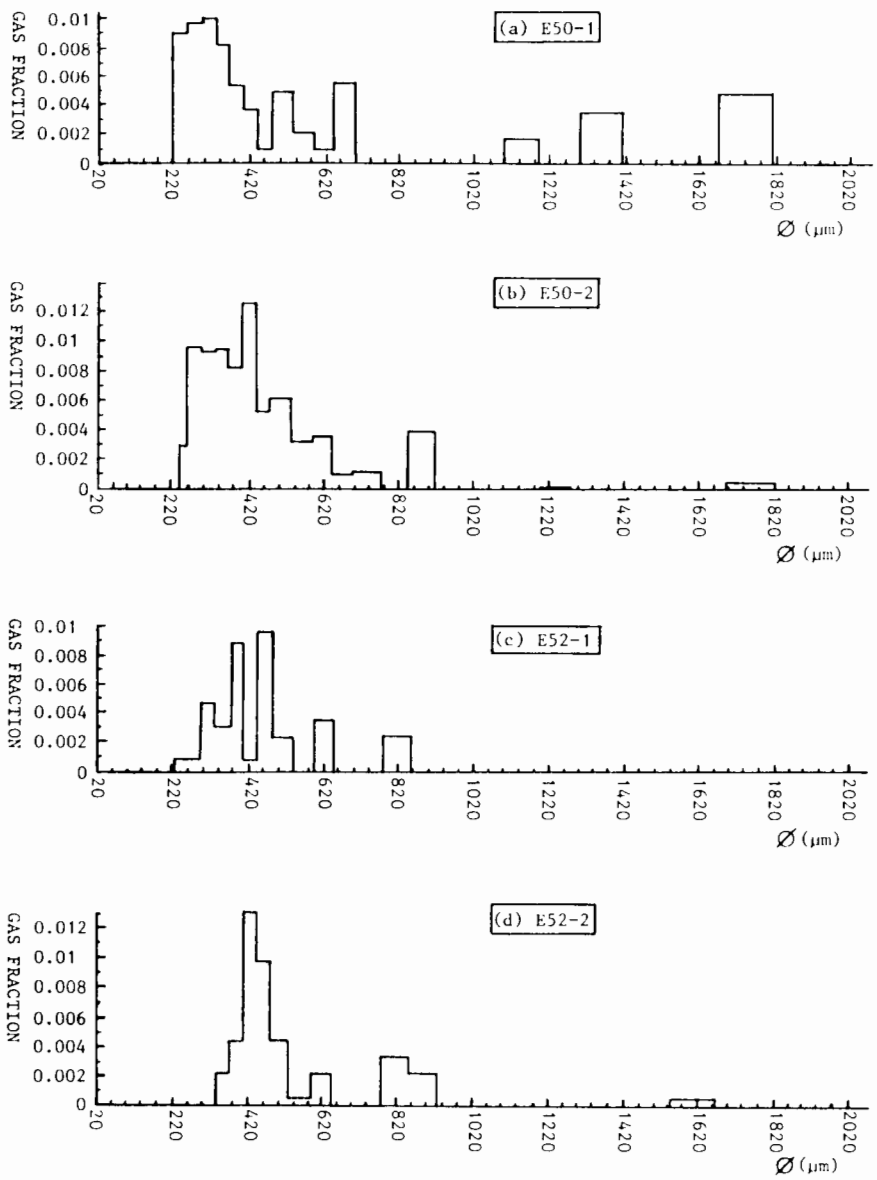


Figure 5·1 – BSD histograms; cumulative grouped bin sizes



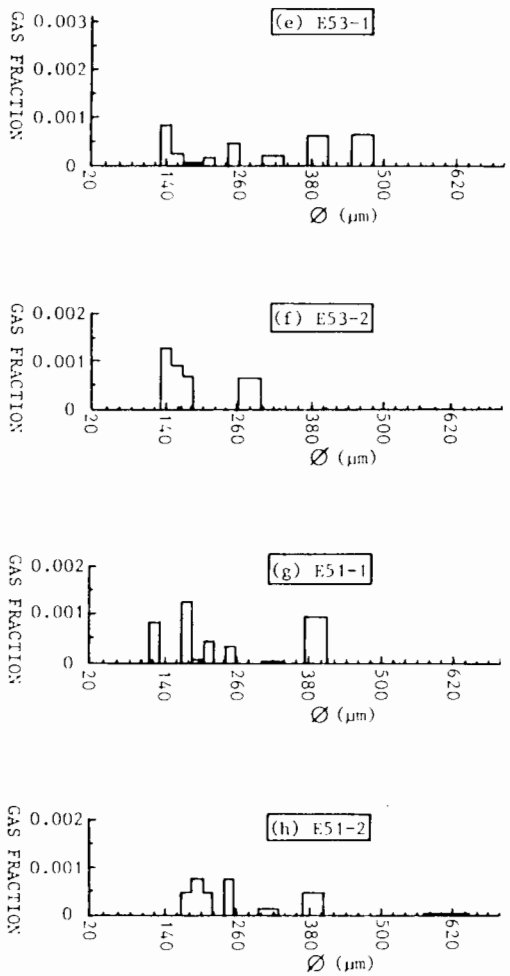
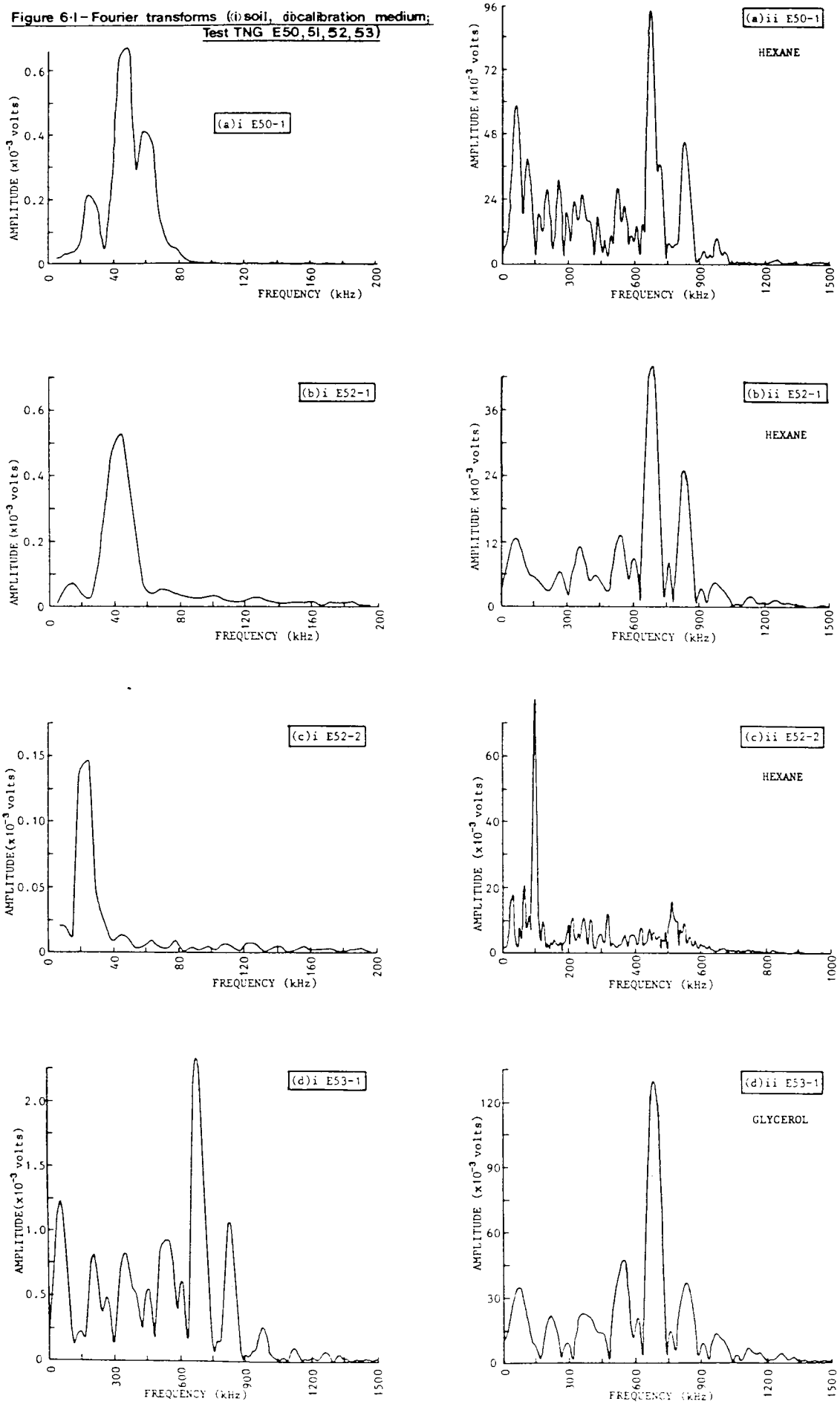
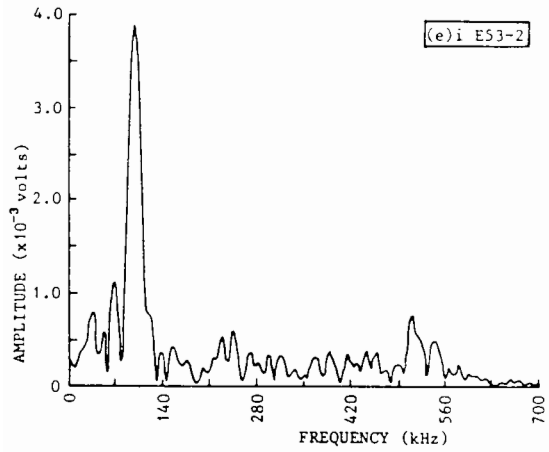


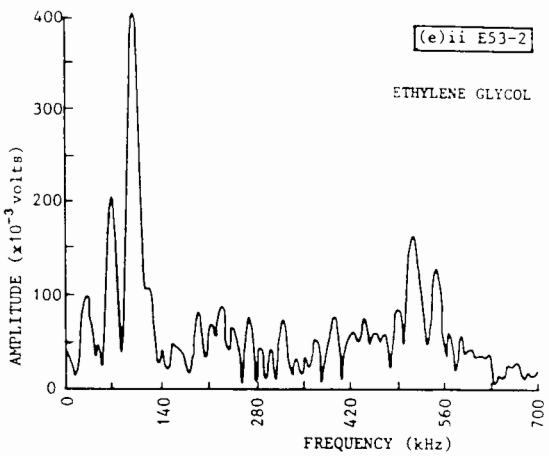
FIGURE 5·2 - BSD HISTOGRAMS; SINGLE BIN SIZES

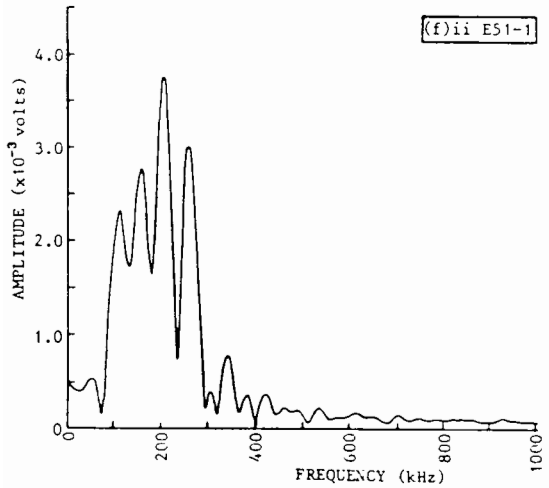
Figure 6·1 – Fourier transforms ((i) soil, decalibration medium; Test TNG E50, 51, 52, 53)

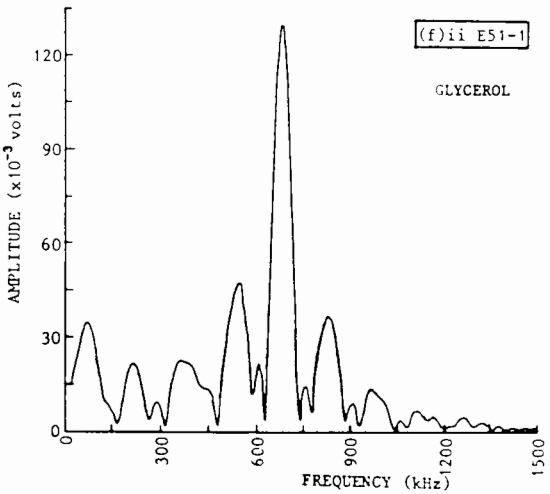


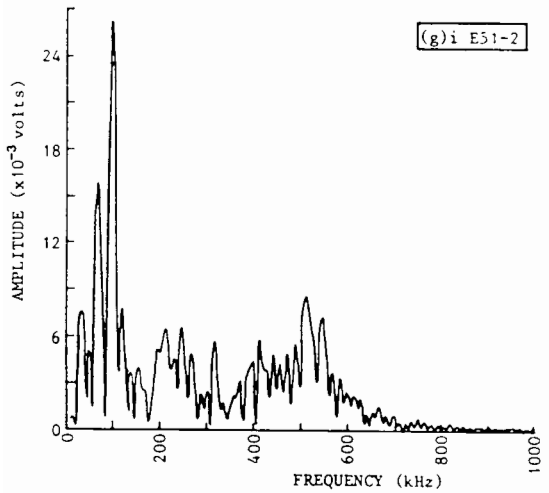
Note - The scales of frequency in (i) are not equal to those of (ii).











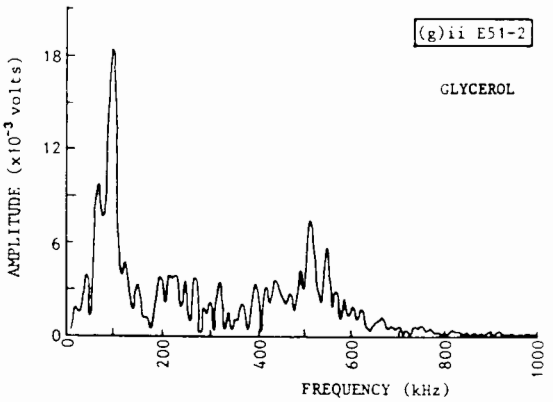


Figure 6·1 – Continued

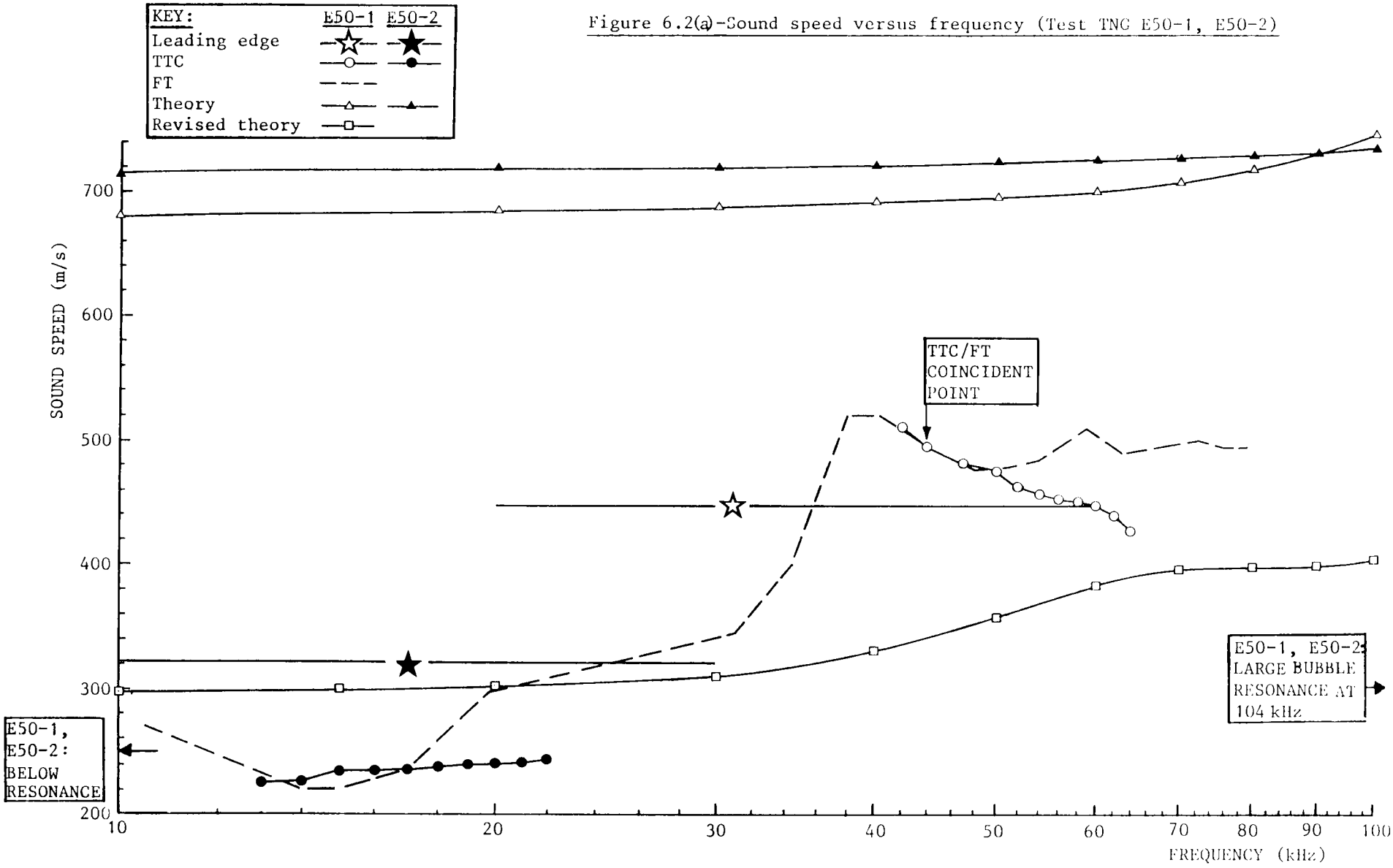


Figure 6.2(a)-Sound speed versus frequency (Test TNG E50-1, E50-2)

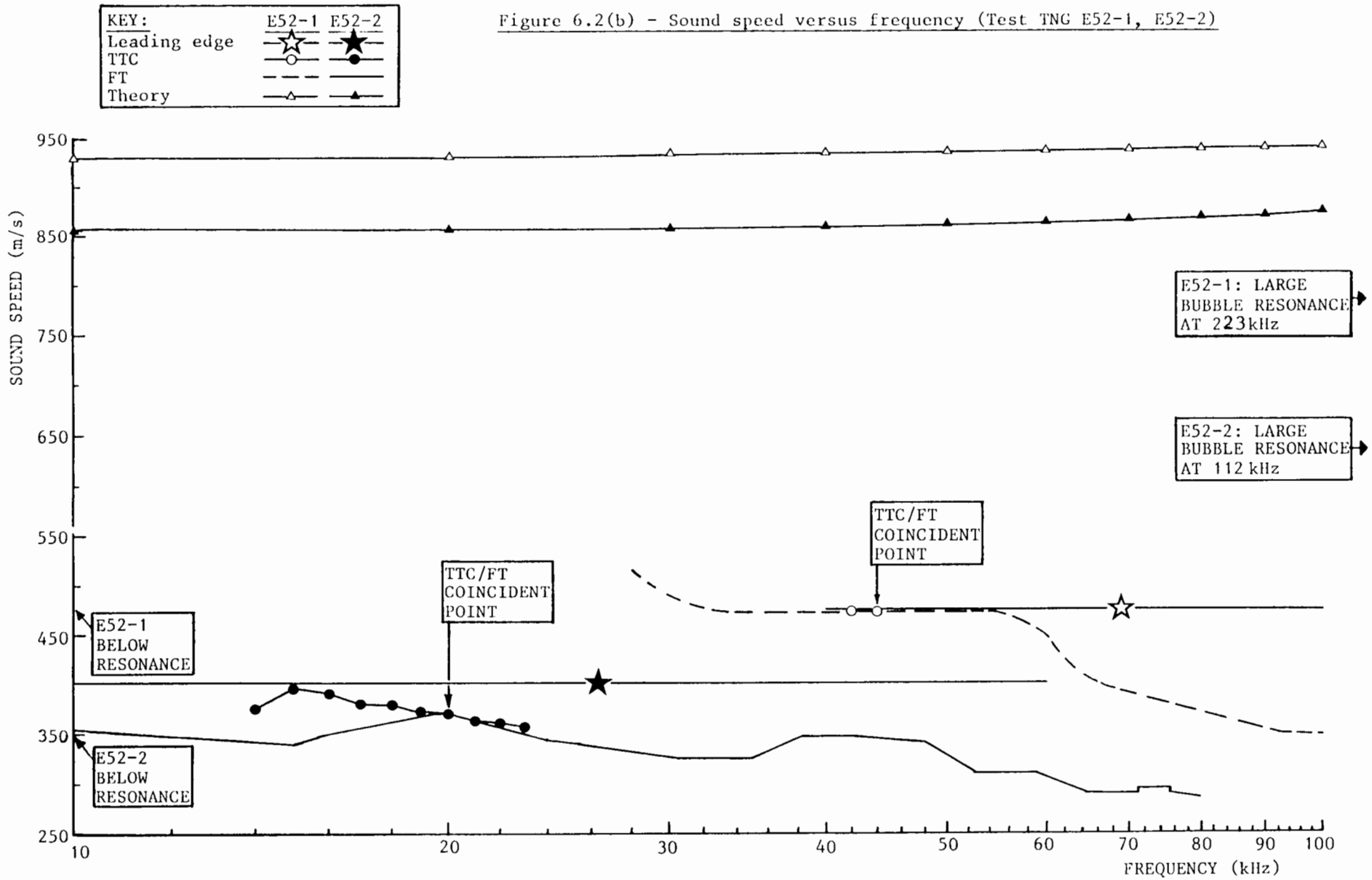


Figure 6.2(b) - Sound speed versus frequency (Test TNG E52-1, E52-2)

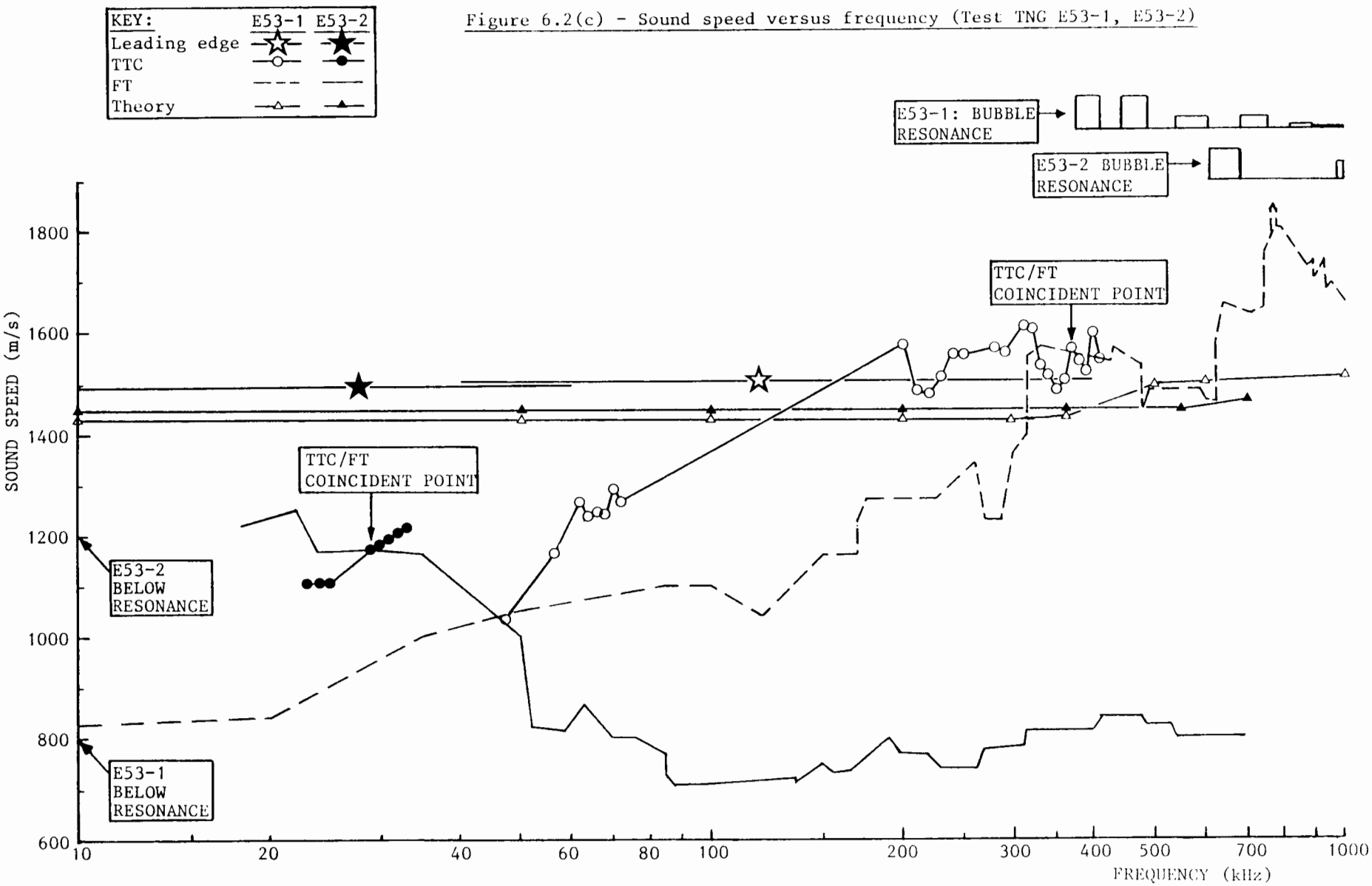


Figure 6.2(c) - Sound speed versus frequency (Test TNG E53-1, E53-2)

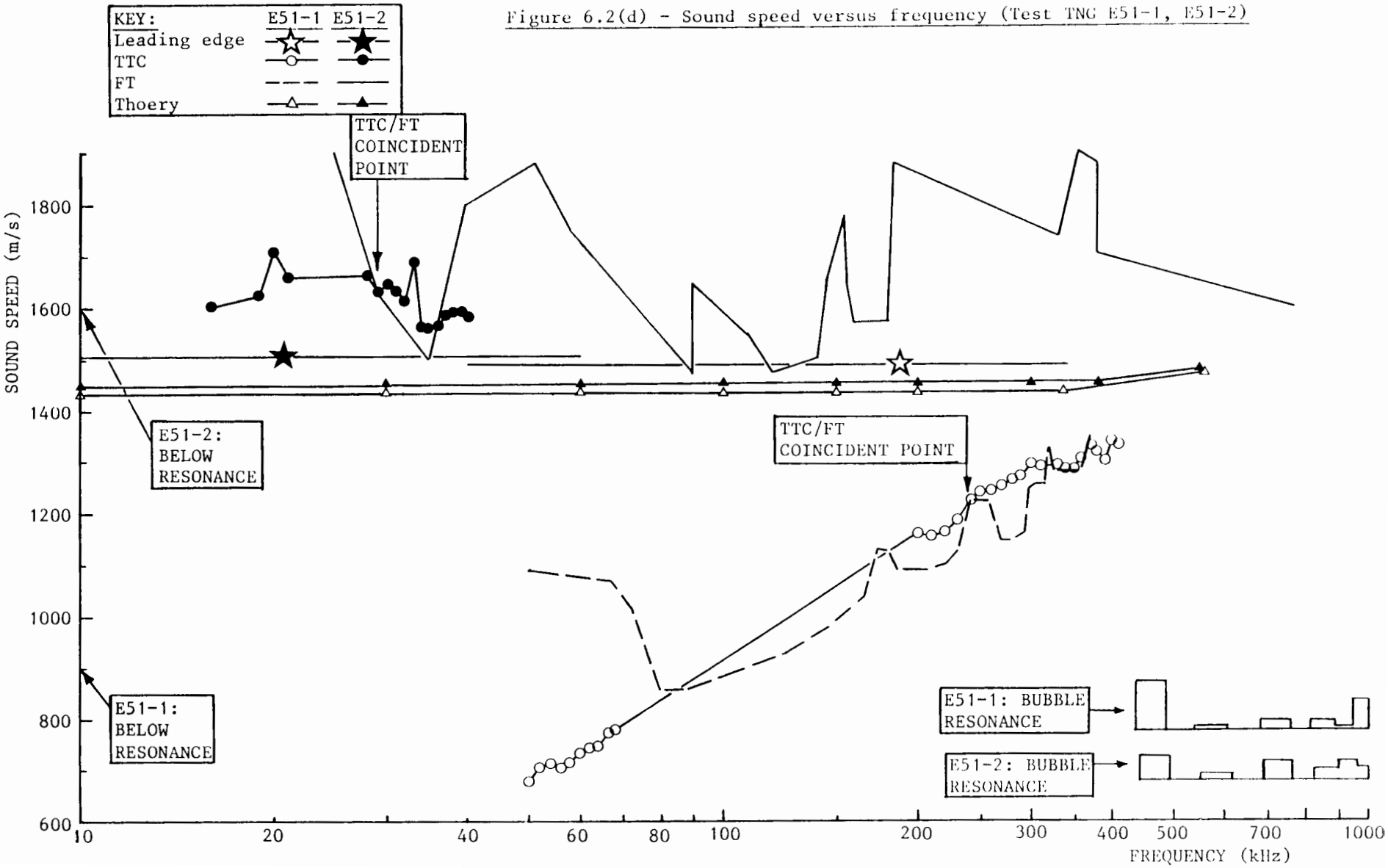


Figure 6.2(d) - Sound speed versus frequency (Test TNG E51-1, E51-2)

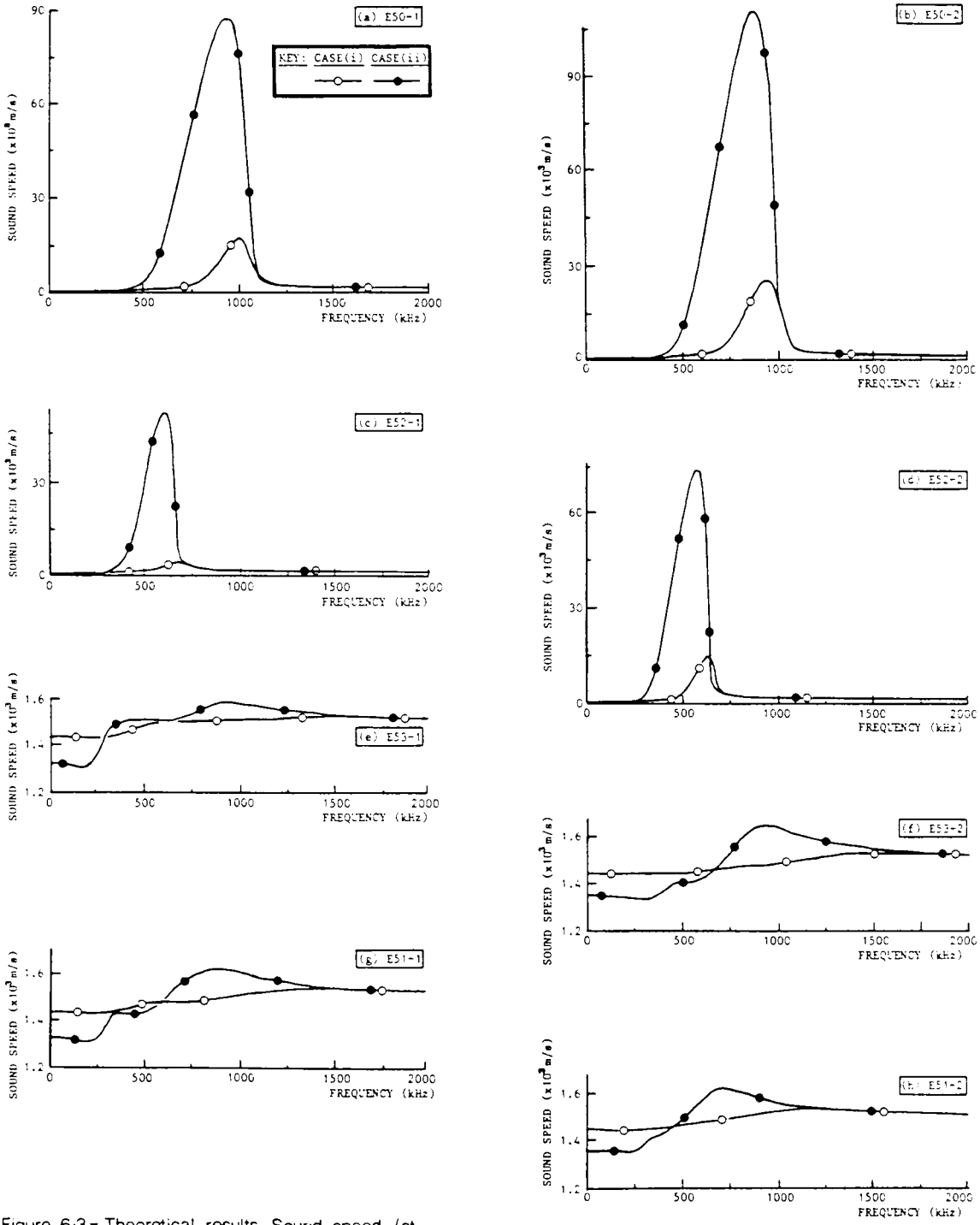


Figure 6.3 - Theoretical results - Sound speed (at resonance) versus frequency (Test TNG E50,51,52,53)

Note - The symbols do not denote data points. Actual points are at 2.441 kHz intervals.

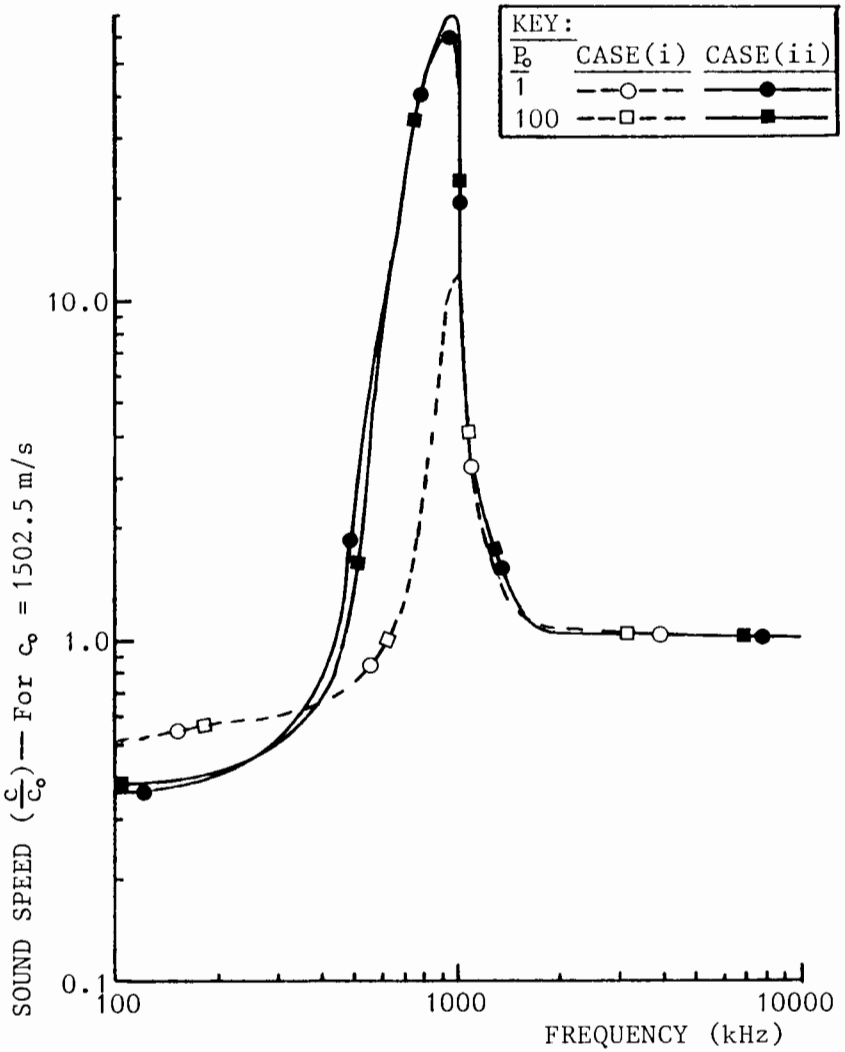


Figure 6.4 - Varying ambient hydrostatic pressure ('at resonance'; Test TNG E50-1; P_o in atmospheres)

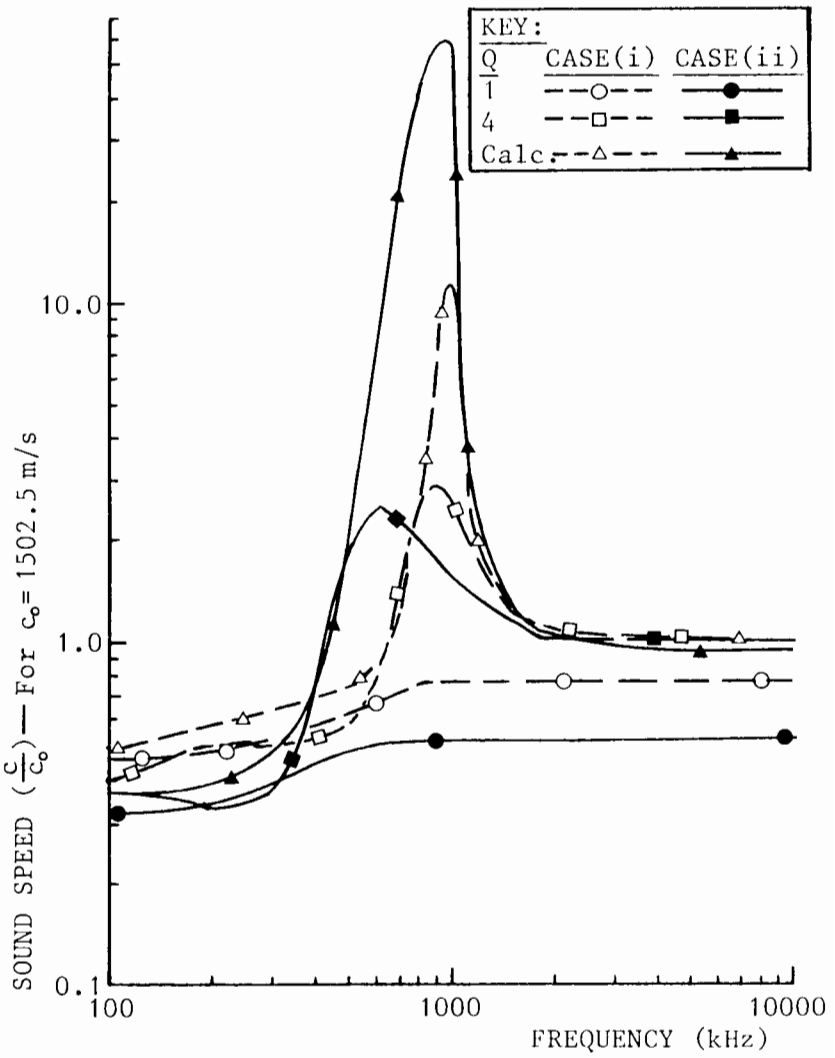


Figure 6.5 - Varying reciprocal specific dissipation function ('at resonance'; TNG E50-1)

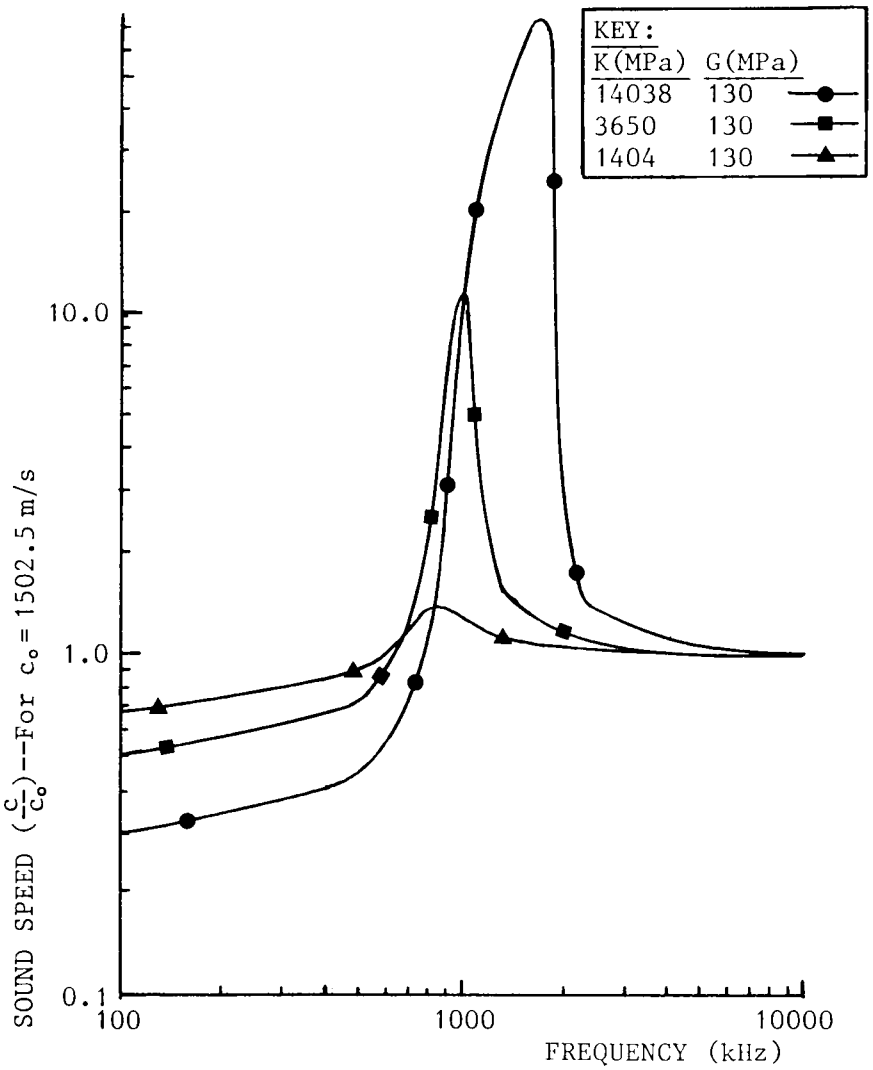


Figure 6.6(a) - Varying bulk modulus ('at resonance'; Test TNG E50-1)

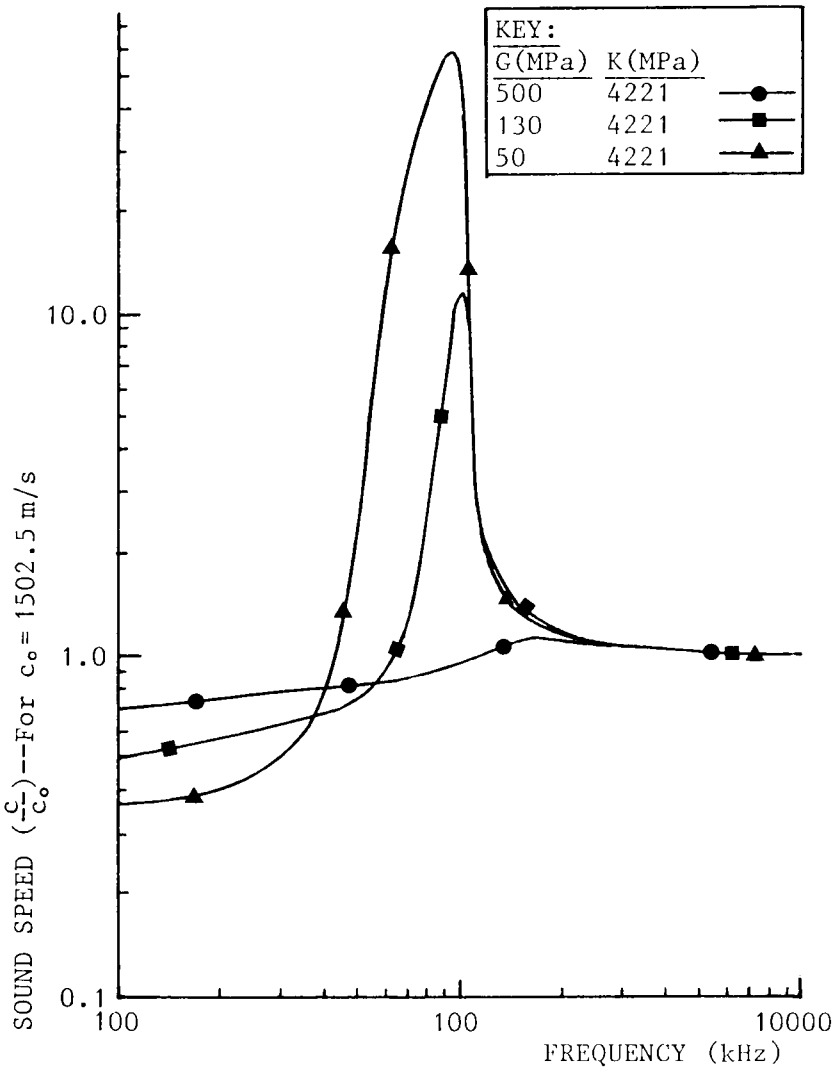


Figure 6.6(b) - Varying shear modulus ('at resonance'; Test TNG E50-1)

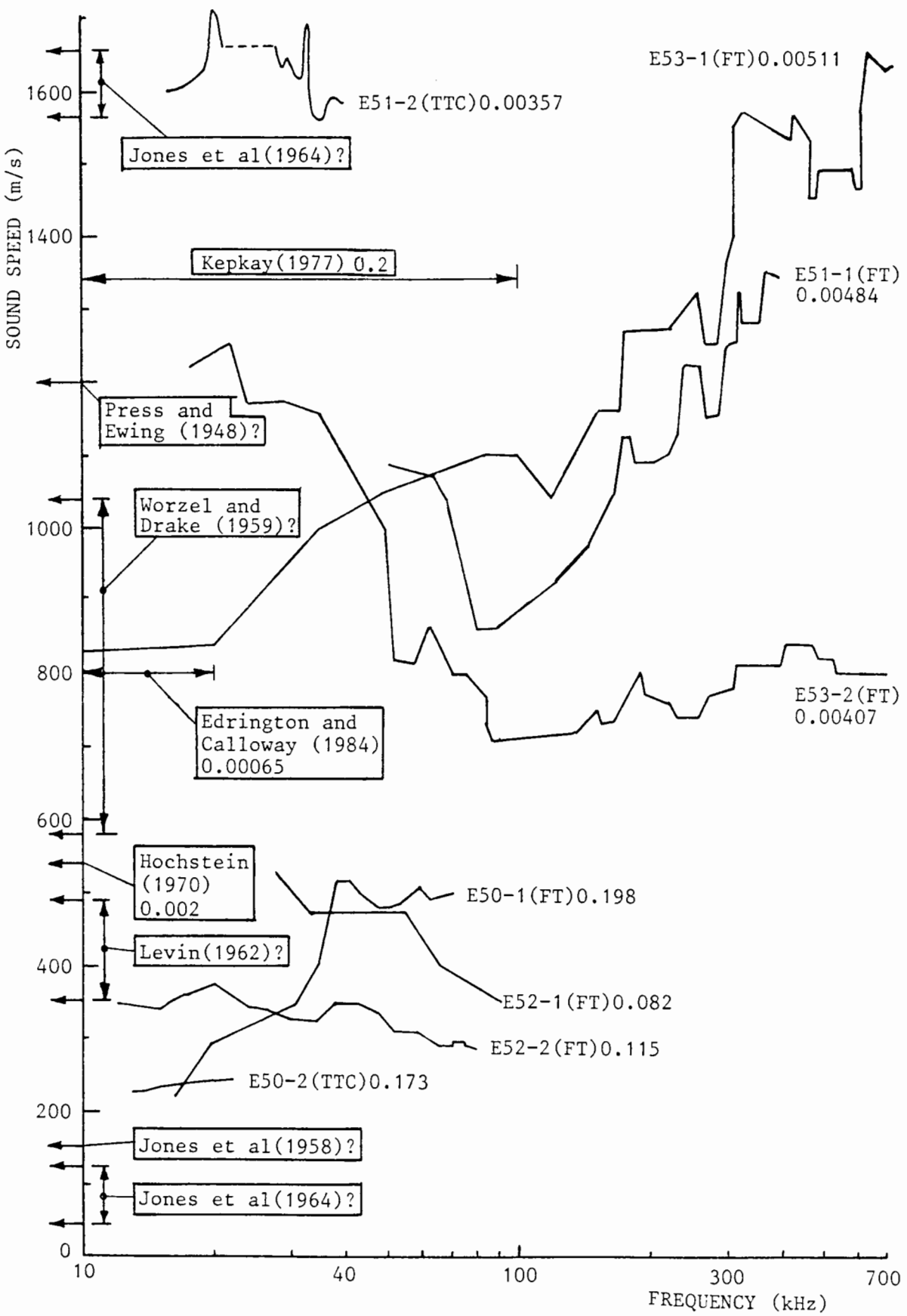


Figure 6.7 - A comparison between sound speed results 'at resonance' (Experiment/Literature)

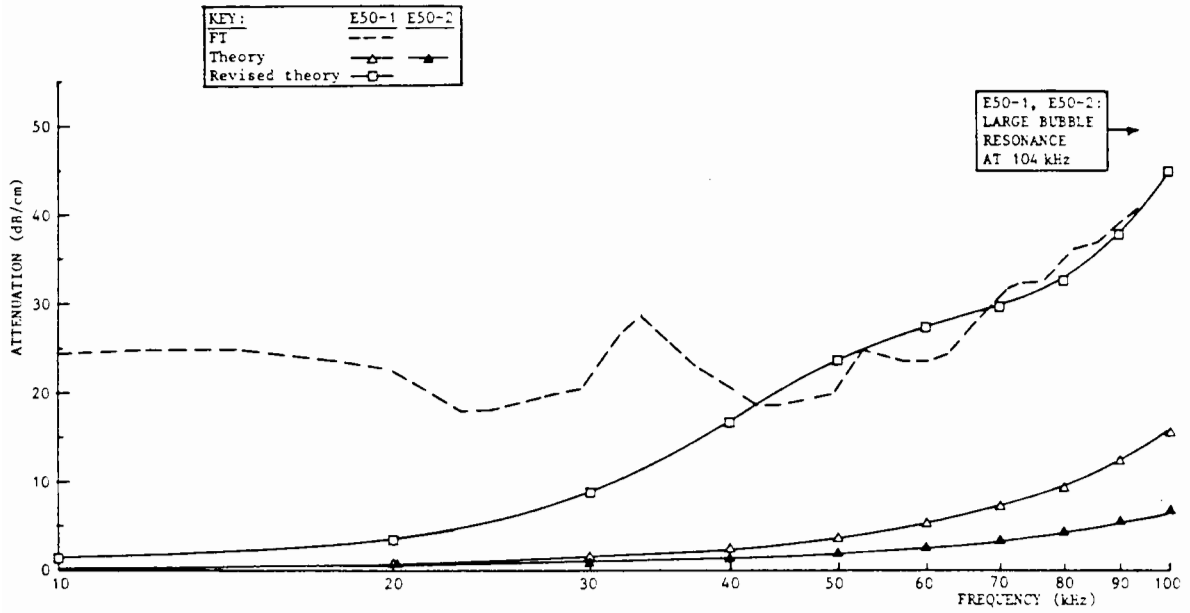


Figure 7.1(a) - Attenuation versus frequency (Test TNG E50-1, E50-2) - 'At resonance'

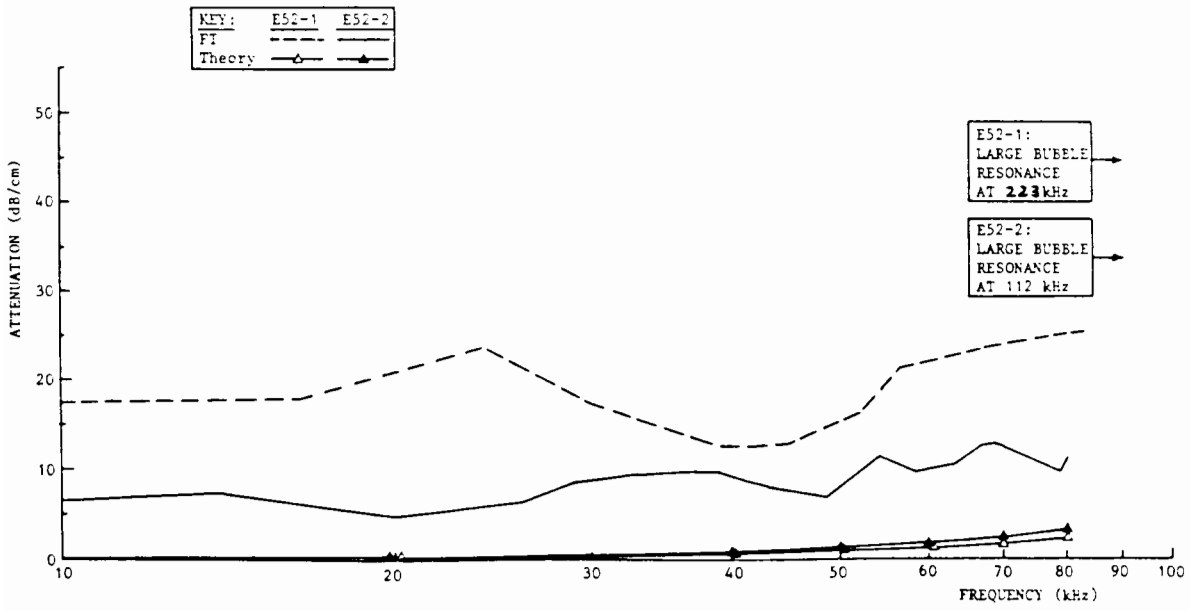


Figure 7.1(b) - Attenuation versus frequency (Test TNG E52-1, E52-2)- 'At resonance'

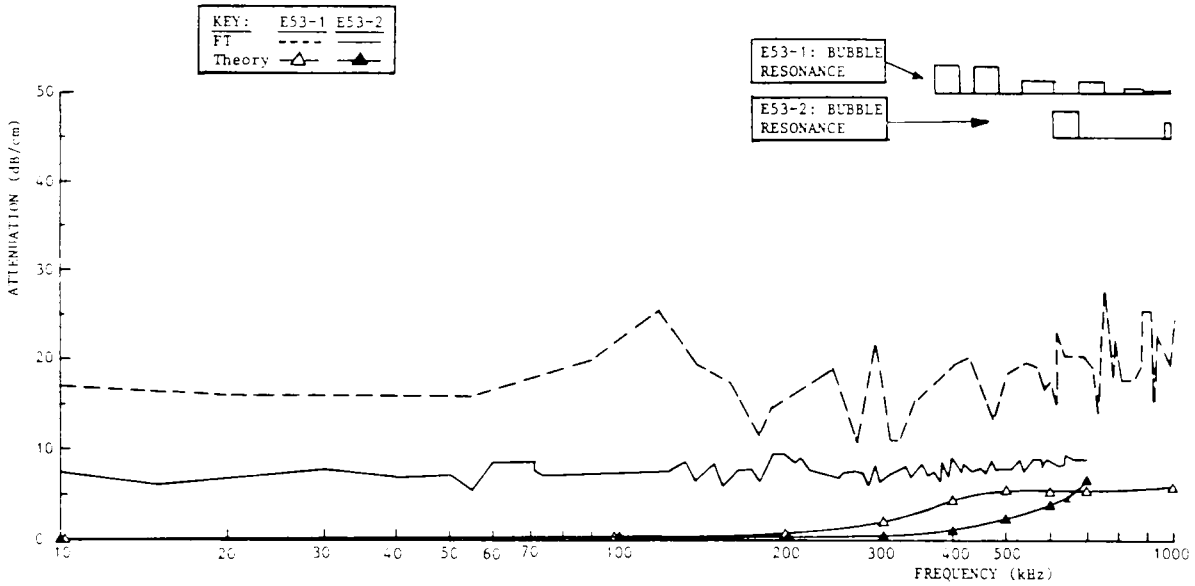


Figure 7.1(c) - Attenuation versus frequency (Test TNG E53-1, E53-2) - 'At resonance'

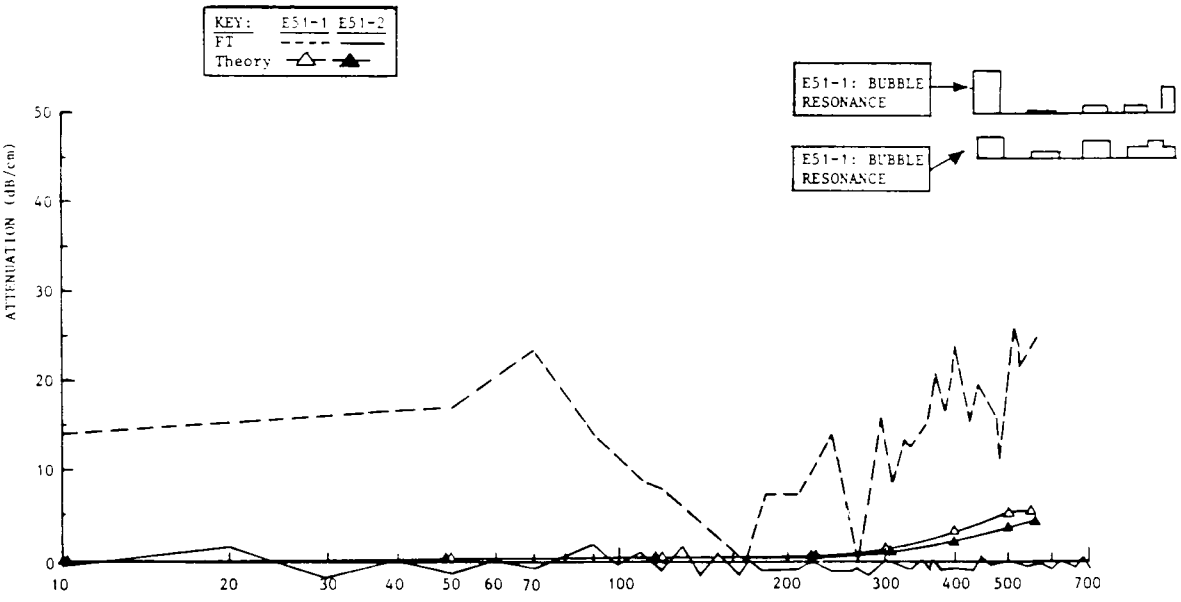
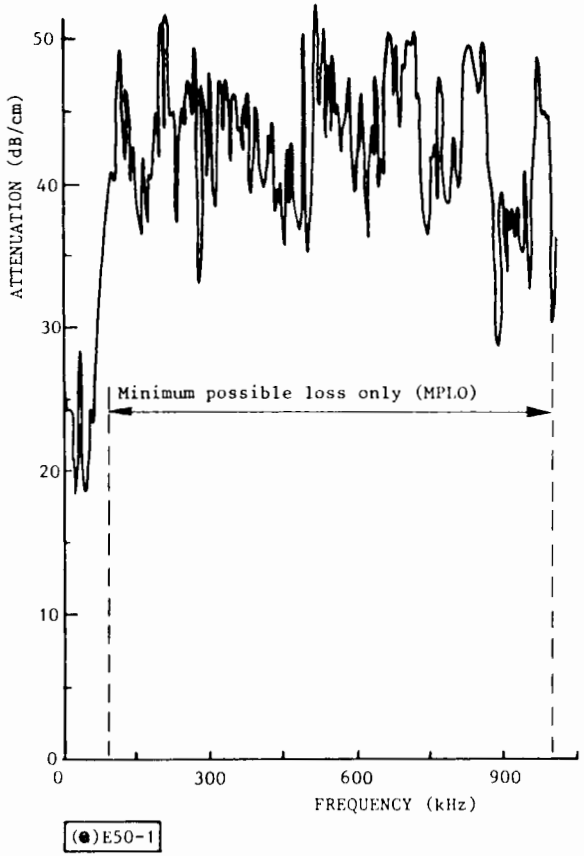
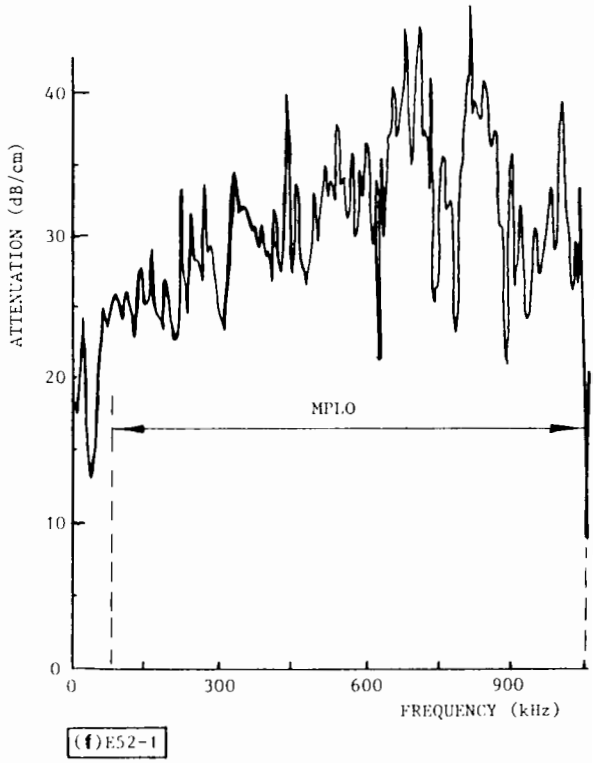


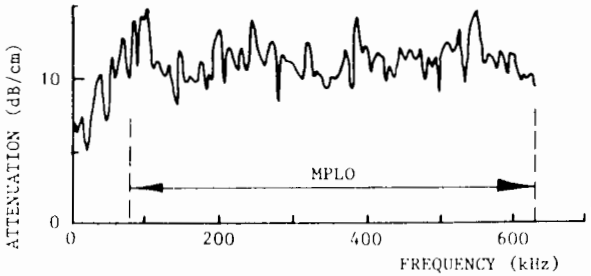
Figure 7.1(d) - Attenuation versus frequency (Test TNG E51-1, E51-2) - 'At resonance'



(e)E50-1



(f)E52-1



(g)E52-2

Figure 7.1 - Extended range of attenuation results (Minimum values)

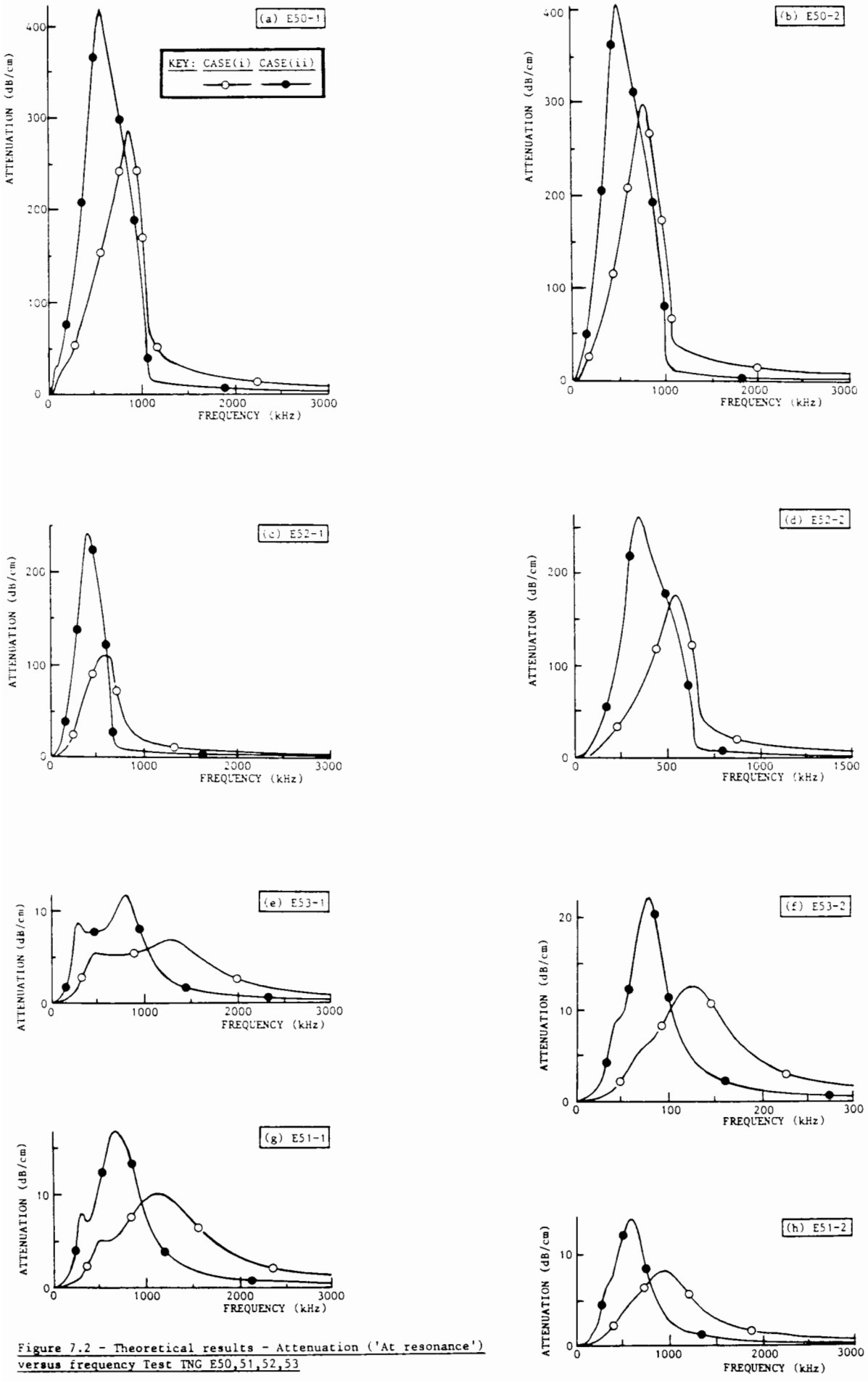


Figure 7.2 - Theoretical results - Attenuation ('At resonance') versus frequency Test TNG E50,51,52,53

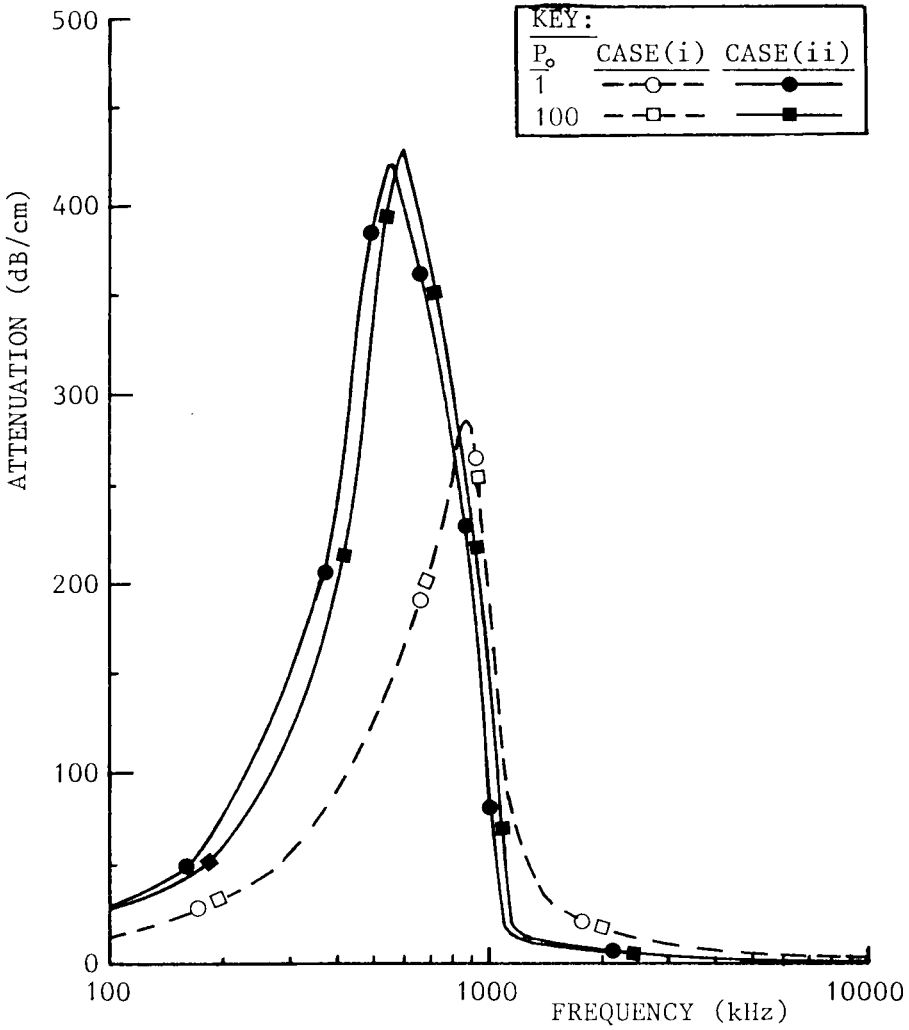


Figure 7.3 - Varying ambient hydrostatic pressure ('at resonance'; Test TNG E50-1; P_o in atmospheres)

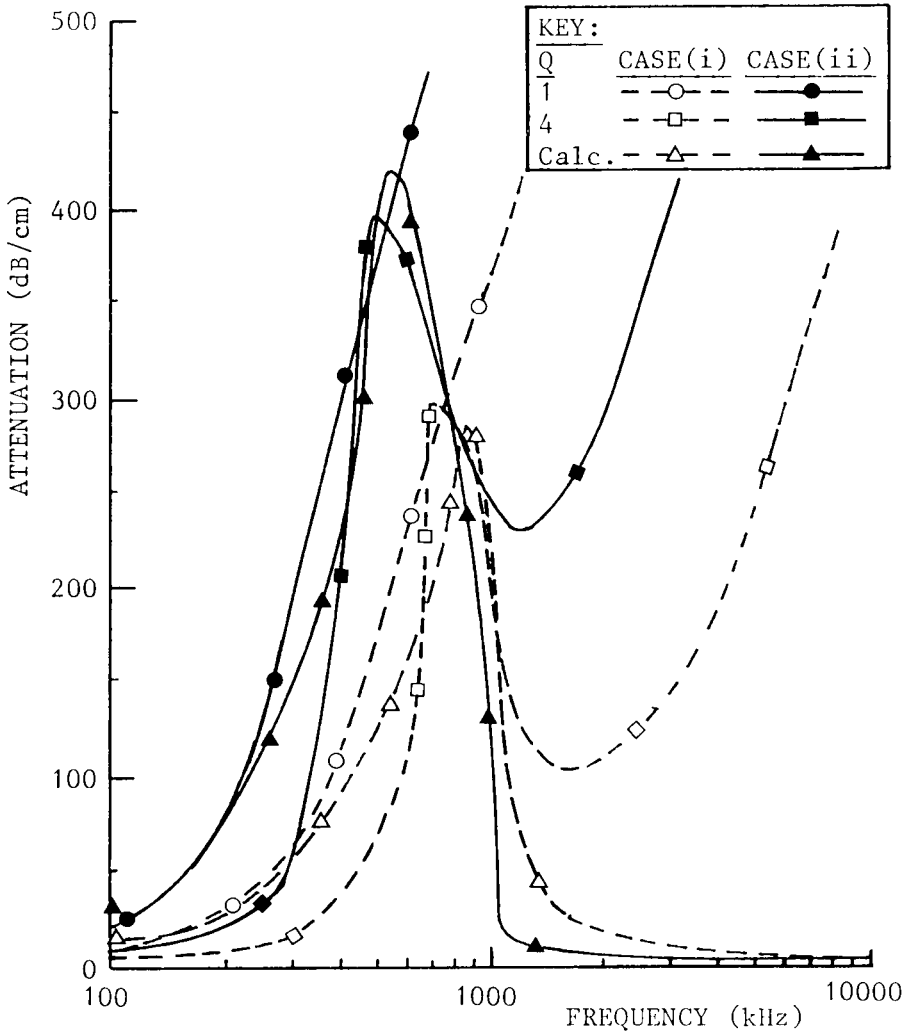


Figure 7.4 - Varying reciprocal specific dissipation function ('at resonance'; Test TNG E50-1)

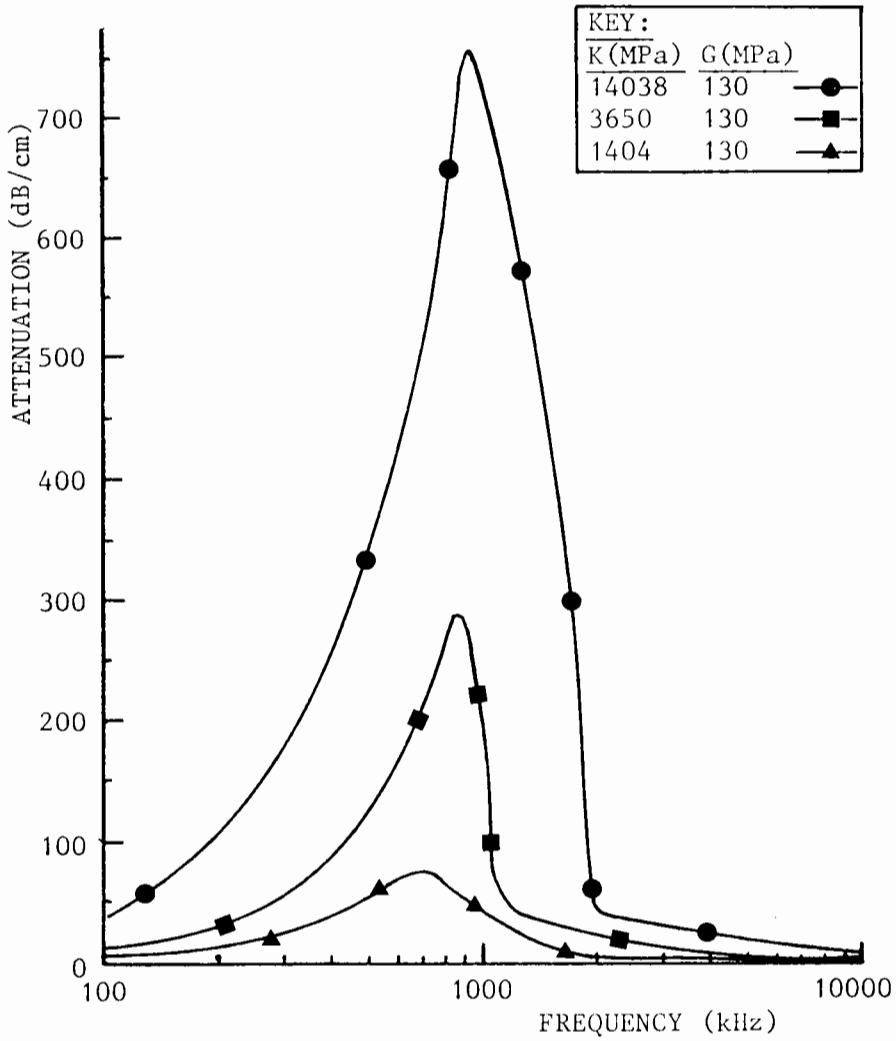


Figure 7.5(a) - Varying bulk modulus ('at resonance'; Test TNG E50-1)

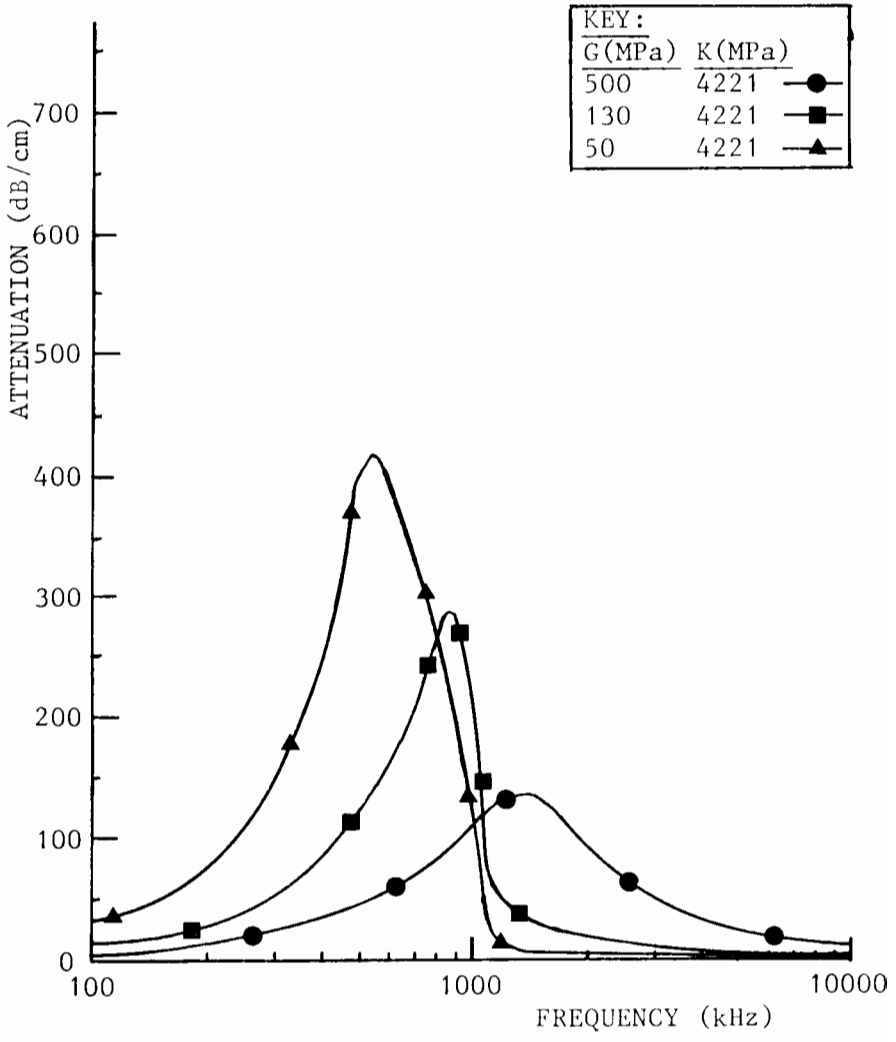


Figure 7.5(b) - Varying shear modulus ('at resonance'; Test TNG E50-1)

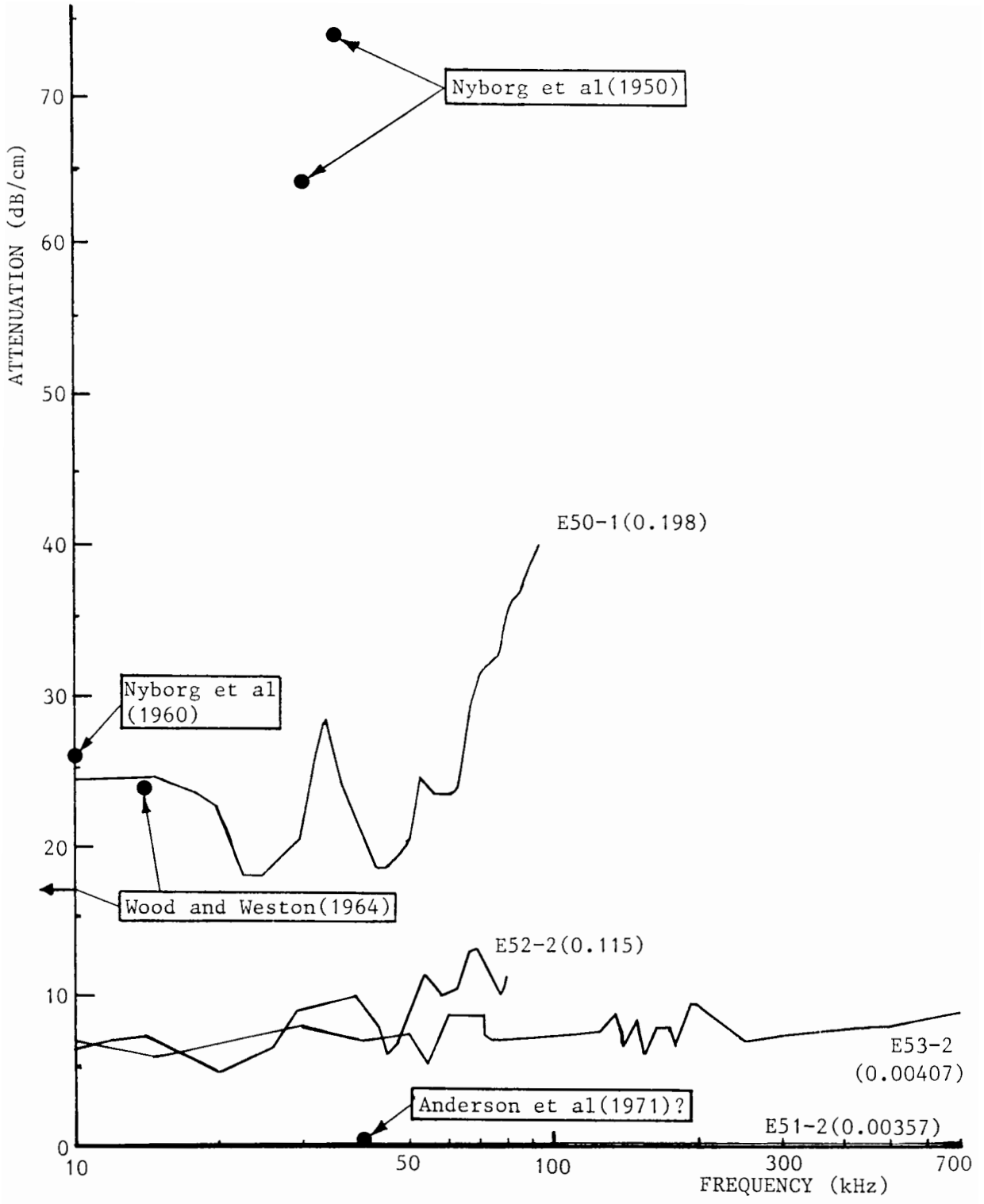


Figure 7.6 - A comparison between attenuation results 'at resonance' (Experiment/Literature)

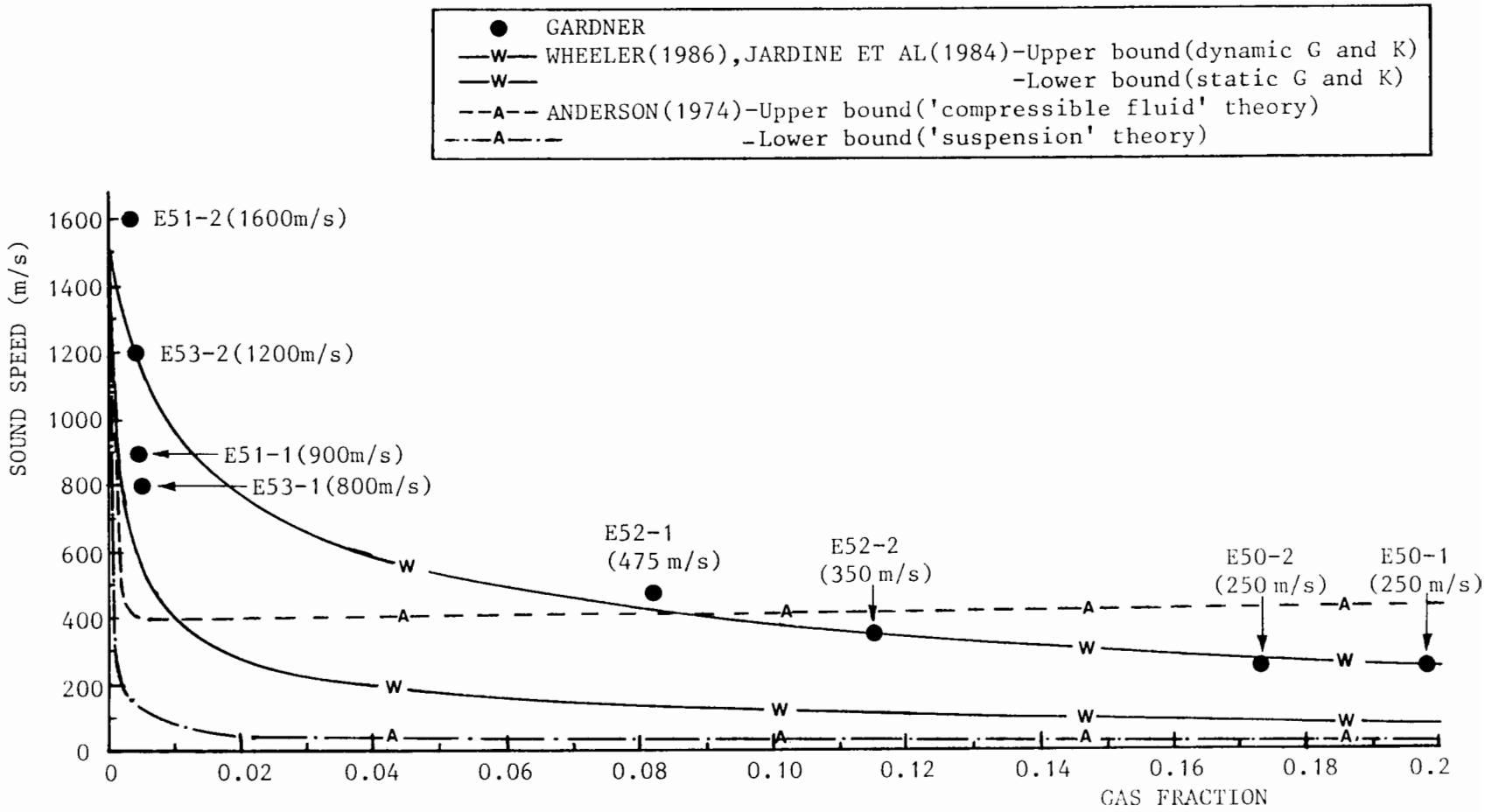


Figure 8.1 - A comparison between sound speed results 'below resonance' (Experiment/Theoretical; Test TNG E 50,51,52,53)

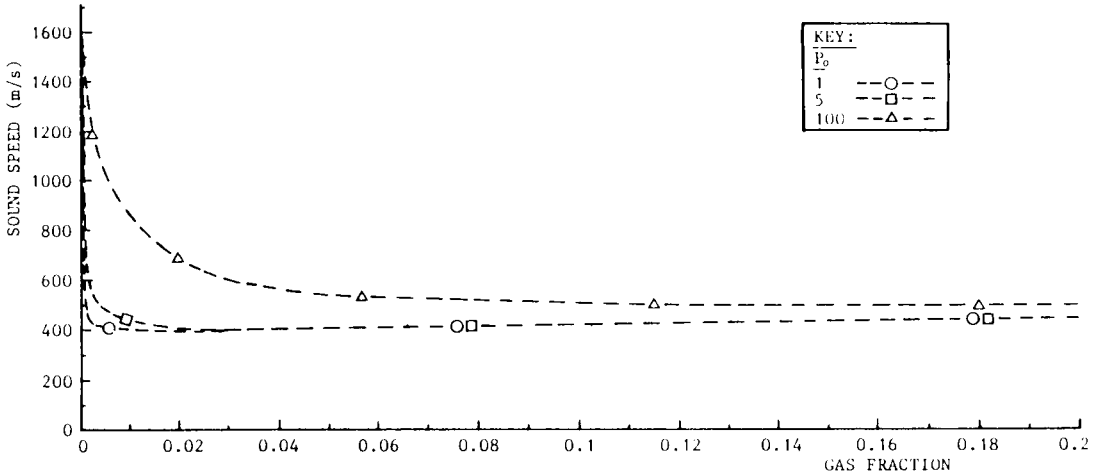


Figure 8.2 - Varying ambient hydrostatic pressure (Anderson's 'compressible fluid' model; 'below resonance'; Test TNG E50,51,52,53)

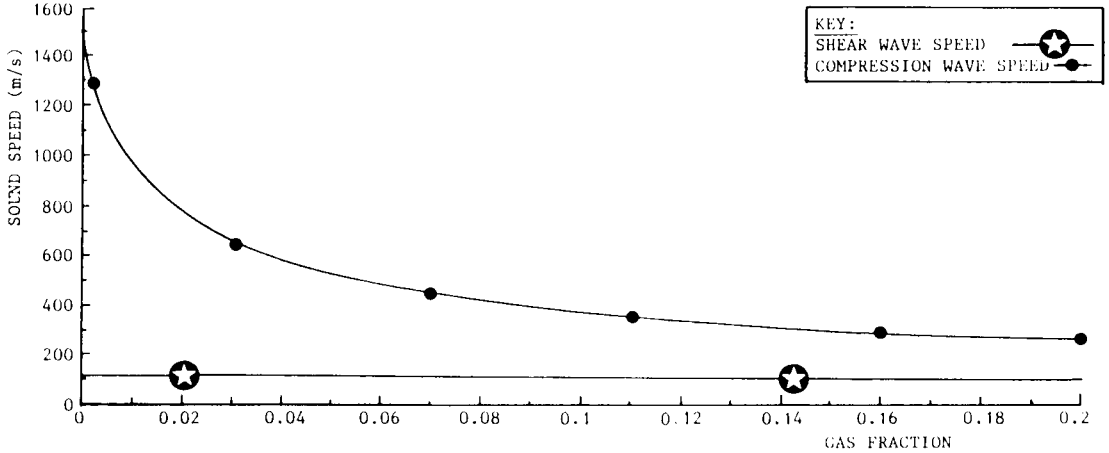


Figure 8.3 - A comparison between bulk shear and compression wave speeds ('below resonance'; Test TNG E50,51,52,53)

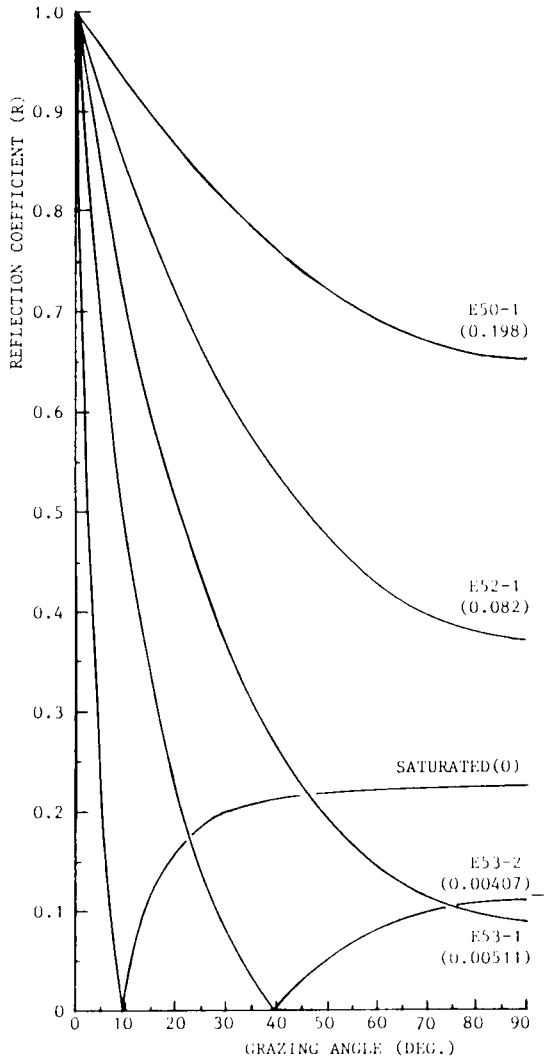


Figure 8.4 - Theoretical reflection coefficients versus grazing angles('below resonance'; Test TNG E50,51,52,53)

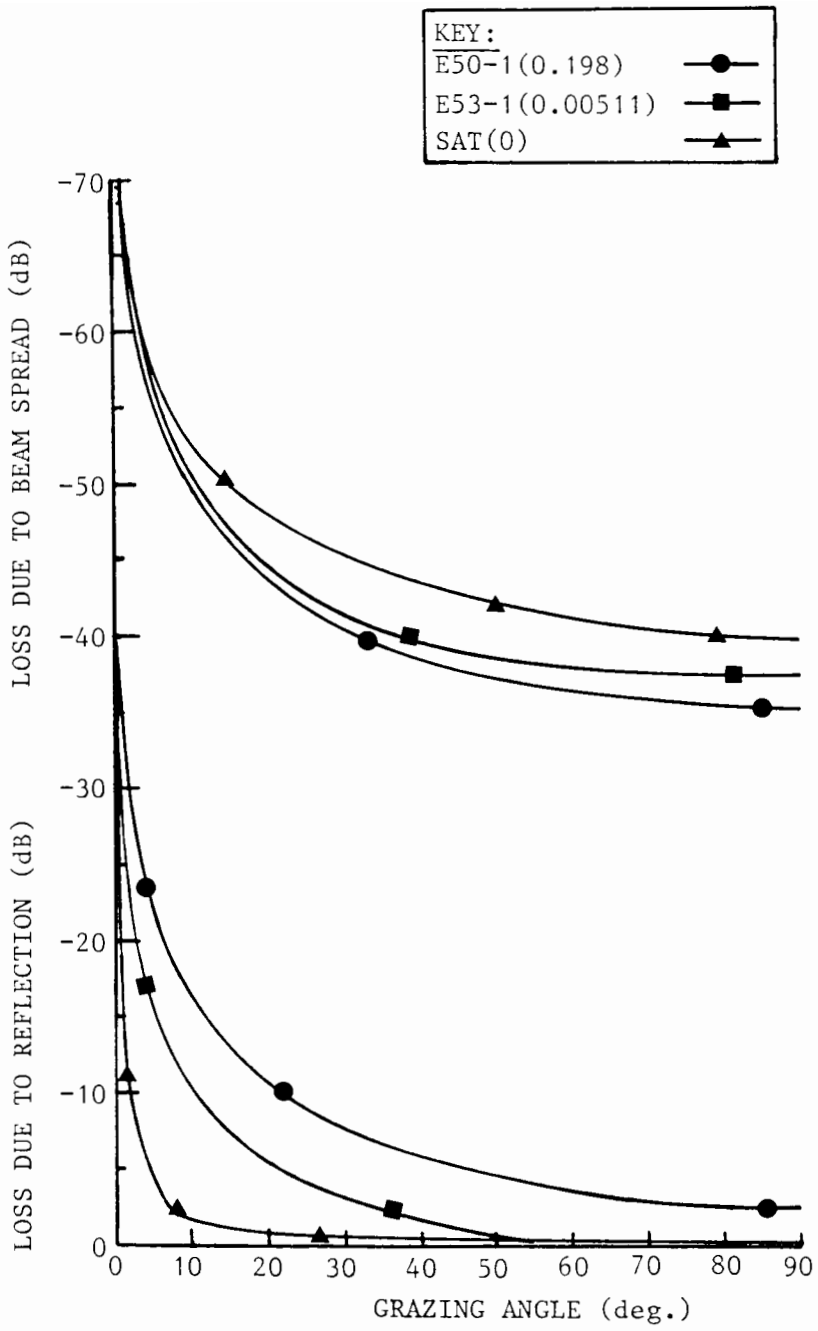


Figure 8.5 - Theoretical losses at a mudline interface, versus grazing angle ('below resonance')

TABLE 3.1 Transducer dimensions

Transducer frequency range (kHz)	Diameter (cm) (D)	THICKNESS (cm) (l_S) Steel	PZT-4	(l_{Al}) Aluminium	(l_A) Araldite
20-40	5	3.83	0.2	4.08	1.9
40-95	4	1.76	0.2	2.04	0.95
95-200	2	0.68	0.2	0.98	0.46

Table 3.2 - Sound speed measurement accuracy -- $\Delta C = C \left(\frac{\Delta S}{S} + \frac{\Delta T}{T} \right)$
(C = sound speed, S = soil depth, T = transit time)

	LEADING EDGE METHOD		TTC METHOD		FT METHOD			
					WITHOUT TTC		WITH TTC	
	Cell 1	Cell 2	Cell 1	Cell 2	Cell 1	Cell 2	Cell 1	Cell 2
S (mm)	20	65	20	65	20	65	20	65
ΔS (mm)	±0.025	±0.025	±0.025	±0.025	±0.025	±0.025	±0.025	±0.025
T = S/C (μs) (C = 1500 m/s)	13.33	43.33	13.33	43.33	13.33	43.33	13.33	43.33
T = S/C (μs) (C = 350 m/s)	57.14	185.71	57.14	185.71	57.14	185.71	57.14	185.71
ΔT (μs) (C = 1500 m/s)	±0.05	±0.05	±0.62	±0.62	±0.08	±0.13	±0.08	±0.13
ΔT (μs) (C = 350 m/s)	±0.05	±0.05	±0.62	±0.62	±0.34	±0.56	±0.34	±0.56
ΔC (m/s) (c = 1500 m/s)	±7.50	±2.31	±70.34	±22.04	±10.88	±5.08	±81.22	±27.12
ΔC (m/s) (C = 350 m/s)	-	-	±4.24	±1.30	±2.52	±1.19	±6.76	±2.49

TABLE 3.3 - Phase shift measurements due to beat effects

FREQ. 1 (kHz)	FREQ. 2 (kHz)	FREQ. 1 AMP. (V)	FREQ. 2 AMP. (V)	AMP. RATIO			
100	110	0.11	0.22	1:2	109	-0.79	+0.07
100	120	0.11	0.22	1:2	118	-0.94	+0.12
100	150	0.11	0.22	1:2	143	-2.10	+0.25
130	150	0.11	0.22	1:2	147	-0.60	+0.10
130	180	0.11	0.22	1:2	172	-1.29	+0.17
150	180	0.11	0.22	1:2	178	-0.69	+0.04
150	200	0.11	0.22	1:2	192	-1.10	+0.15
190	200	0.11	0.22	1:2	199	-0.17	+0.02
190	200	0.11	0.165	1:1.5	198	-0.14	+0.04

Table 3.4 - Transit time corrections versus frequency and separation in water (pulsed CW system)

Frequency (kHz)	Separation (mm)	MTT (µs)	TTT (µs) @ 1493m/s	TTC (µs)	Comparisons
450	30	28.02	20.09	7.93	*
300	30	27.83	20.09	7.74	**
450	25	24.62	16.74	7.88	*
300	25	24.43	16.74	7.69	**
450	20	21.42	13.40	8.02	*
300	20	21.03	13.40	7.63	**
53.19	30	23.10	20.09	3.01	***
69.90	30	24.56	20.09	4.47	****
53.19	25	19.90	16.74	3.16	***
69.90	25	21.60	16.74	4.86	****
52.10	20	16.76	13.40	3.36	***
69.90	20	18.09	13.40	4.69	****

TABLE 3.5 - TTC CALIBRATION RESULTS (in μs) - (a) CELL 1

NOTE: The values of acoustic impedance for the different liquids are recorded in brackets in units of (x 10^6 kg/m^2s)

Frequency (kHz)	Hexane (0.725)	Kerosene (1.030)	Distilled Water (1.483)	Ethylene glycol (1.877)	Glycerol (2.463)
40	-	- 2.38	-	-	- 1.27
42	- 4.73	- 4.76	-	- 4.46	- 2.80
44	- 6.12	- 6.14	-	- 5.16	- 4.92
46	- 7.25	- 7.03	-	- 5.98	- 6.00
47	- 7.74	- 7.69	- 7.30	- 6.52	- 6.16
50	- 9.04	- 8.82	- 8.26	- 7.98	- 6.91
52	- 9.18	- 9.62	- 8.94	- 8.43	- 7.47
54	- 9.84	- 9.90	- 9.12	- 8.96	- 7.49
56	-10.26	-10.05	- 9.64	- 9.65	- 7.89
58	-11.01	-10.66	-10.65	-10.28	- 8.64
60	-11.56	-11.45	-	-11.08	- 8.99
62	-11.77	-11.80	-	-11.45	- 9.44
64	-11.66	-11.97	-	-	-10.00
66	-11.84	-12.62	-	-	-10.50
68	-	-12.68	-	-	-10.68
70	-12.58	-	-	-12.60	-11.35
72	-12.35	-	-	-12.62	-11.47
74	-12.41	-	-	-12.72	-11.96
76	-12.53	-	-	-12.93	-11.61
78	-12.18	-12.54	-	-12.95	-11.62
82	-11.85	-12.30	-	-12.30	-11.53
86	-12.21	-12.06	-	-	-12.02
90	-12.29	-12.14	-	-	-
94	-12.34	-12.06	-	-	-
98	-12.50	-12.06	-	-	-
101	-12.17	-12.08	-	-11.89	-
105	-12.23	-11.50	-	-11.70	-
110	-12.09	-11.86	-	-11.88	-
115	-11.93	-11.72	-	-11.73	-
120	-12.29	-11.87	-	-11.79	-
125	-12.26	-11.73	-	-11.82	-
130	-12.96	-12.38	-	-12.03	-
135	-	-	-	-11.86	-
140	-	-	-	-11.79	-
145	-	-	-	-11.15	-
150	-	-	-	-10.67	-
155	-	-	-	-	-
160	-	-	-	-	-
165	-	-	-	-	-
170	-	-	-	-	-
175	-	-	-	-	-
180	-	-	-	-	-
185	-	-	-	-	- 8.88
190	-	-	-	-	- 8.70
200	-	-	- 8.65	-	- 8.74
210	- 8.17	- 8.09	- 8.14	-	- 8.36
220	- 8.72	- 8.46	- 8.52	-	- 8.36
230	- 9.04	- 8.82	- 8.80	- 9.04	- 8.63
240	- 8.96	- 8.77	- 8.83	- 8.98	- 8.96
250	- 8.64	- 7.89	- 9.04	- 8.91	- 8.96
260	- 8.92	- 8.69	- 8.97	- 8.96	- 8.84
270	- 8.82	- 8.76	- 8.80	- 8.79	- 8.77
280	- 8.62	-	- 8.69	- 8.73	- 8.76
290	- 8.69	- 8.59	- 8.59	- 8.70	- 8.65
300	- 8.64	- 8.77	- 8.69	- 8.88	- 8.76
310	- 8.99	- 8.77	- 8.67	- 8.72	- 8.82
320	- 8.65	- 8.50	- 8.51	- 8.70	- 8.71
330	- 8.34	- 8.16	- 8.25	- 8.41	- 8.27
340	- 8.44	- 8.47	- 8.37	- 8.31	- 8.25
350	- 8.12	- 7.92	- 7.94	- 8.04	- 8.05
360	- 8.37	- 8.14	- 8.14	- 8.20	- 8.23
370	- 8.50	- 8.51	- 8.52	- 8.59	- 8.61
380	- 8.44	- 8.31	- 8.28	- 8.36	- 8.43
390	- 8.17	- 8.02	- 8.15	- 8.17	- 8.23
400	- 8.51	- 8.31	- 8.40	- 8.45	- 8.62
410	- 8.47	- 8.31	- 8.13	- 8.20	- 8.26

TABLE 3.5 - TTC CALIBRATION RESULTS (in μs) - (b) CELL 2

Note - as Table 3.5(a)

Frequency (kHz)	Hexane (0.725)	Kerosene (1.030)	Olive Oil (1.348)	Distilled Water (1.483)	Ethylene glycol (1.877)	Glycerol (2.463)
47	-	-	-	-21.79	-17.95	-
46	-	-	-	-20.97	-20.02	-17.16
45	-	-	-	-	-19.71	-17.86
44	-	-	-	-20.67	-19.67	-18.22
43	-	-	-	-20.54	-19.35	-17.76
42	-	-	-	-20.00	-19.20	-17.99
41	-	-	-	-19.85	-19.32	-17.90
40	-	-	-	-19.55	-19.32	-18.02
39	-	-	-	-19.09	-18.45	-17.99
38	-20.96	-	-	-18.77	-17.92	-17.54
37	-20.12	-19.55	-	-17.96	-17.35	-16.90
36	-19.40	-18.83	-17.63	-16.81	-16.36	-16.08
35	-18.78	-18.70	-16.67	-16.53	-15.31	-15.04
34	-17.98	-17.59	-16.23	-15.76	-14.85	-13.78
33	-16.62	-16.58	-15.10	-14.93	-13.87	-13.96
32	-14.67	-14.82	-13.90	-13.54	-12.48	-13.12
31	-13.66	-13.48	-13.16	-12.96	-11.88	-12.58
30	-12.19	-12.04	-11.24	-11.21	-10.52	-11.25
29	-10.26	-10.50	-10.16	- 9.93	- 9.44	-10.03
28	- 8.38	- 8.66	- 7.82	- 8.16	- 7.78	- 9.19
27	- 5.97	- 6.90	- 6.13	- 6.88	- 5.81	-
26	- 3.78	-	-	-	- 3.78	-
25	- 1.87	-	-	-	- 1.82	- 4.41
24	+ 0.66	-	-	-	- 0.39	- 1.95
23	+ 3.67	-	-	-	+ 1.90	- 0.01
22	+ 5.94	-	-	-	+ 4.15	+ 0.40
21	+ 8.94	+ 5.42	+ 5.87	+ 7.12	+ 6.59	+ 3.64
20	+12.24	+ 9.07	+ 8.57	+ 9.62	+ 9.29	+ 5.59
19	+15.61	+13.11	+12.14	+12.09	+12.28	+ 9.52
18	+19.34	+16.04	+16.10	+16.53	-	+12.64
17	+23.52	+21.13	+20.86	+21.66	-	+17.60
16	+28.22	+24.94	+27.94	+24.83	-	+23.69
15	+33.54	+29.63	-	+31.01	-	+28.58
14	+46.77	-	-	+38.27	-	+36.73
13	+52.20	-	-	+46.43	-	+41.85
12		-	-	+56.65	-	+53.85
11		-	-	-	-	+66.78

TABLE 3.6 - TTC values for distilled water (varying frequency and path length) C.W waveform

Frequency (kHz)	Separation = 20 mm TTT = 13.39 μs		Separation = 25 mm TTT = 16.74 μs		Separation 30 mm TTT = 20.09 μs	
	MTT (μs)	TTC (μs)	MTT (μs)	TTC (μs)	MTT (μs)	TTC (μs)
47	19.65	- 6.25	26.60	- 9.9	27.30	- 7.2
49.4	24.40	-11.00	23.80	- 7.1	28.00	- 7.9
51	21.96	- 8.56	26.35	- 9.65	27.95	- 7.85
53	24.45	-11.05	27.00	-10.30	28.95	- 8.85
54.9	23.85	-10.45	26.15	- 9.45	31.55	-11.45
57.8	24.00	-10.60	26.15	- 9.45	28.20	- 8.1
61.3	24.95	-11.45	30.15	-13.45	32.55	-12.45
63.3	25.65	-12.25	31.05	-14.35	33.60	-13.50
65.2	29.00	-15.60	32.45	-16.25	34.20	-14.10
65.6	29.00	-15.60	33.30	-16.60	34.20	-14.10

TABLE 4.1 (a) Raw input planar data and (b) Reconstructed planar data.

Bin Number	(a) Raw input planar data		(b) Reconstructed planar data	
	Void fraction	Cum void fraction	Void Fraction	Cum void fraction
1	0.006161	0.006165	0.006165	0.006165
2	0.004584	0.010749	0.004584	0.010749
3	0.003549	0.014298	0.003549	0.014298
4	0.003108	0.017405	0.003108	0.017406
5	0.002481	0.019886	0.002481	0.019887
6	0.002066	0.021952	0.002066	0.021953
7	0.001238	0.023190	0.001238	0.023191
8	0.001553	0.024743	0.001553	0.024744
9	0.002077	0.026820	0.002077	0.026821
10	0.002030	0.028850	0.002030	0.028851
11	0.001149	0.029999	0.001149	0.030000
12	0.001357	0.031357	0.001357	0.031357
13	0.001024	0.032381	0.001184	0.032541
14	0.003511	0.035892	0.003511	0.036052
15	0.003250	0.039143	0.003250	0.039302
16	0.003878	0.043020	0.003878	0.043180
17	0.005185	0.048206	0.005185	0.048365
18	0.004330	0.052536	0.004488	0.052835
19	0.007355	0.059891	0.007355	0.060208
20	0.009284	0.069176	0.009284	0.069492
21	0.002855	0.072030	0.002855	0.072347
22	0.000000	0.072030	0.000912	0.073259
23	0.001357	0.073387	0.001357	0.074616
24	0.001630	0.075017	0.001692	0.076308
25	0.002970	0.077987	0.002970	0.079278
26	0.002347	0.080334	0.002347	0.081625

Note - Bins 27 to 34 are zero since no voids have been found to exist larger than bin size 26 for the sample tested here.

Table 4.2 - Gas contents of the four soil specimens

SAMPLE	METHANE IMPREGNATION PERIOD (HOURS)	PYCNOMETER VOID RATIO	PYCNOMETER DEGREE OF SATURATION (%)	PYCNOMETER GAS VOID FRACTION	BSD GAS VOID FRACTION	Maximum bin number of the void sizes filled with water (not gas) as found by:	
						PYCNOMETER	BSD
A	0	1.06	100	0	0	14	14
B	2	1.23	91.1	0.049	0.074	16	14
C	12	1.24	86.1	0.077	0.098	15	14
D	17	1.26	86.1	0.078	0.099	16	14

Note - Gas void fraction = $\frac{\text{Volume of gas}}{\text{Total volume of soil}}$

Table 4.3 - Soil confining pressures for the specimens of Figure 4.8(d)

Sample	Total stress (σ_1) (kPa)	Back pressure (u_w) (kPa)	($\sigma_1 - u_w$) (kPa)
SAT	100	0	100
0	100	0	100
100	200	100	100
400	500	400	100

Table 4.4 - Soil confining pressures for the specimens of Figure 4.8(f)

Sample	Total stress (σ_1) (kPa)	Back pressure (u_w) (kPa)	($\sigma_1 - u_w$) (kPa)
200	200	100	100
300	300	100	200
100	100	0	100

TABLE 5.1 - Properties of soil used in the research programme tests

TEST	Methane/ zeolite Proportion (100%)	Gas fraction (F_g)	Degree of saturation (%) (S_d)	Bulk density (kg/m^3)	Void ratio (e)	Total void fraction (F_v)
E50-1	100	0.198	72	1322	2.311	0.698
E50-2	100	0.173	75	1363	2.215	0.689
E52-1	50	0.082	87	1513	1.899	0.655
E52-2	50	0.115	83	1459	2.003	0.667
E53-1	17	0.00511	99.18	1639	1.674	0.626
E53-2	17	0.00407	99.35	1640	1.674	0.626
E51-1	2.5	0.00484	99.23	1640	1.674	0.626
E51-2	2.5	0.00357	99.43	1643	1.667	0.625

TABLE 6.1 - Resonance frequencies of bubble groups (calculated from equation A8, Appendix A)

Average bubble diameter (μm)	SAMPLE NUMBER (and frequency in kHz)							
	E50-1	E50-2	E52-1	E52-2	E53-1	E53-2	E51-1	E51-2
137	-	-	-	-	1302	1297	1297	-
155	-	-	-	-	1149	1145	1145	-
174	-	-	-	-	1028	1024	1024	1039
192	-	-	-	-	930	927	927	940
210	-	-	-	-	849	846	846	858
229	793	-	-	-	781	778	778	790
247	734	734	-	-	723	721	721	731
276	661	661	653	-	651	649	649	658
312	583	583	577	-	574	-	572	581
348	521	521	516	516	514	-	512	520
385	472	472	467	467	465	-	463	470
422	431	431	426	426	425	-	-	429
458	396	396	392	392	391	-	-	395
504	361	360	356	356	-	-	-	359
559	325	325	321	321	-	-	-	324
614	296	296	293	293	-	-	-	295
669	271	271	269	269	-	-	-	270
734	248	248	245	245	-	-	-	-
807	225	225	223	223	-	-	-	-
880	206	206	-	204	-	-	-	-
963	189	189	-	187	-	-	-	-
1055	172	172	-	170	-	-	-	-
1146	159	159	-	157	-	-	-	-
1247	146	146	-	144	-	-	-	-
1357	134	134	-	132	-	-	-	-
1476	123	123	-	121	-	-	-	-
1605	113	113	-	112	-	-	-	-
1746	104	104	-	-	-	-	-	-

TABLE 6.2 - ($f_o r$) products from experiment sound speed results

SAMPLE	PEAK GAS CONTENT BUBBLE SIZE			LARGEST BUBBLE SIZE	
	Average Bubble diameter (μm)	Transition point (kHz)	$f_o r$ product (Hz.cm)	Average Bubble diameter (μm)	$f_o r$ product (Hz.cm)
E50-1	312	20	312	1746	1746
E50-2	422	20	422	1746	1746
E53-1	-	20	-	458	458
E51-1	137	80	548	385	1540

TABLE 7.1 - ($f_o r$) products from experiment attenuation results

SAMPLE	PEAK GAS BUBBLE SIZE			LARGEST BUBBLE SIZE	
	Bubble diameter (μm)	Change point in rate of loss increase (kHz)	$f_o r$ product (Hz.cm)	Bubble diameter (μm)	$f_o r$ product (Hz.cm)
E50-1	312	50	780	1746	4365
E52-1	458	45	1031	807	1816
E52-2	422	45	950	1605	3611
E53-1	-	340	-	458	7786
E51-1	137	170	1165	385	3273

TABLE 8.1 - Values of the elastic moduli (below resonance)

Sample	(a) Anderson upper bound (compressible fluid model)		(b) Anderson lower bound (suspension theory)	
	G (MPa)	K (MPa)	G (MPa)	K(MPa)
E51-2	130	116.46	0	36.884
E53-2	130	111.99	0	32.394
E51-1	130	106.89	0	27.279
E53-1	130	105.46	0	25.848
E52-1	130	81.32	0	1.622
E52-2	130	80.85	0	1.157
E50-2	130	80.47	0	0.769
E50-1	130	80.37	0	0.672

Sample	(a) Wheeler upper bound (Large bubble model, dynamic (G) and (K))		(b) Wheeler lower bound (Measured static (G) and (K))	
	G (MPa)	K (MPa)	G (MPa)	K(MPa)
E51-2	19.880	2360.0	1.988	685.0
E53-2	19.870	2250.0	1.987	600.0
E51-1	19.840	2140.0	1.984	510.0
E53-1	19.830	2070.0	1.983	490.0
E52-1	17.170	230.0	1.718	26.0
E52-2	16.000	160.0	1.601	15.0
E50-2	13.850	80.0	1.388	7.0
E50-1	12.910	67.0	1.298	6.8

TABLE 8.2 - Values of (K) for varying (P_o) - Anderson's 'compressible fluid' model (below resonance)

Sample	K(MPa) for P_o = 1 atmospheres	K(MPa) for P_o = 5 atmospheres	K(MPa) for P_o = 100 atmospheres
E51-2	116.46	256.20	1895.06
E53-2	111.99	235.46	1776.94
E51-1	106.89	211.59	1623.89
E53-1	105.46	204.87	1576.55
E52-1	81.32	87.76	233.27
E52-2	80.85	85.45	190.57
E50-2	80.47	83.53	154.17
E50-1	80.37	83.04	144.94

NOTE - The value of (G) for each sample, regardless of (P_o), is 130 MPa.

APPENDIX A - The equations of Anderson (1974) used to develop expressions for sound speed

(I) Below resonance

$$K = \frac{K_g K_w K_m}{n_g K_w K_m + (1-n) K_w K_g + (n-n_g) K_m K_g} \quad \text{A1}$$

$$\rho = n_g \rho_g + (1-n) \rho_m + (n-n_g) \rho_w \quad \text{A2}$$

where:

K_g = gas bulk modulus
K_w = water bulk modulus
K_m = mineral particle bulk modulus
n = total void porosity
n_g = gas porosity
ρ_g = gas density
ρ_m = mineral density
ρ_w = water density

$$K = K_m \left(\frac{K_f + Q'}{K_m + Q'} \right) \quad \text{A3}$$

where: K_f = sediment frame bulk modulus, and

$$Q' = \frac{K_w' (K_m - K_f)}{n (K_m - K_w')} \quad \text{A4}$$

$$K_w' = \frac{K_w \gamma P_o}{n_g' K_w + (1-n_g') \gamma P_o} \quad \text{A5}$$

where:

γ = ratio of specific heats
ρ_o = ambient hydrostatic pressure
n_g' = fraction of sediment pore volume occupied by gas

(II) At resonance

$$f_o = \frac{1}{2\pi r_o} \sqrt{\left[\frac{3\gamma p_o}{A \rho_w} \right]} \quad \text{A6}$$

where:

r_o = equilibrium bubble radius

$$A = [\, 1+B^2] \, [\, 1 + \frac{3(\gamma-1)}{X} \, (\frac{\sinh X - \sin X}{\cosh X - \cos X})$$

$$B = 3(\gamma-1)\left[\frac{X(\sinh X + \sin X) - 2(\cosh X - \cos X)}{X^2(\cosh X - \cos X) + 3(\gamma-1)(\sinh X - \sin X)}\right]$$

$$X = r_o\ \omega\ \rho_g \frac{S_p}{c_g}$$

ω = rotational frequency (=$2\pi f$)
f_o = resonance frequency
f = frequency
ρ_s = sediment matrix bulk density
S_p = specific heat of gas at constant pressure
c_g = conductivity of gas

$$f_o = \frac{1}{2\pi r}\ \sqrt{\left(\frac{3\gamma P_o + 4G}{\rho_s}\right)} \qquad \text{A7}$$

where:

r = bubble radius

$$f_o = \frac{1}{2\pi r}\ \sqrt{\left(\frac{3\gamma P_o}{A\rho_s} + \frac{4G}{\rho_s}\right)} \qquad \text{A8}$$

$$X_1 = \sum_{l=1}^{M} \frac{v_l(1-f_{*l}^2)}{(1-f_{*l}^2)+d_{*l}^2} \qquad \text{A9}$$

$$Y_1 = \sum_{l=1}^{M} \frac{v_l\ d_{*l}^2}{(1-f_{*l}^2)+d_{*l}^2} \qquad \text{A10}$$

where:

$f_{*l} = f/f_{ol}$
$d_{*l} = d\ f_{*l}^2$
$d_r = k\ r\left(\frac{\omega_o}{\omega}\right)$
ω_o = rotational frequency at resonance (=$2\pi f_o$)
k = wave number (= $2\Pi/\lambda$)
λ = wave length (= c/f)
$d_t = B$ (thermal damping constant)
$d_f = \frac{4G'}{\rho_s \omega^2 r^2}$ (friction/viscous damping constant)
$d = d_r + d_t + d_f$ (damping constant)
$G^* = G + i\ G'$ (complex shear modulus)

APPENDIX B - Table 1 - Parameter values for equation 1.2(Chapter 1) and A9, A10 (Appendix A)

FIRST OPTION (ANDERSON G AND K)

γ = 1.313 (Kaye and Laby [1973])

$\frac{\rho_g S_p}{c_g}$ = 500 sec/m (see note 2 below)

ρ_s = 1597 kg/m^3 (measured-saturated soil sample)

ρ_w = 1020 kg/m^3 (measured from water)

ρ_g = 0.6623 kg/m^3 (CRC Handbook [1981])

c_o = 1502.5 (measured-experiment E53)

G = 1.3×10^8 N/m^2 (Value of a dynamic, saturated, surficial sediment - Smith (1973), Hamilton (1971))

G′ = 0.325×10^8 N/m^2 (25% of G - Anderson (p129, 1974))

K = 3.64986×10^9 N/m^2 (from Gassman equations A3, A4, (Appendix A))

K_f = 0.00797×10^{10} N/m^2 (Anderson (Table VI-3), 1974) - saturated soil

K_m = 5.0×10^{10} N/m^2 (Anderson (Table VI-3, 1974) - saturated soil)

K_w = 0.23×10^{10} N/m^2 (Anderson (Table VI-3, 1974) - saturated soil)

P_o = 1.01325×10^5 N/m^2

n = 0.625 (measured saturated soil sample)

r_o = $(\frac{P}{P}1)^{1/3\gamma} r_1$ (adiabatic compression where (P_1) is the new back pressure and (r_1) is the measured bubble radius)

SECOND OPTION (WHEELER G AND K)

As above except for G and K as follows:

G = 0.5×10^8 N/m^2 (G′ = 0.125×10^8 N/m^2)

K = 4.211×10^9 N/m^2

NOTE 1

To avoid the problems of dealing with hyperbolic function numbers of excessive numeric value, resulting from the equations of A and B (A6), the value of X was constrained to no higher than 60. For X=60, the following terms in A and B were redefined to the approximate values:

$$\left(\frac{\sinh X - \sin X}{\cosh X - \cos X}\right) = 1.0$$

and $$B = 3(\gamma-1)\left[\frac{X - 2}{(X^2 - 3(\gamma-1))}\right]$$

NOTE 2

This value is used by Anderson (page 70, 1974). Although the units are not consistent with the three parameters shown, they are consistent with the non-dimensional term X where $\left(\frac{\rho_g S_p}{c_g}\right)$ is used (see the variables of equation A6).

REFERENCES

Adler, L., Rose, J.H. and Mobley, C. (1986). Ultrasonic method to determine gas porosity in aluminium alloy castings: Theory and experiment. J. of Applied Physics, Vol. 59(2), pp336-347.

Anderson, A.L., Muir, T.G.Jn., Adair, R.S. and Tolbert, W.H. (1968). A geoacoustic survey of the Brazos River, Part 1: Environment studies. Defence Research Laboratories, University of Texas at Austin.

Anderson, A.L., Harwood, R.J. and Lovelace, R.T. (1971). Investigation of gas in bottom sediments. Applied Research Laboratories, University of Texas at Austin, Report ARL-TR-70-28.

Anderson, A.L. (1974). Acoustics of gas bearing sediments. University of Texas. Report ARL-TR-74-19.

Andreeva, I.B. (1964). Scattering of sound by air bladders of fish in deep sound scattering ocean layers. Sov. Phys. Acoust., Vol.10, pp17-20.

Bedford, A. and Stern, M. (1983). A model for wave propagation in gassy sediments. J.A.S.A., Vol.73(2), pp409-417.

Biot, M.A. (1956). Theory of deformation of a porous viscoelastic anisotropic solid. J. of Applied Physics, Vol.27(5), pp459-467.

Biot, M.A. (1962). Mechanics of deformation and acoustic propagation in porous media. J. of Applied Physics, Vol.33(4), pp1482-1498.

Biot, M.A. (1962). Generalized theory of acoustic propagation in porous dissipative media. J. of Applied Physics, Vol.34(9), pp1254-1264.

Blanchard, D.C. and Woodcock, A.H. (1957). Bubble formation and modification in the sea and its meteorological significance. Tellus, Vol. 9, pp145-158.

Boehme, H., Chotiros, N.P., Rolleigh, L.D., Pitt, S.P., Garcia, A.L., Goldsberry, T.G. and Lamb, R.A. (1985). Acoustic backscattering at low grazing angles from the ocean bottom. Part 1, Bottom scattering strength. J.A.S.A., Vol.77(3), pp962-974.

Boyes, E.D., Goringe, M.J., Gill, J.J., Muggeridge, B.J., Northover,J.P. and Salter, C.J. (1983). Slow scan imaging applications of a digital video framestore system. Electron Microscopy and Analysis.

Bracewell, R.N. (1978). The Fourier transform and its applications. McGraw-Hill Kogakusha, Ltd., Second edition.

Brandt, H. (1960). Factors affecting compressional wave velocity in unconsolidated marine sand sediments. J.A.S.A., Vol.32, pp171-179.

Brekhovskikh, L.M. (1960). Waves in layered media. Academic, New York, pp15-22.

Breslau, L.R. (1965). Classification of sea floor sediments with a shipborne acoustical system. Woods Hole Ocean. Inst., Contribution No. 1678.

Breslau, L.R. (1967). The normally incident reflectivity of the sea floor at 12kc and its correlation with physical and geological properties of naturally occuring sediments. Woods Hole Ocean Inst. Ref.67-16.

Bucker, H.P. and Morris, H.E. (1973). Reflection of sound from a layered ocean bottom. Proceedings of a conference on oceanic acoustic modelling, SACLANT-ASW Res. Centre, La Spezia, Italy, pp19-35.

Butenko, J. and Barbot, J.P. (1979). Geological hazards related to offshore drilling and construction in the Orinoco River Delta, Venezuala. Offshore Techn. Conf., Houston, Paper no. OTC 3395, Vol.1, pp323-329.

Chapman, N.R. (1983). Modelling ocean-bottom reflection loss measurements with the plane-wave reflection coefficient. J.A.S.A., Vol.73, pp1601-1607.

Chiou, Wen - Au, (1981). Clay fabric of gassy submarine sediments. PhD. Thesis. A and M Texas University.

Chotiros, N.P., Boehme, H., Goldsberry, T.G., Pitt, S.P., Lamb, R.A. Garcia, A.L. and Altenburg, R.A. (1985). Acoustic backscattering at low grazing angles from the ocean bottom, Part 2. Statistical characteristics of bottom backscatter at a shallow water site. J.A.S.A., Vol. 77(3), pp975-983.

Clay, C.S., Medwin, H. and Wright, W.M. (1973). Specularly scattered sound and the probability density function of a rough surface. J.A.S.A., Vol.53, pp1677.

Clay, C.S. and Leong, W.K. (1974). Acoustic estimates of the topography and roughness spectrum of the sea floor south west of Iberian Peninsula. Phys. of Sound in Mar. Sed., L. Hampton, Ed. New York: Plenum, pp373-446.

Clay, C.S. and Medwin, H. (1977). Acoustical Oceanography, Wiley.

Claypool, G.E. and Kaplan, I.R. (1974). The origin and distribution of methane in marine sediments. Natural gases in marine sediments, Edited by I.R. Kaplan. Plenum Press, pp99-139.

Denbigh, P.N. and Tucker A. (1983). Sea-bed characterization from measurements of backscattering strength. Acoustics and the sea bed Proceedings of an Institute of Acoustics underwater acoustics group conference,Bath University Press.

Devin C.Jn. (1959). Survey of thermal, radiation and viscous damping of pulsating air bubbles in water. J.A.S.A., Vol.31, pp1654-1667.

Domenico, S.N. (1976). Effect of brine gas mixtures on velocity in an unconsolidated sand reservoir. Geophysics, Vol.41, pp882-894.

Duncan, A.R. and Pantin, H.M. (1969). Evidence for submarine geothermal activity in the Bay of Plenty. N.Z. J. of Marine and Freshwater Res., Vol.3, No.4, pp602-606.

Dunsiger, A.D., Cochrane, N.A. and Vetter, W.J. (1981). Seabed characterization from broad-band acoustic echo-sounding with scattering models. IEEE Transactions of Oceanic Engineering, Vol.OE-6, NO.3, pp 94-106.

Eckart, C. (1953). The scattering of sound from the sea surface. J.A.S.A., Vol.25, pp566-570.

Edrington, T.S. and Calloway, T.M. (1984). Sound speed and attenuation measurements in gassy sediments in the Gulf of Mexico. Geophysics, Vol.49(3), pp297-299.

Egerton, H.E. (1965). Sub-bottom penetration in Boston Harbour. J. of Geophys. Res., Vol.70, pp2931-2934.

Emery, K.O. (1945). Entrapment of air in beach sand. J. Sediment. Petrol. Vol.15, pp39-49.

Erikson, E. (1960). The yearly circulation of chloride and sulfur in nature; meteorological, geochemical and pedological implications - II, Tellus 12, pp63-109.

Esrig,M.I. and Kirby, R.C. (1977). Implications of gas content for predicting the stability of submarine slopes. Marine Geotechnology, Vol. 2, pp81-100.

Fannin, N.G.T. (1979). I.G.S. pockmark investigations 1974-78. I.G.S. Report No. 98.

Fitzpatrick E.A. (1984). Micromorphology of soils. Chapman and Hall.

Frisk, G.V., Doutt, J.A. and Hays, E.E. (1981). Bottom interaction of low frequency acoustic signals at small grazing angles in the deep ocean. J.A.S.A., Vol.69(1), pp84-93.

Fryer, G.J. (Jan. 1978). Reflectivity of the ocean bottom at low frequency. J.A.S.A., Vol. 63.

Gassman, F. (1951). Elastic waves through a packing of spheres. Geophysics, Vol.16, pp673-685.

Gill, J.J (1983). Part 2, D.Phil thesis, Department of Metallurgy, Oxford University.

Greene-Kelly, R. (1973). The preparation of clay soils for the determination of structure. J. of Soil Science, Vol.24, No.3.

Grindley, J. (1955). River Thames pollution of gas from the bottom deposites of the estuary. Dock and Harbour Authority, Vol.36, pp79-80.

Grubnik, N.A. (1961). Investigation of the acoustic properties of underwater soil at high acoustic frequencies. Sov. Phys.-Acoust., Vol.6, pp447-454.

Hamilton, E.L. (1971). Elastic properties of marine sediments. J. of Geophys. Res., Vol.76, pp579-604.

Hamilton, E.L. (1972). Compressional wave attenuation in marine sediments. Vol.37, No.4, pp620-646.

Hamilton, E.L. and Backman R.T. (Dec. 1982). Sound velocity and related properties of marine sediments. J.A.S.A. Vol.72(6), pp1891-1904.

Hastrup, O.F. (1970). Digital analysis of acoustic reflectivity in the Tyrrhenian Abyssal Plain. J.A.S.A., Vol.70.

Hochstein, M.P. (1970). Seismic measurements in Suva Harbour (Fiji). N.Z. J. Geol. Geophysics, Vol.13, pp269-281.

Hovland, M. (1984). Gas-induced erosion features in the North Sea. Earth Surface Processes and Landforms, Vol.9, pp209-228.

Hoyt, J.H. and Henry Jn., J. (1964). Developement and geologic significance of soft beach sand. Sedimentology, Vol.3, pp44-51.

Hutchinson, G.E. (1957). Treatise on Limnology. Vol.1, Geography, Physics, Chemistry. Wiley, New York.

Jardine, R.J., Symes, M.J. and Burland, J.B. (1984). The measurement of soil stiffness in the triaxial apparatus. Geotechnique, Vol.34, No.3.

Jensen, M.L. (1960). Sulfur isotopes in the marine environment. Marine Geochemistry, edited by D.R. Schink and J.T. Corless. Occasional publication no.3, symposium at University of Rhode Island, Narragansett Marine Laboratory, pp131-148.

Jensen, E.B. (1984). A design-based proof of Wicksell's integral equation. J. of Microscopy, Vol.136, Part 3.

Jones, J.L., Leslie, C.B. and Barton, L.E. (1958). Acoustic characteristics of a lake bottom. J.A.S.A., Vol.30(2), pp142-145.

Jones, J.L., Leslie, C.B. and Barton, L.E. (1964). Acoustic characteristics of underwater bottoms. J.A.S.A., Vol.36(1), pp154-157.

Jones, G.B., Floodgate, G.D., and Bennel, J.D. (1985). Chemical and microbiological aspects of acoustically turbid sediments: Preliminary investigations. Marine Geotechnology, Vol.6(3), pp315-331.

Kanwisher, J. (1962)[a]. Gas exchange of shallow marine sediments. 'The Environmental Chemistry of Marine Sediments'. Proceedings of a symposium at Rhode Island, Narragansett Marine Laboratory, 13-19.

Kanwisher, J. (1962)[b]. Sulfur chemistry in marine muds. 'Biochemistry of Sulfur Isotopes', edited by M.L. Jensen, (NSF Symposium Volume, Yale University, New Haven, CT), pp94-103.

Kaplan, I.R. (1974). Natural gases in marine sediments. Plenum Press. New York, p324.

Kaye, J.V.C. and Laby, T.H. (1973). Tables of physical and chemical constants. Edition 14, Longman.

Kepkay, P.E. (1977). Preliminary investigation of free gas as the control of a sub-bottom acoustic reflector in the fine-grained sediments of Halifax Harbour and St. Margaret's Bay, Nova Scotia. MSc. Thesis, Dalhousie University.

King, L.H. and Maclean, B. (1970). Pockmarks of the Scotian Shelf. Geol. Soc. of Am. Bull., Vol.81, pp3141-3148.

Kinney, W.A. and Clay, C.S. (1982). Spatial coherence of sound scattered from a wind-driven surface: comparison between experiment and the Facet-Ensemble Method. J.A.S.A., Vol.72(2), S 84.

LeBlanc, L.R., Middleton, F.H., Nacci, V.A. and Cohn, R.F. (1980). Correlation between estuarine sea floor acoustic reflection signatures and engineering sediment measurements. J.A.S.A., Vol.68, pp1135-1141.

Lee, K. (1979). The analytical and experimental study of large strain soil consolidation. DPhil. thesis, University of Oxford.

Leslie, C.B. (1960). Normal incident measurement of acoustic bottom constants. NAVORD Report No. 6832, U.S. Naval Ordnance Laboratory, Silver Spring, Maryland.

Levin, F.K. (1962). The seismic properties of Lake Maracaibo. Geophysics, Vol.27, pp35-47.

MacKensie, K.V. (1960). Reflection of sound from coastal bottoms. J.A.S.A., Vol.32(2), pp221-231.

Martens, C.S. and Berner, R.A. (1974). Methane production in the interstitial waters of sulphate-depleted marine sediments. Science, Vol.185, pp1167-1169.

McCann, C. and McCann, D.M. (1985). A theory of compressional wave attenuation in non-cohesive sediments. Geophysics.

McCartney B.S. and Bary, B.McK. (1965). Echo-sounding on probable gas bubbles from the bottom of Saanich Inlet, British Columbia, Deep Sea Res., Vol.12, pp285-294.

McKinney, R.E. (1962). Microbiology for sanitary engineers. McGraw Hill, New York.

McKinney, C.M. and Anderson, C.D. (1964). Measurements of backscattering of sound from the ocean bottom. J.A.S.A., Vol.36(1), pp158-163.

McQuillin, R., Bacon, M. and Barclay, W. (1979)[a]. Introduction to seismic interpretation. Graham and Trotman, London, p199.

McQuillin, R. and Fannin, N.G.T. (1979)[b]. Explaining the North Sea's lunar floor. New Scientist, Vol.1163, pp90-92.

McQuillin, R., Fannin, N.G.T. and Judd, A.G. (1979)[c]. I.G.S. pockmark investigations 1974-78. Institute of Geological Sciences, Marine Geophysics Unit, Report no. 98, p50.

Mechalas, B.J. (1974). Pathways and environmental requirements for biogenic gas production. Natural gases in marine sediments, edited I.R. Kaplan, Plenum Press, pp11-25.

Medwin, H. (1983). Experimental studies of near grazing, low frequency, forward scatter at rough surfaces. Acoustics and the sea bed - Proceedings of an Inst. of Acoust., underwater acoust. group, conf. Bath University Press.

Milligan, S.D., LeBlanc, L.R. and Middleton, F.H. (Sept.1978). Statistical grouping of acoustical reflection profiles. J.A.S.A., Vol.64, pp795-807.

Minnaert, M. (1933). On musical air bubbles and the sound of running water. Phil. Mag., Vol.10, pp235-248.

Mortimer, C.H. (1941). The exchange of dissolved substances between mud and water in lakes. J. Ecol., Vol.29, pp280-329 and Vol.30, pp147-201.

Muir, T.G. (1972). Experimental capabilities of the ARL sediment tank facility in the study of buried object detection. Applied Research Laboratories, University of Texas at Austin, Report ARL-TM-72-32.

Muir, T.G., Horton, C.W. and Thomson, L.A. (1979). The penetration of highly directional acoustic beams into sediments. J. of Sound and Vibration, Vol.64(4), pp539-551.

Nageswaran, S. (1983). Effect of gas bubbles on the sea bed behaviour. D.Phil. thesis, University of Oxford.

Newton, R.S., Cunningham, R.C. and Schubert, C.E. (1980). Mud volcanoes and pockmarks: Sea floor engineering hazards or geologic curiousities? Offshore Techn. Conf., Paper no. 3729, pp425-435.

Novarini, J.C. and Medwin H. (1978). Diffraction, reflection and interference during near-grazing and near-normal ocean surface backscattering. J.A.S.A., Vol.64(1), pp260-268.

Nyborg W.L., Rudnick, I. and Schilling, H.K. (1950). Experiments on acoustic absorption in sand and soil. J.A.S.A., Vol.22, pp422-425.

Ohle, W. (1959). Blick in die Tiefe des Gr. Ploner Sees mit Fernseh-und Photokameras. Nat. Volk. 89, pp177-188.

Ohle, W. (1960). Fernsehen, Photographie und Schallortung der Sedimentoberflache in Seen. Arch. Hydrobiol. 57, pp135-160.

Platt, J. (1977). Significance of pockmarks for engineers. Offshore Engineer, p45.

Press, F. and Ewing, M. (1948). Low-speed layer in water-covered areas. Geophysics, Vol.13(3).

Rawson, S. (1976). An investigation into the occurence of acoustic turbidity in marine sediments of the U.K. continental shelf. Tech. Report 65, I.G.S., Mar. Geophysics Unit, Edinburgh, U.K.

Ruff, G.A. (1967). Acoustic characteristics of Black Moshannon Lake bottom. J.A.S.A., Vol.42, pp524-525.

Rutherford, S.R. and Hawker, K.E. (1978). The effects of density gradients on bottom reflection loss for a class of marine sediments. J.A.S.A., Vol.63, pp750-757.

Rutherford, S.R., Hawker, K.E. and Payne S.G. (1979). A study of the effects of ocean bottom roughness on low-frequency sound propagation. J.A.S.A., Vol.65, pp381-386.

Schubel, J.R. (1974). Gas bubbles and the acoustically impenetrable, or turbid, character of some estuarine sediments. I.R. Kaplan, Plenum Press.

Silberman, E. (1957). Sound velocity and attenuation in bubbly mixtures measured in standing wave tubes. J.A.S.A., Vol.29, pp925-933.

Sills, G.C., Hoare, S.D.L. and Baker, N. (1985). An experimental assessment of the restricted flow consolidation test. A.S.T.M. Symposium on consolidation behaviour of soils, Fort Lauderdale, Florida.

Smith, D.T. (1973). Acoustic and mechanical loading of marine sediments. O.N.R. Symposium on Physics of Sound in Marine Sediments. Lakeway Inn, Austin, Texas.

Spitzer, L.Jn. (1943). Acoustic properties of gas bubbles in a liquid. OSRD 1705, Division of War Research, Columbia University.

Stainer, R.Y., Doudoroff, M. and Adelberg, E.A. (1963). The microbial world. Prentice-Hall, Englewood Cliffs, NJ.

Stanton, T.K. (1983). Sonar estimates of sea floor microroughness. J.A.S.A., Vol.75(3), pp809-819.

Stoll, R.D. (1980). Theoretical aspects of sound transmission in sediments. J.A.S.A., Vol.68, pp1341-1350.

Stoll, R.D. and Kan, T.K. (1981). Reflection of acoustic waves at a water-sediment interface. J.A.S.A., Vol.70(1), pp149-156.

Stoll, R.D. (1985). Marine sediment acoustics. J.A.S.A., Vol.77(5), pp1789-1799.

Strutt, Lord Rayleigh J.W. (1877). The theory of sound.

Tappert, F.D. (1977). The parabolic approximation method. Wave propagation and underwater acoustics - J.B. Keller and J.S. Papadakis (Springer-Berlin, 1977). Lecture notes in physics, Vol.70.

Thomas, S.D. (1987). The consolidation behaviour of gassy soil. DPhil. thesis, University of Oxford.

Thomson, D.J. (1983). The determination of material properties of the sea-bed from the acoustic plane wave reflection response. Proceedings of an Insitute of Acoustics, underwater acoustics group conference, Bath University Press (N.G. Pace, Acoustics and the sea bed).

Thorne, P.D. and Pace, N.G. (1983). Broad band studies of acoustic scattering from a model rough surface. Proceedings of an Inst. of Acoustics Underwater Acoustics Group Conference, Bath University Press.

Tolstoy, I. (1979). The scattering of spherical pulses by slightly rough surfaces. J.A.S.A., Vol.66, pp1135-1144.

Tolstoy, I. (1982). Coherent sound scatter from a rough interface between arbitrary fluids with particular reference to the roughness element shapes and corrugated surfaces. J.A.S.A., Vol.72, pp960-972.

Trefethen, J.M. (1941). Dominant factors in the formation of firm and soft sand beaches - a discussion. J. Sediment Petrol., Vol.11, pp42-43.

Weast, R.C. (1981). C.R.C. Handbook (Chemistry and Physics). Edition 61, C.R.C. Press Inc.

Wheeler, S.J. (1986). The stress strain behaviour of soils containing gas bubbles. DPhil. thesis.

Whelan, T.III , Coleman, J.M., Suhayda, J.N. and Roberts, H.H. (1977). Acoustical penetration and shear strength in gas-charged sediment. Marine Geotechnology, Vol.2, pp147-159.

Whelan, T.III., Coleman, J.M. and Suhayda, J.N. (1976). The occurance of methane in recent deltaic sediments and its effects on soil stability. Bull. Int. Assoc. Eng. Geol., No.14, pp55-64.

Whelan, T.III and Lester, C.D. (1980). Excess gas bubble pressures in modern Mississippi Delta sediments. The Delta Project, Vol. 4,pp1-9.

Wicksell, S.D. (1925). The corpuscle problem. A mathematical study of a biometric problem. Biometrica, Vol.17

Wood, A.B. (1930). A textbook of sound. Third edition, 1955, McGraw-Hill Book Company, New York.

Wood, A.B. and Weston, D.E. (1964). The propagation of sound in mud. Acustica, Vol.14.

Wood, E.J.F. (1946). Marine microbial ecology. Reinhold, New York.

Worzel, J.L. and Drake, C.L. (1959). Structure section across the Hudson River at Nyack, N.Y., from seismic observations. Ann. N.Y. Acad. Sci., Vol.80.

Yakubov, A.A., Ali-Zade, A.A. and Zeinalov, M.M. (1971). Mud volcanoes of the Azerbaijan, SSR; Atlas Academy of Science of Azerbaijan, SSR; Baku, U.S.S.R. p258.

Ying, C.F. and Truell, R. (1956). J. of Applied Physics, Vol. 27, p1086. A collection of formulas for various cases is given by K. Goebbels in 'Research Techniques in Non-destructive Testing', edited by R.S. Sharpe, Academic, New York, 1980, Vol. IV, p87.

Zobell, Z.E. (1946). Marine microbiology. Cronica Botanica, Waltham, M.A.